Laser Cooling of High Temperature Superconductors

Thesis submitted in fulfilment of the requirements for the degree of Doctor of Philosophy at the University of Oxford

Anastasia Susanna Dagmar Dietrich

St. Anne's College, Oxford



Hilary Term, 2019

Abstract

In this dissertation, we theoretically demonstrate laser light induced control and cooling over the order parameter of superconducting cuprates. We predict a non-equilibrium state with enhanced robustness against thermal fluctuations when pumped with coherent pulses. This might ultimately increase the critical temperature of the cuprate.

In particular, we propose a parametric cooling scheme for a bilayer cuprate modelled phenomenologically as a stack of long intrinsic Josephson junctions. We identify a parameter regime, which according to the switching current distribution allows a reduction of the effective system temperature by approximately 25%. This cooling scheme suppresses the thermal excitation of Josephson vortices. This might lead to an indirect mechanism for controlling topological excitations in the phase of the superconducting order parameter.

We further find that the strong driving of the cuprates can lead to parametric instabilities. To investigate the effect strong driving can have on the dissipative dynamics, we derive a Floquet-Markov master equation. We find that strong driving is a measure for probing the bath spectral density of otherwise inaccessible condensed matter systems.

Contents

Introduction **1**

1 Background: Equilibrium superconductivity **7**
1.1 Conventional superconductivity . . . 7
1.1.1 BCS theory . . . 7
1.1.2 Ginzburg Landau theory . . . 9
1.1.3 Josephson effect . . . 11
1.2 High-temperature superconductivity . . . 17
1.3 Effect of an alternating field in conventional superconductors . . . 19
1.4 Chapter summary . . . 21

2 Background: Driving macroscopic open quantum systems **23**
2.1 Laser cooling . . . 23
2.1.1 Sideband cooling in optomechanics . . . 24
2.1.2 Sideband cooling of a long Josephson Junction in the presence of a bias current . . . 29
2.1.3 Parametric cooling of bilayer stacks of short Josephson Junctions . . . 32
2.2 Parametric amplification in Josephson junctions . . . 40
2.2.1 Parametric instability . . . 40
2.2.2 Parametrically enhanced interlayer current . . . 41
2.3 Strongly driven open quantum systems . . . 45
2.3.1 Floquet-Markov master equation . . . 47
Floquet theory . . . 47
2.4 Chapter summary . . . 54

3 Controlling phase dynamics of long Josephson Junctions **55**
3.1 Josephson electrodynamics for HTSC . . . 56
3.1.1 Coupling mechanisms between intrinsic Josephson junctions . . . 56
Phenomenology of cuprate superconductor . . . 56
Capacitive coupling . . . 59
Inductive coupling . . . 60
3.1.2 Hamiltonian for coherent dynamics of coupled sine-Gordon equations 61
3.1.3 Dissipative contributions to coupled sine-Gordon equations . . . 63
Out-of-plane quasi-particle current . . . 63
In-plane quasi-particle current . . . 63
Adiabatic elimination of high-frequency modes . . . 65

3.1.4 Driving schemes . . . 66
Modulation of the critical current ($J^C(t)$-Model) . . . 66
Modulation of the permittivity ($\epsilon(t)$-Model) . . . 67
3.1.5 Coherent part of the coupled sine-Gordon equation for a driven system 68
3.2 Linearised equations of motion . . . 70
3.2.1 Normal mode frequencies . . . 72
3.3 Thermalisation . . . 77
3.4 Parametric cooling of long Josephson Junctions . . . 81
3.4.1 Quantisation of the linearised Hamiltonian . . . 81
3.4.2 Analytical cooling rate and ratio . . . 85
3.4.3 Heating due to resonance catastrophes . . . 86
3.5 Simulations . . . 88
3.5.1 Simplified linearised model . . . 88
3.5.2 Simulations of full non-linear equations of motion . . . 96
Switching current distribution . . . 99
Sample trajectories . . . 102
3.5.3 Summary of findings . . . 106
3.6 Switching between resistive, superconducting and soliton states . . . 107
3.7 Chapter summary . . . 109

4 Strongly driven open quantum systems 111
4.1 Learning coupling mechanism to an environment . . . 112
4.2 Probing for dissipation mechanism through strong parametric driving . . . 113
4.2.1 Single strongly parametrically driven harmonic oscillator . . . 113
4.2.2 Isolated system dynamics . . . 114
System-bath coupling H_{I}^{α} . . . 115
4.2.3 Driven version of the Born-Markov master equation . . . 115
4.3 Results . . . 117
4.3.1 Observables . . . 118
4.3.2 Numerical results . . . 119
4.4 Discussion of α-dependence . . . 122
4.5 Future work . . . 126
4.6 Chapter summary . . . 127

5 Conclusion and Outlook 129

A Josephson Electrodynamics 131
A.1 Modified Josephson relation including capacitive coupling . . . 131
A.1.1 Capacitive coupling . . . 131
A.1.2 Ampère's law relating phase to magnetic field . . . 135
A.2 Derivation of inductive coupling in terms of supercurrent difference . . . 135
A.2.1 Equation of motions of supercurrent difference . . . 137
A.2.2 Non-local Josephson electrodynamics . . . 138
A.3 Hamiltonian for phase difference and supercurrent difference . . . 138
A.4 Analytic expressions . . . 142

A.4.1 Transformation matrix . . . 142
A.4.2 Diagonalising Hamiltonian for spatially inhomogeneous driving . . . 142
A.4.3 Spatial structure of normal modes for finite stack . . . 143
A.4.4 Definition of cooling ratios . . . 145
A.4.5 Solving for physical parameters in a two-junction toy model . . . 147
A.5 Approaching the phase transition . . . 150
A.5.1 XY model . . . 150

B Open quantum system **155**
B.1 Quantum treatment of a single Josephson junction . . . 155
B.2 Numerical exact solution of a parametrically driven harmonic oscillator . . . 158
B.3 Derivation of the Born-Markov master equation . . . 159
B.3.1 Master equation for an undriven system . . . 165
B.3.2 Unitary transformation to $\mathcal{H}^{\alpha}$ . . . 166
B.4 General Floquet Born-Markov master equation . . . 168
B.5 Quantum Langevin equation . . . 169
B.6 Parametric cooling for two coupled springs . . . 171
B.7 Fluctuation-dissipation theorem . . . 176
B.8 Engineering of dissipative dynamics . . . 177

Bibliography **185**

Introduction

The miniaturisation of electronic circuits leads to inevitable heating due to the restriction of electrons to ever smaller circuits [1, 2]. Approximately 99% of the power loss in electronic chips currently arises from the powering of different electronic components and not the logical operations themselves [3]. This development was one of the reasons that the semiconductor industry association was ultimately forced to abandon Moore's law [4]. Current approaches to reducing the heating range from the redesign of chips to eliminate the separation between memory and processor to genuinely new schemes based on spintronics, neuromorphic computing[1] and quantum computers [2,6,7]. Though all these approaches are actively being pursued, they are mostly still in their infancy and have not made it beyond the research laboratory.

Ever since the discovery of superconductivity by Heike Kamerlingh Onnes more then a century ago [8], superconductors have been envisioned to revolutionise both energy and transport infrastructures [9] as they allow for completely dissipation-less current. However, real-life applications of superconductivity are rare, being mainly restricted to diagnostic and scientific tools. One of the reasons for this is that currently known *conventional* and *high-temperature superconductors* (HTSC) [10] need to be cooled with liquid helium and nitrogen respectively, with liquid helium being particularly expensive. The quest for a room temperature superconductor necessary to overcome the need of expensive refrigeration is still haunting the physical communities and led, among others, to the search and construction of new materials [11–13] and the application of enormous pressure [14–16]. Transient deformations [17–20] induced by the use of coherent external THz and infrared laser pulses, allow to gain a better physical understanding of HTSC and provide insights into how room temperature SC might one day be achieved.[2] The last approach was made possible through recent advances in THz technologies, which have enabled the mode-selective coherent control of the lattice dynamic by driving vibrations and other low energy degrees of freedom [21,22]. This coherent driving selectively couples to the low-energy degrees of freedom responsible for superconductivity and avoids unnecessary heating of the material. Besides the controlled creation of transient superconductivity [17–19], driving strongly correlated condensed matter systems with intense terahertz radiation has opened up unprecedented possibilities to manipulate the quantum dynamics of strongly correlated electron systems [17–19,21,23–32]. Examples include the melting of charge density waves [23–25], the generation of synthetic

[1] Analog circuits inspired by the brain [5].

[2] The THz and infrared techniques used in these experiments could provide the basis for new technologies allowing for fast switching in electronic components. However, such real-world applications require far lower laser intensities then studied in Ref. [17–20].

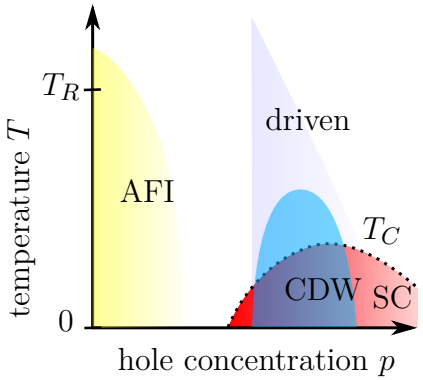


Figure 1: Sketch of a phase diagram of YBCO as a function of temperature T and hole concentration p from Ref. [33]. The phases of the equilibrium material respectively correspond to the antiferromagnetic insulator (yellow labelled AFI), charge density wave (turquoise labelled CDW) and superconducting phase (red labelled SC), which disappears at a doping dependent critical temperature T_C indicated by a dashed line around the SC regime. The blue driven phase indicates a transiently enhanced superconducting state excited by coherent driving pulses up to room temperature T_R.

magnetic fields [26], the control of heterointerfaces [27–29], the possibility to drive metal-insulator transitions [21, 30], the parametric cooling of bilayer cuprate superconductors [31] and the control of transport modes in cuprate superconductors [32].

The driving results into small changes of the system parameters, which are sufficient to tilt the balance between competing orders, stabilise otherwise unstable new states of matter with drastically different magnetic and electronic properties [21]. Irradiating strongly correlated electron systems such as high-temperature superconductors with mid-IR and THz light pulses, a transient increase of the zero frequency component of the imaginary part of the conductivity, i.e. $\sigma_2(\omega)_{\omega\to 0}$, has been observed after the excitation through laser pulses. In an equilibrium state, the imaginary part of the conductivity is proportional to the superconducting density n_s, i.e. $n_s \propto (\omega\sigma_2(\omega))_{\omega\to 0}$ [10] as explained later on page 20. In the transient non-equilibrium state, an increase of the imaginary part of the conductivity can be interpreted as an enhancement of superconductivity [17, 18, 20, 33–37]. The theoretical attempts to explain these experiments have been very diverse [31, 36, 38–46] and are often material dependent, ranging from suppression of an order competing with superconductivity [38, 41], e.g. charge stripes in Ref. [47], activation of Josephson coupling from striped state [20], static lattice distortions [42], enhanced pairing due to electronic squeezing of phonons expected for K_3C_{60} [48], to dynamical effects [38–40, 44, 46] resulting in enhancement of superexchange pairing in the Hubbard model [44] or increases in the superconducting coupling constant due to parametric driving of a phonon mode [40]. Many promising proposals based on Floquet theory of isolated many-body systems focus on achieving enhanced superconductivity in a pre-thermal state. In the long time limit, driving of an isolated many-body system generally heats it to an infinite temperature state [49–51].

Experiments on the bilayer cuprate YBCO [18, 52] have shown that the excitation of phonon modes leads to transiently enhanced superconductivity like feature characterised by an increase in the imaginary part of the conductivity up to room temperature. In these

experiments, the phonon modes, corresponding to oscillations of apical oxygen atoms that are perpendicular to the CuO_2 plane, lead to an enhancement of the zero frequency limit of the imaginary part of the conductivity $(\sigma_2(\omega))_{\omega\to 0} > 0$ far above the equilibrium critical temperature T_C [18, 35]. The corresponding equilibrium phase diagram is schematically shown in Fig. 1 as a function of temperature and doping concentration. Driving induces a transiently enhanced superconducting like state, which is labelled as "driven". Although removing a charge density wave (CDW) [53] appears to play a role; the effect is also present in the absence of CDW [18]. Hu et al. [18] find that the temperature at which the enhancement drops to zero follows the boundary of the pseudogap phase [54], which is a phase where the quasiparticles have been suggested to be still forming pairs. However, the pairs do not possess the long-range phase coherence that is necessary for superconductivity [55–57]. The observation of photoinduced superconductivity in the pseudogap phase could potentially be explained by coherence transfer from the light pulses to these preformed Cooper pairs [18,33, 36]. As YBCO is a bilayer cuprate, it can be characterised by two collective excitations, the so-called plasma modes. The pumping of infrared phonon modes was found to lead to a loss of strength of a high-frequency plasma mode with the simultaneous gain in the sharpness of the low-frequency plasma mode. This redistribution agrees with X-ray diffraction data showing a deformation of the lattice [52], which, according to density functional theory calculations, is combined with a "self-doping effect" leading to a charge transfer from the CuO_2 planes to the Cu−O bond [58]. Additional to transient deformations of the lattice structure [52], the pulse also leads to coherent oscillations in the apical oxygen, which give rise to genuine dynamical effects such as the redistribution of phase fluctuations proposed in Ref. [43, 45, 59]. Surprisingly, the melting of a transverse phonon mode [60] only leads to an enhancement of superconductivity for bilayer $YBa_2Cu_3O_{6.5}$ but not the trilayer cuprate $Bi_2Sr_2Ca_2Cu_3O_{10}$. Therefore, a multitude of different effects appears to be playing a role, and the underlying mechanism is not completely understood yet.

According to simulations in Ref. [40] the lifetime of the photo-induced superconductivity is limited by inelastic scattering of electrons from the excited phonon modes, which ultimately leads to heating of the material. To stabilise superconductivity in a steady state, it is therefore necessary, to design efficient protocols for extracting excessive energy that is deposited by the drive, and selectively exploit dissipative dynamics so as to laser cool those degrees of freedom, which are relevant for controlling superconductivity. Recent advances in THz technology [36, 61] now allow the coherent, non-linear control of lattice vibrations and other low energy degrees of freedom [21, 22]. This coherent control of the lattice dynamics allows theoretical methods to be applied to HTSC that are commonly used for laser cooling of atoms with the aim of enhancing or stabilising superconductivity in a non-equilibrium state.

Cooling schemes for artificial atoms based on artificial Josephson junctions often take advantage of the discrete energy levels [62, 63]. For sufficiently low temperatures, macroscopic tunnelling and quantisation have been even observed in HTSC [64–66] and theoretical captured by models based on intrinsic Josephson junctions [67, 68]. However, for higher temperature and large capacitance [69] the phase dynamics in HTSC is usually well described classically and the discreteness of the energy levels not relevant. However, some of the changes that occur when translating cooling schemes from atomic physics to artificial

Josephson junctions are also relevant for implementing purely classical cooling schemes in HTSC, e.g. the omnipresence of a heat bath [70] and the typically lower energies involved, i.e. THz radiation for addressing intrinsic and microwave radiation for addressing artificial Josephson junctions. Further, different to laser cooling of atoms, the system and its environment, e.g. constituted respectively by a cuprate and its phonon modes, are not spatially separated, and thermal noise is expected to be omnipresent such that it cannot be ignored on the cooling timescales.

The **first aim** of this thesis is to *develop a laser cooling scheme to selectively cool degrees of freedom of HTSC such as to stabilise superconductivity at higher temperatures*. Given the impact laser cooling had on the atomic and laser physics community, laser cooling in condensed matter systems has a large potential to reach otherwise inaccessible regimes. In this thesis, we only cool a particular degree of freedom of complex materials, e.g. the phase fluctuations in long Josephson junctions in order to stabilise superconductivity at higher temperatures.

As there is no commonly accepted theory for HTSC [71], we phenomenologically model HTSC as a stack of two dimensional intrinsic Josephson junctions throughout this thesis. This type of model has been successfully used in studies of HTSC as potential sources of THz radiation [72–77]. This simple approach allows to phenomenologically include the coupling of the system to heat baths, which can stabilise superconductivity by absorbing the energy dissipated by the drive. Our treatment only captures the many-body character of the underlying wavefunction phenomenologically. Any type of inelastic scattering of electrons, which could ultimately limit the cooling efficiency, is assumed to be sufficiently suppressed through the coupling to a heat bath.

In all these examples the driving is very strong such that it influences the dissipation and conventional treatment of open quantum systems based on weak driving assumptions are expected to break down. The **second aim** of this thesis is to *reinvestigate the interplay between strong dissipation and driving*, in the limit where the influence of the driving on the dissipation mechanism cannot be ignored, even if the coupling to the bath is sufficiently weak to justify a Born- Markov approximation. We are therefore interested in the effects the driving can have on the dissipative dynamics. For this purpose, we study the parametrically driven harmonic oscillator in Chapter 4 as a function of the system-bath interaction, which we continuously tune between position and momentum coupling via a coupling parameter. We derive a master equation for the reduced density operator of the oscillator in Born-Markov approximation and investigate its quasi-steady state as a function of the driving parameters, the temperature of the bath and the coupling parameter. We find that the driving introduces a strong dependence of the time-averaged variance of position and momentum on these parameters. In particular, we identify parameter regimes that maximise the dependence on the coupling parameter between system and bath.

Structure of the thesis

In Chapter 1, we start with an overview of conventional superconductivity and the Josephson effect, which provides the basic building blocks for the phenomenological model for HTSC as

a stack of intrinsic Josephson junctions in Chapter 3. Though we restrict ourselves to equilibrium physics in the first part of Chapter 1, we establish differences between conventional and high-temperature superconductivity, which provide the setting and motivation for the experiments on driven superconductors from Ref. [17, 18, 20, 34–36].

In Chapter 2, we extend our focus to non-equilibrium physics and discuss the sideband cooling scheme as used in optomechanics. Given the first aim of this thesis, our focus is on the applicability of this laser cooling scheme to either conventional superconductors or HTSC. For this purpose, we review the implementation of sideband cooling in a single long Josephson junction from Ref. [78] and for capacitively coupled Josephson junctions from Ref. [31]. Subsequently, we discuss effects occurring, when Josephson junctions are driven close to parametric instabilities. We finish the chapter with a discussion of strongly driven open quantum systems and the assumptions behind different approximations in the Floquet-Markov master equation, which provides the basis for Chapter 4.

Chapter 3 contains our main work regarding the parametric cooling of low-frequency phases in capacitively and inductively coupled stacks of long Josephson junctions. We start with a description of the coherent dynamics of intrinsic Josephson junctions as a phenomenological model for HTSC (Sec. 3.1). We then introduce dissipative contributions due to out-of-plane and in-plane quasi-particle currents (Sec. 3.1.3). We finish the description of the model by motivating modulations of different system parameters through the excitation of phonon modes (Sec. 3.1.4). To determine relevant parameters for the parametric cooling scheme based on Sec. 2.1.3, study the linearised equations of motion (Sec. 3.2). We finally present and discuss our results for the simulations of both linearised and full non-linear equations (Sec. 3.5).

In the parametric cooling scheme in Chapter 3, we identified a range of parametric instabilities inherent to finite size system. To better understand their influence, in Chapter 4, we focus on the strong driving regime from Chapter 2.3 such that the driving cannot be ignored in the dissipative dynamics. We study a parametrically driven harmonic oscillator as a function of different types of coupling operators to the heat bath. Subsequently, the controlling coupling parameter is related to the bath spectral density.

Finally, in Chapter 5 we summarise our main results and provide an outlook.

Publications

- Chapter 3 includes a discussion of work published in F. Schlawin, A. S. D. Dietrich, M. Kiffner, A. Cavalleri, and D. Jaksch, *Phys. Rev. B* **96**, 064526 (2017).
- Part of Chapter 3 is being prepared for publication.
- Chapter 4 is based on A. S. D. Dietrich, M. Kiffner, and D. Jaksch, *Phys. Rev. A* **98**, 012122 (2018).

Chapter 1

Background: Equilibrium superconductivity

In this chapter, we are going to briefly outline the equilibrium physics of both conventional (Sec. 1.1) and HTSC (Sec. 1.2) as captured by both microscopic and phenomenological theories. We further devote a large section of this chapter to different aspects of the Josephson effect (Sec. 1.1.3), which will be helpful for the model of HTSC in terms of stacks of Josephson junctions in Chapter 3.

1.1 Conventional superconductivity

Conventional superconductivity was first discovered in 1911 by Heike Onnes [8] using liquid helium as a cooling medium. Since then superconductivity has gained applications for the generation of strong magnetic fields, e.g. in magnetic resonance imaging (MRI) or particle accelerators.

1.1.1 BCS theory

The microscopic theory for conventional superconductors, BCS theory [79] is named after its inventors Bardeen, Cooper, Schrieffer. Cooper showed that for low enough temperature, an arbitrarily weak attractive interaction between electrons close to the Fermi surface destabilises the Fermi surface against the formation of Cooper pairs, which are singlets consisting of two fermions of opposite momentum and spins [80]. In conventional isotropic s-wave superconductors the necessary small attraction between electrons arises from the exchange of phonons [10]. Intuitively each electron induces a distortion of the lattice potential, which persists sufficiently long that it can interact with a second electron of opposite spin [81]. This phonon-mediated attractive interaction can be modelled by the BCS Hamiltonian of the form [10, 82]

$$H = \sum_{\boldsymbol{k}\sigma} \epsilon_{\boldsymbol{k}\sigma} c^\dagger_{\boldsymbol{k}\sigma} c_{\boldsymbol{k}\sigma} + \sum_{\boldsymbol{k}\boldsymbol{q}} V_{\boldsymbol{k},\boldsymbol{q}} c^\dagger_{\boldsymbol{k}\uparrow} c^\dagger_{-\boldsymbol{k}\downarrow} c_{-\boldsymbol{q}\downarrow} c_{\boldsymbol{q}\uparrow}, \tag{1.1}$$

where we introduced $c^\dagger_{\boldsymbol{k},\sigma}$ and $c_{\boldsymbol{k},\sigma}$ as the creation and annihilation operator for an electron of momentum $\boldsymbol{k}$ and spin $\sigma \in \{\uparrow,\downarrow\}$. The operators obey the standard Fermi commutation relation $\{c^\dagger_{\boldsymbol{k},\sigma}, c_{\boldsymbol{q},\sigma'}\} = \delta_{\boldsymbol{k},\boldsymbol{q}}\delta_{\sigma,\sigma'}$. The first term in Eq. (1.1) is simply the free electron energy $\epsilon_{\boldsymbol{k}\sigma}$, which arises from a Fermi liquid description of the underlying normal state metal. The phonon-mediated interaction is captured by the second term proportional to $V_{\boldsymbol{k},\boldsymbol{q}}$, which describes the scattering between electron pairs $c_{-\boldsymbol{k}\downarrow}c_{\boldsymbol{k}\uparrow}$ of opposite momentum and spin across the Fermi surface. The interaction is attractive and restricted to an energy range around the Fermi surface as $V_{\boldsymbol{k},\boldsymbol{q}} = -g_0/V$ for $|\epsilon_{\boldsymbol{k}\sigma}| < \hbar\omega_D$ and $V_{\boldsymbol{k},\boldsymbol{q}} = 0$ otherwise, where the energy range is limited by the Debye frequency ω_D as the maximum phonon frequency. We notice that Coulomb repulsion between electrons is only taken into account implicitly in the energies $\epsilon_{\boldsymbol{k}\sigma}$ of the underlying Fermi-liquid. Physically, this is justified for weak electron-phonon interactions because of the separation of timescales between the almost instantaneous Coulomb interaction and the retarded electron-phonon interaction[1] [84].

Using a mean-field description[2] of the BCS Hamiltonian from Eq. (1.1), the ground state wavefunction was approximated by Schrieffer as [10, 82]

$$\psi = \prod_{\boldsymbol{k}} (u_{\boldsymbol{k}} + v_{\boldsymbol{k}} c^\dagger_{-\boldsymbol{k}\downarrow} c^\dagger_{\boldsymbol{k}\uparrow}) \left|0\right\rangle, \tag{1.2}$$

where the coefficients $u_{\boldsymbol{k}}$, $v_{\boldsymbol{k}}$, i.e. coherence factors, are normalised such that $|u_{\boldsymbol{k}}|^2 + |v_{\boldsymbol{k}}|^2 = 1$. The exact expression for the coherence factors is not important for the purposes here. Using the Pauli exclusion principle the wavefunction can be shown to arise from the lowest order terms of a coherent state formed from pairs without a fixed particle number. This state is characterised by an off-diagonal long-range order [10, 82]

$$\Delta e^{\mathrm{i}\varphi} = -\frac{g_0}{V} \sum_{\vec{k}} \langle c_{-\boldsymbol{k}\downarrow} c_{\boldsymbol{k}\uparrow} \rangle, \tag{1.3}$$

which is a complex order parameter with both amplitude Δ and phase φ of the superconducting state (see also Ginzburg-Landau theory in Sec. 1.1.2). The sum in Eq. (1.3) is restricted to an energy band $|\epsilon_{\boldsymbol{k}\sigma}| < \hbar\omega_D$ determined by the Debye frequency ω_D. The order parameter quantifies the excitation gap and therefore also determines the binding energy of the Cooper pairs as 2Δ. For excitation above the gap the excited states of the BCS Hamiltonian from Eq. (1.1) contains quasi-particles excitations of the form [10]

$$\gamma^\dagger_{\boldsymbol{k}\uparrow} = u_{\boldsymbol{k}} c^\dagger_{\boldsymbol{k}\uparrow} + v_{\boldsymbol{k}} c_{-\boldsymbol{k}\downarrow}, \tag{1.4}$$

which are linear combinations of creation and annihilation operators. These quasi-particles have both electron and hole character quantified by the coefficients $u_{\boldsymbol{k}}$ and $v_{\boldsymbol{k}}$ from Eq. (1.2). Thermal excitations with energies larger then the binding energy of the Cooper pairs can break the superconducting pairs [84]. In a conventional superconductor, superconductivity is, therefore, lost due to the breaking of superconducting pairs approaching the phase transition [10]. The excitation of quasi-particles leads to a depletion of the superconducting gap

[1] The Hamiltonian in Eq. (1.1), however, treats the electron-phonon interaction as instantaneous, but for the Debye cutoff [83].

[2] A mean-field treatment is justified as fluctuations in the order parameter from Eq. (1.3) scale with volume V as $\langle \delta\Delta^2 \rangle \propto 1/V$.

with temperature T, with the gap eventually closing as [10]

$$\frac{\Delta(T)}{\Delta(0)} \approx 1.74 \left(1 - \frac{T}{T_C}\right)^{1/2}, \tag{1.5}$$

close to the critical temperature T_C.

1.1.2 Ginzburg Landau theory

As an emergent phenomenon [82, 84] the behaviour of superconductors is not immediately obvious from the underlying microscopic Hamiltonian given in Eq. (1.1). Already before the discovery of BCS theory (see Sec. 1.1.1), Ginzburg and Landau developed a phenomenological description of conventional superconductors, which was successfully used to describe the interaction of superconductors with electromagnetic fields. Both approaches were unified, when Gorkov showed [85] that close to the critical temperature T_C, the Ginzburg-Landau equations can be derived from the microscopic BCS theory. This connection finally allowed the interpretation of order-parameters in terms of microscopic quantities.

In superconductivity, the symmetry of the underlying Hamiltonian is broken such that a macroscopic number[3] of particles lock into a quantum state

$$\Psi(\vec{r}) = |\Psi(\vec{r})| e^{i\varphi(\vec{r})} \tag{1.6}$$

described by a common but in general arbitrary phase $\varphi(\vec{r})$ and amplitude $|\Psi(\vec{r})| \propto \sqrt{n_s(\vec{r})}$ with superconducting density $n_s(\vec{r})$ [84]. In Ginzburg Landau theory [86], the macroscopic quantum state from Eq. (1.6) is identified as a position $\vec{r}$ dependent complex order parameter (proportional to the one given in Eq. (1.3)). Using symmetry requirements for a superconductor close to a second order phase transition, the free energy of the composite system consisting of superconductor and electromagnetic field can be approximated by [10,80,82,84]

$$f_{GL} = \frac{\hbar^2}{2m^*} \left| \left(\vec{\nabla} - \mathrm{i}\frac{2\pi}{\Phi_0}\vec{A}\right)\Psi \right|^2 + v|\Psi|^2 + \frac{u}{2}|\Psi|^4 + \frac{(\vec{\nabla}\times\vec{A})^2}{2\mu_0}, \tag{1.7}$$

where $u > 0$ and v are real parameters, μ_0 is the free space permeability, $\hbar = h/2\pi$ is the reduced Planck constant and $\Phi_0 = h/2e$ is the magnetic flux quantum. Using the interpretation in terms of Cooper pairs from BCS theory (Sec. 1.1.1), the order parameter Ψ describes a condensate of superconducting pairs of effective mass m^* chosen as twice the electron mass m. Equation (1.7) also includes the interaction of the phase with the vector potential $\vec{A}$, which gives rise to a magnetic field $\vec{B} = \vec{\nabla}\times\vec{A}$. The last term in Eq. (1.7) can therefore be directly identified as magnetic energy density. The physical role played by each of the terms in Eq. (1.7) is discussed in the following.

Firstly, in the absence of gradients of the phase and fields the energy minima of Eq. (1.7) are determined purely by the second and third term. If $v > 0$, the superconductor is in the

[3] Locking of a macroscopic number of particles into a quantum state is known from Bose-Einstein condensation [84].

normal state with zero order parameter $|\Psi|^2 = 0$, while for $v < 0$ the system is in the superconducting state with a non-zero order parameter $|\Psi|^2 = -v/u$ [10]. The superconducting state ($v < 0$) is characterised by a finite density of superconducting pairs $|\Psi(\vec{r})|^2 = n_s(\vec{r})$. The symmetry of the ground-state is spontaneously broken by selecting a specific value for the phase $\varphi(\vec{r})$.

Secondly, allowing for gradients in the phase but still keeping $\vec{A} = 0$ and assuming a constant number of superconducting pairs $n_s = |\Psi|^2$, the first term of Eq. (1.7) is given by [82]

$$f_{GL} = \frac{\rho_\varphi}{2}\left(\vec{\nabla}\varphi\right)^2, \tag{1.8}$$

with phase stiffness $\rho_\varphi = \frac{\hbar^2}{m^*} n_s$. The phase stiffness arises from the conspiracy of all the electrons participating in the quantum state and quantifies the energy cost associated with the gradients in the phase of the superconducting order parameter [80, 84].

Varying Eq. (1.7) with respect to the vector potential $\vec{A}$ and using the ansatz from Eq. (1.6) one obtains the standard Ampère's law [10, 82, 84]

$$\vec{\nabla} \times \vec{B} = \mu_0 \vec{J}_s \tag{1.9}$$

with gauge-invariant[4] super-current density [82]

$$\vec{J}_s = \frac{1}{\mu_0 \lambda^2}\left(\frac{\Phi_0}{2\pi}\vec{\nabla}\varphi - \vec{A}\right), \tag{1.10}$$

where

$$\frac{1}{\lambda^2} = \frac{\mu_0 n_s \hbar^2}{m^*}\left(\frac{2\pi}{\Phi_0}\right)^2 = \mu_0 \rho_\varphi \left(\frac{2\pi}{\Phi_0}\right)^2, \tag{1.11}$$

is the London penetration depth [10, 82]. According to the second expression in Eq. (1.11) the magnitude of the super-current is characterised by the phase stiffness $\rho_\varphi \propto n_s$ [80] from Eq. (1.8). According to the Eq. (1.10), a twist of the superconducting or finite vector potential leads to a super-current response, which is characterised by the absence of any resistivity. The first and second term of Eq. (1.10) correspond to the parametric and diamagnetic response to an external magnetic field[5]. The diamagnetic response is proportional to $\vec{A}$ and is responsible for the Meissner effect, i.e. the expulsion of the magnetic field from the superconducting material. Taking the curl of Ampère's law from Eq. (1.9) using Maxwell's equation $\vec{\nabla} \cdot \vec{B} = 0$, $\vec{B} = \vec{\nabla} \times \vec{A}$ and $\vec{\nabla} \times \vec{\nabla}\phi = 0$, and assuming the number of superconducting pairs $n_s(\vec{r})$ to be constant, we obtain an equation for the penetration of the magnetic field into the superconductor [10]

$$\nabla^2 \vec{B} = \frac{1}{\lambda^2}\vec{B}. \tag{1.12}$$

According to this equation, external magnetic fields applied to the material decay over a distance characterised by the London penetration depth λ defined in Eq. (1.11). The

[4] Eq. (1.10) remains unchanged under a gauge transformation described by [82] $\varphi \to \varphi + \alpha$ and $\vec{A} \to \vec{A} + \frac{\Phi_0}{2\pi}\vec{\nabla}\alpha$.

[5] Only the total current density from Eq. (1.10) is gauge-invariant. Choosing the Coulomb gauge $\vec{\nabla} \cdot \vec{A} = 0$ allows us to give both terms physical relevance [82].

magnetic field is screened by a superconducting current from Eq. (1.10), which also decays over the same length scale λ leading to the exclusion of magnetic fields through the Meissner effect. On a more fundamental level, the Meissner effect arises from the breaking of the gauge invariance in the interaction between the superconducting phase and the electromagnetic field. The breaking of a continuous symmetry gives rise to a massless Goldstone mode, i.e. low energy excitations corresponding to a change in the phase of the order parameter. These Goldstone modes can be absorbed into the gauge field, giving it a finite mass through the Anderson-Higgs mechanism. It is essentially this mass term, which is responsible for the Meissner effect [81].

In the derivation of the Meissner effect above, we assumed the density of superconducting pairs to be spatially constant. However, the magnetic field can also break superconducting pairs. Varying Eq. (1.7) with respect to the order parameter Ψ gives rise to an effective non-linear, Schrödinger-like equation [82]

$$v\Psi + u|\Psi|^2\Psi + \frac{\hbar^2}{2m^*}\left(-\mathrm{i}\nabla - \frac{2\pi}{\Phi_0}\vec{A}\right)^2\Psi = 0, \tag{1.13}$$

that describes the change in both the phase and amplitude of the order parameter at the interface between superconducting and normal metals [82]. Keeping only terms linear in Ψ from Eq. (1.13), we can identify the coherence length $\zeta = \sqrt{\frac{\hbar^2}{2m^*|v|}}$ as the length-scale associated with the decay of the amplitude of the order parameter. The ratio of the London penetration depth λ from Eq. (1.11) to the coherence length ζ of the material, i.e. the length-scale associated with the decay of the magnetic field and the amplitude of the order parameter [82], allows distinguishing two types of superconductors. Type I superconductors with $\lambda/\zeta < \frac{1}{\sqrt{2}}$ show perfect diamagnetic properties throughout the material, while for type II superconductors with $\lambda/\zeta > \frac{1}{\sqrt{2}}$ magnetic fields can penetrate the bulk through the formation of (pancake [10]) vortices. Vortices are topological excitations in the phase, which are quantised in units magnetic flux quantum $\Phi_0 = h/2e$. Depending on the external field strength and boundary effects in type II superconductors such as HTSC, magnetic fluxes can eventually arrange themselves into an ordered Abrikosov lattice [10].

1.1.3 Josephson effect

The Josephson effect was originally predicted by Brian Josephson [87, 88] studying the electron tunnelling between two superconductors separated by a weak link, e.g. an insulating barrier, a combination which is now known as a Josephson junction (Fig. 1.1). The Josephson relations can be derived microscopically either by treating the tunnelling as a second order perturbation or exactly in terms of quasiparticle bound states [89] by summing over the contributions from different conduction channels. Here, we instead follow a simpler but popular "two-level atom" motivation of the Josephson effect originally proposed by Feynman [90], which can ultimately also be derived from BCS theory [91]. We start from the macroscopic wavefunctions $\Psi_{L,R}$ of two superfluids of energy $E_{L,R}$ weakly coupled by a coupling constant

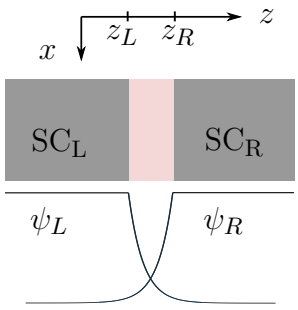


Figure 1.1: Josephson junction consisting of two identical superconductors ($SC_{L,R}$) with order parameter $\psi_{L,R}$ (grey area) separated by an insulating layer (pink area).

K such that the Schrödinger equations are [90, 92]

$$\mathrm{i}\hbar\frac{d}{dt}\Psi_L = E_L\Psi_L + Ke^{-\mathrm{i}\frac{2\pi}{\Phi_0}\int_{z_L}^{z_R}\vec{A}\cdot d\vec{z}}\Psi_R, \tag{1.14}$$

and

$$\mathrm{i}\hbar\frac{d}{dt}\Psi_R = E_R\Psi_R + Ke^{\mathrm{i}\frac{2\pi}{\Phi_0}\int_{z_L}^{z_R}\vec{A}\cdot d\vec{z}}\Psi_L, \tag{1.15}$$

with magnetic flux quantum $\Phi_0 = h/2e$. The explicit phase $e^{-\mathrm{i}\frac{2\pi}{\Phi_0}\int_{z_L}^{z_R}\vec{A}\cdot d\vec{z}}$ of the coupling term arises due to the presence of a vector potential along the z-axis taking into account possible magnetic fields applied to the junction. Integrating the vector potential over the barrier of the junction from z_L to z_R ensures the gauge invariance of the coupling terms.[6] Each of the superconductors is described by a macroscopic wavefunction [90, 92] given by Eq. (1.6) as

$$\Psi_m = \sqrt{n_m}e^{\mathrm{i}\varphi_m} \tag{1.16}$$

for $m = L, R$ with phase of order parameter φ_m and density of superconducting pairs n_m. Substituting Eq. (1.16) as an ansatz into Eq. (1.14) and (1.15) and separating the equations for real and imaginary part, we obtain in total four equations. The two equations corresponding to the real part describe charge conservation $\dot{n}_L = -\dot{n}_R$ and, assuming that charges over an effective length-scale b participate in the current, an expression for the dissipation-less super-current density given by

$$J^z = 2eb\dot{n}_L = J^C\sin(\phi), \tag{1.17}$$

with critical current density[7] $J^C = 4Keb\sqrt{n_L n_R}/\hbar$ and gauge invariant phase difference of the Josephson junction given by [10]

$$\phi = \varphi_R - \varphi_L - \frac{2\pi}{\Phi_0}\int_{z_L}^{z_R}\vec{A}\cdot d\vec{z}. \tag{1.18}$$

In a microscopic model derivation, this current would arise as a second-order correction to the groundstate of the BCS Hamiltonian due to the presence of the weak link [92]. This term is dissipation-less as it only arises from the virtual excitation of quasi-particles [89].

[6] Gauge invariance of the expression is important for the Anderson-Higgs mechanism by which the order parameter can get "eaten" by the electromagnetic field such as to give rise to a finite mass term of the photon, which is ultimately responsible for the Meissner effect [82].

[7] For very large charge reservoirs with superconducting density $n_s^c \approx n_L \approx n_R$ and using $K = \hbar^2/2Dbm^*$ we obtain $J^C = 2e\hbar n_s^c/Dm^*$ [10].

In the presence of a voltage V across the junction, the relative energy of the two superconductors is shifted by $E_L - E_R = 2eV$. Taking the difference of the imaginary part of Eq. (1.14) and (1.15) using Eq. (1.16) we obtain the *AC-Josephson* relation between voltage V and time derivative of the phase [10]

$$\frac{\Phi_0}{2\pi}\frac{d\phi}{dt} = V, \tag{1.19}$$

with magnetic flux quantum $\Phi_0 = h/2e$. Due to the AC-Josephson effect applying a DC voltage V_{dc} to the junction leads to oscillations of the supercurrent at frequency $f = 2eV_{dc}/h$, which makes the Josephson junctions a natural voltage to frequency converter.

Hamiltonian The phase dynamics of the Josephson junction of area A_{area} along the xy axis in Fig. 1.1 is captured by the Hamiltonian (see Ref. [10], Appendix B.1)

$$\mathcal{H}_\phi = \frac{p_\phi^2}{2m_\phi} - \frac{\Phi_0}{2\pi}\left(I^C\cos(\phi) + I_{\text{bias}}\phi\right), \tag{1.20}$$

where ϕ is the gauge invariant phase difference, $I^C = J^C A_{\text{area}}$ is the critical current and $I_{\text{bias}} = J_{\text{bias}} A_{\text{area}}$ an additional spatially homogeneous bias current applied across the Josephson junction. According to the first Hamilton's equation $\frac{\mathrm{d}\phi}{\mathrm{d}t} = +\frac{\partial \mathcal{H}_\phi}{\partial p_\phi}$ we obtain the conjugate momentum $p_\phi = m_\phi \frac{\mathrm{d}\phi}{\mathrm{d}t}$ with effective[8] mass $m_\phi = \left(\frac{\Phi_0}{2\pi}\right)^2 \epsilon_0\epsilon_r A_{\text{area}}/D = \left(\frac{\hbar}{2e}\right)^2 C$, where $C = \epsilon_r\epsilon_0 A_{\text{area}}/D$ is the capacitance of two parallel plates, $\Phi_0 = h/2e$ the magnetic flux quantum, D the junction thickness and A_{area} the area of the junction, ϵ_0 and ϵ_r the free space and relative permittivity respectively. Using these expressions the AC-Josephson relation from Eq. (1.19) becomes $\frac{\Phi_0}{2\pi} m_\phi^{-1} p_\phi = V$. The conjugate momentum p_ϕ is, therefore, proportional to the electric field E or voltage $V = ED$ across the junction of thickness D.

The Josephson potential $\propto -I^C\cos\phi$ (second term in Eq. (1.20)) has the same form of spin exchange interaction $-\vec{S}_2 \cdot \vec{S}_1$ for two classical spins $\vec{S}_m$ with $m = 1, 2$ of fixed length $|\vec{S}| =$ const oriented at an angle ϕ with respect to each other. In the absence of the gauge field, the orientation and magnitude of the two spins are determined by the relative phase $\varphi_R - \varphi_L$ and magnitude of the order parameter $|\psi_{L,R}|$ in Eq. (1.16) respectively. Historically, this interpretation goes back to the iso-spin formulation of the BCS theory due to Anderson [82, 89]. The Josephson current takes a role analogous to the super-current in the bulk, with the respective magnitude quantified by the Josephson coupling and the phase stiffness ρ_φ from Eq. (1.8).

RCSJ model In addition to the coherent dynamics captured by the Hamiltonian from Eq. (1.20), thermal excitation of quasi-particles can lead to an additional resistive current contribution $\frac{V}{R}$ proportional to the voltage V and characterised by a finite resistance R. Especially in HTSC the quasi-particle contribution cannot be ignored as the superconducting

[8] As ϕ is dimensionless, this effective mass has units of mass times area to ensure the usual commutation relations, when promoting ϕ and p_ϕ to operators $\hat{\phi}$ and $\hat{p}_\phi$ such that $[\hat{p}_\phi, \hat{\phi}] = -\mathrm{i}\hbar$. The momentum defined here is related to the number of Cooper pairs n or charge Q across the junction as $n = p_\phi/\hbar = Q/2e$ (see Sec. B.1).

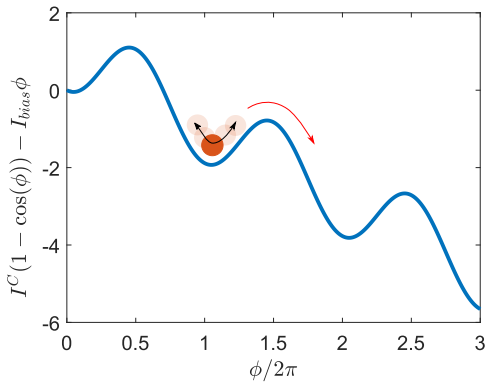
gap is suppressed to zero at specific angles in the crystal plane, such that there are always conduction channels open for quasiparticles [89] (see Sec. 1.2). Adding this quasi-particle current to the Hamilton's equation $\frac{\mathrm{d}p_\phi}{\mathrm{d}t} = -\frac{\partial \mathcal{H}_\phi}{\partial \phi}$ from Eq. (1.20), we obtain [10]

$$I_{\text{bias}} = C\frac{dV}{dt} + I^C \sin(\phi) + \frac{V}{R}, \tag{1.21}$$

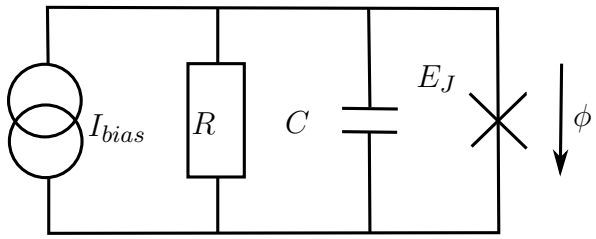
i.e. the bias current respectively divides into a component over the capacitor C, a super-current and a quasi-particle current. The corresponding situation is conveniently expressed in terms of a circuit model given in Fig. 1.2b, known as resistive and capacitative shunted junction model (RCSJ) with capacitance C, critical current I^C and external bias current I_{bias}. Using the AC-Josephson relation from Eq. (1.19) we obtain a relation between voltage and time derivative of the supercurrent as $V = L_J(\phi)\frac{dI}{dt}$ with inductance

$$L_J(\phi) = \frac{\Phi_0}{2\pi I^C \cos(\phi)}. \tag{1.22}$$

The Josephson junction can therefore be viewed as a non-linear inductor.



(a)



(b)

Figure 1.2: a) Oscillating dynamics (black curved arrow) of a phase particle given by the red ball around one of the local minima of a washboard potential given by $U(\phi) = I^C(1-\cos(\phi)) - I_{\text{bias}}\phi$ (blue line) at bias current $I_{\text{bias}}/I^C = 0.3$. The bias current determines the tilt of the washboard potential. The red arrow indicates the thermal escape of the phase particle. In the case of an underdamped junction, the energy gained by the phase particle cannot be dissipated quickly enough to retrap it in the next minima and it keeps on running down the potential. In this case, the junction has switched into a resistive state characterised by a finite time-averaged voltage. b) RCSJ circuit model for a Josephson junction biased by a current source consisting of capacitance C, Josephson potential $E_J\cos(\phi)$ and resistance R, which characterises the quasi-particle current across the junction.

Washboard potential For sufficiently low temperatures T compared to the Josephson coupling energy $E_J = \frac{\hbar I^C}{2e}$, i.e. $k_B T \ll E_J$ the Hamiltonian from Eq. (1.20) can be linearised around one of the energy minima of the washboard potential shown in Fig. 1.2a. In the absence of a bias current, small excitations of the phase around one of these equilibria

positions can be described by a phase particle of mass m_ϕ oscillating at the Josephson plasma frequency[9] ω_0 given by

$$\omega_0^2 = \frac{2\pi}{\Phi_0 \epsilon_0} \frac{J^C D}{\epsilon_r} = \frac{2e}{\hbar} \frac{I^C}{C}, \tag{1.23}$$

with the different terms defined below Eq. (1.20).

Applying a bias current across the junction shifts the equilibrium position of the energy minima of the washboard potential from $\phi^0 = 2\pi k$ $(k \in \mathbb{Z})$ in absence of the current to $\phi^0 = \arcsin\left(I_{\text{bias}}/I^C\right) + 2\pi k$ $(k \in \mathbb{Z})$ and decreases the oscillation of the phase particle to

$$\omega(I_{\text{bias}}) = \omega_0 \sqrt{\cos\phi^0} = \omega_0 \left[1 - (I_{\text{bias}}/I^C)^2\right]^{1/4}. \tag{1.24}$$

The bias current in Eq. (1.20) further lowers the height of the trapping potential of the phase particle shown in Fig. 1.2a to approximately [10]

$$\Delta U(\phi) \approx 2E_J(1 - I_{\text{bias}}/I^C)^{3/2}. \tag{1.25}$$

Depending on the junction height and temperature, the phase particle in the washboard potential picture can be thermally activated out of one of the local minima as indicated by the red arrow in Fig. 1.2a. For sufficient weak damping, the energy gained by slipping down the potential cannot be lost through dissipation and the phase particle continues running down the potential with a final "velocity" determined by the dissipation strength. The junction has therefore switched from a superconducting to a resistive state characterised by a finite time-averaged voltage according to the Josephson relation $V = \frac{\Phi_0}{2\pi}\dot{\phi}$ from Eq. (1.19).

One way to measure the temperature of the junction is to slowly sweep the bias current density from 0 to the critical current density J^C and measure the bias current density at which the junction becomes resistive [93]. The thermal activation is a stochastic process described by a switching current distribution $P_{\text{switch}}(j_{\text{bias}})$, whose mean value can be approximated by [10]

$$\langle J^C_{\text{switch}} \rangle = J^C\{1 - [(k_B T/2E_J)\ln(\omega_0 \Delta t/2\pi)]^{2/3}\}, \tag{1.26}$$

where Δt is the duration spent sweeping the highly populated states of the distribution, which has to be chosen large compared to the Josephson plasma frequency, i.e. $\Delta t \gg 2\pi/\omega_0$, by controlling the ramp speed. Under this condition, the suppression of the mean current can be significant even when $k_B T$ is only a few percents of E_J, as the argument of the logarithmic part is relatively large and the logarithm only weakly sensitive to the exact value of the ramping speed [10]. To a good approximation, the width of the switching current distribution σ is proportional to $T^{2/3}$ [93,94]. This measure allows us to distinguish between two regimes. One where the switching is dominated by thermal activation from quantum tunnelling regime, and another where the width becomes approximately independent of temperature.

Throughout this thesis we treat the phase of the superconducting order parameter classically, which is justified if the capacitance of the junction is large enough such that the

[9] Josephson *plasma* frequency is different to the oscillations at frequency $f = 2eV_{dc}/h$ due to Eq. (1.19).

capacitive energy characterised by $E_C = \frac{(2e)^2}{2C} = \frac{\hbar^2}{2m_\phi}$ is much smaller than the Josephson coupling energy $E_J = \frac{\hbar I^C}{2e}$, i.e. $E_J \gg E_C$ [69, 95]. Promoting phase $\phi \to \hat{\phi}$ and momentum $p_\phi/\hbar \to \hat{Q}/2e$ to operators, we obtain the standard commutation relation $[\hat{\phi}, \hat{Q}] = \mathrm{i}2e$ (see also Appendix B.1). The conjugate variable $\hat{Q}$ can be identified as the charge difference across the junction. For most junctions with a sufficiently large capacitance, $E_J \gg E_C$, such that the width of the wave-function describing the phase satisfies $\langle\hat{\phi}^2 - \langle\hat{\phi}\rangle^2\rangle \ll 1$. In this case, the value of the phase is well-defined and can be treated as a classical quantity. Due to the uncertainty relation, the dispersion in the conjugate variable is, however, large in this limit, i.e. $\langle\hat{Q}^2 - \langle\hat{Q}\rangle^2\rangle \gg (2e)^2$ and the charge difference across the junction is not well-defined.

In a quantum mechanical treatment of the phase, the energy levels around the equilibrium of the washboard potential form discrete energy separated by approximately $\hbar\omega_0$, which have been experimentally observed in small Josephson junctions [96]. In order to ignore the discreteness of the energy levels, we require $k_B T \gg \hbar\omega_0$. In HTSC, the situation is complicated by the omnipresence of quasi-particles, which arise due to the closing of the gap at specific nodes [64] (see Sec. 1.2). Using the expression for capacitive and inductive energies, the Josephson plasma frequency from Eq. (1.23) can be expressed as $\omega_0^2 = \frac{2E_C E_J}{\hbar^2}$ for a junction with large capacitance $1 \gg E_J/E_C$. Combined with $k_B T \ll E_J$, we, therefore, obtain $E_C \gg E_J$ for a classical description of the linearized equations. The situation becomes more complicated in the presence of strong damping, where the environment can suppress the spread of the dispersion of one of the operators by effectively performing a "measurement" [95].

Coupling a collective degree of freedom to an environment A priori, it is not clear that a collective quantum field such as the phase of a Josephson junction, which describes the many-body state of the system in the absence of dissipation, should be suitable to also characterise the system in the presence of a heat bath [69,97]. For specific noise processes, this assumption can be rigorously shown from first principles starting with a microscopic model. For the phase across Josephson junctions, for example, a Feynman path integral, which is non-local in the action of the imaginary time, can be derived for a range of dissipation processes, starting from a microscopic BCS Hamiltonian [69]. Due to the non-linearity of the Josephson potential, the symmetry of the action is modified by the coupling to the bath, which can have observable consequences for the charge transport, e.g. Coulomb blockade[10]. It can even lead to a dissipation induced phase transition (see Appendix B.1). By suppressing quantum fluctuations, which are destructive for superconductivity, dissipation can lead to a well defined "localised" phase and therefore be used to stabilise superconductivity [69,98–102]. For ultra-small Josephson junctions, the non-linear terms of the system Hamiltonian due to the Josephson potential can lead to observable consequences dependent on the microscopic origin of the noise [69]. Keeping only quadratic terms in the Josephson potential, on the other hand, the microscopic details of the coupling between system and bath do not matter, and a phenomenological description in terms of effective decay rates seems to be enough (see

[10] For small enough junctions the capacitance of the junction is very small such that the charge on each junction becomes well-defined (see AppendixB.1).

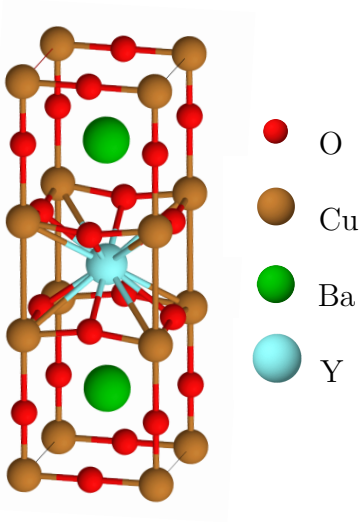


Figure 1.3: Unit cell of the crystal structure of the bilayer cuprate $YBa_2Cu_3O_7$, which has two copper oxides respectively just above and below the Yttrium atom (crystal structure generated with http://molview.org).

also Appendix B.1 and Ref. [69]).

Different from conventional superconductors, there exists no commonly accepted microscopic Hamiltonian for HTSC considered in Sec. 1.2, and it is therefore impossible to derive the type of coupling to the environment rigorously. However, whenever the noise process does not lead to a phase transition, which would change the character of the collective degree of freedom, it should only lead to the thermalisation of the collective degree of freedom. In this limit, it is justified to assume that the bath couples to a collective degree of freedom of the quantum field. In Chapter 4, we consider a single parametrically driven harmonic oscillator, where the coupling to the heat bath is described by such a collective degree of freedom. We find that strong driving allows distinguishing between different types of system-bath coupling operators or equivalently to learn about the bath spectral density.

1.2 High-temperature superconductivity

The discovery of high-temperature superconductors (HTSC) based on ceramic superconductors by Bednorz and Müller [103] in 1986 was surprising as the normal state of the cuprates in questions are in fact very bad conductors, obtained by doping a Mott-insulating[11] parent compound with electrons or holes [104]. Though the microscopic pairing mechanism leading to superconductivity is unknown [11], strong interaction and correlation lead to a rich phase diagram with many exotic states [104]. The respective role of these phases in either promoting or destroying superconductivity has been subjected to intense experimental and theoretical investigations as some of the features such as antiferromagnetic order [105], spin and charge stripes [106] and strange metal correlation [107] survive into the superconduct-

[11] In Mott insulator the conductivity is blocked through particularly strong Coulomb repulsion. Virtual super-exchange interaction of electrons on neighbouring lattice sites leads to an anti-ferromagnetic orientation of electron spins.

ing state. Most microscopic models for HTSC focus on the fact that cuprates all share a common two-dimensional copper oxide plane, which is believed to be the main location of the superconductivity, e.g. the two horizontal planes around the Yttrium atom in Fig. 1.3 for YBCO. Different planes are only weakly coupled to each other [104, 106]. The strongly correlated physics in the planes are often believed to be captured by the deceivingly simple two-dimensional Fermi-Hubbard [106]. Studying the two-dimensional Fermi-Hubbard model is numerically challenging, to the extent that it is a potential application for quantum emulators [108–112].

While there exists no commonly accepted theory for the pairing mechanism in cuprates, the observation of flux quantisation and Josephson effect seem to indicate that the superconductivity in HTSC involves Cooper pairs [113]. However, different to phonon-mediated superconductivity leading to anisotropic s-wave gap function Δ (see Sec. 1.1), the gap function $\Delta_{\boldsymbol{k}}$ of HTSC is highly anisotropic. The gap function $\Delta_{\boldsymbol{k}}$ is generally believed to be of d-wave character [106], which mirrors the underlying lattice structure with maximum values along the Cu-O-Cu bounds in the copper oxide planes shown in Fig. 1.3. In general, such a gap function arises due to the presence of both repulsive $V_{\boldsymbol{kq}} > 0$ and attractive terms $V_{\boldsymbol{kq}} < 0$ in the interaction potential, which leads to nodes $\Delta_{\boldsymbol{k}} \to 0$ for specific orientations of $\boldsymbol{k}$ [82]. The presence of nodal quasi-particles arising at $\Delta_{\boldsymbol{k}} \to 0$ might play a role at suppressing the phase stiffness at very low temperatures, see discussion in Ref. [114].

Phenomenological models of HTSC, such as an anisotropic version of the Ginzburg-Landau model, e.g. the Lawrence-Doniach model [10], take into account the two-dimensional structure of the HTSC. These phenomenological models allow the description of effects directly related to the macroscopic order parameter such as the Josephson effect [115, 116] arising due to the interlayer coupling between the copper oxide planes. Phenomenologically, cuprates can, therefore, be viewed as a stack of particularly clean intrinsic Josephson junctions [72, 73, 75–77, 117–126], which has stimulated research into their use for the generation of coherent THz radiation [73]. HTSC is characterised as a type II superconductor (see discussion below Eq. (1.13)). Applying a magnetic field to a type II superconductor leads to the penetration of magnetic fluxes into the superconductor, which can eventually arrange themselves into ordered Abrikosov lattices [10].

Transition mechanism The comparison of different energy scales in HTSC compared to one of the conventional superconductors allows some insight. The superconducting gap Δ from Eq. (1.3), for example, characterises the binding energy of superconducting pairs from breaking into quasiparticle excitation. In a conventional superconductor, the gap and supercurrents appear simultaneously, i.e. $\Delta \sim T_C$. On the other hand, there does not appear to be a clear connection between the superconducting gap and T_C in HTSC, i.e. $\Delta_{\boldsymbol{k}} \nsim T_C$ (see for example the discussion in Ref. [127]). In fact, the gap and therefore some form of pairing mechanism is even believed to persist above T_C leading to a peculiar pseudogap phase for underdoped materials [128–131]. Scanning tunnelling microscope experiments have also shown that the energy gap is also retained inside the vortex cores of HTSC [132, 133].

The existence of superconducting pairs is not sufficient to establish superconductivity as the pairs have to be phase coherent in order to carry a supercurrent. At zero temperature,

fluctuations in the phase are characterised by $E_\theta = \hbar^2 n_s(T=0)a/4m^*$ [55] with reduced Planck constant $\hbar$, effective mass of superconducting pairs m^*, typical transverse length scale[12] a and zero temperature superfluid density $n_s(T=0)$ [55, 56, 134]. In conventional superconductors, Δ is typically much smaller then the energy-cost associated with variation in the phase of the superconducting order parameter, i.e. the phase stiffness is small. For HTSC, on the other hand, Uemura et al. [134] noticed a linear relation between the critical temperature T_C and the phase-stiffness ρ_φ from Eq. (1.8) or equivalently the zero-temperature superconducting density, i.e. $T_C \propto n_s(T=0)$. These findings indicate that the relative magnitude of the energy scales associated with the formation of superconducting pairs and phase coherence is of similar magnitude or even inverted in HTSC [55, 135, 136], which is very different to the expectation from a conventional superconductor. It, therefore, seems that due to the low phase-stiffness associated with a small charge density, phase fluctuations play a major role in phase transition [55, 135, 136]. These fluctuations are expected to be purely classical, as for temperatures close enough to T_C, quantum fluctuations are screened by background normal fluid [55, 56, 135–137]. Such a phase transition might be described by an XY-type of model [55], which allows for the formation and unbinding of vortices. Vortices are topological excitations in the phase characterised by multiple of 2π around a point suppression in the amplitude of the order parameter. There are indications that the vortex core energy deviates from the two-dimensional XY prediction in the case of HTSC and might instead be described by a three-dimensional extension of the XY model see Ref. [104, 127, 138, 139]. Interestingly, inhomogeneities in the phase might also play a role in raising the transition temperature [140].

1.3 Effect of an alternating field in conventional superconductors

Large static magnetic fields induce screening currents, which can lead to breaking of Cooper pairs and thereby reduce the critical temperature [141]. However, in conventional superconductors, this situation becomes significantly more complicated in the presence of alternating fields. At finite temperature, states relevant for the formation of Cooper pairs get blocked by thermally excited quasi-particles. Electromagnetic radiation with frequency ω_L smaller than the superconducting gap Δ, i.e. $\Delta > \hbar\omega_L$, can redistribute these quasiparticles from low to high-energy states without breaking any Cooper pairs. Exciting the quasi-particles away from the Fermi surface leads to a temporary enhancement of the superconducting gap [142–144] as first observed in weak links in Ref. [145] and further studied in quantum point contacts [146] and SNS junctions [147] among others. The resulting non-equilibrium distributions of quasi-particles are generally high in energy and can ultimately lead to significant heating due to incoherent scattering [148] (see also discussion in Ref. [33]).

Two fluid model for interpretation of c-axis reflectivity The existence of a non-zero superconducting gap above the critical temperature T_C in HTSC [128–131], can potentially

[12] This is the typical length-scale for an underlying XY model simulation of the phase transition [127].

be understood to arise due to the existence of superconducting pairs above T_C without phase coherence. This raises the intriguing question, whether it might be possible to make these pairs coherent and thereby stabilise superconductivity in a non-equilibrium state, either by suppressing the phase fluctuations or destroying a competing state, which has inspired the experiments in Ref. [17, 18, 33–37].

In these experiments, the optical c-axis[13] conductivity is measured. The conductivity $\sigma(\vec{r}) = \sigma_1(\omega) + \mathrm{i}\sigma_2(\omega)$ with real part $\sigma_1(\omega) = \Re(\sigma(\omega))$ and imaginary part $\sigma_2(\omega) = \Im(\sigma(\omega))$ describes the current density response $\vec{j}(\vec{r}) = \sigma(\vec{r})\vec{E}(\vec{r})$ to an external applied electric field $\vec{E}(\vec{r})$. According to the two fluid model[14] [10], the total conductivity in frequency space $\sigma(\omega, T)$ at temperature T can be divided into a normal $\sigma_n(\omega, T)$ and superconducting contribution $\sigma_s(\omega, T)$ with normal electron density n_n and c-axis superconducting electrons density n_s^c for a given fixed total electron density $n = n_s^c + n_n$. According to the Drude's model, the conductivity of an electron gas consisting of electrons of charge e and effective mass m^* with an effective scattering time τ_n in the presence of an alternating electric field of frequency ω is given by [10]

$$\sigma_n(\omega) = \frac{\sigma_n(0)}{1 - \mathrm{i}\omega\tau_n}, \tag{1.27}$$

where $\sigma_n(0) = n_n e^2 \tau_n / m^*$ is the finite DC response ($\omega = 0$). From Eq. (1.10) in the absence of phase gradients $\vec{J} = -\frac{n_s^c (2e)^2}{m^*}\vec{A}$ with effective mass m^* we obtain a purely imaginary conductivity (no power dissipation) as

$$\sigma_s(\omega) = \frac{\mathrm{i}}{\omega}\frac{n_s^c (2e)^2}{m^*}. \tag{1.28}$$

Formally, this expression could also be obtained by letting the scattering time $\tau_n \to \infty$ in the expression for the conductivity from Eq. (1.27). Focussing on the low frequency response $\omega\tau_n \ll 1$ sufficiently below both the plasma frequency of the electron gas and the superconducting gap, i.e. $\hbar\omega/\Delta \ll 1$ (so that any change of the conductivity due to breaking of superconducting pairs can be ignored) we obtain [10]

$$\sigma(\omega, T) = \frac{n_n e^2 \tau_n}{m^*} + \mathrm{i}\frac{n_s^c (2e)^2}{m^*}\left[\frac{1}{\omega} - \mathrm{i}\pi\delta(\omega)\right], \tag{1.29}$$

where the delta function, missing in Eq. (1.28), is added to satisfy causality following Kramers-Kronig relations [150, 152]. Physically the delta function describes the response in the presence of a DC field. Though the two fluid model is an oversimplification, it shows that the low-frequency limit of the imaginary part of the conductivity provides a measure for the c-axis superfluid density in the system $n_s^c = m^* \left(\sigma_2(\omega)\omega\right)_{\omega\to\infty} / (2e)^2$. As the c-axis superfluid density arises from Josephson coupling it is reduced by large phase fluctuations, i.e. $n_s^c \propto \omega_0^2 \langle\cos(\phi)\rangle$ [149], where $\langle\rangle$ denotes a thermal average. As higher temperatures automatically lead to larger phase fluctuations, it costs less energy to excite the phase at higher temperatures. In order to enhance superconductivity, it is therefore necessary to reduce the phase fluctuations, which ultimately should lead to an increase in the transition temperature associated with c-axis fluctuations.

[13] C-axis of cuprates in aligned perpendicular to the cupper oxide planes.

[14] For a more rigorous treatment describing the c-axis electrodynamics in HTSC see Ref. [149–151]

1.4 Chapter summary

In this chapter, we provided a brief outline of the phenomenological and microscopic theories for both conventional and HTSC as well as a simple motivation and intuitive description of the Josephson effect. We also outlined the effect of alternating electromagnetic radiation on conventional superconductors. The concepts and background material introduced in this chapter allow for the discussion of driven superconductivity in the following chapters.

Chapter 2

Background: Driving macroscopic open quantum systems

In this chapter, we start by giving a brief introduction to cavity optomechanics in Sec. 2.1.1, which will facilitate the discussion of cooling of phase fluctuations in both a sideband cooling scheme for a single long artificial Josephson junctions from Ref. [78] (Sec. 2.1.2) and a parametric cooling scheme for short capacitively coupled intrinsic Josephson junctions based on Ref. [31] (Sec. 2.1.3). The parametric cooling scheme serves as the essential building block for the parametric cooling scheme of capacitively and inductive coupled long Josephson junctions discussed in Chapter 3. In the present Chapter, we use a toy model version of two short linearised parametric Josephson junctions, which allows us to concentrate on the cooling mechanism and working principle of the parametric cooling scheme. In Sec. 2.2, we discuss the different driving regimes leading to parametric instabilities (Sec. 2.2.1) and parametric enhancement of the interlayer coupling from Ref. [43,45] (Sec. 2.2.2). Section 2.3 is devoted to a more general discussion of the Floquet-Markov master equation.

2.1 Laser cooling

In ionic and neutral atomic systems laser cooling has allowed reaching temperatures of a few microkelvins [153–155]. In molecules [156], Doppler limited cooling has been only achieved recently [157]. Instead of exploiting the properties of a cryogenic cooling medium, a laser pumps energy quanta out of the system by taking advantage of the internal structure of the atom and its interaction with the environment. With increasing system complexity, only selective degrees of freedom can be cooled. In optomechanical systems, which study the interaction of mechanical oscillators with light, much progress has been made towards the realisation of ground state cooling of the oscillator [158], but it is only the displacement of the macroscopic mirror which is cooled and not the motion of all atoms in the oscillator. Using lasers to cool selective degrees of freedom in solids is not new, e.g. anti-Stokes fluorescence cooling has been proposed and observed for a variety of materials see Ref. [159]. The purity of the material and the recycling of the fluorescence photons pose challenges in this case as otherwise risking heating the material.

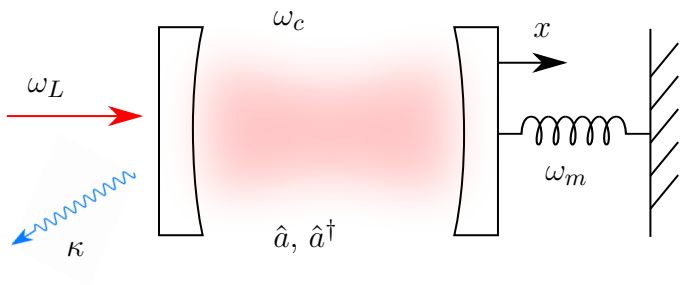


Figure 2.1: Basic optomechanical setup consisting of a single mode cavity with one movable mirror oscillating at frequency ω_m and driven with laser of frequency ω_L. Displacement x of the mirror modifies the length of the cavity leading to a change of the cavity frequency from the equilibrium frequency $\omega_c = \frac{\pi c}{L_c}$ for a cavity of equilibrium length L_c.

2.1.1 Sideband cooling in optomechanics

Optomechanics studies the interaction and control of a mechanical system through the interaction with an electromagnetic field. Historically, optomechanics originated from the pursuit of possible improvements to the sensitivity of interferometers, e.g. in gravitational wave detection [160]. The underlying principle of radiation pressure induced (anti-)damping of a harmonic oscillating mirror, was first perceived and experimentally realised by Braginsky in microwave cavities [161, 162]. Further advances in detection technology have allowed the experimental realisation of feedback cooling of interferometer [163], where the system position is measured in order to apply an appropriate feedback signal. Since then optomechanics has been realised in a variety of cavity setups among others in microtoroid [164, 165] and suspended micromirrors [166]. The physical mechanism has also been generalised to setups not requiring cavities such as photonic circuits [167] and crystals [168].

Here, we review the basic physics behind the optomechanical cooling scheme. The simplest case of a cavity with one movable mirror, depicted in Fig. 2.1, is captured by a Hamiltonian of the form [158]

$$\mathcal{H}_0 = \hbar\omega_m \hat{b}^\dagger \hat{b} + \hbar\omega_c(\hat{x})\hat{a}^\dagger \hat{a}, \tag{2.1}$$

where $\hat{a}^\dagger$ and $\hat{a}$ ($\hat{b}^\dagger$ and $\hat{b}$) are the creation and annihilation operators of the cavity field (mechanical oscillator) corresponding to the equilibrium position and ω_c (ω_m) are the corresponding frequencies [169]. Displacement $\hat{x}$ of the mechanical oscillator around its equilibrium position (Fig. 2.1) can be quantized as $\hat{x} = x_{\text{zpf}}(\hat{b}^\dagger + \hat{b})$ with zero-point fluctuation $x_{\text{zpf}} = \sqrt{\hbar/2m_{\text{eff}}\omega_m}$ and m_{eff} as the effective mass of the oscillator. The resulting small changes of the equilibrium cavity length L_c, modify the effective cavity frequency $\omega_c(\hat{x})$ as [158, 169]

$$\omega_c(\hat{x}) = \omega_c\left(1 - \frac{\hat{x}}{L_c}\right). \tag{2.2}$$

A formal derivation of this Hamiltonian can be found in Ref. [169]. The expression given here is only valid if the spacing between different cavity modes is large in comparison to the mirror oscillations, such that only a single mode of the cavity effectively interacts with the mirror. This requires the mirror motion to be adiabatically slow, such that scattering into other spatial modes and two-photon processes can be ignored, i.e. ω_m is respectively much

smaller than the free spectral range $\nu_{FSR} = \pi \frac{c}{L_c}$ and $2\omega_c$ [169, 170].

The necessary energy to overcome the large separation in energy between ω_m and the laser frequency ω_L is supplied by a laser of amplitude α_{in} captured by a driving Hamiltonian [158]

$$\mathcal{H}_{\text{driv}}(t) = \mathrm{i}\hbar\sqrt{\kappa_{ex}}\left(\alpha_{in}e^{-\mathrm{i}\omega_L t}\hat{a}^\dagger - \alpha_{in}^* e^{\mathrm{i}\omega_L t}\hat{a}\right), \tag{2.3}$$

where κ_{ex} is the input coupling loss rate. The time dependence can be eliminated by a transformation into a frame rotating at the laser frequency ω_L using the unitary $U = e^{-\mathrm{i}\omega_L \hat{a}^\dagger \hat{a} t}$ such that the total Hamiltonian is given by

$$\mathcal{H} = -\hbar\Delta_o \hat{a}^\dagger\hat{a} + \hbar\omega_m \hat{b}^\dagger\hat{b} - \hbar g_0 \hat{a}^\dagger\hat{a}(\hat{b}+\hat{b}^\dagger) + \mathrm{i}\hbar\sqrt{\kappa_{ex}}\left(\hat{a}^\dagger\alpha_{in} - \hat{a}\alpha_{in}^*\right), \tag{2.4}$$

where $\Delta_0 = \omega_L - \omega_c$ is the detuning between laser and cavity and $g_0 = \frac{\omega_0}{L_c} x_{\text{zpf}}$ is the optomechanical coupling. The third non-linear coupling term $H_{int} = -\hbar g_0 \hat{a}^\dagger\hat{a}(\hat{b}+\hat{b}^\dagger)$ arises originally from Eq. 2.2. This term gives rise to the radiation pressure force $F = -\frac{dH_{int}}{dt} = \frac{g_0}{x_{\text{zpf}}}\hat{a}^\dagger\hat{a}$, which is proportional to the density of radiation in the cavity.

The Hamiltonian from Eq. (2.4) can be linearised by separating the cavity field into a coherent excitation $\langle\hat{a}\rangle = \bar{a}$ and a perturbation $\delta\hat{a}$. The coherent excitation leads to a mean shift in the position coordinates of the oscillator by $\delta\bar{x} = \frac{2g_0|\bar{a}|^2 x_{zpf}}{\omega_m}$. It also shifts the frequency difference to $\Delta_n = \Delta_0 + g_0\frac{\delta\bar{x}}{x_{zpf}}$. In the steady state, the drive creates a coherent amplitude $\langle\hat{a}\rangle = \bar{a} = \mathrm{i}\sqrt{\kappa}_{ex}\alpha_{in}/\Delta_n$. The Hamiltonian (2.4) reduces to

$$\mathcal{H} = -\hbar\Delta_n \delta\hat{a}^\dagger\delta\hat{a} + \hbar\omega_m\hat{b}^\dagger\hat{b} - \hbar g\left(\delta\hat{a}+\delta\hat{a}^\dagger\right)\left(\hat{b}+\hat{b}^\dagger\right), \tag{2.5}$$

where we dropped $\hbar g_0 \delta\hat{a}^\dagger\delta\hat{a}(\hat{b}+\hat{b}^\dagger)$, which is $\bar{a}$ smaller than the third term linear in $\delta\hat{a}$. We also introduced $g = g_0\bar{a}$ after restricting $\bar{a}$ to be real[1].

In addition to the coherent interaction described by the Hamiltonian (2.5), the cavity (mechanical oscillator) decays at a rate κ (γ_m). Here, we restrict ourselves to the resolved sideband regime with $\gamma_m, \kappa \ll \omega_m$. The finite size of the decay rate leads to a retarded component of the radiation pressure, which is out of phase with the mechanical oscillators and allows for a net energy flow between cavity field and oscillator, i.e. cooling and heating [158, 160, 171].

The effect of the optomechanical coupling due to finite g in Hamiltonian (2.5) can be described by its modification of the mechanical susceptibility. The action of the environment can be included in the form of quantum Langevin equations using input-output theory [171, 172]. However, as optomechanical cooling is captured by classical dynamics, it will be sufficient to consider the classical version obtained after taking the expectation value. In that case external noise due to environment disappears. Letting $\delta\alpha(t) = \bar{\alpha} + \langle\delta\hat{a}(t)\rangle$ with $\bar{\alpha} = \frac{\mathrm{i}\sqrt{\kappa_{ex}}\alpha_{in}}{\Delta_n + \frac{\mathrm{i}\kappa}{2}}$ and x be a classical variable, the fluctuations of the cavity field are governed by [158]

$$\delta\dot{\alpha} = (\mathrm{i}\Delta_n - \frac{\kappa}{2})\delta\alpha + \mathrm{i}\bar{\alpha}Gx, \tag{2.6}$$

[1] Formally, this is achieved by absorbing the imaginary part of $\bar{a}$ into the creation and annihilation operators $\delta\hat{a} \to \frac{\bar{a}}{|\bar{a}|}\delta\bar{a}$

with coupling constant $G = \frac{g}{\bar{\alpha} x_{zpf}}$. The first and last term arises from the expectation value of the Heisenberg equation from Hamiltonian (2.5) $\frac{d}{dt}\delta\hat{a}(t) = \frac{\mathrm{i}}{\hbar}[\mathcal{H}, \delta\hat{a}(t)]$ and the second corresponds to the decay into the environment. Correspondingly, the equation of motion of the mechanical oscillator is given by

$$m_{\mathrm{eff}}\ddot{x} = -m_{\mathrm{eff}}\omega'^2_m x - m_{\mathrm{eff}}\gamma_m \dot{x} + \hbar G\bar{\alpha}(\delta\alpha + \delta\alpha^*) \tag{2.7}$$

with $\omega'^2 = \omega_m^2 + (\frac{\gamma_m}{2})^2$ including a small modification to the frequency of the oscillator, which we ignore in the following. These equations of motion can be solved by going to Fourier space [158, 173]. Considering first the decoupled mechanical oscillator from Eq. (2.7) with $G = 0$, the linear response to a small perturbation added on the right hand side $F_{ex}(t)$ is given by $x(\omega) = \chi_m(\omega)F_{ex}(\omega)$ in frequency space, where we defined the Fourier transform $x(\omega) = \int_{-\infty}^{\infty} e^{\mathrm{i}\omega t}x(t)dt$ and susceptibility $\chi_m^{-1}(\omega) = m_{\mathrm{eff}}[(\omega_m^2 - \omega^2) - \mathrm{i}\gamma_m\omega]$.

For finite $G \neq 0$, oscillator and cavity are opto-mechanically coupled leading to a dynamical backaction such that we need to solve Eq. (2.7) and Eq. (2.6) simultaneously. The linear response of the mechanical oscillator is then captured by the new effective susceptibility $\chi_{m,\mathrm{eff}}(\omega)$ of the form

$$\chi_{m,\mathrm{eff}}^{-1}(\omega) = m_{eff}[\omega_m^2 + 2\omega\delta\omega_m(\omega) - \omega^2 - \mathrm{i}\omega[\gamma_m + \gamma_{opt}(\omega)]], \tag{2.8}$$

consisting of a frequency-dependent contribution to the damping rate [158, 173, 174]

$$\gamma_{opt}(\omega) = g^2\frac{\omega_m}{\omega}\left(\frac{\kappa}{\kappa^2/4 + (\Delta_n + \omega)^2} - \frac{\kappa}{\kappa^2/4 + (\Delta_n - \omega)^2}\right), \tag{2.9}$$

and a small change (since $g \ll \omega_m$) of the mechanical oscillator frequency $\delta\omega_m(\omega)$ given by

$$\delta\omega_m(\omega) = g^2\frac{\omega_m}{\omega}\left(\frac{\Delta_n + \omega}{\kappa^2/4 + (\Delta_n + \omega)^2} + \frac{\Delta_n - \omega}{\kappa^2/4 + (\Delta_n - \omega)^2}\right). \tag{2.10}$$

Formally, this treatment in terms of increased effective damping rates is only valid for weak optomechanical coupling $g \ll \kappa$. In the strong coupling limit, where the coupling becomes more substantial than the dissipative dynamics, i.e. for $g \sim \kappa$, the mechanical oscillator and cavity mode cannot be treated independently and we have to consider the combined system [175, 176]. However, we are restricting ourselves to $g \ll \omega_0$, not entering the ultrastrong coupling regime [177], where the coupling has to be taken into account in both coherent and dissipative dynamics [178].

The thermal noise of the mechanical oscillator can be characterised with the help of the classical power spectral density given by the Fourier transform of the autocorrelation function as [171]

$$S_{xx}(\omega) = \frac{1}{2}\int_{-\infty}^{\infty} dt e^{\mathrm{i}\omega t}\langle\{x(t), x(0)\}\rangle, \tag{2.11}$$

with anti-commutator $\{A, B\} = AB + BA$. Due to the fluctuation-dissipation relation [179, 180], the power spectral density $S_{xx}(\omega)$ can be related to the linear susceptibility of the system, i.e. $S_{xx}(\omega) = \frac{2k_BT}{\omega}\Im(\chi_{m,\mathrm{eff}}(\omega))$ in the classical limit $k_BT \gg \hbar\omega_m$ [158, 171]. Integrated

over all frequencies the power spectral density yields the variance, i.e.

$$\langle x^2 \rangle = \frac{1}{2\pi} \int_{-\infty}^{\infty} d\omega S_{xx}(\omega) = \frac{k_B T_{\text{eff}}}{m_{\text{eff}} \omega_m^2}, \tag{2.12}$$

with effective temperature T_{eff} used as the definition of temperature in later sections.

For sufficiently weak optomechanical coupling $g \ll \kappa$ and damping $\gamma_m + \gamma_{opt}(\omega_m) \ll \kappa$ the mechanical oscillator only samples values close to the unperturbed frequency $\omega = \pm\omega_m$. In this case, Eqs. (2.10) and (2.9) can be evaluated at $\omega = \omega_m$. The change to the optical damping $\gamma_{opt}(\omega_m)$ is positive when the cavity is driven below its resonance frequency at $\Delta_n = -\omega_m$ and negative at $\Delta_n = \omega_m$. The effect of the enhanced damping due to dynamical backaction by a laser red-detuned from the cavity resonance can be understood in terms of a classical equation for the mean energy of the oscillator [160]

$$\frac{d}{dt}\langle E_m \rangle = -(\gamma_{opt}(\omega_m) + \gamma_m)\langle E_m \rangle + k_B T_0 \gamma_m, \tag{2.13}$$

where we neglect any additional noise due to the presence of the laser. The final temperature is proportional to the initial temperature T_0 of the environment in this classical treatment, i.e. $T = T_0 \frac{\gamma_m}{\gamma_m + \gamma_{opt}(\omega_m)}$. Here, the cooling arises from cold damping, that is the enhancement of the effective decay rate without an increase in the associated thermal noise, i.e. the environment appears colder. A more rigorous fully quantum mechanical derivation based on the adiabatic elimination of the high-frequency mode can be found in Ref. [174]. The resulting structured environment has an increased damping rate, which by itself does not have any influence on the effective temperature of the structured bath. It is instead the effective thermal occupation of the structured environment consisting of an environment and a driven cavity, which is lower, corresponding to coupling to a bath with a smaller effective temperature.

The effect of the driving of the cavity can also be understood in terms of the sideband formalism in the resolved sideband regime $\kappa \ll \omega_m$ [160, 181, 182]. To first order in G, the mirror performs oscillations of the form $x(t) = x_0 \cos(\omega_m t)$ with a small amplitude x_0 at frequency ω_m. The two lowest order terms of a perturbative solution of Eq. (2.6) for small G are [158]

$$\delta\alpha = \frac{i g_0 x_0}{2 x_{zpf}} \bar{\alpha} \left(\frac{e^{-\mathrm{i}\omega_m t}}{-\mathrm{i}(\omega_m + \Delta_n) + \frac{\kappa}{2}} + \frac{e^{\mathrm{i}\omega_m t}}{-\mathrm{i}(-\omega_m + \Delta_n) + \frac{\kappa}{2}} \right), \tag{2.14}$$

which is still in the rotating frame. The oscillations of the mechanical oscillator Doppler shifts the cavity frequency by $\pm\omega_m$ corresponding to two resonances at $\Delta_n = \pm\omega_m$ respectively. Transitions due to these two sidebands are also shown as red and blue solid straight arrows in Fig. 2.2 in terms of transitions between Fock states of the joint Hilbert space of the cavity and the mechanical oscillator.

When translating the optomechanical cooling scheme to other setups, i.e. electro-mechanical oscillators or Josephson Junctions, additional effects start to play a role. First of all, the thermal occupation of the high-frequency mode, i.e. the cavity ω_c, into which the energy is being dumped, cannot be ignored in general. The necessary temperature to achieve a thermal occupation of the cavity is determined from $\hbar\omega_c = k_B T$ as $T = 24000\,\text{K}$ for an optical

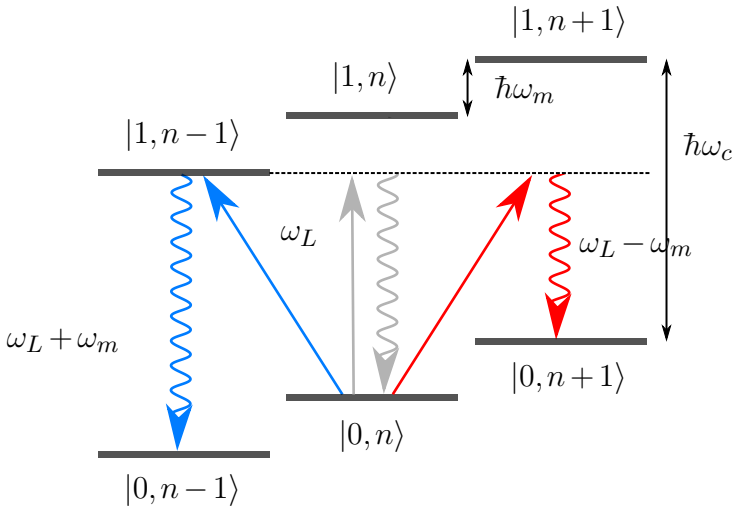


Figure 2.2: Tuning the laser to the red sideband excites the transition $|0,n\rangle \to |1,n-1\rangle$ (blue arrow) expressed in the joint Fock basis $|n_c,n_m\rangle$ of $n_{c,m}$ quanta in the cavity and mechanical oscillator respectively. The blue shifted photon gained in this transition can decay out of the cavity (vertical wiggly arrows), leading to a net decrease in the occupation number of the mechanical oscillator in one cycle. Both transition corresponding to the blue sideband $|0,n\rangle \to |1,n+1\rangle$ (red arrow leading to a red shifted photon) and $|0,n\rangle \to |1,n\rangle$ (grey arrow) are both off-resonant on the other hand. We only show the lowest two energy levels of the cavity, which is the situation encountered in the sideband cooling of an atom, where the cavity is replaced by a two-level atom and the mechanical oscillator by its vibrational states. *The color scheme is chosen to indicate the energy shift of the photon due to the interaction and not the detuning of the laser with respect to the oscillator transition.*

cavity with $\omega_c = 2\pi \times 500\,\mathrm{THz}$, $T = 0.05\,\mathrm{K}$ for a microwave cavities, e.g. electromechanical circuits, with $\omega_c = 2\pi \times 1\,\mathrm{GHz}$. Consequently, the thermal occupation for microwave cavities cannot be ignored at room temperature and limits the cooling efficiency [158, 175, 176]. In fact, the cooling ratio of final n_f vs initial n_m thermal occupation of the low-frequency oscillator is lower bounded as $n_f \geq n_m \frac{\omega_m}{\omega_c}$ [176] by the frequency ratio between the low frequency mode ω_m and the cavity ω_c. As we will see in Sec. 2.1.3, this also limits the cooling efficiency of the Josephson plasma modes in HTSC, where the low and high-frequency mode take the role of mechanical oscillator and cavity are of both of the order of terahertz such that $\omega_c = 2\pi \times 1\,\mathrm{THz}$ with temperature $T = 48\,\mathrm{K}$ obtained from $\hbar\omega_c = k_B T$.

While for weak coupling the coherent energy transfer between the mechanical oscillator and cavity is suppressed by fast decoherence rates to the respective local environments, dissipation has to be treated perturbatively in the strongly coupled regime. Similar to the dressing of atoms in cavities in the strongly coupled regime, the cavity dresses the mechanical mode leading to normal mode splitting for $2g \geq \kappa/2$, which was first observed in Ref. [183] and has been increased further since then [184, 185]. Contributions from the counter-rotating terms in Eq. (2.5) limit the cooling efficiency for ground state cooling for $\kappa \ll g \ll \omega_m$ [175, 176]. In Ref. [176], in the classical regime corresponding to large thermal occupation n_m, it was found that the final thermal occupation of the low frequency oscillator n_f is limited by $n_f \geq \frac{\gamma_m}{4g^2/\kappa} n_m$ for weak coupling $g \ll \kappa_m$ and $n_f \geq \frac{\gamma}{\kappa} n_m$ in the strong coupling regime $\gamma \ll \kappa$, which is independent of g and only limited by the dissipation rate of the cavity mode κ. These limits agree with the cooling ratios n_f/n_m we will derive in Sec. 2.1.3.

Ultimately, the cooling efficiency is also limited by the type of dissipation process. In optomechanics, the heat bath of the cavity and mechanical oscillator, e.g. vacuum modes and phonon modes, are physically separated. Energy pumped out of the mechanical oscillator can dissipate from the cavity without any danger of reheating the mechanical oscillator through non-Markovian effects or a common, shared heat bath. The assumption of non-Markovian dynamics and physically separated heat baths is, therefore, most likely strongly system dependent and has to be considered in detail in a case to case basis.

2.1.2 Sideband cooling of a long Josephson Junction in the presence of a bias current

In this section, we discuss the sideband cooling for a single long Josephson junction implemented by Hammer et al. [78] in an artificial Josephson junction built from two conventional superconductors. An extension of the scheme to arrays of complex-oxide heterostructures has been proposed in Ref. [186]. The junction has a finite length L aligned along the x-axis, therefore, the spatial dependence of the phase $\phi(x)$ along the junction cannot be ignored as for the short junctions considered in Sec. 1.1.3. The phase dynamics in the absence of an external magnetic field is then governed by [187]

$$\mathcal{H}_\phi = \frac{E_J}{L} \int_0^L dx \left[\frac{1}{2\omega_0^2} \left(\frac{d\phi(x)}{dt} \right)^2 - \left(\cos\left(\phi(x)\right) + \frac{J_{\mathrm{bias}}}{J^C} \phi(x) \right) + \frac{\lambda_J^2}{2} (\partial_x \phi(x))^2 \right], \tag{2.15}$$

with Josephson coupling energy density $E_J = \frac{\hbar I^C}{2e}$, Josephson plasma frequency ω_0 given by $\omega_0^2 = \frac{2eD}{\hbar}\frac{J^C}{\epsilon_0\epsilon_r}$ for a junction of thickness D, total critical current $I^C = A_{\text{area}}J^C$, spatially homogeneous critical current density J^C and bias current density J_{bias}. The first three terms are equivalent to the ones for a short Josephson junction from Eq. (1.20). They describe the dynamics of a hypothetical phase particle in a washboard potential depicted in Fig. 1.2a. The last term accounts for additional energy cost due to spatial variations of the phase, which are characterised by the Josephson penetration length λ_J. Considering small fluctuations $\delta\phi(x)$ around one of the minimum position of the washboard potential, $\phi^0 = \arcsin\left(J_{\text{bias}}/J^C\right)$, in the presence of a spatially homogeneous bias current density J_{bias} i.e. $\phi(x) = \phi^0 + \delta\phi(x)$, Eq. (2.15) reads

$$\mathcal{H}_\phi = \frac{E_J}{L}\int_0^L dx\left[\frac{1}{2\omega_0^2}\left(\frac{d\delta\phi(x)}{dt}\right)^2 + \frac{1}{2}\cos(\phi^0)\delta\phi^2(x) - \frac{1}{3!}\sin(\phi^0)\delta\phi^3(x)\right] + O(\delta\phi^4(x)). \quad (2.16)$$

Assuming non-radiating Neumann boundary conditions corresponding to a flat phase $\partial_x\phi|_{x=0,L}=0$, $\delta\phi(x)$ can be expanded in a cosine series, i.e.

$$\delta\phi(x) = \sum_w \phi_w \cos(k_w x) \quad (2.17)$$

with momenta $k_w = \frac{\pi w}{L}$ with $w \in \mathbb{N}$ [116, 118, 188–191]. For sufficiently small junctions the resonance frequencies of spatial modes with $w > 1$ are sufficiently detuned from the ones of the $w = 0, 1$ modes such that there is no danger of accidentally addressing them. Using the expansion from Eq. (2.17) in the Hamiltonian from Eq. (2.16) we obtain

$$\mathcal{H}_\phi = \mathcal{H}_{w=0} + \mathcal{H}_{w=1} + \mathcal{H}_{\text{int}}. \quad (2.18)$$

$$\mathcal{H}_{w=0} = E_J\left[\frac{1}{2\omega_0^2}\left(\frac{d\phi_0}{dt}\right)^2 + \frac{1}{2}\cos(\phi^0)\phi_0^2\right] + O(\phi_0^4) \quad (2.19)$$

$$\mathcal{H}_{w=1} = \frac{1+\delta_{w,0}}{2}E_J\left[\frac{1}{4\omega_0^2}\left(\frac{d\phi_1}{dt}\right)^2 + \frac{\omega_1^2}{4\omega_0^2}\phi_1^2\right] + O(\phi_0^4) \quad (2.20)$$

with the frequency of the cavity mode given by $\omega_1^2 = \omega_0^2(\cos(\phi_0) + \lambda_J^2 k_1^2)$

$$\mathcal{H}_{\text{int}} = -\frac{\hbar J_{\text{bias}}}{2eD}\frac{1}{4}\phi_0\phi_1^2 + O(\phi_0^2, \phi_1^2), \quad (2.21)$$

with the coupling between modes proportional to the bias current. The bias current leads to a reduction of the oscillation frequency of the spatially homogeneous mode to $\omega_0\sqrt{\cos(\phi_0)}$ in Eq. (2.19), while the frequency ω_1 of the $w = 1$ mode remains unaffected in Eq. (2.20). As we discussed in Sec. 1.1.3 considering the washboard potential in a short Josephson junction, the presence of the homogeneous bias current leads to a reduction of the height of the trapping potential as given by Eq. (1.25). On the other hand, the dynamics of the first cavity mode $w = 1$ is only indirectly affected by the bias current through the coupling term from Eq. (2.21). To suppress thermal excitation out of the washboard potential, it is therefore only necessary to cool the spatially homogeneous phase. If $\omega_1 \gg \omega_0$, the thermal occupation of $w = 1$ mode is negligible. In this case, we can use an interpretation of the

present situation in terms of the setup from optomechanics (Sec. 2.1.1) with the $w=0$ ($w=1$) mode taking the role of the mechanical oscillator (cavity).

In Appendix B.1, we diagonalise $\mathcal{H}_{w=0,1}$ from Eq. (2.19) and (2.20), in terms of the respective creation $\hat{b}_w^\dagger$ and annihilation operator $\hat{b}_w$, i.e. $\phi_w \sim \hat{b}_w + \hat{b}_w^\dagger$. The interaction term from Eq. (2.21) becomes

$$\mathcal{H}_{\text{int}} = -\frac{\hbar\Omega_{\text{bias}}}{2}(\hat{b}_0+\hat{b}_0^\dagger)(\hat{b}_1+\hat{b}_1^\dagger)^2, \tag{2.22}$$

where the coupling frequency is given by

$$\Omega_{\text{bias}} = \frac{J_{\text{bias}}}{J^C}\frac{\omega_0^2}{\omega_1}\sqrt{\frac{2\hbar\omega_0}{\sqrt{\cos(\phi_0)}E_J}}. \tag{2.23}$$

Interpreting the spatially homogeneous mode ϕ_0 as the mechanical oscillator and the spatially dependent mode as the cavity field, Eq. (2.22) is formally equivalent to optomechanical coupling due to radiation pressure $(\hat{b}+\hat{b}^\dagger)\hat{a}^\dagger\hat{a}$ between the displacement of the mechanical oscillator and the number density in the cavity field. For small bias currents the coupling strength in Eq. (2.23) depends linearly on the bias current. Using this scheme, it is therefore impossible to cool phase fluctuations in the absence of the bias current. Increasing the bias current towards the critical current $J_{\text{bias}} \to J^C$ ($J_{\text{bias}} \leq J^C$) the coupling strength diverges as the normal mode frequency of the spatially homogeneous mode is reduced to zero. In Section 2.1.1, we showed that the coupling is further enhanced by a factor $\bar{a}$ corresponding to the amplitude of the coherent state $\bar{a}$ created by an external laser drive. Here, the first spatial mode of the superconducting phase, i.e. the cavity mode, can be selectively driven by applying a time and spatially dependent voltage $V = \mathrm{i}V_1 e^{\mathrm{i}\omega_1 t}\cos(k_w x)$, which according to the AC-Josephson relation from Eq. (1.19) leads to a solution for the first spatial mode of the form $\phi_1 = a_1 e^{\mathrm{i}\omega_1 t}$ with amplitude $a_1 = 2\pi V_1/\omega_1\Phi_0$. The maximum driving strength a_1 is limited by the maximum possible voltage that can be selectively applied either due to discharge or other experimental constraints.

Oscillations in the spatially homogeneous Josephson phase lead to sidebands in the cavity resonance at $\omega_1 \pm \omega_0$. By tuning the driving to these sidebands the spatially homogeneous phase of the Josephson junction can be respectively heated or cooled. For a high finesse cavity, the retardation of the cavity field results into a change of the effective damping rate Γ_{eff} of the $w=0$ mode given by Eq. (2.9). A change in the effective damping rate without modification of the thermal noise leads to a proportional change in the effective temperature $T_{\text{eff}} = T\frac{\gamma_m}{\Gamma_{\text{eff}}}$ from Eq. (2.13), where γ_m is the decay rate of the spatially homogeneous mode in the absence of driving and T the system temperature. A change in the effective temperature leads to both a modification of the width σ_I of the switching current distribution as $\sigma_I \propto \Gamma_{\text{eff}}^{3/2}$ [93] such that $\sigma_I \propto T_{\text{eff}}^{2/3}$ and mean value according to Eq. (1.26).

Though a bias current is necessary to allow for coupling between the modes, increasing the bias current reduces the height of the activation barrier in the washboard potential given by Eq. (1.25). To avoid switching from a superconducting to a resistive state, the cooling mechanism is limited to low enough temperatures such that the phase particle remains trapped in one of the potential wells and the system does not switch into a resistive state.

Hammer et al. implemented the scheme at very small temperature T such that the switching into a resistive state occurs at large bias currents J_{bias}. Due to these large bias currents, they only observed a change of 0.3% in the mean critical current in the presence of the drive. Interpreting the temperature reduction in terms of changes to the width of the switching current distribution σ_I, they determine an effective temperature of 320 mK at an initial cryostat temperature of 600 mK. One of the limitations of this cooling scheme lies in the ambivalent role played by the bias current, which on the one hand is necessary to introduce the coupling between the modes but also lowers the trapping potential.

We notice that similar to the implementation of the optomechanical cooling scheme in microwave cavities, the thermal occupation of the cavity modes of the long Josephson Junction cannot be ignored, which limits the cooling efficiency. Here, this effect could potentially be mitigated by increasing the frequency of the cavity mode ω_1 through a decrease of the junction length. The minimal junction size is limited by the requirement that the driving frequency is sufficiently below the superconducting gap $\omega_L \ll \Delta/\hbar$ such that it is possible to ignore the breaking of the superconducting pairs. In an HTSC implementation of the cooling scheme, both the cavity length and the selective driving of the $w = 1$ mode become even more challenging experimentally as HTSC is very brittle and THz frequency still less controlled. Finally, we emphasize that this scheme is fundamentally constraint to low temperatures and does not allow approaching the phase transition.

2.1.3 Parametric cooling of bilayer stacks of short Josephson Junctions

In this section, we are going to discuss the physical mechanism behind the parametric cooling scheme proposed in Ref. [31]. The model treats bilayer cuprates as stacks of two alternating short Josephson junctions. The careful discussion of the Josephson electrodynamics is postponed to Sec. 3.1, where we discuss the cooling of phase fluctuations in long Josephson junctions. Here, we would like to instead focus on the underlying parametric cooling mechanism. This allows us to point out different driving regimes and potential issues encountered later in the full model, without the technical clutter associated with the full treatment. For this purpose we only consider two capacitively coupled short Josephson junctions indexed by l and h of thickness $D_{l,h}$ and critical current $J^C_{l,h}$ respectively, as shown in a) of Fig. 2.3. Careful discussion of the underlying physics will be mostly postponed to Chapter 3.

For intrinsic Josephson junctions as found in HTSC, the thickness of the superconducting sheets is very thin compared to the Debye length, such that electric fields in one junction are not screened by a single sheet and penetrate neighbouring junctions. These fields induce charges and influence the phase dynamics in neighbouring junctions [192–194], which is modelled by a capacitive coupling between the junctions of the stack and can be described in terms of a modified version of the original Josephson relation (see Eq. (3.3)) given by

$$\frac{\Phi_0}{2\pi}\partial_t\vec{\phi}(x) \quad = \quad \mathbf{C}\vec{E}^z(x), \tag{2.24}$$

where we arranged the gauge invariant phase difference and junction parameters into vectors, e.g. $\vec{E}^z$ for the electric field along the z-axis and $\vec{\phi}$ for the gauge invariant phase differences

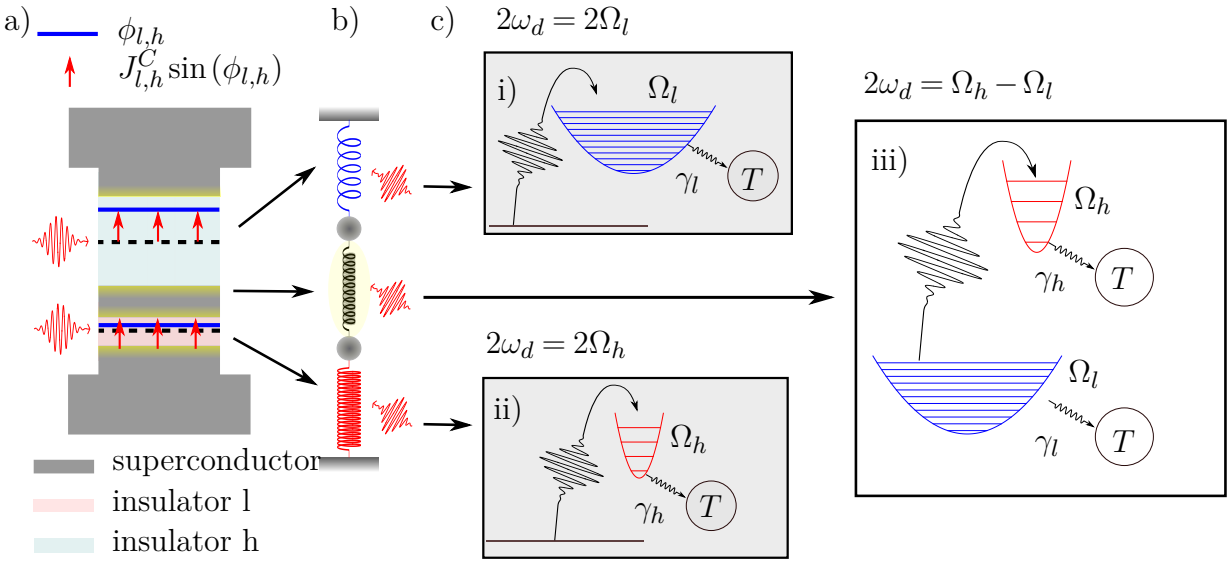


Figure 2.3: **a)** Stack of two different short Josephson junction aligned along the z-axis consisting of superconducting sheets (grey) and two different insulators (bright blue and red area). The two Josephson junctions differ in critical current density $J^C_{l,h}$ and thickness $D_{l,h}$. The blue lines indicate deflection of the gauge-invariant phase difference $\phi_{l,h}$ from the equilibrium position (black dashed line), which leads to a supercurrent density $J^C_{l,h}\sin\phi_{l,h}$ (red vertical arrows). As the superconducting sheets are very thin, an electric field can penetrate the neighbouring junction and lead to capacitive coupling as indicated by the yellow shades. Also indicated is an incident infrared pulse, which is modelled as a modulation of the critical current (Sec. 3.1). **b)** In the normal-mode frame of the time-averaged problem, the linearised equations of motion are formally equivalent to two particles oscillating with normal mode frequency $\Omega_{l,h}$ as indicated by the red and blue springs. The external driving leads to a parametric modulation of the coupling strength. **c)** Different terms in the Hamiltonian become resonant depending on the driving frequency. In this section, we focus on driving at the frequency difference $2\omega_d = \Omega_h - \Omega_l$ such that the model reduces to the situation shown in panel **iii)**, which is equivalent to the situation found in optomechanics with each oscillator coupled to its respective heat bath at temperature T with decay rates $\gamma_{l,h}$. **i)** and **ii)** In Sec. 2.2.1, on the other hand, we consider driving frequencies $2\omega_d = 2\Omega_{l,h}$, where the relevant system reduces to either **i)** for $2\omega_d = 2\Omega_l$ or **ii)** for $2\omega_d = 2\Omega_h$ corresponding to a single parametrically driven Hamiltonian weakly coupled to a heat bath at temperature T with decay rates $\gamma_{l,h}$. The other oscillator is sufficiently detuned to remain unaffected by the drive.

such that the two entries of

$$\vec{\phi} = \begin{pmatrix} \phi_l \\ \phi_h \end{pmatrix}, \tag{2.25}$$

correspond to the phase difference in the corresponding junction l, h and

$$\mathbf{C} = \begin{pmatrix} 1+2\alpha_1 & -2\alpha_2 \\ -2\alpha_1 & 1+2\alpha_2 \end{pmatrix} \mathbf{D}, \tag{2.26}$$

is a matrix responsible for the capacitive coupling with capacitive coupling parameters $\alpha_{1,2}$ [193,194] taking values from 0.1 to 3 depending on the material [195], Φ_0 is the magnetic flux quantum and $\mathbf{D}$ is a diagonal matrix containing the thickness of the two insulators as $\mathbf{D} = \mathrm{diag}(D_l, D_h)$. Correspondingly, the critical currents of each junction are arranged into a diagonal matrix $\mathbf{I}^C = \mathrm{diag}(I_l^C, I_h^C)$. The strong excitation of a phonon mode by an external infrared pulse is modelled as a modulation of the critical current $\mathbf{I}^C(1 + \mathbf{A}/2(1 - \cos(2\omega_d t))$ with $\mathbf{A} = \mathrm{diag}(A_l, A_h)$ being a diagonal matrix for the amplitudes $A_{l,h}$ in the respective junction. In the short junction regime the corresponding Hamiltonian of the two coupled junctions from Sec. 3.1 is given by

$$\mathcal{H}_{\mathrm{cap}}(t) = \frac{1}{2}\vec{p}^{\top}\mathbf{M}^{\phi^{-1}}\vec{p} - \frac{\Phi_0}{2\pi}\mathrm{diag}(\vec{I}^C)\top(1 + \mathbf{A}/2(1 - \cos(2\omega_d t))\cos(\vec{\phi}), \tag{2.27}$$

where $\vec{p} = \mathbf{M}^{\phi}\partial_t\vec{\phi}$ is the conjugate variable to the $\vec{\phi}$ field and

$$\mathbf{M}^{\phi} = \left(\frac{\Phi_0}{2\pi}\right)^2 \epsilon_0\epsilon_r A_{\mathrm{area}}\mathbf{C}^{-1}, \tag{2.28}$$

is the mass matrix for a junction of area A_{area} with relative permittivity ϵ_r and free space permittivity ϵ_0.

For this approach to be valid, the absolute value of the order parameter ψ, which is proportional to the charge density, $n_s \propto |\psi|^2$, is taken to be constant and only the phase varies. Due to the d-wave character (see Sec. 1.2), the gap-function closes at specific momentum directions [82], which means that nodal quasi-particles are essentially omni-present. They are expected to play a role in suppressing the phase stiffness at very low temperatures [114]. The present treatment does not include the suppression of the phase stiffness due to nodal quasi-particles. For HTSC, this is justified as phase fluctuation play a major role in the phase transition due to the small charge density [55, 135, 136]. We only include classical thermal fluctuations, as for temperatures close enough to T_c, quantum fluctuations are screened by the background normal electron fluid [55, 135, 136]. Any external driving frequency ω_d is assumed to be significantly below the superconducting gap, i.e. $\omega_d \ll \Delta/\hbar$ [119] to avoid breaking of superconducting pairs.

Two parametrically coupled springs In the following we assume the thermal fluctuations of the phase to be sufficiently small that we can expand the full non-linear Josephson potential in Eq. (2.27) around one of the minima, i.e. $\vec{\phi}_0 = 0$, to quadratic order. The time-averaged part of the Hamiltonian (2.27) (obtained by setting $\cos(2\omega_d t)$ to zero) can

be diagonalised using a time-independent similarity transformation $\mathbf{P}$ (Sec. 3.2 and Appendix A.4.1). In this frame the transformed spring constant is given by

$$\mathbf{K}(t) = \mathbf{m}\boldsymbol{\Omega}^2 - \mathbf{K}^d \cos(2\omega_d t), \tag{2.29}$$

with driving amplitude

$$\mathbf{K}^d = \frac{1}{2}\frac{\Phi_0}{2\pi}\mathbf{P}^\top \mathbf{I}^C \mathbf{A}\mathbf{P} \tag{2.30}$$

and normal mode frequencies $\Omega_{l,h}$ (mass $m_{l,h}$) arranged as $\boldsymbol{\Omega} = \mathrm{diag}(\Omega_l, \Omega_h)$ ($\boldsymbol{m} = \mathrm{diag}(m_l, m_h)$), where the difference between low and high normal modes $\Omega_l < \Omega_h$ is inherited from the difference in magnitudes of the critical current and thickness of the two layers. Using the transformed coordinates $\vec{\mathfrak{q}} = \mathbf{P}^{-1}\vec{\phi}$ and momentum $\vec{\mathfrak{p}} = \mathbf{m}\partial_\tau \vec{\mathfrak{q}} = \mathbf{P}^\top \vec{p}$ we obtain the total Hamiltonian as

$$\mathcal{H}_{\mathrm{cap}}(t) = \frac{1}{2}\vec{\mathfrak{p}}^\top \mathbf{m}^{-1}\vec{\mathfrak{p}} + \frac{1}{2}\vec{\mathfrak{q}}^\top \mathbf{K}(t)\vec{\mathfrak{q}}. \tag{2.31}$$

This Hamiltonian is formally equivalent to two particles of masses m_l and m_h attached to springs of a low Ω_l and high Ω_h frequency as shown in panel b) of Fig. 2.3, which are decoupled in the absence of a drive. The two particles are coupled to each other by a weak spring with a time-dependent spring constant. Coordinate and momentum can be promoted to operators, i.e. $\mathfrak{q}_{r=l,h} \to \hat{\mathfrak{q}}_{r=l,h}$ and $\mathfrak{p}_{r=l,h} \to \hat{\mathfrak{p}}_{r=l,h}$, that satisfy the standard commutation relation $\left[\hat{\mathfrak{q}}_r, \hat{\mathfrak{p}}_s\right] = \mathrm{i}\hbar\delta_{rs}$ with $r, s = \{l, h\}$. Introducing the standard creation $a_r^\dagger$ an annihilation operator a_r for both oscillators $r = l, h$ as

$$a_r = \sqrt{\frac{m_r\Omega_r}{2\hbar}}\left(\hat{\mathfrak{q}}_r + \mathrm{i}\frac{\hat{\mathfrak{p}}_r}{m_r\Omega_r}\right) \tag{2.32}$$

$$a_r^\dagger = \sqrt{\frac{m_r\Omega_r}{2\hbar}}\left(\hat{\mathfrak{q}}_r - \mathrm{i}\frac{\hat{\mathfrak{p}}_r}{m_r\Omega_r}\right), \tag{2.33}$$

satisfying $[a_r, a_s^\dagger] = \delta_{rs}$ with $r, s = \{l, h\}$, the Hamiltonian can be divided as $\mathcal{H}_{\mathrm{cap}}(t) = \mathcal{H}^u_{\mathrm{cap}} + \mathcal{H}^d_{\mathrm{cap}}(t)$ into an undriven part

$$\mathcal{H}^u_{\mathrm{cap}} = \sum_{r=l,h} \hbar\Omega_r a_r^\dagger a_r, \tag{2.34}$$

where we ignored the zero-point energy, and a driven part

$$\mathcal{H}^d_{\mathrm{cap}}(t) = -\cos(2\omega_d t)\,\hbar \sum_{r,s=l,h} \Lambda_{rs}\left(a_r + a_r^\dagger\right)\left(a_s + a_s^\dagger\right), \tag{2.35}$$

where the driving strength is characterised by the frequencies Λ_{rs} obtained from the driven part of the spring constant as

$$\Lambda_{rs} = \frac{1}{2^2\sqrt{m_r m_s \Omega_r \Omega_s}}\mathbf{K}^d_{rs}, \tag{2.36}$$

which only has off-diagonal terms in the presence of capacitive coupling, i.e. $\alpha_{1,2} \neq 0$.

Here we are interested in driving either close to the frequency difference (cooling sideband) or sum (heating sideband) $2\omega_d = \Omega_h \pm \Omega_l$, which respectively allows for resonant energy transfer between the two normal modes (Appendix B.6) and non-degenerate parametric amplification. For a bilayer cuprate such as YBCO the high frequency mode is approximately an

order of magnitude larger than the low frequency mode [18], i.e. $\Omega_h \approx 10\Omega_l$. For weak driving $\Lambda_{lh} \ll \Omega_{lh}$, we can eliminate fast oscillating terms through a rotating wave approximation (in Sec. 2.2.2 we consider other driving frequencies). Using the unitary $U = e^{-\mathrm{i}2\omega_d t a_h^\dagger a_h}$ the system Hamiltonian reduces to a time-independent one given by

$$\bar{\mathcal{H}}_{\mathrm{cap}}(t) \approx \hbar\Omega_l a_l^\dagger a_l + \hbar(\Omega_h - 2\omega_d) a_h^\dagger a_h - \hbar\Lambda_{lh}\left(a_l + a_l^\dagger\right)\left(a_h + a_h^\dagger\right), \tag{2.37}$$

which is formally equivalent to the optomechanical Hamiltonian (2.5) with the low and high-frequency mode respectively taking the role of the mechanical oscillator and fluctuation in the cavity field.

Due to the frequency difference $\Omega_h \approx 10\Omega_l$, thermal excitation of the low-frequency mode costs little energy compared to thermal occupation of the high-frequency mode. The low-frequency normal mode corresponds to excitations in the blue shaded junction from Fig. 2.3, which are associated with a small critical current[2]. As the trapping potential is approximately $\propto J_l^C$ (from Eq. 1.25) excitations in the low frequency mode are prone to transition to a resistive state characterised by a finite time-averaged voltage (see discussion around Fig. 1.2), destroying superconductivity. Therefore, it is desirable to cool this mode, effectively reducing its thermal occupation. This is achieved by pumping energy quanta into the high-frequency normal mode by driving the system at approximately the frequency difference between Ω_h and Ω_l, such that the detuning [158]

$$\Delta\omega_{\mathrm{diff}} = 2\omega_d - (\Omega_h - \Omega_l), \tag{2.38}$$

is approximately zero. Here the drive provides the necessary energy allowing for quanta to be exchanged between the low-frequency mode and the high-frequency mode in the system. For this driving frequency Hamiltonian (2.37) further simplifies to

$$\mathcal{H}_{sys}^{d,I}(t) = -\Lambda_{hl} e^{\mathrm{i}\Delta\omega_{\mathrm{diff}} t} a_l{}^\dagger a_h - \Lambda_{hl}^* e^{-\mathrm{i}\Delta\omega_{\mathrm{diff}} t} a_l a_h{}^\dagger. \tag{2.39}$$

Master equation for driven system We assume that each of the normal modes of frequency Ω_r with $r = l, h$ is coupled to its own independent[3] Markovian bath of phonon modes. More specifically, the total Hamiltonian is given by

$$\mathcal{H}(t) = \mathcal{H}_{\mathrm{cap}}(t) + \mathcal{H}_{\mathrm{B}}^l + \mathcal{H}_{\mathrm{B}}^h + \mathcal{H}_{\mathrm{coupl}}^l + \mathcal{H}_{\mathrm{coupl}}^r, \tag{2.40}$$

where the first term is the system Hamiltonian, the second& third term $\mathcal{H}_{\mathrm{B}}^{r=l,h}$ is the Hamiltonian of the heat bath of the $r = l, h$ mode and the fourth& fifth term $\mathcal{H}_{\mathrm{coupl}}^{r=l,h}$ describes the respective interaction between the respective heat bath and normal mode. Each heat bath is modelled as an ensemble of harmonic oscillators with a continuous spectrum [172, 196]

$$\mathcal{H}_{\mathrm{B}}^r = \hbar \int_{\Delta_\omega^r} d\omega \omega b_{r,\omega}^\dagger b_{r,\omega}. \tag{2.41}$$

[2] In the absence of capacitive coupling, this can be seen from the Josephson plasma frequency $\omega_0^2 = \frac{2eD_l}{\hbar}\frac{J_l^C}{\epsilon_0\epsilon_l}$ (from Sec. 1.1.3), if the two junction have a comparable thickness $D_l \sim D_h$ and permittivity $\epsilon_l = \epsilon_h$.

[3] The oscillators are only approximated separated physically insofar as their largest contribution arises from one of the junctions respectively.

where $b_{r,\omega}$ ($b^\dagger_{r,\omega}$) is the annihilation (creation) operator of a harmonic oscillator at frequency ω satisfying $\left[b_{r,\omega}, b^\dagger_{s,\omega'}\right] = \delta(\omega-\omega')\delta_{rs}$. The frequency density of the rth heat bath is taken to be constant over the respective frequency interval $\Delta^r_\omega = \left[\Omega_r - \frac{\Delta_c}{2}, \Omega_r + \frac{\Delta_c}{2}\right]$ with coupling bandwidth[4] Δ_c. Both baths are taken to be in a thermal state at temperature T with Bose occupation number $n(\omega) = 1/(e^{\hbar\omega/k_BT}-1)$ with k_B the Boltzmann constant. They are respectively coupled to the system operator a_r via the fourth and fifth term in Eq. (2.40) with $r = l, h$ as

$$\mathcal{H}^r_{\text{coupl}} = \mathrm{i}\hbar \int_{\Delta^r_\omega} d\omega \kappa_r(\omega) \left[b^\dagger_{r,w} a_r - a^\dagger_r b_{r,w}\right], \tag{2.42}$$

where the coupling strength $\kappa_r(\omega)$ is taken to be constant over the bath interval Δ^r_ω (first Markov approximation) such that $\kappa_r(\omega) = \sqrt{\gamma_r/2\pi}$ with decay rate γ_r for $r = l, h$ (here $\gamma_l < \gamma_h$). For weak system-bath coupling, the time-scale, $\tau_R = 1/\gamma_r$, the system needs to establish thermal equilibrium after a quench is large. If τ_R is large compared to the thermal bath correlation time τ_B, we can define a coarse-graining time-scale Δt such that $\tau_B \ll \Delta t \ll \tau_R$ [196–198]. Physically, this separation of time-scales and the two inequalities respectively allow us to perform the Born and Markov approximation (see also discussion around Eq. (B.27)). The Born approximation assumes the coupling to the bath to be sufficiently weak such that is is sufficient to treat it perturbatively, keeping only second-order correlation function. The Markov approximation allows ignoring any memory effects of the bath, i.e. the thermal correlation time τ_B is so short that excitations in the bath decay very quickly on the time-scale of the system evolution and cannot re-enter the system (see full derivation in Appendix. B.3 and Appendix B.3.1). To consistently describe the dynamics on time scales determined by Δt, we have implicitly ignored energy non-conserving terms $b_{r,w}a_r$ and $b^\dagger_{r,w}a^\dagger_r$ from the Hamiltonian given in Eq. (2.42). In the absence of driving, this secular approximation is valid for $\tau_S \ll \Delta t$ with $\tau_S = 1/\Omega_r$ [196] (Appendix B.3.1). As the driving couples the normal modes, this RWA in the coupling to the heat bath requires the interaction between the oscillators in the different bath to be weak enough such that $\Lambda_{lh}/2 \ll \max(\sqrt{\Omega_l\gamma_h}, \Omega_l)$ [175].

In the Born-Markov approximation with $1/\Delta_c, \tau_B \ll \Delta t \ll \tau_s$, the weakly driven system $\Lambda_{lh}/2 \ll \max(\sqrt{\Omega_l\gamma_h}, \Omega_l)$ can be described by the quantum optical master equation given by [175]

$$\dot{\rho} = -\frac{\mathrm{i}}{\hbar}[\mathcal{H}_{sys}(t), \rho] + \sum_r \gamma_r \left(n(\Omega_r)+1\right)\mathcal{D}[a_r](\rho) + \sum_r \gamma_r n(\Omega_r)\mathcal{D}[a^\dagger_r](\rho), \tag{2.43}$$

where the first describes the coherent dynamics due to the system Hamiltonian $\mathcal{H}_{sys}(t)$ and the dissipative dynamics is characterised by the Lindblad superoperator in terms of the Lindblad jump-operator c as

$$\mathcal{D}[c](\rho) = c\rho c^\dagger - \frac{1}{2}\left(c^\dagger c\rho + \rho c^\dagger c\right). \tag{2.44}$$

[4]The coupling bandwidth Δ_c has to be chosen small enough that one is able to approximate the coupling strength as constant over the interval Δ^r_ω but also sufficiently large to be able to define the coarse graining timescales, which satisfies $\Delta t \gg 1/\Delta_c$ [197]. The system dynamics is expected to be independent of the coupling bandwidth for $\Delta_c \geq \frac{1}{\tau_B}$, where τ_B is the thermal correlation time. With increasing temperature the bath correlation time decreases such that the bath cannot resolve the frequency of the oscillator. In order to avoid modifying the system dynamics, the coupling bandwidth has to be extended. In the limit where Δ_c can be chosen small compared to the frequency separation between $\Omega_{l,h}$, the assumption that the two oscillator couple to physically different thermal baths has no influence on the dynamics.

Here the coupling to two independent heat baths only enters as additive contributions to the master equation in Eq. (2.43), which means that it does not include quantum interference between the baths. Quantum interference terms are expected to become relevant in the non-Markovian limit [199]. The master equation given in Eq. (2.43) is valid for arbitrary ratios of $\Lambda_{lh}/\gamma_{h,l}$ as long $\Lambda_{lh} \ll \Omega_l$ ($\Lambda_{lh} \ll \max(\sqrt{\Omega_l \gamma_h}, \Omega_l)$) and $\gamma_{l,h} \ll \Omega_l$ [175]. In this limit, it can also describe the strong coupling regime leading to normal mode splitting [176]. Increasing the coupling strength further requires to implement the rotating wave approximation in the interaction frame of the coupled system dynamics. The decay rates and normal modes are shifted by the coupling between the two harmonic oscillators [200]. We emphasise that the master equation in Eq. (2.43) cannot describe the ultrastrong coupling [177] limit[5] corresponding to coupling strengths $\Lambda_{lh} \sim \Omega_{l,h}$. Using this master equation would not guarantee the relaxation to the true ground state of the system [178, 200].

For specific driving strength on the cooling sideband, the high-frequency oscillator and drive can both be eliminated at the cost of introducing a structured environment with an effective lower bath temperature [175]. However, this approach breaks down[6] for intermediate coupling strengths $\Lambda_{lh} \sim \gamma_h$. We will therefore instead directly calculate the thermal occupation of both modes. Using the master equation from Eq. (2.43), we can derive the equation of motion for the expectation value of an operator D, given by $\frac{d\langle D\rangle}{dt} = \mathrm{tr}\,(D\dot{\rho})$. For the vector

$$\vec{\tilde{u}}^{\top}(t) = \left(\langle a_l^\dagger a_l\rangle, \langle a_h^\dagger a_h\rangle, e^{\mathrm{i}2\omega_d t}\langle a_l^\dagger a_h\rangle, e^{-\mathrm{i}2\omega_d t}\langle a_h^\dagger a_l\rangle\right)^{\top}, \tag{2.45}$$

we obtain a closed set of equations of motion given in Appendix B.6. Using the Hamiltonian (2.39) for driving on the cooling sideband and keeping only contributions, which are large in the classical regime[7], where $n(\Omega_{l,h})$ is large, such that $n(\Omega_l)/n(\Omega_h) = \Omega_h/\Omega_l$ we obtain steady state values given by

$$\frac{\tilde{u}_1}{n(\Omega_l)} = 1 - \eta\left(1 - \frac{n(\Omega_h)}{n(\Omega_l)}\right), \tag{2.46}$$

and

$$\frac{\tilde{u}_2}{n(\Omega_h)} = 1 + \left(\frac{n(\Omega_l)}{n(\Omega_h)} - 1\right)\eta\frac{\gamma_l}{\gamma_h}, \tag{2.47}$$

where the cooling (heating) strength is characterised by a Lorentzian as

$$\eta = \frac{|\Lambda_{lh}|^2(\gamma_h+\gamma_l)/\gamma_l}{\Delta\omega_{\mathrm{diff}}^2 + \left(\frac{\Lambda}{2}\right)^2}, \tag{2.48}$$

with width

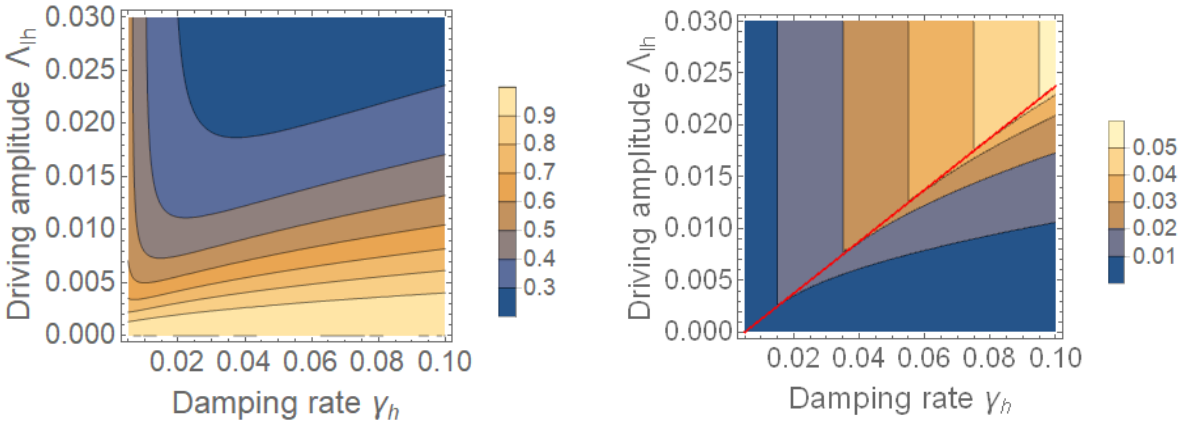
$$\Lambda = \sqrt{\frac{(\gamma_h+\gamma_l)^2\left(4|\Lambda_{lh}|^2+\gamma_h\gamma_l\right)}{\gamma_h\gamma_l}}. \tag{2.49}$$

[5] To describe the ultrastrong-coupling regime, it is necessary to derive a master equation in terms of the eigenstates of the coupled system, with the decay rates depending on the spectral weights of the environment at the transition frequencies keeping the counter-rotating terms as done in Ref. [178] for a QED system (see also Chapter 4).

[6] The resulting reduced master equation for only the low-frequency oscillator and low-frequency normal mode has been derived in Ref. [175] for the $\Lambda_{lh} \gg \gamma_h$ and $\Lambda_{lh} \ll \gamma_h$ regime respectively. In the strong coupling limit, the low-frequency normal mode contains admixtures from the high-frequency mode.

[7] We ignore zero-point motion due to quantum fluctuations.

The lower bound for this cooling width is dominated by the damping rates $\gamma_h + \gamma_l$ for weak coupling and becomes proportional to Λ_{lh} for strong coupling. Increasing the driving strength further it approaches the heating sideband and can eventually lead to an instability. The cooling ratio $\tilde{u}_1/n(\Omega_l)$ (Eq. (2.46)) can be diminished by reducing γ_l as shown in Fig. **(a)**, while there is an optimal value at $\gamma_h \approx 2\Lambda_{lh}$. The coherent energy transfer of quanta happens on a time-scale $2\pi/\Lambda_{lh}$. A low damping rate of the low-frequency oscillator allows for coherent energy transfer out of the low-frequency oscillator to the high-frequency oscillator. A large dissipation rate γ_h allows to quickly dissipate additional energy quanta to re-establish the equilibrium value before they could be coherently transported back to the low-frequency mode. However, a large γ_h also destroys the coherence of the transport, effectively "measuring" and freezing the high-frequency oscillator as in the quantum-Zeno effect, which explains the optimal value for γ_h.



(a) ***(b)***

Figure 2.4: **(a)** Cooling ratio $\frac{\tilde{u}_1}{n(\Omega_l)}$ obtained from Eq. (2.46) as a function of the damping rate of the high frequency mode γ_h and driving strength Λ_{lh}. The strongest cooling efficiency obtained by maximising both damping γ_h and driving strength Λ_{lh}, while keeping the damping of the low frequency mode low $\gamma_l = 0.005$. **(b)** Approximate cooling rate obtained from the equation of motion of $\vec{\tilde{u}}$ from Eq. (2.45) as a function of γ_h and driving strength Λ_{lh} from the decay rates of $d\vec{\tilde{u}}/dt$ ($\gamma_l = 0.005$).

For $4|\Lambda_{lh}|^2 \gg \gamma_h\gamma_l$ at resonant driving we obtain $\eta \to \frac{\gamma_h}{\gamma_l+\gamma_h}$ (Eq. (2.48)), such that the corresponding cooling ratio for the thermal occupation of the low frequency mode in the driven steady state vs thermal initial state becomes

$$\tilde{u}_1(4|\Lambda_{lh}|^2 \gg \gamma_h\gamma_l)/n(\Omega_l) = \frac{\gamma_l}{\gamma_l+\gamma_h} + \frac{\gamma_h}{\gamma_l+\gamma_h}\frac{\Omega_l}{\Omega_h}, \tag{2.50}$$

which is independent of the driving strength and depends only on the frequency ratio $\frac{\Omega_l}{\Omega_h}$ (here $\frac{\Omega_l}{\Omega_h} \approx 1/10$) and the damping rate ratio γ_l/γ_h. The first term arises from the thermal occupation of the low-frequency mode and can be decremented by a decrease in γ_l/γ_h, which allows for efficient, coherent transfer out of the low-frequency mode and fast thermal decay into the high-frequency bath. The second term arises due to the thermal occupation of the high-frequency mode, which can be decremented by decreasing the frequency ratio, and can be reduced by an increase in γ_l/γ_h, i.e. weaker coupling to the high-frequency bath. For

sufficiently weak driving strength it is possible to achieve $\Lambda_{lh}^2 \gg \gamma_l\gamma_h/4$ before entering the ultrastrong coupling regime.

The cooling rate for u_1 obtained from the equation of motion of $\vec{\tilde{u}}$ is shown in Fig. 2.4b (including counter-rotating terms in the coherent part of the Hamiltonian), where $\Lambda_{lh} \geq \gamma_l$ is shown to increase with driving strength up to a critical line (red in Fig. 2.4b given by $|\gamma_h - \gamma_l| = 4\Lambda_{lh}$). Increasing the damping strength beyond this critical line the real part of the decay rates becomes independent of the coupling strength and the driving strength only contributes to the splitting of the normal modes as observed experimentally in Ref. [176]. This normal mode splitting is characteristic of the regime, where the coupling is strong enough such that the coherent energy exchanges between the oscillator survives the dissipation and becomes visible. Surprisingly, the counter-rotating terms increase the cooling rate by a factor of approximately 2. This increase could potentially be explained by additional decay channels, which are otherwise eliminated through a rotating wave approximation. In the weak driving regime and $\gamma_l \nsim \gamma_h$ the cooling rate is approximated by

$$\gamma_d = \gamma_l + \frac{|\Lambda_{hl}|^2}{\gamma_h - \gamma_l} + O(\Lambda_{hl}^3), \tag{2.51}$$

which is lower bounded by γ_l.

2.2 Parametric amplification in Josephson junctions

In this section, we are going to consider a single parametrically driven harmonic oscillator. In Sec. 2.2.1, we start with a discussion of stability requirement in the presence of resonant driving. In Sec. 2.2.2 we outline the mechanism behind the parametrically enhanced interlayer current from Ref. [43, 45]. The expressions in these sections are only used to estimate the stability of resonantly driven modes. The strong driving regime away from parametric instabilities is discussed in Chapter 4.

2.2.1 Parametric instability

We now chose the driving frequency $\omega_L = 2\omega_d$ in the Hamiltonian from Eq. (2.35) such that the r-th normal mode is approximately driven at twice its resonance frequency (see Fig. 2.3**c)i)** and **ii)**), i.e. the detuning $\Delta = \Omega_r - \omega_L/2$ is small. After a RWA, the normal mode decouples into two separate subspaces $\mathcal{H}_{\text{cap}}(t) = \mathcal{H}_\phi^{(r)}(t) \otimes \mathcal{H}_\phi^{(\bar{r})}$ $(\bar{r} \neq r \in \{l, h\})$ with driving independent part $\mathcal{H}_i^{(r')} = \hbar\Omega_{r'} a_{r'}^\dagger a_{r'}$ $(r' = \{r, \bar{r}\})$ and $\mathcal{H}_\phi^{(r)}(t)$ as the total Hamiltonian of the resonantly driven oscillator given by

$$\mathcal{H}_\phi^{(r)}(t) = \mathcal{H}_i^{(r)} + \frac{\hbar}{2}\left(\Lambda_{rr} e^{-2\mathrm{i}\Delta t} a_r a_r + \Lambda_{rr}^* e^{2\mathrm{i}\Delta t} a_r{}^\dagger a_r{}^\dagger\right). \tag{2.52}$$

The Hamiltonian in Eq. (2.52) is of the form of parametric down conversion used for the generation of squeezed states [201] (see Appendix B.6). This type of Hamiltonian generically arises from the interplay of non-linearity and a pumping term, i.e. light propagating through

a medium with a large non-linear susceptibility [202], non-linear Josephson potential driven by a transmission line [203] or lattice anharmonicity in the presence of an infrared pulse, which was even shown to lead to parametrically enhanced electron-phonon coupling [46]. The presence of the strong pump pulses combined with the non-linearity of the Josephson potential was also shown to lead to a parametric amplification of Josephson plasma waves in HTSC [204].

The additive structure of the master equation in Born-Markov approximation from Eq. (2.43) allows us to focus on the subspace of the almost resonantly driven rth oscillator. Following the same procedure as for Eq. (2.45), we obtain a closed set of equation of motion given in Eq. (B.121) for the expectation values of all components of the vector $\vec{\tilde{u}} = (\langle a_r^\dagger a_r\rangle, \langle a_r a_r\rangle e^{2\mathrm{i}(\Omega_r+\Delta)t}, \langle a_r^\dagger a_r^\dagger\rangle e^{-2\mathrm{i}(\Omega_r+\Delta)t})^\top$ (Appendix B.6). For sufficiently weak driving, coupling the system to a heat bath can inhibit the parametric instability characterised by an exponential growth of $\tilde{u}_1$ and lead to a steady state $\frac{d\vec{\tilde{u}}(t)}{dt} = 0$ given by

$$\vec{\tilde{u}} = \frac{1}{\gamma_r^2 - 4\Lambda_{rr}^2 + 4\Delta^2} \begin{pmatrix} \gamma^2 n(\Omega_r) + 2\Lambda_{rr}^2 + 4n(\Omega_r)\Delta^2 \\ (-\mathrm{i}\gamma_r + 2\Delta)\Lambda_{rr}(1+2n(\Omega_r)) \\ (\mathrm{i}\gamma_r + 2\Delta)\Lambda_{rr}(1+2n(\Omega_r)) \end{pmatrix} \tag{2.53}$$

Close to resonance we only find a steady state if the damping is sufficiently strong or the driving sufficiently detuned from resonance that $\gamma_r^2 + 4\Delta^2 \geq 4\Lambda_{rr}^2$. In Sec. 2.3) we extend the parametric cooling scheme from Sec. 2.1.3 to long Josephson junctions, where a plethora of additional normal modes can be potentially resonantly driven. However, for sufficiently strong coupling to the heat bath any increase in the thermal occupation due to the driving is dissipated quickly, and the occupation is effectively "glued" the thermal one, i.e. letting[8] $\gamma_r \to \infty$ leads to $\vec{\tilde{u}} = (n(\Omega_r), 0, 0)^\top$.

Though, it is possible to suppress the parametric amplification using dissipation, in the presence of dissipation the dynamics cease to be coherent and the combination of driving with dissipation in general leads to heating, i.e. an increase in the product of the dispersion ($\Delta(A) = \sqrt{\langle A^2\rangle - \langle A\rangle^2}$ for A either phase ϕ or its momentum p_ϕ see Sec. 1.1.3) of the two quadrature operators. For the example of a damped parametric driven oscillator, it was shown in Ref. [205] with the help of a Magnus expansion, which is an expansion in the inverse driving frequency used to approximate the low-frequency dynamics of a system, that fast parametric driving not only gives rise to a renormalization in the effective frequency but also an increase in the effective temperature of the system. We now focus on the effect of parametric driving on physically measurable quantities for driving close to a parametric instability, but still sufficiently detuned that it is possible to achieve a steady state.

2.2.2 Parametrically enhanced interlayer current

In Ref. [43,45], the parametric enhancement of the interlayer current was studied for a bilayer model of short Josephson Junctions to explain the enhancement of the optical conductivity

[8] The validity of the expressions breaks down, but this gives an idea of the expected effect of very strong coupling.

in the zero frequency limit observed in Ref. [18]. The essence of the effect can be captured by including parametric driving in the Hamiltonian of a single Josephson junction of thickness D, area A_{area} and effective permittivity ϵ_r from Eq. (1.20) leading to [43]

$$\mathcal{H}_\phi = \frac{p_\phi^2}{2m_\phi} - \frac{\Phi_0}{2\pi}\left(I^C(t)\cos(\phi) + I_{\text{bias}}(t)\phi\right), \tag{2.54}$$

where ϕ is the gauge invariant phase difference, $p_\phi = m_\phi \partial_t \phi$ the conjugate momentum with mass $m_\phi = \left(\frac{\Phi_0}{2\pi}\right)^2 \epsilon_0 \epsilon_r A_{\text{area}}/D$ with magnetic flux quantum $\Phi_0 = h/2e$ and free space permittivity ϵ_0. The spatially homogeneous bias current $I_{\text{bias}}(t)$ allows to probe the linear system response and driving of a phonon mode is modelled as a parametric modulation of the critical current $I^C(t) = I^C(1 + A_J \cos(\omega_L t))$, where A_J is the driving amplitude and I^C is the critical current in absence of driving.

Okamoto et al. [43] model the decay classically by introducing a decay rate γ to the Hamilton's equation of Eq. (2.54). The corresponding equation of motion for ϕ is given by

$$\ddot{\phi} + \gamma\dot{\phi} + \omega_0^2\left(1 + A_J\cos(\omega_L t)\right)\sin(\phi) = \tilde{I}, \tag{2.55}$$

where $\tilde{I} = \frac{\Phi_0}{2\pi m_\phi} I_{\text{bias}}$ and ω_0 is the Josephson plasma frequency given by $\omega_0^2 = \frac{2eD}{\hbar}\frac{J^C}{\epsilon_0\epsilon_r}$ with $J^C = I^C/A_{\text{area}}$. The expression on the left hand side has the form of a damped Mathieu equation, which depending on the damping and driving strength can have instabilities at approximately

$$\omega_L/\omega_0 = 2/n \tag{2.56}$$

with $n = 1, 2....$ For constant damping γ, the linewidth of the resonances becomes narrower with increasing order n and requires larger driving strengths to become unstable [206]. In Section 2.2.1 we considered driving close to the principal instability corresponding to $n = 1$ with $\omega_L = 2\Omega_r$ ($\Omega_r = \omega_0$). The parametric enhancement of Josephson coupling [43,45] occurs for driving close to the $n = 2$ instability from Eq. (2.56) and requires strong driving strengths up to $A_J = 1$.

Keeping only terms linear in the phase, i.e. $\sin(\phi) \to \phi$ and Fourier transforming Eq. (2.55) such that $\phi(\omega) = \frac{1}{\sqrt{2\pi}}\int_{-\infty}^{\infty} dt e^{\mathrm{i}\omega t}\phi(t)$ we obtain

$$\left(\frac{-\omega^2 - \mathrm{i}\gamma\omega}{\omega_0^2} + 1\right)\phi(\omega) + \frac{A_J}{2}\left(\phi(\omega+\omega_L) + \phi(\omega-\omega_L)\right) = \tilde{I}(\omega)/\omega_0^2, \tag{2.57}$$

where the linear system response is probed by a bias current $\tilde{I}(\omega) = \tilde{I}_{\text{probe}}\delta(\omega - \omega_p)$ with $\tilde{I}_{\text{probe}} = \frac{\Phi_0}{2\pi m_\phi} I_{\text{probe}}$ oscillating at frequency ω_p. The parametric driving couples the system response at different harmonics of the driving frequency leading to a set of coupled linear equation for the nth harmonic $\phi_n = \phi(\omega_p + n\omega_L)$. According to Ginzburg Landau theory (see Eq. (1.17)), the Josephson coupling is proportional to the superconducting current density n_s^c as $J^C = \frac{\hbar}{D}\frac{2en_s^c}{m^*} = I^C/A_{\text{area}}$ with effective mass m^* [10]. Using the expression for the imaginary part of the conductivity $\Im(\sigma(\omega)) = \frac{n_s^c(2e)^2}{m^*\omega}$ obtained from the two-fluid model from Eq. (1.29), we can define the effective Josephson coupling as [33]

$$J_{\text{eff}}(\omega_L) = \frac{\hbar}{2eD}\Im(\omega\sigma(\omega))_{\omega\to 0}. \tag{2.58}$$

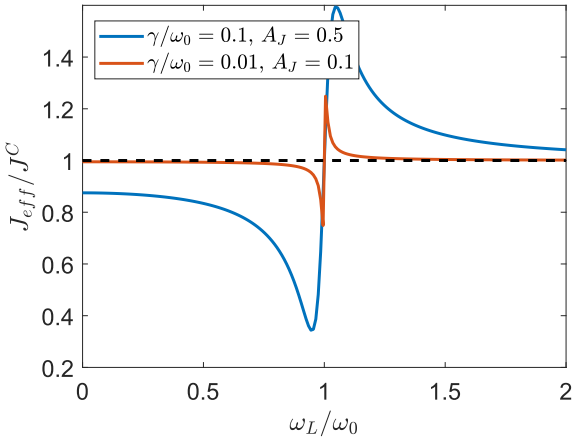


Figure 2.5: Effective interlayer current $J_{\text{eff}}(\omega_L)/J^C$ from Eq. (2.61) as a function of the ratio between parametric driving frequency and Josephson ω_L/ω_0 for $A_J = 0.5$, $\gamma/\omega_0 = 0.1$ (blue) and $A_J = 0.1$, $\gamma/\omega_0 = 0.01$. Driving close to $\omega_L \approx \omega_0$ can lead to a parametric instability.

To determine the conductivity of the driven system, we Fourier transform the AC-Josephson relation from Eq. (1.19) leading to $E(\omega_p) = \frac{\Phi_0}{2\pi}\frac{-\mathrm{i}\omega\phi(\omega_p)}{D}$. From the inverse of Ohm's law $E(\omega_p) = \frac{1}{\sigma(\omega_p)}J_{\text{probe}}(\omega_p)$, we further obtain the linear electric field response to a weak bias current density $J_{\text{probe}} = I_{\text{probe}}/A_{\text{area}}$ (Appendix B.6). The phase $\phi_{n=0} = \phi(\omega_p)$ can be obtained from Eq. (2.57) as a function of $\tilde{I}_{\text{probe}}$. Ignoring the coupling to second harmonics we obtain [43]

$$\sigma(\omega_p) = \frac{\epsilon_r\epsilon_0}{\mathrm{i}\omega_p}\frac{1}{4}A_J^2\omega_0^4\left(\frac{1}{\omega_0^2-(\omega_p+\omega_L)(\mathrm{i}\gamma+\omega_p+\omega_L)}+\frac{1}{\omega_0^2-(\omega_p-\omega_L)(\mathrm{i}\gamma+\omega_p-\omega_L)}\right) \quad (2.59)$$

$$+\frac{\epsilon_r\epsilon_0}{\mathrm{i}\omega_p}\left(\omega_p(\omega_p+\mathrm{i}\gamma)-\omega_0^2\right) \quad (2.60)$$

such that the effective enhancement of the Josephson coupling is given by

$$J_{\text{eff}}(\omega_L) = J^C\left(1-\frac{A_J^2\omega_0^2\left(\omega_0^2-\omega_L^2\right)}{2\left(\omega_0^2-\omega_L^2\right)^2+2\gamma^2\omega_L^2}\right). \quad (2.61)$$

In Figure 2.5 we plot Eq. (2.61) as a function of the driving frequency of the parametric drive for two pair of damping rates and driving amplitudes. The parametric driving of the critical current of a single Josephson Junction with frequencies just above the Josephson plasma resonance leads to an enhancement of the effective Josephson coupling. Driving below the resonance frequency, on the other hand, leads to a suppression of the effective coupling strength. For strong driving, care has to be taken to avoid unstable regions. The maximum enhancement of the effective Josephson coupling is obtained at $\omega_L = \sqrt{\omega_0}\sqrt{\gamma+\omega_0}$ with $J_{\text{eff}}/J = 1+\frac{A_J^2\omega_0^2}{2\gamma^2+4\gamma\omega_0}$. In a follow-up paper [45], the same authors showed that an even more substantial transient is possible in pulsed operation as in a pump-probe scheme instead of continuous driving.

The full model studied by Okamoto et al. [43] consists of a bilayer stack of short capacitive coupled Josephson junctions similar to the parametric cooling scheme studied in Ref. [31]

from Sec. (2.1.3). In agreement with Ref. [31], Okamoto et al. observe that driving on the cooling ($\omega_L^c = \Omega_h - \Omega_l$) and heating sideband ($\omega_L^h = \Omega_h + \Omega_l$) leads to a decrease and increase in the phase quadratures, $\langle \phi_l^2 \rangle$ and $\langle p_l^2 \rangle$, of the low frequency Josephson junction from Fig. 2.3. However, driving on the cooling and heating sideband is additionally also close to the $n = 2$ parametric instability of the high-frequency oscillation from Eq. (2.56) with $\omega_0 = \Omega_h$. Okamoto et al. [43] observe that driving on the cooling (heating) sideband is associated with a decrease $J_{\text{eff}}(\omega_L^c)/J^C < 1$ (increase $J_{\text{eff}}(\omega_L^h)/J^C > 1$) of the effective coupling strength due to the respective detuning $\omega_L^c < \Omega_h$ ($\omega_L^h > \Omega_h$) of the cooling (heating) sideband from resonance.

Okamoto et al. [43] analyse the influence of the driving on the Fourier transform of the current-current auto-correlation function[9] $S_{JJ}(\omega)$ of the Josephson current in the low frequency bilayer (see Sec. 2.1.3). The total area under the auto-correlation curve is proportional to the quadrature value, i.e. $\langle \phi_l^2 \rangle \propto \int d\omega S_{JJ}(\omega)$ (see discussion below Eq. (2.11)). Consequently, the total area under the $S_{JJ}(\omega)$ curve decreases (increases) for driving on the cooling (heating) sideband. However, the low frequency part of $S_{JJ}(\omega)$ changes in the opposite direction as it is related to a change in the low-frequency part of the conductivity according to the Kubo formula [180, 207], i.e. for driving on the heating sideband $\omega_L^h > \Omega_h$ Okamoto et al. observe a decrease in the low-frequency part of $S_{JJ}(\omega)$.

As the enhancement of J_{eff} for $\omega_L > \Omega_h$ is combined with heating, i.e. an increase in $\langle \phi_l^2 \rangle$, driving above the resonance does not make the system more stable against thermal fluctuation. In fact, including an additional stochastic Langevin term in Eq. (2.55) to model the effect of thermal noise, Okamoto et al. [45] show that though the steady-state value of J_{eff} averaged over multiple trajectories is enhanced in a driven junction, it also drops to zero at a lower temperature than in an undriven junction. Consequently, the critical temperature is reduced through driving. We emphasize that the driving terms responsible for the enhancement of the effective coupling and the parametric cooling are different, while the cooling arises from $\Lambda_{lh} = \Lambda_{hl}$ in Eq. (2.35) being non-zero, the enhancement of the effective interlayer current relies on $\Lambda_{hh} \neq 0$ (or for driving close to Ω_l on $\Lambda_{ll} \neq 0$). It is claimed in Ref. [43], that driving of critical current, i.e. $J^C(t)$, is equivalent to driving of the permittivity $\epsilon_r(t)$ motivated in Ref. [31]. Both schemes are studied in Chapter. 3. However, we find that the relative magnitude of off-diagonal terms $\Lambda_{lh} = \Lambda_{hl}$ and diagonal terms Λ_{hh}, Λ_{ll} differs significantly between different driving schemes. It is even possible to choose the driving amplitudes in the different junctions of the bilayer such that there is no off-diagonal terms, i.e. $\Lambda_{lh} = 0$, which makes cooling impossible. Any driving effect for the linearised model arising from the diagonal terms in the coupling matrix is then clearly a single junction effect and can be captured by the analytic treatment above.

[9] The current-current auto-correlation function is obtained from Eq. (2.11) by replacing x by the Josephson current $J_l^C \sin(\phi_l)$ of the low frequency junction with phase difference ϕ_l and critical current density J_l^C.

2.3 Strongly driven open quantum systems

As the driving required for Floquet engineering of Hamiltonians is usually very strong, it modifies the dissipative dynamics leading to a breakdown of simplistic phenomenological models for the dissipative dynamics. In order to establish the foundations for a steady state driven superconductor, we require theoretical frameworks which combine powerful tools such as Floquet theory with ultimate stabilisation of the open system dynamics through an open environment. Embracing both driving and dissipative dynamics might allow stabilising the state in new exotic states not accessible otherwise.

Heating through driving We start by discussing the effect of a drive on an external stimulation on a closed quantum system. The energy of a static Hamiltonian is conserved according to Noether's theorem due to time-translational symmetry. However, the energy E of a driven system changes as

$$\frac{dE}{dt} = \underbrace{\mathrm{tr}(H\dot{\rho})}+\mathrm{tr}(\dot{H}\rho). \tag{2.62}$$

In a naive interpretation, the first term could be called "heat" and the second "work" [208], through the distinction is not rigorous [209]. In the absence of a thermal bath, the evolution is governed by the Liouville equation $\dot{\rho} = -\frac{\mathrm{i}}{\hbar}[\mathcal{H}^{d,I}_{sys}(t), \rho]$. For this unitary evolution, the first term in Eq. (2.62), "heat", is zero and von Neumann entropy of the system does not change[10]. According to this definition, the drive performs work on the system but does not necessarily generate heat, which is generated through stochasticity and irreversibility due to the interaction with an environment or a measurement [209]. In a cyclic process of the closed quantum system, where the Hamiltonian returns to its original form, any energy change is therefore due to "work" [208], which is in agreement with the expectation for reversible processes.

However, from thermodynamics, it is expected that when compressing and decompressing an isolated gas, heat is generated unless the process is done adiabatically. Therefore, heat in quantum mechanics is often instead defined as the irreversible transition between instantaneous energy levels, while work corresponds to the reversible part, i.e. the changes in energy eigenstates controlled by the drive [211, 212]. In this framework, the system only remains in the ground state of the instantaneous Hamiltonian, if the process is performed sufficiently slowly, compared to the inverse of the minimum energy gap size, a problem commonly encountered in quantum annealing [213]. Though heat can, therefore, be generated in a closed quantum system undergoing a periodic drive, coherences still survive, and it is experimentally possible to apply the inverse transformation such as to transform the system back to its initial state. In the following, we will be using the second definition of heat and work.

The situation becomes significantly more complicated for an interacting many-body system [50, 214–216]. While a single driven particle only coherently exchanges energy with the

[10] This can be shown for the von Neumann entropy $S(\rho) = \mathrm{tr}(\rho\log(\rho))$ using cyclicity of the trace. Other measures for entropy can change, such as d-entropy based only on the diagonal elements of the density matrix [210].

drive, the presence of inter-particle interactions can lead to inelastic scattering processes resulting in heating [217].

Closed driven many-body system The natural way to describe the dynamics of a many-body system undergoing a time-periodic drive is Floquet theory (see Sec. 2.3.1), which can be considered as the time analogue of Bloch's theorem, which describes spatial periodicity. The stroboscopic time evolution over one period is governed by an effective time-independent Floquet Hamiltonian [218], which is in general hard to find. However, if the driving is of relatively high frequency compared to the system dynamics, it can be approximated for example through a truncated Magnus series in inverse driving frequency $\frac{1}{\omega_L}$. This high-frequency expansion has opened the possibility of Floquet engineering [218], allowing the stabilisation of quantum systems in non-equilibrium states or exotic phases, e.g. inverted position for a Kapitza pendulum and many body version of it [219] or generation of topological non-trivial band structures [220, 221].

The driving regime necessary for the generation of non-trivial, i.e. not simply time-averaged, Floquet Hamiltonian involves frequencies comparable to microscopic timescale in the system [44, 51, 214], where in general the Magnus expansion does not converge. However, a Floquet Hamiltonian approximated by a truncated Magnus series can still describe the pre-thermal regime [51, 214] relevant for Floquet engineering, where the system ceases to absorb energy. For later times, the system is generically expected to heat to infinite temperature [49–51], which can be understood as a driven analogue to the eigenstate thermalisation hypothesis (ETH). In the absence of a drive, ETH suggests that an isolated system prepared in a superposition of sufficiently closely spaced energy states can evolve towards a microcanonical ensemble with the same energy see Ref. [222]. In the presence of an external drive, the system energy is not conserved and the unitary operator inherits properties from random matrices leading to a featureless random steady state with an infinite temperature [50, 51]. A complementary view for driven many-body systems is that Floquet states are exponentially large combinations of eigenstates of the undriven Hamiltonian even when switching on the driving perturbatively [215]. As the relative phases of the combination are uncorrelated, the expectation values lose any information about the initial state[11].

Heating to an infinite temperature state can be avoided for specific systems, for example in the presence of disorder leading to many-body localisation [224]. There are indications that energy localisation, which prevents the energy from increasing indefinitely, is connected to the convergence in the Magnus series and is often encountered in integrable systems such as the Kapitza pendulum, but has also been found by driving originally ergodic many-body systems [216].

[11] This situation is also found for realistic preparations of an undriven system many-body system. The energy eigenstates are too densely packed for the realistic experimental preparation of an isolated one [223]. In the subsequent evolution, the coherence between the eigenstates is lost, resulting in a thermal like state.

2.3.1 Floquet-Markov master equation

Periodic driving can become so strong that it cannot be ignored in the dissipative dynamics and the details of the bath-system coupling start to matter [225–227] (Chapter 4). This strongly driven regime can be described within the framework of the Floquet-Born-Markov Master equation (FBM) approach [196, 228–232], which combines ideas from open quantum systems in Born-Markov approximation with Floquet theory [233–235]. FBM has been applied among others to strongly driven Rydberg atoms [229], two-level systems [236–238] and the parametrically driven harmonic oscillator [230].

One of the potential applications of FBM is engineering of dissipative dynamics. The most basic form of engineering dissipative dynamics is achieved by stabilising the exotic behaviour originally generated through Floquet engineering. In the presence of driving, the bath does not merely stabilise the system towards the thermal state but instead shows a strong dependence on the dissipation process beyond the temperature see for example [226, 227]. In Ref. [227], it was found that the coupling to the fermion bath can be designed such as to suppress photon-assisted tunnelling and achieve a Floquet-insulator state [227] in a one dimensional model of a driven semiconductor coupled to both phonon and fermionic baths. Despite the lack of coherence, the resulting diagonal steady-states are therefore still rather complicated, far beyond what would be expected from a thermal state. Using circularly polarised light to drive non-interacting electrons governed by a massless Dirac Hamiltonian leads to an effective magnetic field and results into a laser-induced Quantum Hall effect [226]. In the absence of the heat bath, the final spin density due to the electron distribution shows a strong anisotropy controlled by the way the driving field was switched on. Coupling to a phonon bath, the electron distribution becomes isotropic and ceases to depend on the initial state and switching on procedure [226].

Floquet theory

Many interesting transient states excited by strong pumps do not arise from the time-averaged Hamiltonian and are suggested to have a dynamical origin [40, 44, 46, 205, 219]. Even a very simple Hamiltonian can give rise to intriguing behaviour, e.g. inverted states for a Kapitza pendulum [218] or its many-body version [219]. Floquet theory is the standard theoretical toolbox to analyse the dynamics of a system undergoing a periodic drive in both condensed matter and atomic physics [235], though it does not capture the transient nature of the ultrashort pulses [45]. However, a continuous wave operation might be necessary to realised the ultimate goals of stabilising non-equilibrium HTSC in a steady state at room temperature.

The dynamics of a quantum system with time periodic Hamiltonian $H_{sys}(t) = H_{sys}(t + T_L)$ of period $T_L = \frac{2\pi}{\omega_L}$ undergoing a monochromatic periodic drive with frequency ω_L is governed by the Schrödinger equation

$$\left[H_{sys}(t) - \mathrm{i}\,\hbar\partial_t\right]|\psi(t)\rangle = 0. \tag{2.63}$$

According to Floquet theory [234, 236, 239, 240] there exist a complete set of Floquet states

$|\psi_\alpha(t)\rangle$ given by

$$|\psi_\alpha(t)\rangle = e^{-\mathrm{i}\mu_\alpha t}\,|\phi_\alpha(t)\rangle\,, \quad |\phi_\alpha\,(t+T_L)\rangle = |\phi_\alpha(t)\rangle\,, \tag{2.64}$$

where $|\phi_\alpha(t)\rangle$ are periodic Floquet modes of quasienergy $\epsilon_\alpha = \hbar\mu_\alpha$ and Floquet frequencies μ_α. As $e^{-\mathrm{i}\mu_{\alpha,k}t}\,|\phi_{\alpha,k}(t)\rangle = e^{-\mathrm{i}\mu_\alpha t}\,|\phi_\alpha(t)\rangle$ with $\mu_{\alpha,k} \equiv \mu_\alpha + k\omega_L$, the quasienergy forms bands labelled by integer k, i.e. it is only defined up to a multiple of ω_L. It follows that the Floquet modes satisfy an eigenvalue equation for the hermitian quasi-energy operator $H_Q(t) = \left[H_{sys}(t) - \mathrm{i}\,\hbar\partial_t\right]$ that is [241]

$$H_Q(t)\,|\phi_\alpha(t)\rangle = \left[H_{sys}(t) - \mathrm{i}\,\hbar\partial_t\right]|\phi_\alpha(t)\rangle = \epsilon_\alpha\,|\phi_\alpha(t)\rangle\,. \tag{2.65}$$

Promoting $H_Q(t)$ to an operator $\hat{H}_Q(t)$ acting in the combined Hilbert space $\mathcal{L}_{T_L} \otimes \mathcal{H}$ of the original system Hilbert space $\mathcal{H}$ extended by the space of square-integrable T_L-periodically time dependent functions $\mathcal{L}_{T_L}$ [241], this eigenvalue equation reduces to a time independent problem. The definition of scalar product in the combined Hilbert space consists of the scalar product of the original system Hilbert space $\mathcal{H}$ extended by time averaging such that

$$\langle\langle a|b\rangle\rangle = \frac{1}{T}\int_0^{T_L} dt\langle a(t)|b(t)\rangle, \tag{2.66}$$

where $|a(t)\rangle\rangle$ and $|b(t)\rangle\rangle$ are elements of the full Hilbert space as indicated by double kets, while $|a(t)\rangle$ and $|b(t)\rangle$ are the corresponding states of the original Hilbert space. A complete basis in the extended Hilbert space can for example be constructed by combining the complete basis of the original Hilbert space $|a\rangle$ with periodic functions $e^{\mathrm{i}m\omega_L t}$, i.e. $|a\rangle e^{\mathrm{i}m\omega_L t}$. Using the definition of the scalar product, the eigenvalue in Eq. (2.65) can then easily be expressed and solved as a time independent problem in the extended Hilbert space (see Ref. [241]).

The basis $\{|\psi_\alpha(t)\rangle\}$ is complete and orthonormal at every point in time [239,240]. Therefore, any solution of the time-dependent Schrödinger equation involving only the system Hamiltonian can be written as

$$|\psi(t)\rangle = \sum_\alpha a_\alpha e^{-\mathrm{i}\mu_\alpha t}\,|\phi_\alpha(t)\rangle\,, \tag{2.67}$$

where a_α are time-independent expansion coefficients. Finding the exact Floquet state is only feasible for special small quantum systems. The presence of a heat bath leads to transitions between states of different quasi-energy. The periodic wavefunctions can be expanded in a Fourier series

$$|\phi_\alpha(t)\rangle = \sum_k |\phi_{\alpha,k}(t)\rangle\, e^{\mathrm{i}k\omega_L t}. \tag{2.68}$$

In the next subsection, we will outline limits studied in the literature, in which the Floquet-Born-Markov Master equation has a particularly simple form such that the coherences of the density matrix in the Floquet basis can be ignored. We distil different effects due to the combination of driving and dissipation, by discussing a range of Born-Markov master equations used in the literature. We start with strong approximations to the form of the master equation, which pose strong restrictions regarding the driving frequency, coupling strength to the bath and form of the Hamiltonian. These restrictions are successively relaxed. After that, we discuss the regime of environment governed dynamics, which occurs close to quasi-degeneracies in the quasi-energy spectrum, where the system depends strongly on the dissipation mechanism (see Chapter 4).

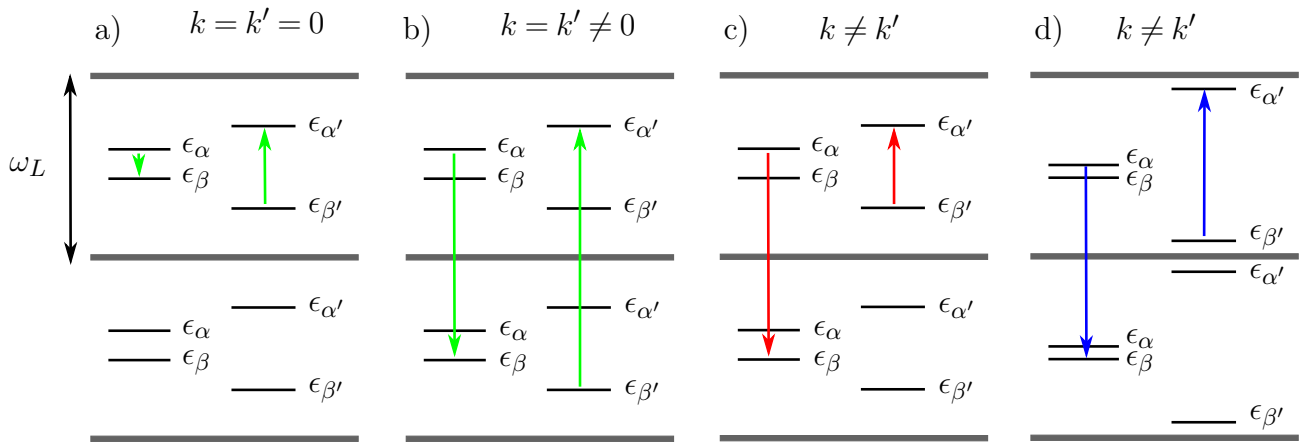


Figure 2.6: Typical transition processes between Floquet quasi-energies involving either one or two Floquet bands. Each arrow corresponds to a transition $\Delta_{\alpha,\beta,k}$, while their length difference corresponds to $|\Delta_{\alpha,\beta,k} - \Delta_{\alpha',\beta',k'}|$. Transitions with a) $k = k' = 0$ and b) $k = k' = 1$ are both allowed by the PSA, though they might not be perfectly resonant. The transition in c) corresponding to $k = k'$ is much stronger detuned (length of arrows is very different) and therefore eliminated by the PSA. However, if the model would have quasi-energies close to the boundaries of the Brillouin zone, the process d) corresponding to $k \neq k'$ would be eliminated by a PSA even though it is only weakly detuned.

Model The total Hamiltonian considered in the following

$$H_{tot}(t) = H_{sys}(t) + H_B + H_{SE}, \tag{2.69}$$

consists of a time periodically driven system Hamiltonian $H_{sys}(t)$ and a bath Hamiltonian H_B and the coupling Hamiltonian between system and environment as schematically given by [237]

$$\mathcal{H}_{SE} = gA \otimes E, \tag{2.70}$$

where A and E are operators acting on the system and environment, respectively, and g is a very small dimensionless quantity characterising the coupling strength. The FBM allows the description of a strongly driven system, which is weakly coupled to a memoryless heat bath. The master equation relies on the coherent evolution due to the driven system dynamics being treated exactly, while the dissipative dynamics is taken into account perturbatively. The basic steps of the derivation are almost identical to the ones used for the undriven Born-Markov master equation (given in Appendix B.3). However, the system evolution includes the driving, which therefore has to be taken into account in the rotating wave approximation.

Expressing the master equation in the basis of Floquet states (see Appendix B.4), the dissipative part contains terms oscillating as $e^{\mathrm{i}(\Delta_{\alpha,\beta,k} - \Delta_{\alpha',\beta',k'})t}$, where [236, 237]

$$\Delta_{\alpha,\beta,k} = \mu_\alpha - \mu_\beta + k\omega_L, \tag{2.71}$$

is the transition frequency between the α and β Floquet frequencies up to an integer k multiples of the driving frequency ω_L. As the dissipation is described as a second-order process, only the differences between these two transition frequencies enter.

The FME equations can be drastically simplified after the implementation of a modified rotating wave approximation (mRWA), which ignores all terms unless they are perfectly

resonant, i.e. $\Delta_{\alpha,\beta,k} = \Delta_{\alpha',\beta',k'}$ [230] and therefore eliminates all time dependence from the master equation. This approximation is hard to justify in general due to the presence of near degeneracies in the Floquet spectrum [242,243], which would require infinitely weak coupling to the heat bath. We consider this limit on page 50. However, it is possible to justify a less restrictive version of this approach, a partial secular approximation (PSA) [237,242], which does not ignore quasi-degeneracies of the Floquet states (see Appendix B.4). Instead it only time-averages rates over a driving period, by dropping all terms corresponding to $k \neq k'$ [237] panel c) in Fig. 2.6, while process a) $k = k' = 0$ and b) $k = k' = 1$ of Fig. 2.6 are both allowed. Dropping $k \neq k'$ can be justified for fast enough driving, whenever it is possible to project the quasi-energies of the Floquet spectrum onto an interval of length $\hbar\omega_L$ in a way that there are no quasi-energies close to the boundaries of the Brillouin zone. Otherwise, the process potentially ignores inelastic interband processes [217], e.g. the process schematically depicted in d) of Fig. 2.6. If the Floquet quasi-energies of the isolated system dynamics have a gap, such a selection is possible, and the resulting master equation only requires the coupling to the bath to be weak in comparison to the driving frequency ω_L.

For the case of a parametrically driven oscillator considered in Chapter 4, this situation is complicated by the infinite ladder of equally spaced quasi-energies, which when projected down to the first Brillouin zone in frequency space, contain a plethora of uncontrolled near degeneracies. To keep the discussion more general, we will, therefore, start by focussing on the simpler case, where this approximation is justified, e.g. two level system [236–238], which allows for a much cleaner discussion of potential effects due to the combination of driving and dissipation.

Expressing the Floquet Markov master equation for the density matrix elements in the basis of Floquet modes instead of Floquet states, i.e. $\rho_{\alpha,\beta} = \langle\phi_\alpha(t)|\,\rho\,|\phi_\beta(t)\rangle$, eliminates any remaining time dependence, as the rates have been effectively averaged over one period [242] (see Appendix B.4). The calculation of the steady-state is then reduced to solving a linear equation. Such a FFM is schematically given by [236,237,242] (see Eq. (B.74))

$$\dot{\rho}_{\alpha,\beta} = -\mathrm{i}(\mu_\alpha - \mu_\beta)\rho_{\alpha\beta} + \sum_{\gamma,\delta} \rho_{\gamma\delta}\mathcal{R}_{\alpha,\beta,\gamma,\delta}, \tag{2.72}$$

where the first two terms correspond to the coherent evolution involving quasi-energy differences $\mathcal{E}_{\alpha,\beta} = \epsilon_\alpha - \epsilon_\beta$. The rate $\mathcal{R}_{\alpha,\beta,\gamma,\delta}$ given in Eq. (B.75) depends on the bath properties and system-bath coupling. For example, for a Caldeira-Leggett-type of model, it consists of a sum of the Bose-occupation factor $n(\omega)$ and bath spectral density $J(\omega)$ evaluated at the transition frequencies between Floquet modes, i.e. $\omega = \Delta_{\alpha,\beta,k}$, see Ref. [229,236,237] and Appendix (B.4). Due to the k-dependence arising from an implicit Fourier series given in Eq. (B.69) and Eq. (B.71), the expression includes harmonics of the driving frequency ω_L [237,242]. Intuitively, this means that the transition amplitudes between Floquet states do not depend on a single spectral line as in an undriven system, but on a series of transition, frequencies equally spaced by ω_L [244]. Therefore, the drive probes the spectral density and occupation number of the bath at different frequencies and the steady-state can still depend on details of the bath spectral density.

Condition for diagonal density matrix in basis of Floquet states Assuming weak enough coupling such that for all splittings in the Floquet spectrum $|\mu_\alpha - \mu_\beta| \gg |\mathcal{R}_{\alpha,\beta,\gamma,\delta}|$, Eq. (2.72) can be simplified further through the stronger mRWA ignoring any fast oscillations between Floquet states [226, 227, 242, 245]. In this limit, the diagonal and off-diagonal expressions decouple [245]. As $\Re(\mathcal{R}_{\alpha,\beta,\alpha,\beta}) < 0$ (see Appendix B.4) the magnitude of the off-diagonal elements decays exponentially as [245]

$$\dot{\rho}_{\alpha,\beta} = \left[-\mathrm{i}(\mu_\alpha - \mu_\beta) + \mathcal{R}_{\alpha,\beta,\alpha,\beta}\right] \rho_{\alpha\beta}, \tag{2.73}$$

moreover, the diagonal elements are captured by a kinetic equation in the basis of Floquet modes as

$$\dot{\rho}_{\alpha,\alpha} = \sum_\gamma \rho_{\gamma\gamma} \mathcal{R}_{\alpha,\alpha,\gamma,\gamma}. \tag{2.74}$$

The steady-state is therefore purely diagonal in the Floquet basis. This approximation can be made for specific, very small or non-interacting models with well-separated Floquet energy spectrum, such as electrons governed by a massless Dirac Hamiltonian driven by circularly polarised light [226]. In the following, we are going to follow Refs. [225, 245] with the discussion of two limiting cases for driven open quantum system in which the thermal state resembles the one of an undriven system.

Floquet-Gibbs states The population of the energy levels of an undriven system is governed by detailed balance, which leads to a relaxation towards a Boltzmann distribution [196]. In this case, the bath temperature is the only bath property entering the distribution. However, in general, a time-dependent drive breaks the reversibility condition necessary for detailed balance [246]. Therefore, the population of the Floquet states depends on the details of the thermal bath beyond temperature. The master equation involves an evaluation of the bath correlation function at frequencies $\omega = \Delta_{\alpha,\beta,k}$ from Eq. (2.71) see also Appendix B.4. Consequently, the steady-state depends on the form of the damping, even though it is still independent of the damping rate itself [245, 246].

Under specific conditions derived in Ref. [245], the steady-state corresponding to Eq. (2.74), can simplify to a Gibbs distribution over the Floquet modes of the form $\rho_{ss}(t) \propto e^{-\beta H_F(t)}$ with bath temperature $T = \frac{1}{k_B \beta}$, where $H_F(t)$ is a constructed "effective" Floquet Hamiltonian of the form

$$H_F(t) = \sum_m E_m \left|\phi_m(t)\right\rangle \left\langle\phi_m(t)\right|, \tag{2.75}$$

where the arbitrariness of the Floquet quasi-energies is absorbed into an "effective" energy $E_m = \epsilon_m + k_m \omega_L$ with integer k_m for each Floquet state.

Separating the system Hamiltonian in a time-independent H_0 and a time-dependent $H_{ex}(t) = H_{ex}(t + T_L)$ part with period T_L,

$$H_{sys}(t) = H_{sys} + H_{ex}(t), \tag{2.76}$$

these conditions are given by [245]

i $\|H_{sys}\| \ll \frac{\hbar}{T_L}$: The Hamiltonian is bounded and the driving is fast but not necessarily weak, such that the driving frequency ω_L is larger than the spectral width of the undriven

system Hamiltonian. Systems which fulfil this condition are rather small or at least driven by a boring high-frequency driving regime, where the Magnus expansion would converge anyway, and the effect of the driving reduces to a mere re-normalisation of the system parameters.

ii $[H_{ex}(t), H_{ex}(t')] = 0$: The time-dependent part of the driving Hamiltonian commutes at different times. This assumption is the least restrictive, and is valid for most time-dependent Hamiltonian studied, where the time-dependent part of the Hamiltonian is simply a time-dependent function $f(t)$ multiplied by a system operator X, i.e. $H_{ex}(t) = f(t)X$.

iii $[H_{ex}(t), H_I] = 0$: The driving field Hamiltonian commutes with the system-bath coupling H_I of the Hamiltonian. This approximation leads to a time-independent interaction with the bath in the rotating frame, which cannot excite harmonics of the bath at multiple of the driving frequency [225].

For these assumptions, the distribution arises from a detailed balance condition in the basis of Floquet states. While the resemblance to the detailed balance for an undriven system is compelling, the approximations i to iii are restrictive.

***Effective* Floquet-Gibbs states** In a follow up paper Ref. [225] to Ref. [245], Shirai et al. were able to relax the most restrictive condition (i) and (iii), leading to a final *effective* Floquet-Gibbs distribution instead,

$$\rho_{\text{eff}}(t) = \frac{e^{-\beta H_{\text{eff}}^{[t](n_{\text{eff}})}}}{\text{Tr}(e^{-\beta H_{\text{eff}}^{[t](n_{\text{eff}})}})}, \tag{2.77}$$

where $H_{\text{eff}}^{[t](n_{\text{eff}})}$ is the approximation to the Floquet Hamiltonian obtained by using an optimal n_{eff}th-order expansion of the Magnus series. This treatment is also valid for finite system-bath coupling, as instead of starting with a diagonal state governed by Eq. (2.74) or the PSA, only terms that are larger than a truncation frequency ω_{trunc} are eliminated by the RWA. In general, the effective temperature of this effective Floquet-Gibbs distribution is found to be higher than the one of the bath [225].

Apart from condition (ii) from page 52, the effective Floquet-Gibbs state distribution given in Eq. (2.77) only requires

I $\tau_{heat} \gg \tau_{relax}$: While a Floquet system is generically expected to heat up to an infinite temperature state in the long-time limit, this approximation ensures that the system dissipates faster into the heat bath than it is heated by the drive. Heating is not so large for high-frequency driving, as long as there no resonances in the quasi-energy spectrum are driven. These are usually expected to heat the bath and lead to stronger deviation from the expected Floquet Gibbs state. In this case, heating can be suppressed by increasing the coupling strength to the bath, which decreases τ_{relax} as required.

III $\omega_L \gg \Omega_c$ or (iii): By making the driving frequency ω_L larger than the cutoff frequency Ω_c of the bath spectral density (see Eq. (4.15)) any excitation of harmonics in the driving frequency of the bath are avoided.

Condition [III] is still very restrictive. It reduces the coupling to the bath to a single transition frequency instead allowing for a range of harmonics captured by k in the coupling to the bath at all frequencies $\omega = \Delta_{\alpha,\beta,k}$. This approximation is not satisfied for the parametric oscillator in Chapter 4 and explains its deviation from the effective Floquet-Gibbs distribution.

***Generalised* Gibbs ensemble** In Sec. 2.3.1 and Sec. 2.3.1, we considered a generalisation of the Gibbs distribution to the driven regime. Other equilibrium distributions have been generalised to the driven regime as well using a perturbative treatment. In the presence of conservation laws, the equilibrium state of a closed integrable system can be described by a generalised Boltzmann distribution involving one Lagrange parameter, i.e. effective temperature, for each conserved quantity. These generalised Gibbs ensembles have been experimentally observed in Ref. [247] in a one-dimensional atomic gas. Many-particle systems in the presence of a weak integrability-breaking perturbation have been described by a generalised Gibbs ensemble with time-dependent coefficients [248]. Applying a weak perturbation to approximately conserved quantities can drive a system far from its equilibrium steady-state [248]. The idea is inspired by a well-insulated greenhouse or fridge, where the effectively non-equilibrium but well-defined temperature can be significantly different from the outside, due to weak heating by sunlight or some cooling process). Despite the independence from the initial state for the perturbed degrees of freedom, the steady states are well described by truncated generalised Gibbs ensemble with time-dependent Lagrange parameters [248–250].

Environment governed dynamics (EGD) Even in the regime where g in Eq. (2.70) is very small, the effective coupling strength given by [237]

$$\chi = \frac{g^2 \omega_L}{\mathcal{E}}, \tag{2.78}$$

can become large for near degeneracies $\mathcal{E} = \min(|\mathcal{E}_{\alpha,\beta}|) = \min(|\epsilon_\alpha - \epsilon_\beta|)$ in the Floquet quasi-energies. In Ref. [237] this regime is called environment-governed dynamics (EGD). Tuning the Floquet energies of a two level system through the direction of an effective magnetic field, the relaxation basis is shown to depend on the type of noise used [237].

That means that this regime of EGD can potentially allow distinguishing between the different types of microscopic system-bath coupling Hamiltonians. In Chapter 4, we are considering the example of a parametrically driven harmonic oscillator. Due to the presence of an infinite ladder of quasi-energies, it is not possible to have excellent control between EGD and the system governed dynamics. However, EGD is still expected to play a role.

2.4 Chapter summary

In this chapter, we discussed a range of proposals for cooling both artificial and intrinsic Josephson junctions. Depending on the driving frequency, parametric driving can also lead to parametric instabilities or an enhancement of the interlayer current.

To go beyond the weak and moderate driving approximation, we studied the interaction between a system and its environment in the presence of strong driving. We discuss various approximations of the Floquet-Markov master equation as a potential tool to combine strong driving with weak coupling to an environment.

Chapter 3

Controlling phase dynamics of long Josephson Junctions

In Sec. 2.1.3, we used a two-junction toy model to discuss the cooling mechanism of the parametric cooling scheme used in Denny et al. [31]. The full model studied by Denny et al. [31] consists of a large bilayer stack of capacitively coupled short Josephson junctions, which are shaken by an external laser modelled as a modulation of the permittivity. An alternative driving mechanism due to time-dependent critical current of the Josephson junction is studied by Okamoto et al. [43,45]. Both driving mechanisms are inspired by experiments on YBCO [18,251], where short infrared pulses are used to coherently excite phonon modes. Denny et al. show that by reducing the phase fluctuations in those junctions of the bilayer with a smaller critical current the scheme allows stabilising the superconducting state from being thermally activated into a resistive one. The model studied in Ref. [31] is limited to a stack of short junctions, where the spatial variation of the phase can be effectively ignored, and the coupling mechanism between phases in different junctions is entirely capacitive. Increasing the junction length the spatial dependence of the phase cannot be ignored. The inductive coupling strength η^L is then typically much larger than the capacitive coupling strength α. Though inductive coupling is irrelevant for a flat phase, the inductive coupling starts to dominate over capacitive coupling at a critical length-scale $L_{\text{crit}} \approx \pi\sqrt{\alpha/\eta^L}\lambda_c$ with c-axis London penetration length λ_c and $\eta^L \gg \alpha$. In this chapter, we present an extension and modification of the parametric cooling scheme also valid for the situation $L > L_{\text{crit}}$. Two different parametric driving schemes corresponding to time-dependent modulation of the permittivity and critical current, are investigated. We examine the cooling as a function of different material parameters thus providing a guide to the experimental realization of this cooling scheme.

In Sec. 3.1, we introduce the classical Josephson electrodynamics for HTSC in long Josephson junctions. More specifically, we first discuss both capacitive and inductive coupling (Sec. 3.1.1). The resulting model allows us to derive a Hamiltonian (Sec. 3.1.2), which describes the dynamics of a bilayer stack of long Josephson junctions. The terms of the Hamiltonian can be physically interpreted in terms of the electric and magnetic energy densities in the system. Next, we discuss additional dissipative contributions to the system dynamics (Sec. 3.1.3) and time-dependent modulations due to an external drive (Sec. 3.1.4).

The coherent part of the system dynamics is captured by time-dependent coupled sine-Gordon equation (Sec. 3.1.5).

In Sec. 3.2, we discuss both the coherent and incoherent dynamics of the normal modes of the linearised system (Sec. 3.2.1). The linearised dynamics allows us to define the noise processes in Sec. 3.3 and extend and solidify the parametric cooling scheme to a stack of long junctions, allowing for both spatial inhomogeneity and inductive coupling of the phase in Sec. 3.4. More explicitly, we first introduce the quantised version of the linearised Hamiltonian (Sec. 3.4.1), which allows us to derive analytical expressions for the cooling efficiency valid for small phase fluctuations and weak damping (Sec. 3.4.2).

In Sec. 3.5, we present simulations of the cooling scheme. We identify parameters, where cooling is feasible (Sec. 3.5.1), taking advantage of the analytical expression for the cooling ratio of the phase quadratures from Sec. 3.4.2. To address all normal mode frequencies with a significant thermal occupation, we use a broadband pulse modelled as a discrete superposition of driving frequencies. Further, we study the effect of broadband driving addressing all normal mode frequency with large thermal occupation on the switching current distribution for materials with large in-plane dissipation (Sec. 3.5.2). For broadband driving of the permittivity, we find that cooling is still possible in the presence of solitons inherent to long Josephson junctions. For broadband driving of the critical current, we do not obtain any stable results due to the relatively large off-resonant parametric driving strength.

Finally, in Sec. 3.6 we briefly outline a second proposal for the control of the phase dynamics in long Josephson junctions from Ref. [32], in which strong tailored pulses are used to switch between resistive, superconducting and states involving solitons. The switching mechanism corresponds to a destabilisation of the centre of mass excitation of the phase, made possible by the non-linear nature of the light-matter coupling.

3.1 Josephson electrodynamics for HTSC

In this section, we outline the main physics of stacks of capacitively and inductively coupled Josephson junctions following Ref. [117, 126, 192]. Modelling a bilayer cuprate as an alternating stack of superconducting and insulating material, allows us to include the effect of driven phonon modes as modulated system parameters. Details of the derivations can be found in Appendix A.

3.1.1 Coupling mechanisms between intrinsic Josephson junctions

Phenomenology of cuprate superconductor

Panel a) of Fig 3.1 shows the atomic configuration of a unit cell of a bilayer cuprate, YBCO, consisting of copper-oxide layers separated by two different kinds of atoms. These copper-oxide planes are common to all cuprates and lead to the characteristically quasi-two-dimensional physics of the superconducting effect in cuprates [104, 106]. As classical fluctu-

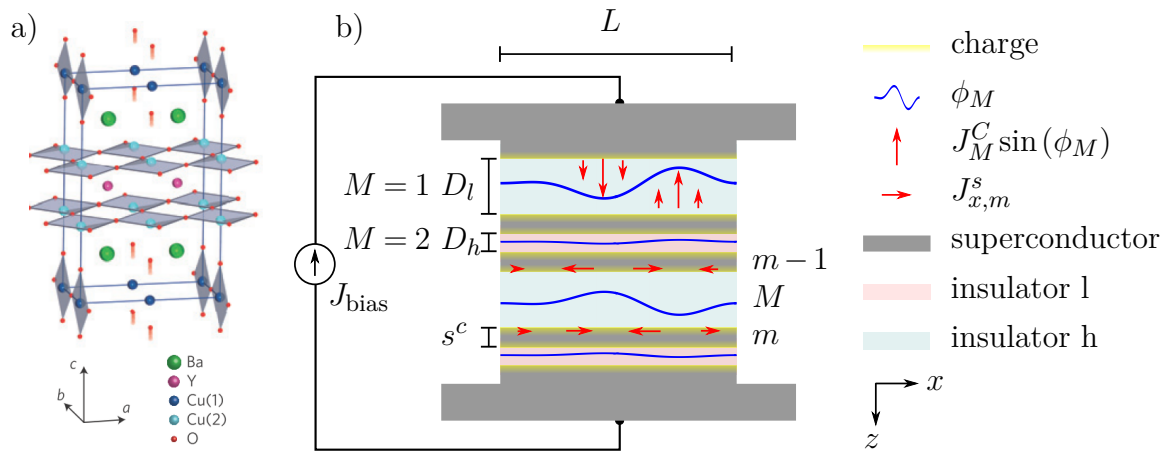


Figure 3.1: a) Atomic configuration of a unit cell of YBCO taken from Ref. [18]. b) The bilayer cuprate is modelled as a stack of n_{junc} Josephson junctions (here $n_{\text{junc}} = 4$) of length L. The thin grey regions indicate the superconducting layers of thickness s^c (labelled by lower case m) and the pink and light blue shaded areas correspond to l (labelled by odd M) and h (labelled by even M) type insulators of thickness $D_{l,h}$ and maximum Josephson current $J_{l,h}^C$ respectively. The gauge-invariant phase difference across the Josephson junction is illustrated by solid blue lines. The horizontal (vertical) red arrows indicate screening currents along the sheets (Josephson currents across the junctions). A spatially homogeneous bias current J_{bias} can be applied along the z-axis. The superconducting sheets are very thin, such that electric fields penetrate into the neighbouring junction and induce charges (a yellow shadowed region in superconducting sheets) leading to capacitive coupling of different junctions.

ations of the phase of the superconducting order parameter play a major role in the phase transition of HTSC in comparison to amplitude fluctuation [55, 56, 134] (see Sec. 1.2), we treat the copper-oxide layers as almost two-dimensional superconducting condensates characterised by a fixed superconducting density n_s and constant amplitude $|\Psi| \propto \sqrt{n_s}$ and only allow the phase $\varphi(\vec{r})$ of the order parameter $\Psi(\vec{r}) = |\Psi| e^{i\varphi(\vec{r})}$ to vary. Different copper-oxide layers are only weakly coupled through the Josephson effect [115]. This phenomenological description of HTSC can be considered as an anisotropic version of Ginzburg-Landau-type theory [10] taking into account the intrinsically two-dimensional structure of the HTSC coupled by Josephson effect.

The resulting model for HTSC as stacks of Josephson junctions is schematically shown in b) of Fig. 3.1 for a bilayer material consisting of a stack of n_{junc} alternating Josephson junctions of different material parameters. The copper-oxide planes are modelled as superconducting sheets, i.e. 2D condensates of superconducting pairs, separated by insulators of different thickness. The Mth junction and insulator are both labelled by capital index M, with odd (even) M correspond to l (h) junction type as shown in Fig. 3.1. The mth superconducting layer and all fields such as superconducting phase $\varphi_m(x)$ and physical quantities directly associated with it are with lower case m. We consider a stack of Josephson junctions of finite length L along the x-axis. The xy-plane is aligned with the crystallographic ab-plane and the z-direction is orientated along the c-axis of the material as shown in Fig. 3.1. An extension along the y-axis is trivial and is not believed to qualitatively change the physics in the linear regime as the dynamics of different spatial modes decouples in the linear regime.

Josephson coupling The gauge-invariant phase difference between the superconducting phases $\varphi_m(x)$ and $\varphi_{m-1}(x)$ of the M-th Josephson junction consisting of the Mth insulator and its adjacent $(m, m-1)$-th superconducting sheets is given by [10]

$$\phi_M(x) = \varphi_m(x) - \varphi_{m-1}(x) - \frac{2\pi}{\Phi_0}\int_{m-1}^{m} A_M^z(x)dz, \tag{3.1}$$

where Φ_0 is the magnetic flux quantum. The integration of the z component of the electromagnetic vector potential $A_M^z(x)$ across the junction ensures the gauge invariance of the expression. In the following, $A_M^z(x)$ is treated as constant across the insulator such that $\int A_M^z(x)dz = D_M A_M^z(x)$.

Non-zero values of $\phi_M(x)$ give rise to a dispersion-less Josephson current across the junction, which is determined by the *DC-Josephson relation* [10] and Eq. (1.17)

$$J_M^z = J_M^C \sin(\phi_M(x)), \tag{3.2}$$

with maximum critical current density $J_M^C \in \{J_{l,h}^C\}$ for the two different junction types of the bilayer model, with the labels chosen according to the magnitude of the critical current as low (l) or high (h). These supercurrents are indicated as the vertical red arrows in the first junction of Fig. 3.1. The corresponding Josephson potential $\propto -J_M^C \cos\phi_M(x)$ from Eq. (1.20) is of the form of spin exchange interaction $-J'\vec{\psi}_2 \cdot \vec{\psi}_1$ with amplitude $J' = J^C/\sqrt{n_s^m n_s^{m+1}}$ and superconducting order parameter $\vec{\psi}_{m'}$ of the m'th superconducting sheet (with $m' = \{m, m+1\}$) taking the role of two classical spins $\vec{\psi}_{m'}$ of length $|\vec{\psi}_{m'}| = \sqrt{n_s^{m'}}$ and relative orientation angle $\phi_M(x)$ [90]. The corresponding Josephson potential is minimised, whenever $\phi_M = 2\pi n$ with integer n, leading to a synchronisation of the superconducting phases at low temperature.

The *AC-Josephson relation* from Eq. (1.19) relates the evolution of the phase difference $\phi_M(x)$ to the voltage V_M across the Mth Josephson junction as [10]

$$\frac{\Phi_0}{2\pi}\dot{\phi}_M(x) = E_M^z D_M = V_M, \tag{3.3}$$

where the $E_M^z(x)$ is the electric field in z-direction in the Mth insulator and D_M is the thickness of the insulator taking values $\{D_{l,h}\}$ for the two junction type and Φ_0 is the magnetic flux quantum.

For a short junction, the spatial dependence of $\phi_M(x)$ can be ignored. Each junction can only be either in a superconducting or resistive state respectively characterised by a zero and non-zero the time-averaged voltage $\langle V_M \rangle_t$ (see discussion around Fig. 1.2a), where $\langle \ldots \rangle_t$ indicates the time-average. The resistive state corresponds to a phase growing approximately linearly in time, leading to AC-oscillations of frequency $\langle V_M \rangle_t / \Phi_0$ in the supercurrent from Eq. (3.2).

Thermal noise leads to fluctuation in $\phi_M(x)$, which are depicted as a deviation of the wiggly blue lines from the middle position of the respective junction in Fig. 3.1. The large difference in the maximum critical current for l,h-type of junctions results into Josephson plasma frequencies of largely different magnitudes from Eq. (1.23). Thermal excitation of the phase in the l-junction are larger and more likely to lead to a transition from the superconducting to resistive state.

Capacitive coupling

For a more compact notation, we arrange the fields and junction parameters in vectors such that the Mth entry of a vector contains the field or quantity evaluated in the Mth Josephson junctions, e.g. $\vec{\phi}$ is a vector for the phase differences given by

$$\vec{\phi} = \begin{pmatrix} \phi_1(x) \\ \phi_2(x) \\ \vdots \\ \phi_{n_{\text{junc}}}(x) \end{pmatrix}. \tag{3.4}$$

Bold notation in generally corresponds to matrices. For physical parameters, e.g. junction thickness $\mathbf{D}$, the corresponding matrix is diagonal and the Mth diagonal element contains the respective parameter for the Mth insulator, e.g. the thickness D_M.

Up to now, we considered each of the Josephson junctions of the stack to be only coupled through the Josephson effect. For intrinsic Josephson junctions as in HTSC, the thickness s^c of the superconducting sheets is of the same order as the Debye length $\lambda_c^{(D)}$, i.e. $\lambda_c^{(D)} \sim s^c$, such that electric fields are not screened by a single sheet and penetrate into neighbouring junctions, where they induce charges (yellow shades in Fig. 3.1). In Appendix A.1, we show the induced charge density leads to capacitive coupling of the different junction of the stack, resulting in a modification of the original Josephson relation given in Eq. (3.3) as [192–194]

$$\frac{\Phi_0}{2\pi}\partial_t\vec{\phi}(x) \quad = \quad \mathbf{C}\vec{E}^z(x), \tag{3.5}$$

where we defined a tridiagonal coupling matrix

$$\mathbf{C} = r^c \underbrace{(\boldsymbol{\alpha}^{-1} - \boldsymbol{\Delta})}_{\boldsymbol{c}} \boldsymbol{\epsilon} \tag{3.6}$$

with symmetric second order finite difference matrix $\boldsymbol{\Delta}$[1]. and capacitive coupling strength characterised by a length-scale r^c defined below and diagonal matrix

$$\boldsymbol{\alpha} = \text{diag}(\alpha_1, \alpha_2, \alpha_1, ...), \tag{3.8}$$

for the capacitive coupling parameters $\alpha_{1,2}$ [193, 194]. We take both the superconducting sheets and the permittivity of the insulating layers to be identical in each layer $\epsilon = \epsilon_l = \epsilon_h$ such that they are characterised by a diagonal matrix $\boldsymbol{\epsilon} = \epsilon \boldsymbol{I}$ proportional to the identity $\boldsymbol{I}$. For very thin superconducting sheets compared to the Debye screening length r^c is simply

[1] The symmetric second order finite difference matrix is given by

$$\boldsymbol{\Delta} = \begin{pmatrix} -2 & 1 & 0 & & \\ 1 & -2 & 1 & 0 & \\ 0 & 1 & -2 & 1 & \\ & & \ddots & \ddots & \ddots \end{pmatrix}. \tag{3.7}$$

the junction thickness weighted by capacitive coupling parameter and permittivity as (see Eq. (A.74) and Eq. (A.15))[2]

$$r^c \approx \frac{\alpha_M D_M}{\epsilon_M}. \tag{3.9}$$

In this thin junction limit Eq. (3.5) simplifies to

$$\frac{\Phi_0}{2\pi}\partial_t \vec{\phi}(x) = (\boldsymbol{I} - \boldsymbol{\Delta\alpha})\,\vec{V}(x), \tag{3.10}$$

where we defined voltages $\vec{V}(x) = \mathbf{D}\vec{E}^z(x)$ across each junction, which is identical to the expression given in Ref. [193].

The capacitive coupling parameter $\alpha_{1,2}$ from Eq. (3.8) take values from 0.1 to 3 depending on the material [195], which is many order of magnitudes smaller than inductive coupling parameters of order 10^5 [194] discussed in the next subsection. Therefore, capacitive coupling is often ignored in the discussion of the optical response of the system [73]. However, inductive coupling arises only due to spatial variations of the phases and therefore disappears in short junctions, where the phases become rigid.

Inductive coupling

The thickness s^c of the superconducting sheets is much smaller than the London penetration depth of the bulk λ, which characterises the length-scales over which magnetic fields and screening currents decay in the superconducting sheets according to the Meissner effect from Eq. (1.12). Due to the layered structure of the HTSC, the screening length is highly anisotropic. We follow the convention used in Refs. [121, 252, 253] that the in-plane London penetration depth λ_{ab} (out-of-plane London penetration depth λ_c) of the magnetic field $\vec{B}^y$ along the c-axis (in the ab-plane) is labelled by the direction of the corresponding screening current [10, 254]. Therefore, the in-plane London penetration depth λ_{ab} due to screening current along the ab-plane of the material characterises the decay length of magnetic fields along the c-axis of the material. It is related to the bulk penetration depth as $\lambda = \sqrt{\frac{s^c}{D}}\lambda_{ab}$ [252]. As the c-axis screening current is generally weaker than the in-plane screening current, the out-of-plane London penetration depth is larger than the in-plane London penetration depth such that the anisotropy $\gamma = \lambda_c/\lambda_{ab}$ is larger than unity. Both in-plane and bulk London penetration depths given by λ_{ab} and λ are much larger then the junction thickness, i.e. $s^c, D \ll \lambda_{ab}$ (with $D = D_l + D_h$).

The strong screening currents of the magnetic field arise from gradients in the superconducting phase of the mth superconducting sheet, $\partial_x\varphi_m$ according to Ginzburg-Landau theory [10, 252]

$$J_m^{s,x} = \frac{1}{\mu_0\lambda^2}\left(\frac{\Phi_0}{2\pi}\partial_x\varphi_m - A_m^x\right), \tag{3.11}$$

where μ_0 is the magnetic permeability, A_m^x is the x-component of the vector potential and λ is the bulk London penetration length from Eq. (1.11). These supercurrents are schematically indicated by the horizontal arrows in the superconducting sheet in Fig. 3.1.

[2] For a two-junction toy model $r^c = \frac{\alpha_1\alpha_2}{\epsilon}\frac{D_l - D_h}{\alpha_2 - \alpha_1}$.

In Appendix A.2, we show that by considering the magnetic flux $\Phi = \oint_{\Sigma} \vec{A} \cdot d\vec{\ell} = \int_{\Sigma_l} \vec{B}^y \cdot d\vec{l}$ with vector potential $\vec{A}$ over a surface Σ enclosed by a rectangular path Σ_l across the insulating layer, it is possible to relate the gradient of the gauge-invariant phase difference in neighbouring junctions to the magnetic field $\vec{B}^y$ and the supercurrents from Eq. (3.11) in neighbouring sheets. Using Ampère's law and assuming that the current in the superconducting sheets consists only of the supercurrent $J_m^{s,x}$, the resulting inductive coupling of the phase gradients in neighbouring junctions is described by [117]

$$\frac{\Phi_0}{2\pi} \partial_x \vec{\phi}(x) = \mathbf{L} \vec{B}^y(x), \tag{3.12}$$

where $\mathbf{L}$ is the inductive coupling matrix given by

$$\mathbf{L} = \frac{\lambda_{ab}^2}{D} \underbrace{\left(\boldsymbol{\eta}^{-1} - \boldsymbol{\Delta}\right)}_{=\boldsymbol{\mathcal{L}}}, \tag{3.13}$$

and inductive coupling strength $\boldsymbol{\eta} = \frac{\lambda_{ab}^2}{D} \mathbf{D}^{-1}$, which is equivalent to the coupling derived for a bilayer material in Ref. [193], except for the definition of the coupling strength as $\boldsymbol{\eta}' = \frac{\lambda_{ab}^2}{s^c} \mathbf{D}^{-1}$. This difference arises due to distinct assumptions in the literature regarding whether the superconducting sheets have a finite size s^c and differences in the definition of the screening current, which is either defined as in Eq. (3.11) in terms of the bulk London penetration depth or in terms of the the in-plane London penetration depth, i.e. by replacing $\lambda \to \lambda_{ab} = \lambda (D/s^c)^{1/2}$ in Eq. (3.11) as in Ref. [255]. Depending on whether the superconducting sheets are taken to be infinitely thin as in Ref. [73], this treatment leads to $\boldsymbol{\eta} \to \boldsymbol{\eta}'$ with $\boldsymbol{\eta}' = \frac{\lambda_{ab}^2}{s^c} \mathbf{D}^{-1}$ as in Ref. [193, 194]. This difference does not matter in general as microscopic parameters are only used to estimate $\boldsymbol{\eta}$ or $\boldsymbol{\eta}'$, which is the only quantity entering the simulations.

3.1.2 Hamiltonian for coherent dynamics of coupled sine-Gordon equations

The electric E_M^z and magnetic fields B_M^y associated with the capacitive and inductive coupling interact with current density J_M^z along the z-axis according to Ampère's law along the z-axis, i.e.

$$\partial_x B_M^y = \mu_0 \partial_t \left(\epsilon_0 \epsilon_M E_M^z\right) + \mu_0 J_M^z, \tag{3.14}$$

where the expression in the bracket is the displacement field $\epsilon_0 \epsilon_M E_M^z$. In the absence of dissipative contributions, J_M^z is given purely by the Josephson current from Eq. (3.2). Combining Eq. (3.14) with the respective expressions for the electric and magnetic fields from Eq. (3.5) and Eq. (3.12), we obtain a Hamiltonian describing the coherent dynamics in long Josephson junctions for a junction of area A_{area} in the xy-plane given by (detailed derivation and relation to electric and magnetic energy given in Appendix A.3)

$$\mathcal{H} = \mathcal{H}_{\text{cap}} + \mathcal{H}_{\text{ind}}. \tag{3.15}$$

The first term $\mathcal{H}_{\text{cap}}$ describes the capacitive coupling and Josephson relation for a rigid phase, i.e. it is the only expression present in the short junction regime. The second term $\mathcal{H}_{\text{ind}}$ contains additional terms only present for long junction such as inductive coupling. The first term is given by

$$\mathcal{H}_{\text{cap}} = \frac{1}{L}\int_0^L dx \frac{1}{2}\vec{p}^{\top}\mathbf{M}^{\phi^{-1}}\vec{p} + \frac{\Phi_0}{2\pi}A_{\text{area}}\left[(\vec{J}^C)^{\top}\left(1-\cos(\vec{\phi})\right) - (\vec{J}_{\text{bias}})^{\top}\vec{\phi}\right], \tag{3.16}$$

with $\vec{p} = \mathbf{M}^{\phi}\partial_t\vec{\phi}$ as the conjugate variable to the $\vec{\phi}$ field and mass matrix[3]

$$\mathbf{M}^{\phi} = A_{\text{area}}\left(\frac{\Phi_0}{2\pi}\right)^2 \epsilon_0\boldsymbol{\epsilon}\mathbf{C}^{-1}, \tag{3.17}$$

where $\boldsymbol{\epsilon}$, $\mathbf{J}^C$ are diagonal matrices containing the values of the corresponding physical quantities and $\mathbf{C}$ is the capacitive coupling matrix from Eq. (3.6). The diagonal matrix $\boldsymbol{J}_{\text{bias}} = J_{\text{bias}}\text{diag}(1,1,...,1)$ takes into account a spatially homogeneous bias current J_{bias} applied externally along the z-axis through superconducting electrodes [256] as shown in Fig. 3.1. Equation (3.16) is almost identical to Eq. (2.27) in the absence of driving, i.e. $\boldsymbol{A} = 0$, only here instead of restricting ourselves to two junctions, we now consider a stack of n_{junc} capacitively coupled junctions. The second contribution due to magnetic field and screening currents is given by

$$\mathcal{H}_{\text{ind}} = A_{\text{area}}\frac{1}{L}\int_0^L dx \frac{1}{2\mu_0}\left(\frac{\Phi_0}{2\pi}\right)^2 \partial_x\vec{\phi}^{\top}\mathbf{L}^{-1}\partial_x\vec{\phi}, \tag{3.18}$$

with $\mathbf{L}$ is the inductive coupling matrix from Eq. (3.13). The Hamiltonian formulation of the coupled sine-Gordon equation will be necessary for the quantisation of the model, provides an energy scale used for the definition of thermal noise and allows to clarify the connection to the optomechanical Hamiltonian (Sec. 3.4.1). In contrast to the Hamiltonians studied in the literature [68,124,252,257], this Hamiltonian can describe a bilayer structure. For purely inductive coupling, the Hamiltonian is of the form used in Ref. [124], while for capacitive coupling in short junctions the Hamiltonian reduces to Ref. [257].

Solving the first and second[4] Hamilton's equation of Eq. (3.15) for $\frac{\mathrm{d}^2\vec{\phi}}{\mathrm{d}t^2}$, we obtain the coherent terms of the inductively and capacitively coupled sine-Gordon equation [192]

$$\frac{\Phi_0}{2\pi}\mathbf{L}^{-1}\partial_x^2\vec{\phi} = \frac{\Phi_0}{2\pi c^2}\partial_t\left(\boldsymbol{\epsilon}\mathbf{C}^{-1}\partial_t\vec{\phi}\right) + \mu_0\left[\mathbf{J}^C\sin(\vec{\phi}) - \vec{J}_{bias}\right], \tag{3.19}$$

The formulation of the coupled sine-Gordon equation in this section makes a connection between capacitive and inductive coupling formulated in terms of experimentally observable quantities, as used for example in the monolayer treatment in Ref. [194] to the underlying microscopic parameters as developed in Ref. [192].

[3] This effective mass has units of mass times junction area A_{area}.

[4] The first and second Hamilton's equation are $\frac{\mathrm{d}\vec{p}}{\mathrm{d}t} = -\frac{\partial\mathcal{H}}{\partial\vec{\phi}}$ and $\frac{\mathrm{d}\vec{\phi}}{\mathrm{d}t} = \frac{\partial\mathcal{H}}{\partial\vec{p}}$

3.1.3 Dissipative contributions to coupled sine-Gordon equations

The incoherent dynamics due to quasi-particle excitations (see also discussion below Eq. (2.28) and above Eq. (1.21)) cannot be accounted for in the Hamiltonian formulation above[5]. Here, we will instead treat the incoherent contribution due to out-of-plane and in-plane quasi-particle current phenomenologically.

Out-of-plane quasi-particle current

Up to now we have only considered coherent contributions to the dynamics of $\vec{\phi}$. The free c-axis current J_M^z in Eq. (3.14) flowing across the Josephson junction has an additional contribution besides the supercurrent $J_M^C \sin\phi_M$, i.e.

$$J_M^z = J_M^C \sin\phi_M + \sigma E_M^z, \tag{3.20}$$

where the new term due to a quasi-particle current is of the form of Ohm's law with c-axis conductivity σ and expression for the electric field E_M^z from Eq. (3.5). This phenomenological expression in combination with the electromagnetic fields from Eq. (3.5) and Eq. (3.12) in Ampère's law (Eq. (3.14)) leads to an additional term $\frac{\Phi_0}{2\pi}\mu_0\boldsymbol{\sigma}\mathbf{C}^{-1}\partial_t\vec{\phi}$ on the right hand side of Eq. (3.19), where $\boldsymbol{\sigma}$ is a diagonal matrix for the conductivity.

In-plane quasi-particle current

In order to simulate in-plane dissipation, we have to augment the system through additional high-frequency variables. The dominating contribution due to these terms will be included perturbatively following Ref. [258].

In the derivation of the inductive coupling from Eq. (3.12), we implicitly assumed that the current in the superconducting sheets consists of only the supercurrent $J_m^{s,x}$ from Eq. (3.11). However, the total current along the x-direction of the mth superconducting sheet contains further contributions due to in-plane quasi-particle current [121, 255, 259, 260]

$$J_m^{q,x} = \sigma_{ab} E_m^x, \tag{3.21}$$

where E_m^x is the electric field along the x-axis and σ_{ab} the in-plane conductivity and a small displacement current along the superconducting sheets given by [119, 259]

$$J_m^{d,x} = \epsilon_0\epsilon_{ab}\partial_t E_m^x, \tag{3.22}$$

where ϵ_{ab} is the in-plane permittivity.

In-plane dissipation current $J_m^{q,x}$ from Eq. (3.21) is considered the dominant dissipation mechanism for spatially non-uniform excitations such as Josephson lattices in very

[5]Formally, it would require including additional degree of freedoms describing the coupling to unpaired electrons, which are traced out in order to give rise to the incoherent dynamics. This would require knowledge of a microscopic Hamiltonian as in BCS theory [69, 97], which is still unknown for HTSC [71].

anisotropic stacks [120,121,255,259–262]. For a realistic description of the flux-flow resistivity of the Josephson vortex lattice [255], as well as the synchronisation dynamics of a stack of junctions [259].

Including in-plane dissipation in the derivation of inductive coupling is only possible at the cost of adding a new field, which we chose as the dimensionless difference in screening current in the superconducting sheets adjacent to the insulator $\vec{S}$ (from Eq. (A.34)) given by

$$S_M = \frac{2\pi\mu_0\lambda^2 s^c}{\Phi_0}\left(J_m^{s,x,d} - J_{m-1}^{s,x,u}\right), \tag{3.23}$$

where the index (d,u) in the superconducting screening current $J_m^{s,x}$ from Eq. (3.11) refers to the location at which the current is evaluated, i.e. down and upside of the m and $m-1$ superconducting sheet respectively and λ is the bulk London penetration length. Physically, the necessity for two fields $\vec{\phi}$ and $\vec{S}$ in the description of the dynamics of Josephson junctions arises from the fact that the vector potential of a stack of long junctions has two relevant components, i.e. one along x and one along z [67, 126]. Instead of using $\vec{S}$, one could directly simulate a term proportional to the screening current along the junctions as in Ref. [67,68] for a monolayer or alternatively use a dynamical equation for the magnetic field as in Ref. [32,126] obtained by relating the screening current difference to the magnetic field $\vec{B}^y$ given by

$$\vec{S} = s^c\left(\partial_x\vec{\phi} - \frac{2\pi}{\Phi_0}\mathbf{D}\vec{B}^y\right). \tag{3.24}$$

These approaches are equivalent, however, the present choice for $\vec{S}$ is most convenient due to the bilayer structure of the cuprates and the finite size of the superconducting sheets (see Appendix. A.2). It is also chosen with hindsight as we will later show that it is possible to adiabatically eliminate $\vec{S}$, while still keeping the dominating decay channel arising from the additional damping due to in-plane dissipation. For this purpose, using the difference in screening current $\vec{S}$ has the advantage that we do not influence the coherent dynamics of ϕ, i.e. an almost instantaneously adapting field $\vec{S}$ does not lead to an additional effective potential for ϕ. Due to the first order adiabatic elimination, the dissipative term for $\vec{S}$ due to in-plane quasi-particle current from Eq. (3.21) is shifted to act as a spatially dependent dissipative terms for $\vec{\phi}$.

Including displacement current from Eq. (3.22) and in-plane quasi-particle current from Eq. (3.21), Eq. (3.12) becomes (Eq. A.38)

$$\mu_0\epsilon_0\epsilon_{ab}\partial_t^2\vec{S} + \mu_0\sigma_{ab}\partial_t\vec{S} + \frac{2\pi}{\Phi_0}\frac{D}{\lambda_{ab}^2}\left(\frac{\Phi_0}{2\pi}\partial_x\vec{\phi} - \mathbf{L}\vec{B}^y\right) = 0, \tag{3.25}$$

which is derived in Appendix A.2 using Maxwell equations and Ginzburg Landau physics. The first kinetic part arises from the in-plane displacement current from Eq. (3.22) and the second from the in-plane quasi-particle current from Eq. 3.21. The in-plane quasi-particle current corresponds to a dissipative term for $\vec{S}$ in a similiar fashion as the c-axis quasi particle currents leads to a dissipation term for $\vec{\phi}$ (see Eq. 3.19). The expression in the round brackets is simply the inductive coupling from Eq. (3.12). Using Eq. (3.24) to eliminate the magnetic field, Eq. (3.25) reduces to an equation of motion for $\vec{S}$ coupled only to the gradient in the

phase $\partial_x\vec{\phi}$. Consequently, for short junctions described by a rigid phase $\vec{\phi}$, the equation of motions of field $\vec{S}$ given in Eq. (A.36) and $\vec{\phi}$ decouple and it is sufficient to simulate the low-energy physics described by $\vec{\phi}$. Having a dynamical equation for $\vec{S}$ becomes only necessary for the description of long junctions.

In Appendix A.3, we derive the Hamiltonian for the coherent dynamics of $\vec{\phi}$ and $\vec{S}$, which is shown to allow for a physical interpretation in terms of energy. The displacement term in Eq. 3.25 gives rise to a kinetic term for $\vec{S}$ and allows for the quantisation in terms of two fields, i.e. heavy and light bosonic field discussed in Ref. [67]. These two fields respectively correspond to high-frequency modes and the standard Josephson plasma frequency considered in the short junction limit. In Sec. 3.1.5, we show that the reduced Hamiltonian obtained after the zeroth order adiabatic elimination of the kinetic term of $\vec{S}$ can still be expressed in terms of a single field.[6]

Adiabatic elimination of high-frequency modes

The typical size of the Josephson current and Josephson oscillation is respectively given by $J^C = \Phi_0/2\pi\lambda_c^2\mu_0 D$ [121,126] and $\omega_p = \sqrt{2\pi J^C D/\Phi_0\epsilon_0\epsilon} = c/\lambda_c\sqrt{\epsilon}$ [121] (see Eq. (1.23)). Starting from the equation of motion of $\vec{S}$ from Eq. (A.36), the magnitude of the normal mode frequencies ω_S of $\vec{S}$ can be estimated as $\omega_S^2/\omega_p^2 \sim \gamma_c^2\gamma_d\epsilon/\epsilon_{ab} \gg 1$, where $\gamma_d = \frac{D}{s^c} \gg 1$ is the ratio of the thickness of typical unit cell $D = D_l + D_h$ to superconducting sheet s^c, $\gamma_c = \frac{\lambda_c}{D} \gg 1$ is the ratio of the London penetration depth to the thickness of typical insulator. Consequently, the $\vec{S}$ oscillates much more quickly than $\vec{\phi}$ and can almost instantaneously adapt to changes in ϕ for any timescales of interest here. Considering the dynamics on the timescales $1/\omega_p$ associated with $\vec{\phi}$, we find that contributions from the first term in Eq. (3.25) are suppressed by a factor $\epsilon_{ab}/(\epsilon\gamma_d\gamma^2) \ll 1$ compared to the ones from the third and forth. Consequently, the displacement current $J_m^{d,x}$ from Eq. (3.25) can be neglected for all frequencies well below the superconducting gap [119,255,259].

Setting $\partial_t^2\vec{S} = 0$ and $\partial_t\vec{S} = 0$ to zero, Eq. (3.25) reduces to the original expression for inductive coupling from Eq. (3.12). This zeroth order adiabatic elimination [258] completely ignores not only the contribution due to the displacement current (first term in Eq. (3.25)) but also the larger contributions due to in-plane dissipation (second term in Eq. (3.25)). In this limit, the difference in the screening current from Eq. (3.24) instantaneously adapts to gradients in $\vec{\phi}$ as

$$\vec{S}^{(0)} = s^c(\mathbf{L}-\mathbf{D})\mathbf{L}^{-1}\partial_x\vec{\phi}. \tag{3.26}$$

As we pointed out that damping due to in-plane quasi-particle can become relevant, we only perturbatively eliminate fast degrees of freedom [258] (see discussion around Eq. A.39). The next higher order term leads to additional damping proportional to the second order

[6] In the Lagrangian formulation, terms without a kinetic part are referred to as "irrelevant" terms, e.g. the scalar potential in classical quantum electrodynamics [263] kept only to conserve the gauge invariance of the theory. As the effective conjugate momentum of an irrelevant term is zero it is impossible to impose quantum mechanical commutation relations between conjugate dynamical variables. In this case, it is necessary to eliminate the irrelevant terms leading to a reduced Hamiltonian [263], which allows for a consistent quantisation. Here, $\vec{S}$ becomes such an "irrelevant term" after the adiabatic elimination.

derivative of the phase (Sec. A.2.1). It can be included on the left side of Eq. (3.19) by using a substitution of the form

$$\partial_x^2\vec{\phi} \to \left(1+\mu_0\sigma_{ab}\lambda^2\partial_t\right)\partial_x^2\vec{\phi}. \tag{3.27}$$

As a first order correction term to the adiabatical elimination, this damping term arises from the fact that the second field $\vec{S}$ does not adjust instantaneously to the new $\vec{\phi}$, but lags a bit behind [258]. Its physical form and origin are both purely dissipative as it arises from in-plane dissipation, and acts as a spatially dependent dissipative term for $\vec{\phi}$.

3.1.4 Driving schemes

It is not exactly known how phonon driving acts on the electronic degrees of freedom and different scenarios can be envisaged. In the following two subsections, we describe two plausible driving mechanisms inspired by the experiments on photo-induced superconductivity [18,35] and study the resulting theoretical models. Experimentally, a short infrared pump pulse is used to excite phonon modes and the resulting transient state is probed with a delayed weaker probe pulse. For all external driving frequencies considered here, the driving is well below the superconducting gap, such that it cannot break superconducting pairs. In the following, we simulate the effect of the resulting lattice shaking as either a time-dependent modulation of the critical current or permittivity, which are respectively referred to as $J^C(t)$-Model and $\epsilon(t)$-Model. Both types of driving lead to a parametric modulation, but they respectively only address the potential and kinetic terms of the Hamiltonian and therefore differ in the way they address different normal modes of the system. The first scheme is motivated by the pump-probe formalism from non-linear optics [202, 264], and amounts to using a time-dependent permittivity. The second driving scheme models the effect of the excited phonons as a time-dependent critical current. In Ref. [52], it is pointed out that there are in fact 72 optical phonon modes in YBCO of which 33 are Raman active, which means that they couple directly to an external light pulse. The amplitudes of the crystal lattice distortion of these modes can be either calculated from first principles using density functional theory or experimentally obtained from X-ray diffraction data [52, 251]. In the present work, however, driving of distinct phonon modes is modelled phenomenologically by allowing the relative amplitudes and signs in the two junctions to differ.

In the first part of the chapter, we model the driving by a single monochromatic driving frequency. To simulate the cooling of all low-frequency modes, we later replace this pulse by a broadband pulse in Sec. 3.5.1.

Modulation of the critical current ($J^C(t)$-Model)

In the discussion of the parametric cooling scheme for short Josephson Junctions in Sec. 2.1.3 and parametrically enhanced Josephson current in Sec. 2.2.2, we simulated the driving mechanism as a modulation in the critical current density following Refs. [39, 43, 45]. We now refer to this model as $J^C(t)$-Model. For long Josephson Junctions, the driving of the critical current is included in the Hamiltonian given in Eq. (3.16) by replacing

$$(\vec{J}^C)^\top \cos(\vec{\phi}) \to (\mathbf{J}^C)^\top \left[\mathbf{I}+\mathbf{A}(t)\right]\cos(\vec{\phi}) \tag{3.28}$$

with $\mathbf{A}(t) = \frac{1}{2}(1-\cos(2\omega_d t))\,\mathbf{A}$, where the driving strength is captured in the diagonal matrix $\mathbf{A} = \mathrm{diag}(A_1, A_2, A_1, ...)$ with components $A_{1,2}$ for the low and high-frequency junction.

Modulation of the permittivity ($\epsilon(t)$-Model)

The phonon response in THz experiments can be described by local non-linear phononics of a loss- and dispersionless medium [36, 202]. Expanding the displacement field $D(x,t)$ in terms of a Taylor series in the total electric field $E(x,t)$ [202, 264] and keeping only terms of the lowest two order for a centrosymmetric crystal such as YBCO leads to

$$D(x,t) \approx \epsilon_0 \left(1+\chi^{(1)}\right) E(x,t) + \epsilon_0 \chi^{(3)} E(x,t)E(x,t)E(x,t), \tag{3.29}$$

where $\chi^{(i)}$ is the real (dispersionless) and frequency independent (loss-free) ith order susceptibility.

In the pump-probe experiment, a strong pump electric field $E_{dr}(x,t)$ influences the propagation of a weaker probing field $E_{pr}(x,t)$. Here, both fields are restricted to propagate along the x-axis. Decomposing $E(x,t) = E_{pr}(x,t) + E_{dr}(x,t)$ and keeping only terms up to first order in probing field $E_{pr}(x,t)$ results in

$$D(x,t) = \epsilon_0 \left(1+\chi^{(1)}\right) E_{pr}(x,t) + 3\epsilon_0 \chi^{(3)} E_{dr}(x,t)E_{dr}(x,t)E_{pr}(x,t) + ..., \tag{3.30}$$

where the dots correspond to terms, which only depend on the pump field $E_{dr}(x,t)$. The first term in Eq. (3.30) corresponds to a constant modification of the permittivity, i.e. $\vec{\epsilon} = 1+\chi^{(1)}$, due to local scattering interaction. The second term arises from the pumping of a phonon mode by an external driving electric field $E_{dr}(x,t)$, i.e. it describes the interaction of probe and driving field. This term can be captured by a time and spatially dependent permittivity of the form

$$\boldsymbol{\epsilon}(x,t) = \boldsymbol{\epsilon}\left[1 + 3\chi^{(3)}_{local} E^2_{dr}(x,t)\right]. \tag{3.31}$$

Here we assume the drive forms a standing wave as possibly realisable in a cavity with driving of the form $E_{dr}(x,t) = E_{dr}\sin(\omega_d t)\cos(k_d x)$ with frequency ω_d and wavevector k_d, leading to

$$\boldsymbol{\epsilon}(x,t) = \boldsymbol{\epsilon}\left[1 + \boldsymbol{\nu}\frac{1}{2}(1+\cos(2k_d x))\,\frac{1}{2}(1-\cos(2\omega_d t))\right], \tag{3.32}$$

where $\boldsymbol{\nu} = \mathrm{diag}(\nu_1, \nu_2, \nu_1, ...)$ is a diagonal matrix containing the small amplitudes $\nu_{1,2}$ of the modulation in the two physical junctions and $\boldsymbol{\epsilon}$ is a diagonal matrix containing the (identical) permittivity of each layer (see below Eq. (3.8)). We now refer to this model as $\epsilon(t)$-Model. While it is only possible to efficiently couple to low-momentum modes, even a weak spatial dependence in Eq. (3.32) enables transition between modes with different momentum, which allow the implementation of new cooling mechanisms such as Doppler cooling. To indicate the effect of the such a dependence, we explicitly keep the spatial dependence of the drive up to the point, where it generates unnecessary clutter in the equations in Sec. 3.2.

The effect of a time-dependent permittivity can be captured by replacing the capacitive coupling matrix (see Eq. (3.5) and definition below Eq. (3.8)) $\boldsymbol{\mathcal{C}} \to \boldsymbol{\mathcal{C}}(x,\tau)$ as shown in the

detailed derivation of the capacitive and inductive coupling presented in Appendix Sec. A.1 with

$$\boldsymbol{\mathcal{C}}(x,t) = \boldsymbol{\alpha}^{-1} - \boldsymbol{\Delta} + \frac{\mathbf{D}}{r^c}\left(\boldsymbol{\epsilon}^{-1}(x,t) - \boldsymbol{\epsilon}^{-1}\right). \tag{3.33}$$

Keeping only the lowest order in $\boldsymbol{\nu}$ in Eq. (3.33) we obtain

$$\boldsymbol{\mathcal{C}}(x,t) = \boldsymbol{\alpha}^{-1} - \boldsymbol{\Delta} - \boldsymbol{\mu}\left(1 - \cos\left(2\omega_d t\right)\right)\frac{1}{2}\left(1 + \cos\left(2k_d x\right)\right) + O(\boldsymbol{\nu}^2), \tag{3.34}$$

where we define a diagonal matrix $\boldsymbol{\mu} = \frac{1}{2}\frac{1}{r^c}\mathbf{D}\boldsymbol{\nu}\boldsymbol{\epsilon}^{-1} \approx \frac{\nu}{2}\boldsymbol{\alpha}^{-1}$ for the driving strength.

3.1.5 Coherent part of the coupled sine-Gordon equation for a driven system

In the following, we discuss the coherent dynamics of the coupled sine-Gordon equation as it arises from a parametrically driven version of the Hamiltonian from Eq. (3.15). In order to avoid unnecessary repetition at a later stage, we now introduce the dimensionless notation used in the simulation. The dimensionless time $\tau = t\omega_p$ measured in terms of an effective Josephson plasma frequency given by $\omega_p = \sqrt{2\pi J^C D/\Phi_0\epsilon_0\epsilon} = c/\lambda_c\sqrt{\epsilon}$ [121] and an effective c-axis critical current J^C defined as $J^C = \Phi_0/2\pi\lambda_c^2\mu_0 D$ [121, 126]. Time derivatives are correspondingly given by $\partial_t = \omega_p\partial_\tau$. The spatial dependence is measured in terms of the bulk London penetration depth λ such that $x = x/\lambda$ and $\partial_x = \frac{1}{\lambda}\partial_x$. To account for the driving the capacitive coupling matrix is modified correspondingly as $\mathbf{C} \to \mathbf{C}(x,\tau) = r^c\boldsymbol{\mathcal{C}}(x,\tau)\boldsymbol{\epsilon}(x,\tau)$. Additionally, $\gamma_d = \frac{D}{s^c}$ is the ratio of the thickness of typical insulator to superconducting sheet, $\gamma_c = \frac{\lambda_c}{D}$ is the ratio of the London penetration depth to the thickness of typical insulator, $\gamma = \frac{\lambda_c}{\lambda_{ab}}$ is the anisotropy factor given by the ratio of c to in-plane London penetration depth λ_{ab}.

Time-dependent Hamiltonian The modulation of the permittivity in time results into a modulation of the mass matrix $\boldsymbol{\mathcal{M}}^\phi \to \boldsymbol{\mathcal{M}}^\phi(x,\tau)$ as $\boldsymbol{\mathcal{M}}^\phi(x,\tau) = \frac{D}{\epsilon r^c}\boldsymbol{\mathcal{C}}^{-1}(x,\tau)$ with the corresponding dimensionless momentum given by $\vec{p} = \boldsymbol{\mathcal{M}}^\phi(x,\tau)\partial_\tau\vec{\phi}$ (Appendix A.1). Including both driving terms from Sec. 3.1.4, expressing the Hamiltonian from Eq. (3.1.2) in dimensionless units leads to

$$\mathcal{H} = \frac{1}{L}\int_0^L dx \frac{1}{2}\vec{p}^{\top}\boldsymbol{\mathcal{M}}^{\phi^{-1}}(x,\tau)\vec{p} - (\vec{\boldsymbol{\mathcal{J}}}^C)^{\top}\left[\mathbf{I} + \mathbf{A}(\tau)\right]\cos(\vec{\phi}) - \boldsymbol{j}_{bias}\vec{\phi} + \frac{1}{2}\frac{\gamma^4\gamma_d}{\gamma_c^2}\partial_x\vec{\phi}^{\top}\boldsymbol{\mathcal{L}}^{-1}\partial_x\vec{\phi}, \tag{3.35}$$

where dimensionless diagonal matrix are written calligraphically, i.e $\boldsymbol{\mathcal{J}}^C = \mathbf{J}^C/J^C$ with $J^C = \Phi_0/2\pi\lambda_c^2\mu_0 D$ [121, 126] and $\boldsymbol{\mathcal{D}} = \mathbf{D}/D$ with $D = D_l + D_h$ for critical current and junction thickness of the unit cell respectively ($\vec{\boldsymbol{\mathcal{J}}}^C$ as the vector formed by the diagonal elements of $\boldsymbol{\mathcal{J}}^C$). The dimensionless version of the bias current is given by $\vec{j}_{bias} = \vec{J}_{bias}/J^C$ in vector form or as a diagonal matrix as $\boldsymbol{j}_{bias} = \boldsymbol{J}_{bias}/J^C$. Energy is measured in units of the Josephson energy $E_J = \Phi_0 A_{\text{area}} J^C/2\pi$.

The first Hamilton equation obtained from Eq. (3.35) is trivially satisfied by the definition of momentum, $\frac{\mathrm{d}\vec{\phi}}{\mathrm{d}\tau} = \frac{\partial\mathcal{H}}{\partial\vec{p}}$. Solving the Hamilton's equation of momentum $\vec{p}$, $\frac{\mathrm{d}\vec{p}}{\mathrm{d}\tau} = -\frac{\partial\mathcal{H}}{\partial\vec{\phi}}$, for

$\frac{\mathrm{d}^2\vec{\phi}}{\mathrm{d}\tau^2}$, we obtain the inductively and capacitively coupled sine-Gordon equation including both types of driving,

$$\partial_\tau^2\vec{\phi} = -\boldsymbol{\mathcal{P}}^C(x,\tau)\left[(\mathbf{I}+\mathbf{A}(\tau))\sin\left(\vec{\phi}\right) - \left(\boldsymbol{\mathcal{J}}^C\right)^{-1}\vec{j}_{\mathrm{bias}}\right] - \boldsymbol{\gamma}_{disp}(x,\tau)\partial_\tau\vec{\phi} + \boldsymbol{\mathcal{P}}^L(x,\tau)\partial_x^2\vec{\phi}, \quad (3.36)$$

where we defined a capacitive coupling matrix

$$\boldsymbol{\mathcal{P}}^C(x,\tau) = \frac{\epsilon r^c}{D}\boldsymbol{\mathcal{C}}(x,\tau)\boldsymbol{\mathcal{J}}^C, \quad (3.37)$$

and another inductive coupling matrix

$$\boldsymbol{\mathcal{P}}^L(x,\tau) = \frac{\epsilon r^c}{D}\frac{\gamma^4\gamma_d}{\gamma_c^2}\boldsymbol{\mathcal{C}}(\boldsymbol{x},\tau)\boldsymbol{\mathcal{L}}^{-1}, \quad (3.38)$$

with dimensionless quantities defined in Sec. 3.1.5. These matrices can be conveniently split as $\boldsymbol{\mathcal{P}}^C(x,\tau) = \boldsymbol{\mathcal{P}}_i^C - \boldsymbol{\mathcal{P}}_t^C\left(1-\cos\left(\frac{2\omega_d}{\omega_p}\tau\right)\right)\frac{1}{2}\left(1+\cos\left(2k_dx\right)\right)$ (using Eq. (3.34)) into a driving independent part of the tridiagonal matrix responsible for capacitive coupling of the form $\boldsymbol{\mathcal{P}}_i^C = \frac{\epsilon r^c}{D}\left(\boldsymbol{\alpha}^{-1}-\boldsymbol{\Delta}\right)\boldsymbol{\mathcal{J}}^C \approx (\boldsymbol{I}-\boldsymbol{\Delta}\boldsymbol{\alpha})\boldsymbol{\mathcal{J}}^C\boldsymbol{\mathcal{D}}$ and a contribution arising due to the driving $\boldsymbol{\mathcal{P}}_t^C = \frac{\epsilon r^c}{D}\boldsymbol{\mu}\boldsymbol{\mathcal{J}}^C$. The modulation of $\boldsymbol{\epsilon}(x,\tau)$ in the mass term $\boldsymbol{\mathcal{M}}^\phi(x,\tau)$ gives rise to a time-dependent damping and coupling term of the form

$$\boldsymbol{\gamma}_{disp}(x,\tau) = \frac{2\omega_d}{\omega_p}\sin\left(\frac{2\omega_d}{\omega_p}\tau\right)\frac{1}{2}\left(1+\cos\left(2k_dx\right)\right)\boldsymbol{\mathcal{P}}_t^C\left(\boldsymbol{\mathcal{P}}_i^C\right)^{-1} + O(\nu^2). \quad (3.39)$$

We would like to point out that our choice of mass $\boldsymbol{\mathcal{M}}^\phi(\tau)$ and momentum $\vec{p}$ is not unique. Any pair of canonical variables related by a canonical transformation leads to a physically equivalent formulation, i.e. identical equation of motions [265].[7] Alternatively, one could choose only the time-independent part of $\boldsymbol{\mathcal{M}}^\phi(x,\tau)$ as mass. This choice leads to an additional momentum-position-coupling term in the Hamiltonian[8], which gives rise to the time-dependent damping term in Eq. (3.39).

The time-independent part is conveniently re-expressed in the form used in Ref. [256] (Sec. A.3) as

$$\boldsymbol{\mathcal{P}}_i^C = \begin{pmatrix} (2\alpha_1+1)\varpi_1^2 & -\alpha_2\varpi_2^2 & 0 & \\ -\alpha_1\varpi_1^2 & (2\alpha_2+1)\varpi_2^2 & -\alpha_1\varpi_1^2 & 0 \\ 0 & -\alpha_2\varpi_2^2 & (2\alpha_1+1)\varpi_1^2 & \ddots \\ & 0 & \ddots & \ddots \end{pmatrix}, \quad (3.40)$$

where $\varpi_{1,2}$ are the dimensionless Josephson plasma frequencies of the respective junction defined as

$$\varpi_M^2 = \frac{\epsilon r^c}{D}\frac{\boldsymbol{\mathcal{J}}_M^C}{\alpha_M} \approx \boldsymbol{\mathcal{J}}_M^C\boldsymbol{\mathcal{D}}_M, \quad (3.41)$$

[7] In an extended Hamiltonian, where time is promoted to a coordinate [265], it is even possible to perform a canonical transformation such that new Hamiltonian reduces to a time-independent problem [266].

[8] E.g. see derivation of the cavity optomechanical Hamiltonian in Ref. [170] for a cavity containing a time and spatially dependent dielectric medium with moving mirror boundaries.

where the approximation in the second step becomes exact for infinitely thin superconducting sheets. The modulation matrix is then given by

$$\boldsymbol{\mathcal{P}}_t^C = \begin{pmatrix} \frac{\bar{\mu}_1}{2}\varpi_1^2 & 0 & & \\ 0 & \frac{\bar{\mu}_2}{2}\varpi_2^2 & 0 & \\ & 0 & \frac{\bar{\mu}_1}{2}\varpi_1^2 & 0 \\ & & 0 & \ddots \end{pmatrix}, \tag{3.42}$$

where $\bar{\boldsymbol{\mu}} = \boldsymbol{\alpha}\frac{D}{r^c}\boldsymbol{\mathcal{D}}\boldsymbol{\nu}\boldsymbol{\epsilon}^{-1} = 2\boldsymbol{\alpha}\boldsymbol{\mu}$ is a diagonal matrix characterising the driving strength. Without the driving, the capacitive and inductive sine-Gordon equation given in Eq. (3.36) reduces to the one in Ref. [193] in the infinitely thin junction limit. However, we additionally take in-plane dissipation into account, which is derived in Appendix A.2.1 based on a two field treatment as discussed for a monolayer in Ref. [67, 68, 126].

3.2 Linearised equations of motion

In this section, we restrict ourselves to small fluctuations of the phase around an equilibrium position determined by the externally applied bias current and determine the corresponding normal mode frequencies for a stack of long Josephson Junctions.

Small phase fluctuations around the equilibrium position The presence of an external bias current along the z-axis creates a tilt in the washboard potential as shown in Fig. 1.2. This causes a shift in the equilibrium position of a phase-particle trapped in one of the valleys. In the case of the coupled sine-Gordon Hamiltonian discussed here, the equilibrium position in absence of the current, e.g. $\vec{\phi}^0 = 0$, is shifted by the bias current to $\vec{\phi}^0 = \arcsin\left(\left(\boldsymbol{\mathcal{J}}^C\right)^{-1}\vec{j}_{bias}\right)$, where $\arcsin()$ independently acts on each component of the argument vector. We now consider small fluctuations $\delta\vec{\phi}$ around this minima, i.e. $\vec{\phi}(x,\tau) = \vec{\phi}^0 + \delta\vec{\phi}(x,\tau)$.

In order to satisfy non-radiating Neumann boundary conditions given by $\partial_x\vec{\phi}|_{x=0,L} = 0$, the phase fluctuation $\delta\vec{\phi}(x,\tau)$ is expanded in a cosine series, i.e. $\vec{\phi}(x,\tau) = \sum_w \vec{\phi}_w(\tau)\cos(k_w x) + \vec{\phi}_0$ with momenta $k_w = \frac{\pi w}{L}$ and $w \in \mathbb{N}$ [116, 118, 188–191] for a junction of length L. The corresponding multimode expansion is also used for other quantities such as momentum $\vec{p}(x,\tau) = \sum_w \vec{p}_w(\tau)\cos(k_w x)$. To avoid clutter in the notation the time dependence is implicit in the following, i.e. $\vec{p}_w(\tau) \to \vec{p}_w$ and $\vec{\phi}_w(\tau) \to \vec{\phi}_w$.

Hamiltonian for homogeneous driving $k_d = 0$ In traditional Raman scattering, incident photons can only excite low-momentum phonon due to energy and momentum conservation. Physically, the wavelength of the incident light is much larger then inter-atomic spacing, such that the light can only efficiently couple to phonon modes with low momentum, which can be considered to be essentially dispersionless [267]. As the same consideration holds true in THz-experiments [36], we focus on a spatially homogeneous drive, i.e. $k_d = 0$

in the following. Keeping only quadratic terms in $\delta\vec{\phi}^2$, the linearised equation of motion of each spatial mode decouple, and the total Hamiltonian satisfies

$$\mathcal{H} = \sum_w \mathcal{H}_w, \tag{3.43}$$

where $\mathcal{H}_w$ is the Hamiltonian of the wth spatial mode given by

$$\mathcal{H}_w = \frac{1}{2}\vec{p}_w^{\top}\boldsymbol{\mathcal{M}}_w^{\phi}(\tau)^{-1}\vec{p}_w + \frac{1}{2}\vec{\phi}_w^{\top}\boldsymbol{\mathcal{K}}_w(\tau)\vec{\phi}_w + (\vec{\boldsymbol{\mathcal{J}}}^C)^{\top}\mathbf{A}(\tau)\sin\boldsymbol{\phi}^0\vec{\phi}_w + O(\vec{\phi}_w^3), \tag{3.44}$$

with mass $\boldsymbol{\mathcal{M}}_w^{\phi}(\tau) = \boldsymbol{\mathcal{M}}^{\phi}(0,\tau)(1+\delta_{w,0})/2$ with $\delta_{w,0}$ as a Kronecker delta taking into account the larger value from the spatial integral of the $k_w = 0$ mode in Eq. (3.35) and $\boldsymbol{\mathcal{K}}_w(\tau)$ is the spring constant matrix given by

$$\boldsymbol{\mathcal{K}}_w(\tau) = \left[\cos\boldsymbol{\phi}^0\boldsymbol{\mathcal{J}}^C\left(\mathbf{I}+\mathbf{A}(\tau)\right) + k_w^2\frac{\gamma^4\gamma_d}{\gamma_c^2}\boldsymbol{\mathcal{L}}^{-1}\right](1+\delta_{w,0})/2. \tag{3.45}$$

The lowest order correction to this Hamiltonian is given by a cubic term.

Diagonalising the Hamiltonian for homogeneous driving $k_d = 0$ For weak driving higher harmonics of the drive are very weak and off-resonant. Keeping only the lowest harmonic of the driving, the mass matrix is given by $\boldsymbol{\mathcal{M}}_w^{\phi}(\tau) = \boldsymbol{\mathcal{M}}_w^i + \boldsymbol{\mathcal{M}}_w^t\cos\left(\frac{2\omega_d}{\omega_p}\tau\right) + O(\nu_{1,2}^2)$, where $\boldsymbol{\mathcal{M}}_w^i = \frac{1}{T}\int_0^T \boldsymbol{\mathcal{M}}_w^{\phi}(\tau)d\tau$ with period $T = \frac{2\pi\omega_p}{2\omega_d}$ is the time-independent part and $\boldsymbol{\mathcal{M}}_w^t = -(1+\delta_{w,0})/2\boldsymbol{\mathcal{J}}^C\left(\boldsymbol{\mathcal{P}}_i^C\right)^{-1}\boldsymbol{\mathcal{P}}_t^C\left(\boldsymbol{\mathcal{P}}_i^C\right)^{-1}$ the amplitude of the time-dependent one. For a stack of n_{junc} junctions, a time-independent transformation $\mathbf{P}_w$ can be found such that (see Sec. A.4.1)

$$\mathbf{P}_w^{\top}\boldsymbol{\mathcal{M}}_w^i\mathbf{P}_w = \bar{\mathbf{m}}_w^i, \tag{3.46}$$

with time-averaged (indicated by $\langle\ldots\rangle_\tau$) spring constant

$$\mathbf{P}_w^{\top}\langle\boldsymbol{\mathcal{K}}_w(\tau)\rangle_\tau\mathbf{P}_w = \bar{\mathbf{m}}_w^i\boldsymbol{\Omega}^2(k_w), \tag{3.47}$$

where $\bar{\mathbf{m}}_w^i$ is a diagonal matrix with real positive entries[9] and $\boldsymbol{\Omega}(k_w)$ is a diagonal matrix containing the time-independent part of the n_{junc} normal mode frequencies of the wth spatial mode (Sec. 3.2.1). The time-averaged Hamiltonian is diagonalised in terms of the transformed normal mode coordinate $\vec{Q}_w = \mathbf{P}_w^{-1}\vec{\phi}_w$ and momentum $\vec{\mathfrak{P}}_w = \mathbf{m}_w(\tau)\partial_\tau\vec{Q}_w = \mathbf{P}_w^{\top}\vec{p}_w$ as

$$\langle\mathcal{H}_w\rangle_\tau = \frac{1}{2}\vec{\mathfrak{P}}_w^{\top}(\bar{\mathbf{m}}_w^i)^{-1}\vec{\mathfrak{P}}_w + \frac{1}{2}\vec{Q}_w^{\top}\bar{\mathbf{m}}_w^i\boldsymbol{\Omega}^2(k_w)\vec{Q}_w + (\vec{\boldsymbol{\mathcal{J}}}_P^C)^{\top}\mathbf{A}/2\sin\boldsymbol{\phi}_0\vec{Q}_w(1+\delta_{w,0})/2, \tag{3.48}$$

with $\vec{\boldsymbol{\mathcal{J}}}_P^C = \mathbf{P}_w^{\top}\vec{\boldsymbol{\mathcal{J}}}^C$ where $\langle\ldots\rangle_\tau$ indicates time averaging over an integer number of driving periods and the eigenvalues are given by the normal mode frequencies squared, $\boldsymbol{\Omega}^2(k_w)$. The

[9] This diagonal matrix can be set equal to the identity as it does not enter in any physical observable in real space. This freedom arises because the similarity transformation $\mathbf{P}_w$ is not uniquely determined (see Sec. A.4.1).

last term corresponds to a shift due to the bias currents, which can be absorbed into $\vec{Q}_w$ by shifting the origin. Transforming the time-dependent spring matrix, we obtain

$$\mathbf{P}_w^\top \boldsymbol{\mathcal{K}}_w(\tau)\mathbf{P}_w = \bar{\mathbf{m}}_w^i \boldsymbol{\Omega}_w^2(\tau) = \bar{\mathbf{m}}_w^i \boldsymbol{\Omega}^2(k_w) - \cos\left(\frac{2\omega_d}{\omega_p}\tau\right)\frac{1}{2}\mathbf{P}_w^\top \cos\boldsymbol{\phi}_0 \boldsymbol{\mathcal{J}}^C \mathbf{A}\mathbf{P}_w(1+\delta_{w,0})/2. \tag{3.49}$$

such that the Hamiltonian is given by

$$\mathcal{H}_w = \frac{1}{2}\vec{\mathfrak{P}}_w^\top \mathbf{m}_w(\tau)^{-1}\vec{\mathfrak{P}}_w + \frac{1}{2}\vec{Q}_w^\top \bar{\mathbf{m}}_w^i \boldsymbol{\Omega}_w^2(\tau)\vec{Q}_w + (\vec{\boldsymbol{\mathcal{J}}}_P^C)^\top \mathbf{A}(\tau)\sin\boldsymbol{\phi}_0 \vec{Q}_w(1+\delta_{w,0})/2, \tag{3.50}$$

where the total mass in the time-independent normal mode frame is given by

$$\mathbf{m}_w(\tau) = \mathbf{P}_w^\top \mathbf{M}_w^\phi(\tau)\mathbf{P}_w = \bar{\mathbf{m}}_w^i + \mathbf{m}_w^t \cos\left(\frac{2\omega_d}{\omega_p}\tau\right) + O(\nu^2), \tag{3.51}$$

with $\mathbf{m}_w^t = \mathbf{P}_w^\top \boldsymbol{\mathcal{M}}_w^t \mathbf{P}_w$ as the matrix describing the coupling of different modes together.

3.2.1 Normal mode frequencies

In this subsection, we calculate the dispersion of the normal modes with in-plane momentum for different stack sizes.

Model parameters Most system parameters are chosen as reported for the commonly studied bilayer material $YBa_2Cu_3O_{7-\delta}$ (YBCO). The London penetration depths are approximated $\lambda_{ab} \approx 272\,\mathrm{nm}$ and $\lambda_c \approx 1500\,\mathrm{nm}$ for YBCO, which corresponds to a relatively weak anisotropy of $\gamma = \lambda_c/\lambda_{ab} = 5.5$ [268], though this value varies greatly between different crystal structures and even measurement techniques [268–270]. The distance between the superconducting layers $D_l = 0.82\,\mathrm{nm}$ and $D_h = 0.34\,\mathrm{nm}$, appropriate for YBCO [254, 271], is used as an estimate for the thickness of the insulating layers, i.e. $D = D_l + D_h$. The thickness of the superconducting layer is estimated as $s^c = 0.1\,\mathrm{nm}$. This selection of parameters leads to $\gamma_d = \frac{D}{s^c} = 11.6$, $\gamma_c = \frac{\lambda_c}{D} \approx 1294$ and consequently to an inductive coupling strength of $\eta_l^L = 7.8 \cdot 10^4$, $\eta_h^L = 1.88 \cdot 10^5$, which is of the expected order of magnitude for inductive coupling [194].

To determine the model parameters $\varpi_{l,h}$ in terms of spectroscopically measurable normal mode frequencies, we analytically solve for $\varpi_{l,h}$ in a two-junction toy model in Sec. A.4.5. Setting $\omega_p \approx \min(\boldsymbol{\Omega}_0)$ equal to the lowest normal mode frequency present in the system, we approximate the experimental values observed in Ref. [18] by $\Omega_h(0) \approx 10$ and $\Omega_l(0) \approx 1$. To produce sensible values for the Debye screening length and the permittivity in the superconducting sheets (see Sec. A.4.5), the capacitive coupling parameters $\alpha_{1,2}$ are restricted by (see Eq. (A.72) and Eq. (A.76))

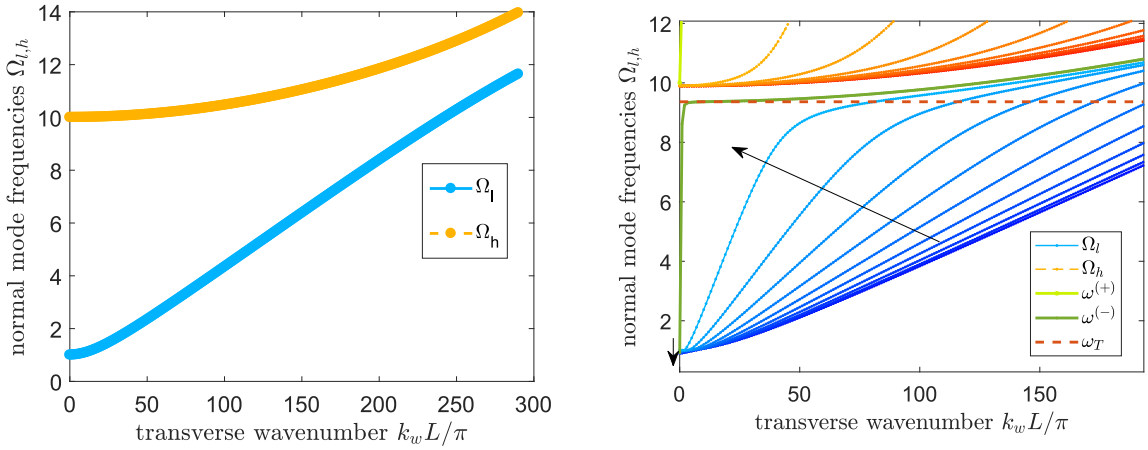
$$\frac{D_h}{D_l}\frac{\epsilon_l}{\epsilon_h}\alpha_1 < \alpha_2 < \alpha_1, \tag{3.52}$$

where the permittivity $\epsilon = \epsilon_{l,h}$.

The cooling efficiency strongly depends on the capacitive coupling $\alpha_{1,2}$, decay rates of the homogeneous modes $\gamma_{l,h}$ and driving amplitudes $A_{1,2}$ and $\nu_{1,2}$. In Sec. 3.5.1, we discuss the dependence of the cooling efficiency on these parameters. This is justified as not all relevant parameters for the present implementation have been unambiguously reported for YBCO and others would have to be optimised to achieve significant cooling.

For the rest of the simulations in this section we use $\alpha_1 = 0.28$, $\alpha_2 = 0.66$ (typical parametric coupling parameters are of the order of unity [195,272]) and a strongly underdamped damping rates $\gamma_l = 0.005$, $\gamma_h = 0.01$ of the spatially homogeneous modes. These damping rates are an order of magnitude lower than the values of roughly 0.1 estimated from the relaxation rate of the excitations in Ref. [18]. Here, the parameters are mainly chosen such as to achieve a high cooling efficiency (see Sec. 3.5.1) consistent with the weak damping and weak driving approximation (see discussion around Eq. (2.43)). From the analytical expression for the cooling ratio in the strong coupling regime from Eq. (2.50), the cooling ratio only depends on the damping and frequency ratio. In order to remain in the strong coupling regime given a linear increase in the damping rates, it is necessary to increase the driving strength quadratically. This way, it might be possible to achieve high cooling even in the strongly damped regime. However, such an approach would require to take into account higher order terms in Eq. (3.34) and is not pursued here.

The Josephson penetration length λ_J characterises the typical length scales over which the superconducting phase varies and provides an estimate for the size of solitons $\sim \lambda_J$. For the parameters considered here, the long junction regime is defined as the limit $L \gg \lambda_J$, where the junction L is much larger than the Josephson penetration length λ_J. The critical length scale at which inductive coupling dominates over capacitive coupling already for the lowest spatial mode can be estimated as $L_{\mathrm{crit}}/\lambda \approx \pi\gamma\gamma_d^{1/2}\sqrt{\alpha/\eta^L} \approx 0.06$ with $\eta^L = 10^5$ and $\alpha = 0.5$. The Josephson penetration length λ_J in the two junctions can be roughly approximated as $\lambda_J/\lambda \sim \sqrt{\frac{\gamma^4\gamma_d}{\gamma_c^2}\frac{\mathcal{D}_M}{\varpi_M^2}}$, which evaluates to 0.01 and 0.001 for l and h-type of junction from Fig. 3.1. This value is very small and does not justify to ignore non-local contribution to the Josephson electrodynamics in general. General solutions to Eq. (3.19) are, however, only valid for local Josephson electrodynamics. For solutions involving high-wavevectors $k_w \gg 1$ the phase varies quickly in comparison to the London penetration length λ_c and therefore the z-axis current evaluated at x "feels" the phase over a distance λ_c around x [68,252,273]. However, due to their high energy, the corresponding high momentum modes are associated with very high frequencies, such that they have a negligible small thermal occupation and are therefore only indirectly excited through low-frequency modes. These high momentum modes are additionally also associated with large decay rates (see Fig. 3.4a and Fig. 3.4b) resulting in a negligible driving to damping strength ratio. We, therefore, cannot expect to modify the propagation of high-momentum modes such as solitons, but rather to suppress the thermal population in the lower normal mode frequencies, which are initially occupied and can themselves facilitate the excitation of high-momentum modes. The present cooling scheme does not rely on λ_J/λ being small, and we could choose a larger λ_J, but for the present choice, the steep dispersion reduces the number of thermally excited normal modes and consequently also the computational effort, which is already now very large.



(a) $n_{\text{junc}} = 2$ junctions ***(b)*** $n_{\text{junc}} = 20$ junctions

Figure 3.2: Normal mode frequencies $\mathbf{\Omega}(k_w)$ obtained from Eq. (3.47), as a function of wavenumber $w = k_w L/\pi$ for a stack of **(a)** two **(b)** twenty junctions of length $L = 5$. The red to orange (blue to turquoise) coloured cross (circular) shaped markers corresponds to $n_{\text{junc}}/2$-highest (lowest) normal mode frequencies. The wavenumber only takes integer values w (corresponding marker points are not resolved). b) The large arrow at large k_w indicates the change of the dispersion curve with increasing stack size, as the dispersion curve for low q_z approaches the continuous limit shown in bright green. The normal mode frequency increases with decreasing q_z. For $k_w = 0$, the normal mode frequencies decrease with decreasing longitudinal momentum q_z due to capacitive coupling as indicated by the small vertical arrow (capacitive coupling parameters $\alpha_1 = 0.28$, $\alpha_2 = 0.66$, other system parameters given in Sec. 3.2.1)

Normal mode frequencies A stack of n_{junc} junctions has n_{junc} normal modes given by the diagonal entries of $\mathbf{\Omega}(k_w)$ from Eq. (3.47) for each momentum $k_w = w\pi/L$ ($w \in \mathbb{Z}^{\geq 0}$). Their frequencies can be divided into two bands l, h given by the vectors $\vec{\Omega}_i(k_w)$ with $i = l, h$ containing the $n_{\text{junc}}/2$ lowest and highest normal mode frequencies respectively. Figure 3.2a (Figure 3.2b) shows the dispersion of the elements $\Omega_i(k_w)$ pertaining to the two bands $\vec{\Omega}_i(k_w)$ with $i = l, h$ as a function of the integer wave numbers $w = k_w L/\pi$ for a stack of $n_{\text{junc}} = 2$ ($n_{\text{junc}} = 20$) junctions of length $L = 5$ (discrete points not resolved). An increase in stack size has only a small effect on the lowest frequency component of each band, e.g. the blue line in Fig. 3.2b resembles the turquoise one in Fig. 3.2a. However, with increasing stack size additional normal mode frequencies branch out at finite k_w from the bundle of lowest frequency components of each band.

Optical wavelengths used for the excitation of Josephson plasma modes are significantly larger than the unit cell of the crystal. Incident radiation therefore only couples to modes with a net macroscopic electric field, obtained by averaging the microscopic electric field from Eq. (3.5) over multiple junctions. The largest net electric field arises from modes with small longitudinal wavevector $q_z \approx 0$, i.e. for synchronised oscillations of the phases along the stack. For out-of-phase modes, the contribution of adjacent unit cells to the electric field are opposite and average out [274].[10] A single unit cell with two Josephson plasmon modes is

[10] Local light sources, e.g. on-chip terahertz sources [275, 276] or scanning near-field microscopy directly

therefore often sufficient to describe the optical response of a bilayer superconductor. Higher q_z-modes, on the other hand, still play a significant role in the intrinsic phase dynamics of the junction as these modes can have a significant thermal occupation and couple to homogeneous modes through non-linear terms of the equation of motion. For example, in the presence of a finite external magnetic field, which gives rise to a Josephson vortex lattice: For small junctions, surface effects can synchronise the resulting Josephson vortex lattice into a $q_z = 0$ mode corresponding to a rectangular Josephson vortex lattice. However, when increasing the junction length, the rectangular lattice becomes unstable to decay into a triangular configuration, which cannot give rise to coherent THz radiation (see discussion in Ref. [73]). Achieving synchronisation of intrinsic Josephson junctions, i.e. exciting modes with low longitudinal momentum q_z, in the presence of a strong static magnetic field is essential for the generation of intense THz radiation by moving Josephson vortex lattices [73].

The limiting behaviour with increasing stack size can be determined analytically by considering purely transverse ($q_z = 0$) plane-wave excitations of a periodically repeating two-junction unit cell using an ansatz

$$\phi_M^l(t) = \Theta_M(k_w, \omega) e^{\mathrm{i}k_w x - \mathrm{i}\omega t}. \tag{3.53}$$

with wavevector k_w and $\phi_M^l(t) = \phi_{M+2}^l(t)$. Solving the corresponding eigenvalue equation, we obtain two transverse Josephson plasma modes given by the dark green line labelled $\omega^{(-)}$ and the bright green line labelled $\omega^{(+)}$ in Fig. 3.2b. With increasing stack size, the normal mode frequencies corresponding to approximately continuous excitation of the two branches such that $q_z \approx 0$[11] (yellow and turquoise lines) converge against the transverse Josephson plasma modes $\omega^{(+,-)}$ as indicated by the large black arrow.

Analytically, we can approximate the corresponding eigenvalue equation by ignoring contributions of the order k_w^4 for large inductive coupling $\eta_{l,h} \gg 1$ and long wavelengths leading to [193, 278]

$$\omega^4 - \left[(1+2\alpha_1)\varpi_1^2 + (1+2\alpha_2)\varpi_2^2 + \gamma^2 k_w^2\right]\omega^2 + (1+2\alpha_1+2\alpha_2)\left[\varpi_1^2\varpi_2^2 + (z_2\varpi_1^2 + z_1\varpi_2^2)\gamma^2 k_w^2\right] = 0, \tag{3.54}$$

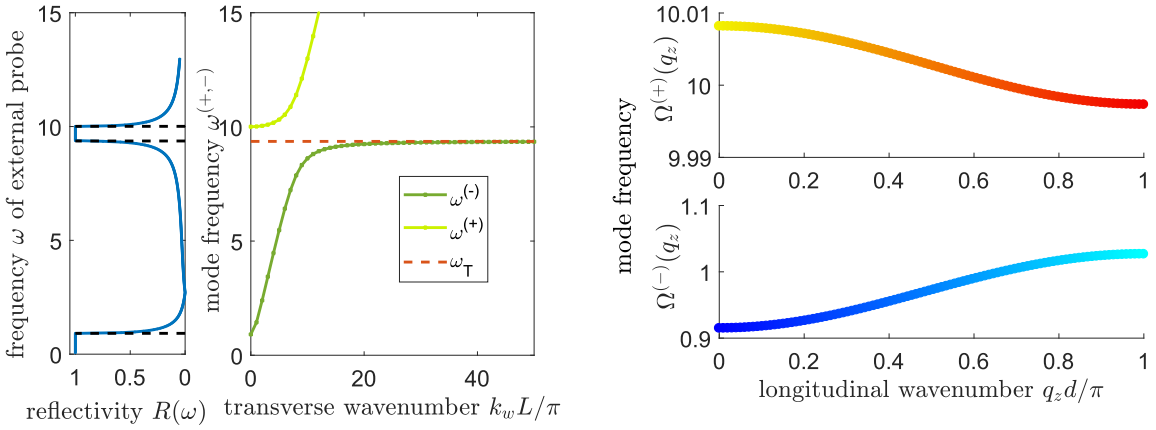
where we took the limit of infinitely thin superconducting sheets such that the expression are identical to the ones in Ref. [193, 279] with $z_i = \frac{D_i}{D_1+D_h}$ for $i = l, h$ (here $\epsilon = \epsilon_{1,2}$). In the absence of the k_w^4 terms, increasing k_w leads to a convergence of the lower transverse Josephson plasma mode $\omega^{(-)}$ to the k_w-independent limit of the transverse plasmon mode given by [193, 279]

$$\omega_T^2 = (1+2\alpha_1+2\alpha_2)\left(\varpi_1^2\frac{D_h}{D} + \varpi_2^2\frac{D_l}{D}\right), \tag{3.55}$$

attached or located above the surface of the superconductor, might allow probing the response of modes with larger q_z.

[11] The spatial structure for a finite stack is shown in Appendix A.4.3. For $k_w = 0$, the coupling between different junctions of the stack is purely capacitive and the ordering of the normal modes with increasing q_z is given by Eq. (3.59) as indicated by the small vertical arrow in Fig. 3.2b. With increasing k_w, the coupling is dominated by inductive coupling leading to a reordering of the normal modes indicated by the larger arrow in Fig. 3.2b [277]. For finite k_w the highest frequency component of the lower band has $q_z \to 0$ with increasing stack size, while the lowest frequency component corresponds to the largest q_z. This reordering can be therefore understood as a competition between capacitive and inductive energies in the system.

which is visible as a peak in the real part of the conductivity [18,278]. For junction of length $L = 5$ (Fig. 3.2b), the dark green curve quickly increases from Ω_l to ω_T at very small non-zero k_w. For an even larger junction $L = 50$, this jump is smoothed out as shown in Fig. 3.3a. The additional k_w^4 terms included in Fig. 3.2b allow $\omega^{(-)}$ to grow beyond ω_T with k_w. In order to satisfy the boundary condition of the electric and magnetic field in each junction for a wave polarised along the c-axis impinging on the side of the junction, it is necessary to keep terms proportional to k_w^4 in Eq. (3.54) [193]. However, such a solution does not lead to additional contribution from the finite k_w modes.



(a) *(b)*

Figure 3.3: **(a)** Left panel shows the reflectivity from Eq. (3.56) as a function of frequency in the absence of damping. The reflectivity can be approximated by only the lowest k_w-mode due to energy and momentum conservation of the electric and magnetic field of the incident wave at the boundary. There are plasma edges corresponding to drops of the reflectivity curves at the two transverse plasma frequency for $k_w = 0$. The reflectivity increases again at ω_T. Right panel shows a dispersion curve for transverse excitations $\omega^{(+,-)}(k_w)$ as determined from a modification of Eq. (3.54) including terms proportional to k^4 for very long junctions $L = 50$. **(b)** Longitudinal excitations $\Omega^{(+,-)}(q_z)$ as a function of out of plane momentum q_z as determined from Eq. (3.59). These excitations are purely longitudinal $k_w = 0$ with dispersion only due to capacitive coupling.

In the left panel of Fig. 3.3a, we show the typical reflectivity [267]

$$R(\omega) = \left| \frac{(1 - \sqrt{\epsilon_{\text{eff}}(\omega)})}{(1 + \sqrt{\epsilon_{\text{eff}}(\omega)})} \right|, \tag{3.56}$$

in the limit where the phases in all unit cells of the crystal oscillate in phase such that $q_z = 0$, obained for c-axis polarised light of frequency ω propagating perpendicular to the sample with an effective refraction index $n_{\text{eff}} = \sqrt{\epsilon_{\text{eff}}(\omega)}$. In absence of dissipation, the effective permittivity is given by [193,278]

$$\epsilon_{\text{eff}} = \epsilon_\infty \frac{(\omega^2 - \omega^+(0)^2)(\omega^2 - \omega^-(0)^2)}{\omega^2(\omega^2 - \omega_T^2)}, \tag{3.57}$$

where ϵ_∞ is the permittivity due to the presence of bound charges. This expression can be obtained by calculating the response to an alternating bias current (see Sec. 2.2.2), ex-

ploiting the relation between optical conductivity and permittivity $\epsilon(\omega) = \mathrm{i}\frac{\sigma(\omega)}{\omega} + \epsilon_\infty$. For $\omega < \omega^{(-)}(0)$ and $\omega_T < \omega < \omega^{(+)}(0)$ (Restrahlenband), the material is perfectly reflecting $R(\omega) = 1$ for radiation polarised along the c-axis. The Josephson plasma edges at $\omega^{(+,-)}(0)$ in the reflectivity curve allow to experimentally identify the location of the plasmon modes.

The spatial dispersion for purely longitudinal modes, i.e. $k_w = 0$, of an infinitely large stack can be found using a plane wave ansatz of the form [193]

$$\phi_M^l(t) = \sum_q \Theta_q^l(\omega) e^{\mathrm{i}qM_b d - \mathrm{i}\omega t}, \tag{3.58}$$

where $d = \frac{D_1+D_2}{D}$ and $M_b = \frac{M-1}{2} + 1$ ($M_b = \frac{M-2}{2} + 2$) counts the unit cell of the odd (even) Mth bilayer. The corresponding longitudinal dispersion relation are given by [193, 279]

$$\Omega^{(+,-)^2}(q_z) = \left(\frac{1}{2} + \alpha_1\right)\varpi_1^2 + \left(\frac{1}{2} + \alpha_2\right)\varpi_2^2 \pm \sqrt{\left[\left(\frac{1}{2} + \alpha_1\right)\varpi_1^2 - \left(\frac{1}{2} + \alpha_2\right)\varpi_2^2\right]^2 + 4\alpha_1\alpha_2\varpi_1^2\varpi_2^2\cos^2\left(\frac{q_z d}{2}\right)}. \tag{3.59}$$

with $\Omega^{(+,-)}(q = 0) = \omega^{(+,-)}(k_w = 0)$. The q dependence for $k_w = 0$ obtained from Eq. (3.59) is very small (Fig. 3.3b).

Without the drive, the different modes of the linearised model evolve independently. The spatially homogeneous parametric driving leads to coupling of pairs of eigenvectors with the same transverse momentum k_w belonging to distinct bands. Which pairs are coupled can be determined by momentum conservation along the z axis according to the choices of $\nu_{1,2}$ and $A_{1,2}$. For homogeneous driving, for example, only those modes with the same transverse k_w and longitudinal momentum q_z are coupled. The linearised normal modes of a stack of n_{junc} junctions effectively take the form of $n_{\mathrm{junc}}/2$ pairs of parametrically coupled harmonic oscillators for each k_w.

3.3 Thermalisation

In this section, noise is modelled phenomenologically by assuming a large heat bath consisting of weakly interacting phonon modes.

Including dissipation in Hamilton's equation There are many sources of dissipative terms for a stack of coupled Josephson junction (see Sec. 3.1.1), ranging from incoherent c-axis and in-plane quasi-particle current given in Eq. (3.20) and (3.21) respectively, which leads to a phase dependent dissipation term and shot noise [69], thermal noise such as Johnson-Nyquist noise due to an effective shunt resistance [69, 280] to dissipation due to long-wavelength phonon modes. Describing the thermalisation of the system theoretically is, therefore, a very challenging task. However, our main aim is not to develop a microscopic model of dissipation, but instead to ensure that in the absence of driving the linearised

system relaxes to a proper thermal state without any artificial correlations between independent normal modes. We notice that in comparison to conventional superconductors HTSC possess an unusually large phonon contribution to the specific heat. Therefore, dissipation and thermal noise are phenomenologically motivated by a long wavelength bath, leading to statistically independent noise. Consequently, each normal mode is effectively coupled to its own independent thermal bath. The different spatial modes are thermalised independently, ignoring any decay from one mode to another, which is a reasonable assumption for weak driving and weakly interacting phonon heat bath spanning the whole junction. Assuming each spatial mode to be thermalised independently, the system size is limited by the phonon speed. We assume that the primary sources of thermal noise are representable by white, independent and Gaussian stochastic forcing determined from the normal modes of the linearised system by the fluctuation-dissipation theorem. The thermalisation in this chapter is implemented in the classical framework of the Langevin equation (Sec. B.7) by including thermal noise and dissipation into the linearised Hamilton's equation of the k_w momentum normal mode as

$$\frac{\mathrm{d}\vec{\mathfrak{P}}_w}{\mathrm{d}\tau} = -\frac{\partial \mathcal{H}}{\partial \vec{Q}_w} + \mathbf{m}_w(\tau)\vec{\bar{\xi}}_w(\tau) - \mathbf{m}_w(\tau)\boldsymbol{\Upsilon}^w\mathbf{m}_w^{-1}(\tau)\vec{\mathfrak{P}}_w, \tag{3.60}$$

where the second term on the right corresponds to the stochastic forcing term and the third term on right to dissipative term. The damping matrix $\boldsymbol{\Upsilon}^w$ is diagonal in the normal mode frame, such that all normal modes are thermalised independently. The noise term contains the time-dependent normal mode mass $\mathbf{m}_w(\tau)$, which is proportional to identity plus a modulation of order ν, to ensure that the driving disappears from the damping term in the equation of motions of $\frac{\mathrm{d}^2\vec{Q}_w}{\mathrm{d}^2\tau}$. This small modification of order $\gamma\nu$ from the usual Langevin equation for a time-independent mass is not expected to have an effect on the results for weak driving, as confirmed numerically (see Chapter 4 for strong driving). The thermal noise is assumed to be white, Gaussian and independent for each normal mode such that

$$\langle \bar{\xi}_w^k(t)\bar{\xi}_{w'}^l(t')\rangle = \delta_{kl}\delta_{ww'}\bar{\Gamma}_w^{kl}\delta(\tau-\tau'). \tag{3.61}$$

The elements $\bar{\Gamma}_w^{kl}$ are obtained from the fluctuation-dissipation theorem (Appendix. B.7) for the time-averaged linearised Hamiltonian through

$$\bar{\Gamma}_w^{kl} = 2\Upsilon_{kl}^w\left(\bar{m}_w^i\right)_{kk}^{-1}\frac{k_BT^r}{E_J}\mathcal{T}\Theta_{step}(\omega^c-\Omega_k), \tag{3.62}$$

where $\Theta_{step}(\Omega)$ is the Heaviside step function, which is 1 if $\Omega \geq 0$ and 0 otherwise, and introduces a cutoff ω^c. The temperature T is measured as $\mathcal{T} = T/T^r$ with reference temperature T^r defined in terms of the Josephson energy $E_J = \Phi_0 A_{\mathrm{area}} J^C/2\pi$ as $k_BT^r/E_J = m_s\Omega_s^2(Q_0^c)^2$, where k_B is the Boltzmann factor and the mass $m_s = 1$, the smallest normal mode frequency $\Omega_s = \min(\boldsymbol{\Omega}_l(0))$ and $Q_0^c = \max(\mathrm{abs}(\mathbf{P}_0^{-1}\vec{\phi}_0^c))$ with $\vec{\phi}_0^c = \pi(1,0,1,0,...)^\top$. The exact value of the cutoff frequency $\omega^c = \max(\boldsymbol{\Omega}_h(0))$ is very high, such that modes with even very small thermal occupation $\langle Q_l^2\rangle$ are included in the simulation, where the brackets $\langle\ldots\rangle$ denote an average over stochastic trajectories obtained from independent realisation of the Langevin equation from Eq. (3.60). According to the equipartition theorem (Sec. B.7) the quadrature value of $\langle Q_l^2\rangle$ is inversely proportional to the square of the normal mode frequencies and therefore largest for low-frequency modes. Next, we are aiming at reducing the thermal occupation of the lowest frequency modes of the system through driving.

Damping For $L \to \infty$ the normal-mode frequency corresponding to the lowest non-zero in-plane momentum k_w^* approaches the spatially homogeneous mode, i.e. $\vec{\Omega}_l(k_w^*) \to \vec{\Omega}_l(0)$. The thermal occupation of low in-plane momentum modes can therefore not be ignored. However, modes with $k_w \neq 0$, have an additional contribution to the damping rate due to in-plane dissipation. Therefore, for the wth momentum mode, the decay rates of the different normal modes are given by

$$\boldsymbol{\Upsilon}_w = \boldsymbol{\Upsilon}^c + \boldsymbol{\Upsilon}_w^{ab}, \tag{3.63}$$

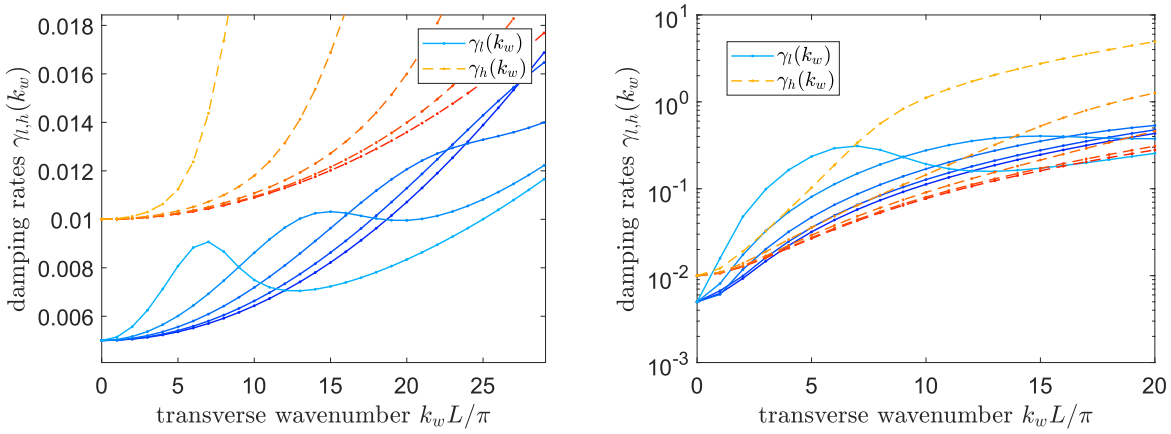
where $\boldsymbol{\Upsilon}^c$ and $\boldsymbol{\Upsilon}_w^{ab}$ are both diagonal matrices. The decay rates of the spatially uniform normal modes $w = 0$ corresponding to $\boldsymbol{\Omega}_l(0)$ ($\boldsymbol{\Omega}_h(0)$) are taken to be identical γ_l (γ_h). For $w \neq 0$ on the other hand there is an additional contribution to the decay rate $\boldsymbol{\Upsilon}_w^{ab}$ originating from in-plane dissipation. The first order adiabatic elimination of the screening current results into an additional damping term for $\vec{\phi}$ (see Sec. 3.1.3). Using the replacement Eq. (3.27) (dimensionless version in Eq. (A.39)) in the coupled sine-Gordon equation Eq. (3.36), we obtain an additional damping term $\bar{\boldsymbol{\Upsilon}}^{ab}\partial_\tau \vec{Q}_w$ for the wth normal mode with damping matrix $\bar{\boldsymbol{\Upsilon}}^{ab} = k_w^2 \frac{\epsilon_{ab}}{\epsilon}\frac{\gamma_{ab}}{\gamma^2\gamma_d}\mathbf{P}_w^{-1}\boldsymbol{\mathcal{P}}_i^L\mathbf{P}_w$, where $\gamma_{ab} = \frac{\sigma_{ab}}{\epsilon_0\epsilon_{ab}\omega_p}$ is a dimension-less constant characterising the in-plane dissipation expressed in terms of in-plane permittivity ϵ_{ab} and conductivity σ_{ab}. Besides diagonal entries, $\bar{\boldsymbol{\Upsilon}}^{ab}$ has one off-diagonal entry for each column, which results into an additional decay channel between high and low frequency modes of same in-plane momentum. However, this term only becomes significant for large k_w-modes, which are neither cooled nor possess a significant thermal occupation for the situations considered here. We, therefore, only approximate this decay rate by its diagonal components.

Physically, as we assume that all normal modes are thermalised independently by a phonon bath, such that each normal mode is only coupled to a heat bath but not to each other. The spatially dependent decay rate in Eq. (3.63) is then approximated by the diagonal components originally arising from in-plane dissipation, i.e.

$$\boldsymbol{\Upsilon}_w^{ab} = k_w^2 \frac{\epsilon_{ab}}{\epsilon}\frac{\gamma_{ab}}{\gamma^2\gamma_d}\mathrm{diag}\left(\mathbf{P}_w^{-1}\boldsymbol{\mathcal{P}}_i^L\mathbf{P}_w\right), \tag{3.64}$$

Using estimates of in-plane to out-of-plane dissipation from Ref. [255, 261][12], we can estimate an upper bound bound for the ratio of the magnitude of out-of-plane dissipation in comparison to γ_{ab}/γ_h. The relative magnitude of in-plane dissipation can then be characterised by the dimensionless constant f in $\gamma_{ab} = f\gamma_h\gamma^2\frac{\epsilon_c}{\epsilon_{ab}}$, where $f = 1$ estimates the relative magnitude if the γ_h would arise purely from in-plane dissipation. Equivalent to $\vec{\Omega}_{l,h}(k_w)$, we separate the decay rates of the low (l) and high (h) frequency branch (see Fig. 3.2b) obtained from the diagonal components of Eq. (3.63) into vectors $\vec{\gamma}_{l,h}(k_w)$. For non-zero k_w, $\gamma_i(k_w)$ is largest for the large normal mode frequencies of each band (orange and turquoise respectively) in Fig. 3.4a for $f = 0.01$ and Fig. 3.4b for $f = 0.75$ respectively. Increasing f leads to enormously large damping rates for large k_w-modes (Fig. 3.4), i.e. extremely strong coupling to the heat bath, which fixes the expectation value of the normal mode to the one determined by the heat bath, weak driving of the corresponding normal modes only leads to a negligible perturbation.

[12] Assuming γ_h to be the dominating decay mechanism, such that it is larger or equal then in-plane dissipation characterised by decay rate γ_c ($\frac{\gamma_{ab}}{\gamma_h} = \frac{\gamma_{ab}}{\gamma_c}\frac{\gamma_c}{\gamma_h} \leq \frac{\gamma_{ab}}{\gamma_c}$). The ratio of in-plane σ_{ab} to out of plane



(a) $f = 0.01$ *(b)* $f = 0.75$

Figure 3.4: Damping rate $\gamma_{l,h}(k_w)$ of the low and high-frequency branch obtained from Eq. (3.63) and Eq. (3.64) for different magnitude of the in-plane dissipation as characterised by f (defined below Eq. (3.64)) of the different normal modes as a function of wavenumber $w = k_w L/\pi$. Color coding from Fig. 3.2b with blue and turquoise (red and orange) respectively damping rates of the lowest and highest normal mode frequency of the low (high) frequency branch (length $L_0 = 0.5$, $\alpha_1 = 0.28$, $\alpha_2 = 0.66$, $n_{\text{junc}} = 10$). For non-zero k_w, $\gamma_i(k_w)$ is largest for the large normal mode frequencies of each band (orange and turquoise respectively).

Noise in real space Combining Eq. 3.36 for spatially independent driving ($k_d = 0$), with the thermal noise and dissipation processes transformed to real space, we obtain the full equation of motion

$$\partial_\tau^2\vec{\phi} + \vec{\zeta}(\tau) + d(\partial_\tau\vec{\phi}) = -\boldsymbol{\mathcal{P}}^C(\tau)\left[(\mathbf{I}+\mathbf{A}(\tau))\sin\left(\vec{\phi}\right) - j_{\text{bias}}\left(\boldsymbol{\mathcal{J}}^C\right)^{-1}\right] - \boldsymbol{\gamma}_{disp}(\tau)\frac{\mathrm{d}\vec{\phi}}{\mathrm{d}\tau} + \boldsymbol{\mathcal{P}}^L(\tau)\partial_x^2\vec{\phi}, \tag{3.65}$$

where

$$\vec{\zeta}(\tau) = \sum_w \mathbf{P}_w \vec{\xi}_w(\tau)\cos(k_w x). \tag{3.66}$$

is obtained from the thermal noise characterised by Eq. (3.62) and

$$d(\partial_\tau\vec{\phi}) = \sum_w \mathbf{P}_w \boldsymbol{\Upsilon}_w \mathbf{P}_w^{-1}\mathrm{dct}(\partial_\tau\vec{\phi})_w\cos(k_w x), \tag{3.67}$$

from the decay rate (Eq. (3.63)), where $\mathrm{dct}(A)_w$ is the wth amplitude of a discrete cosine series, i.e. $\sum_w \mathrm{dct}(A)_w\cos(k_w x) = A(x)$.

For an infinitely thin junction, Eq. (3.65) simplifies to

$$\frac{d}{d\tau}\left[(\boldsymbol{\mathcal{C}}(\tau)\boldsymbol{\alpha}\boldsymbol{\mathcal{D}})^{-1}\frac{d\vec{\phi}}{d\tau}\right] + (\boldsymbol{\mathcal{C}}(\tau)\boldsymbol{\alpha}\boldsymbol{\mathcal{D}})^{-1}\left[\vec{\zeta}(\tau) + d(\partial_\tau\vec{\phi})\right]$$
$$= -\boldsymbol{\mathcal{J}}^C(\mathbf{I}+\mathbf{A}(\tau))\sin\left(\vec{\phi}\right) + \vec{j}_{\text{bias}} + \frac{\gamma^4\gamma_d}{\gamma_c^2}\boldsymbol{\mathcal{L}}^{-1}\partial_x^2\vec{\phi}, \tag{3.68}$$

conductivity σ_c as $\frac{\gamma_{ab}}{\gamma_h} \approx \frac{\sigma_{ab}}{\sigma_c}\frac{\epsilon_c}{\epsilon_{ab}}$. The ratio $\frac{\sigma_{ab}}{\sigma_c}$ can be estimated as superconducting anisotropy squared, γ^2 [255, 261] leading to $\frac{\gamma_{ab}}{\gamma_c} \approx \gamma^2\frac{\epsilon_c}{\epsilon_{ab}}$.

with dimensionless capacitive coupling matrix $\boldsymbol{\mathcal{C}}(\tau) = \boldsymbol{\alpha}^{-1}(\boldsymbol{\epsilon}(\tau)/\epsilon)^{-1} - \boldsymbol{\Delta}$.

Numerically propagating the full non-linear equation from Eq. (3.65) or Eq. (3.68) is computationally expensive due to the combination of mode-dependent damping, noise and non-linearity.

3.4 Parametric cooling of long Josephson Junctions

Opto-mechanical cooling can be explained in a purely classical framework. However, using a discussion in terms of quantised fields as in Sec. 2.1.1 is instructive and allows us to recycle the expressions for cooling limits derived there. We emphasise that for the temperatures considered here, no quantum mechanical description is required, as the phase dynamics of HTSC junction is usually well described by classical physics and we only consider the classical limits of the resulting equation.

3.4.1 Quantisation of the linearised Hamiltonian

For sufficiently low temperature and strong bias currents, macroscopic tunnelling and quantisation have been observed in intrinsic Josephson junctions [64–66]. These observations have stimulated research regarding the quantisation of the phase in intrinsic Josephson Junctions. Savelev et al. [67] study the quantisation of short junctions in terms of gauge invariant phase difference and in-plane screening current, where the problem of macroscopic tunnelling reduces to the tunnelling of a quantum particle through a potential barrier (see Sec. 3.1.3). Sboychakov et al. [281, 282] develop a proper field-theoretical approach, to quantise the dynamics of the spatially dependent phase difference in a single long Josephson junction. Phase fluctuations around a minimum are decomposed into various orthogonal spatial modes, which are quantised into multiple bosonic modes. We follow a combination of the approaches from Ref. [67, 281, 282]. Due to the adiabatic elimination of the screening current in Sec. 3.1.3, we can describe the dynamics in terms of a single spatially dependent field as in Ref. [281, 282]. The phase fluctuation around a potential minimum can be consistently quantised in terms of multiple independent spatial modes and normal modes of the stack. This way, we take into account both the spatial dependence and the complexity arising from considering a stack of junctions.

Here, we only consider the quantisation of a time-independent problem, which means that we are using the quantisation in terms of the creation and annihilation operators of the time-averaged Hamiltonian[13].

[13]The quantisation of a similar time-dependent problem, i.e. an optomechanical Hamiltonian for a cavity field in the presence of time-dependent permittivity and moving mirror, is studied in Ref. [170] (see also discussion at the end of Sec. 3.1.4). The effective Hamiltonian is expressed in terms of instantaneous modes leading to the instantaneous creation and annihilation operators. These modes $\phi_n(x;t)$ are orthogonal with respect to a time-dependent permittivity $\epsilon(x,t)$ as a metric, i.e. $\int dx \epsilon(x,t)\phi_n(x;t)\phi_m(x;t) = \delta_{n,m}$ (see Eq. (2.9) in Ref. [170]). The corresponding time-dependent creation and annihilation operators can be expanded in terms of the creation and annihilation operators of the time-averaged model, which is the procedure implicitly used to motivate the standard form of the optomechanical Hamiltonian for weak driving

Time-dependent current density We first focus on driving arising purely from a time-dependent critical current, i.e. $\nu_{1,2}=0$ and $A_{1,2}\neq 0$ the Hamiltonian of the k_w in-plane momentum is already of the form given in Eq. (3.70) using the identification $\mathbf{m}_w(\tau)=\bar{\mathbf{m}}^i_w$, $\mathbf{K}_w(\tau)=\boldsymbol{\mathcal{K}}_w(\tau)$, $\vec{\mathfrak{p}}_w=\vec{\mathfrak{P}}_w$ and $\vec{q}_w=\vec{Q}_w$, where we assumed the absence of a bias current applied across the junctions such that $\vec{\phi}_0=0$ and the third term in Eq. (3.50) is zero. Using the same quantisation as for time-dependent permittivity, the coupling coefficients of the two coupled normal modes are given by

$$\Lambda_{rs}=\frac{1}{2}\frac{1}{2^2}\frac{\left(\mathbf{P}_w^\top\cos\boldsymbol{\phi}_0\boldsymbol{\mathcal{J}}^C\mathbf{A}\mathbf{P}_w\right)_{g^j_w(r)g^j_w(s)}}{\sqrt{m_r m_s\Omega_r\Omega_s}}, \tag{3.69}$$

with $r,s\in l,h$ and the pair of coupled normal modes with frequencies $(\vec{\Omega}_{g^j_w(l)},\vec{\Omega}_{g^j_w(h)})$ are abbreviated as (Ω_l,Ω_h) and masses $m_n=\left(\bar{\mathbf{m}}^i_w\right)_{g^j_w(n),g^j_w(n)}$ for $n=l,h$ with $\boldsymbol{\phi}_0=0$.

Time-dependent permittivity The driving arises purely from a time-dependent permittivity $\boldsymbol{\epsilon}(t)$ ($\nu_{1,2}\neq 0$ and $A_{1,2}=0$). In order to simplify the comparison with Ref. [31] (see Sec. 2.1.3) and the opto-mechanical Hamiltonian (Eq. 2.5) and get a better physical intuition, we perform a canonical transformation to new momenta $\vec{\mathfrak{p}}_w=-\bar{\mathbf{m}}^i_w\boldsymbol{\Omega}(k_w)\vec{Q}_w$ and positions $\vec{q}_w=(\bar{\mathbf{m}}^i_w)^{-1}\boldsymbol{\Omega}^{-1}(k_w)\vec{\mathfrak{P}}_w$, effectively swapping the role of momentum and position in Eq. (3.50) leading to

$$\mathcal{H}_w=\frac{1}{2}\vec{\mathfrak{p}}_w^\top(\bar{\mathbf{m}}^i_w)^{-1}\vec{\mathfrak{p}}_w+\frac{1}{2}\vec{q}_w^\top\mathbf{K}_w(\tau)\vec{q}_w, \tag{3.70}$$

where $\mathbf{K}_w(\tau)=\boldsymbol{\Omega}(k_w)\bar{\mathbf{m}}^i_w\mathbf{m}_w(\tau)^{-1}\bar{\mathbf{m}}^i_w\boldsymbol{\Omega}(k_w)$ is the new time-dependent spring constant, which can be approximated as $\mathbf{K}_w(\tau)=\bar{\mathbf{m}}^i_w\boldsymbol{\Omega}^2(k_w)-\cos\left(\frac{2\omega_d}{\omega_p}\tau\right)\boldsymbol{\Omega}(k_w)\mathbf{m}^t_w\boldsymbol{\Omega}(k_w)+O(\nu^2)$.

All bilayer unit cells of the stack are driven in phase with respect to each other as the wavelength of the external laser pulse is much larger then the unit-cell of the material. Inside one unit cell, the driving amplitudes of the two physical junctions, $\nu_{1,2}$ and $A_{1,2}$, can, however, differ for the two types of driving depending on the phonon mode excited. As each unit-cell along the stack is driven in-phase, the driving conserves longitudinal momentum q_z from Sec. 3.2.1 and only couples normal mode with the same longitudinal momentum $q_z=0$ such that the matrix $\boldsymbol{\Omega}(k_w)\mathbf{m}^t_w\boldsymbol{\Omega}(k_w)$ has only one large off-diagonal entry per column or row. For a stack of n_{junc} junctions, this structure allows use to decompose the normal mode Hamiltonian for small fluctuations from Eq. (3.70) into $n_{\text{junc}}/2$ formally equivalent subspaces for each in-plane momentum k_w.

The total Hamiltonian for normal modes with in-plane momentum k_w can be decomposed into $n_{junc}/2$ subspace Hamiltonians as

$$\mathcal{H}_w=\mathcal{H}^{(1)}_w\otimes\mathcal{H}^{(2)}_w\otimes\ldots\otimes\mathcal{H}^{(n_{junc}/2)}_w, \tag{3.71}$$

where $\mathcal{H}^{(j)}_w$ acts only on the subspace of the jth pair of normal modes with in-plane momentum k_w. Each of the $\mathcal{H}^j_w$ has the form of two parametrically modulated coupled time-dependent spring constants as studied in Sec. 2.1.3. The whole Hamiltonian structure is shown in schematically in Fig. 3.5.

in Sec. 2.1.1.

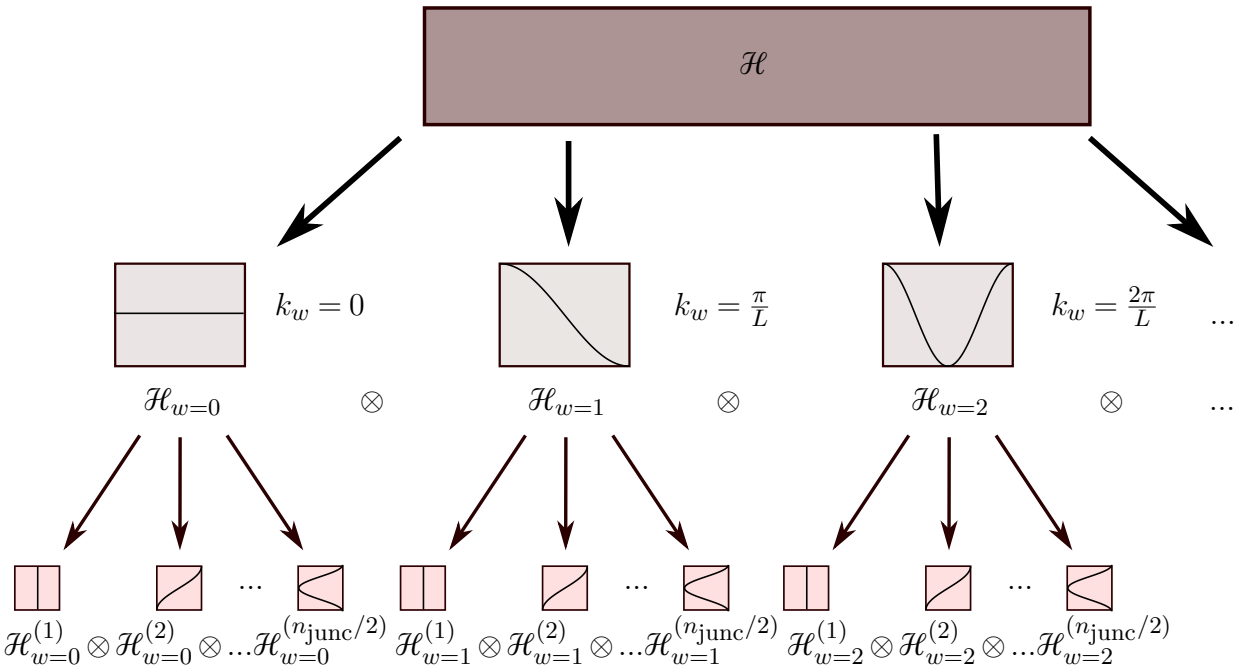


Figure 3.5: Decomposition of the linearised Hamiltonian into subspaces for each in-plane momentum k_w (see Eq. (3.43)). The corresponding spatial modes are sketched in the grey boxes. Each of those is decomposed into subspaces containing coupled low and high frequency mode of the two frequencies bands (see Eq. (3.71)). For infinitely long stacks this decomposition corresponds to a decomposition according to out-of-plane momentum q_z as sketched in the pink boxes in the lowest row.

Thus, we have extended the two-junction model from Sec. 2.1.3 to stacks of long junctions (Fig. 3.1). Their normal modes, however, decompose into multiple pairs of low and high-frequency modes of distinct frequencies and coupling strength for each spatial mode of frequency.

The mapping of the normal modes from the full Hamiltonian to the decomposed one given in Eq. 3.71 can be done using an indexing function $g^j_w(n)$, which gives the index of the the low $n = l$ and high frequency mode $n = h$ of the jth pair for wavenumber w in the full Hilbert space. To avoid clutter, we refer to the normal mode frequencies of the jth pair of momentum k_w, that is $(\vec{\Omega}_{g^j_w(l)}, \vec{\Omega}_{g^j_w(h)})$ simply as (Ω_l, Ω_h). As conjugate dynamical variables for the Hamiltonian formulation of the theory, we can promote the coordinates to operators with implicit w dependence (see Ref. [263]), i.e. $(q_w)_{g^j_w(n)} \to \hat{q}_n$ and $(\mathfrak{p}_w)_{g^j_w(n)} \to \hat{\mathfrak{p}}_n$ for $n = l, h$ corresponding to the low-frequency and high-frequency component with $[\hat{\mathfrak{p}}_r, \hat{\mathfrak{q}}_s] = -\mathrm{i}\delta_{rs}\hbar\omega_p/E_J$, where the unconventional commutation relations stem from the

normalisation, we can define the following ladder operators

$$a = \sqrt{\frac{m_l\Omega_l}{2}}\left(\hat{q}_l + \mathrm{i}\frac{\hat{\mathfrak{p}}_l}{m_l\Omega_l}\right) \tag{3.72}$$

$$a^\dagger = \sqrt{\frac{m_l\Omega_l}{2}}\left(\hat{q}_l - \mathrm{i}\frac{\hat{\mathfrak{p}}_l}{m_l\Omega_l}\right) \tag{3.73}$$

$$b = \sqrt{\frac{m_h\Omega_h}{2}}\left(\hat{q}_h + \mathrm{i}\frac{\hat{\mathfrak{p}}_h}{m_h\Omega_h}\right) \tag{3.74}$$

$$b^\dagger = \sqrt{\frac{m_h\Omega_h}{2}}\left(\hat{q}_h - \mathrm{i}\frac{\hat{\mathfrak{p}}_h}{m_h\Omega_h}\right), \tag{3.75}$$

where the masses are abbreviated as $m_n = \left(\bar{\mathbf{m}}_w^i\right)_{g_w^j(n),g_w^j(n)}$ for $n = l, h$. The quantised Hamiltonian is of a similar form as in optomechanics, i.e.

$$\begin{aligned}\mathscr{H}_w^{(j)} = \Omega_l\left(a^\dagger a + \frac{1}{2}\right) + \Omega_h\left(b^\dagger b + \frac{1}{2}\right)\\ - \cos\left(\frac{2\omega_d}{\omega_p}\tau\right)\left[2\Lambda_{lh}\left(a+a^\dagger\right)\left(b+b^\dagger\right) + \Lambda_{ll}\left(a+a^\dagger\right)^2 + \Lambda_{hh}\left(b+b^\dagger\right)^2\right],\end{aligned} \tag{3.76}$$

where the last three terms contain different elements of the real coupling coefficient

$$\Lambda_{rs}^2 = \frac{1}{2^4}\frac{\left(\mathbf{m}_w^t\right)_{g_w^j(r)g_w^j(s)}\left(\mathbf{m}_w^t\right)_{g_w^j(s)g_w^j(r)}}{m_r m_s}\Omega_r\Omega_s, \tag{3.77}$$

with $r, s \in \{l, h\}$ and $\mathbf{m}_w^t$ the amplitude matrix for the time-dependent part of the mass matrix transformed to the normal mode frame for in-plane momentum k_w. Assuming the driving frequency is approximately $2\omega_d/\omega_p \approx \Omega_h - \Omega_l$, the counter-rotating terms ab and $a^\dagger b^\dagger$ and any other time-dependent terms as aa can be eliminated by a rotating wave approximation. Ignoring the zero-point energy, the subspace Hamiltonian for a pair of normal modes driven on its cooling sideband becomes

$$\mathscr{H}_w^{(j)} \approx \Omega_l a^\dagger a + \Omega_h b^\dagger b - \left(\Lambda(\tau)a^\dagger b + \Lambda^*(\tau)ab^\dagger\right), \tag{3.78}$$

where $\Lambda(\tau) = \Lambda_{lh}\exp\left(\mathrm{i}2\omega_d\tau/\omega_p\right)$ with real $\Lambda_{lh} = \Lambda_{hl}$.

Both harmonic oscillators are connected to their corresponding heat baths at decay rates $\gamma'_{l,h}$ (see panel iii) in Fig. 2.3 with $\gamma_{l,h}$ replaced by $\gamma'_{l,h}$), which, unless $k_w = 0$, differ from $\gamma_{l,h}$ due to in-plane dissipation (see Sec. 3.5.1). The high frequency mode has negligible thermal occupation at the relevant temperatures. By resonant driving at the frequency difference, $2\omega_d/\omega_p = \Omega_h - \Omega_l$, energy can be pumped from the low-frequency mode to the high-frequency mode in the system (see Appendix B.6).

As the linearised Hamiltonian in the normal mode frame (Eq. (3.50)) is of the same form as in Sec. 2.1.3, we can use the analytic cooling rates to study the general parameter dependence for both time-dependent permittivity and critical current density for a wide range of parameters and driving arrangements.

3.4.2 Analytical cooling rate and ratio

According to the washboard picture from Fig. 1.2, the dynamics of a short Josephson junction can be described by a fictitious phase particle. Thermal fluctuations of the phase can excite the particle out of the trapping potential, resulting in a transition from a superconducting into a resistive state. Here, we are going to briefly summarise the analytical cooling ratio derived in Sec. 2.1.3. Equation (3.76) is formally equivalent to the linearised optomechanical Hamiltonian [158] obtained for small fluctuations around the coherent state of a laser field from Eq. (2.5). He, we consider both oscillators to be coupled to their own Markovian reservoir with their relaxation rates ${\gamma'_{l,h}}^{-1}$ as shown in panel iii) of Fig. 2.1.3 similar to the cavity and mechanical oscillator in Sec. 2.1.1 (see discussion around Eq. 2.43)). The parametric cooling process can be understood as a resonant energy transfer between the two harmonic oscillators [31, 283]. For resonant driving, i.e. $2\omega_d/\omega_p = \Omega_h - \Omega_l$, quanta in the low-frequency oscillator Ω_l combine with quanta of the drive $2\omega_d$ to excite quanta in the high-frequency oscillator Ω_h.

For the present HTSC model, the frequency difference is around 10, and the thermal occupation of the high-frequency mode cannot be ignored on the cooling timescales. The solution obtained from a master equation approach, therefore, accounts for the very small thermal occupation of the high-frequency mode. The cooling ratio $R^{(j,l)}(w)$ of the low frequency mode of the jth pair with in-plane momentum k_w is given by (Eq. (2.46) with ${}^{n(\Omega_h)}/_{n(\Omega_l)} \to {}^{\Omega_l}/_{\Omega_h}$ in the classical limit)

$$R^{(j,l)}(w) = \frac{\langle (\vec{Q}_w)^2_{g^j_w(l)} \rangle_{\tau\to\infty}}{\langle (\vec{Q}_w)^2_{g^j_w(l)} \rangle_{\tau=0}} = 1 - \eta \left(1 - \frac{\Omega_l}{\Omega_h}\right), \tag{3.79}$$

where the cooling strength is characterised by a Lorentzian (Eq. (2.48))

$$\eta = \frac{\Lambda^2_{lh} \left(\gamma'_h + \gamma'_l\right)/\gamma'_l}{\Delta\omega^2_{\text{diff}} + \left(\frac{\Lambda}{2}\right)^2}, \tag{3.80}$$

as a function of detuning $\Delta\omega_{\text{diff}} = 2\omega_d/\omega_p - (\Omega_h - \Omega_l)$ from the cooling sideband with width

$$\Lambda = \sqrt{\frac{\left(\gamma'_h + \gamma'_l\right)^2 \left(4\Lambda^2_{lh} + \gamma'_h\gamma'_l\right)}{\gamma'_h\gamma'_l}}. \tag{3.81}$$

The lower bound for the linewidth $\gamma'_h + \gamma'_l$ is dominated by the dissipation rates for weak coupling, and proportional to Λ_{lh} for strong coupling. The corresponding cooling rate is $\gamma_d = \gamma'_l + \frac{\Lambda^2_{lh}}{\gamma'_h - \gamma'_l} + O(\Lambda^3_{lh})$. For parameters such that $\gamma'_h > \gamma'_l$, the relaxation to the steady-state position is enhanced by the driving.

The expression for the cooling ratio is only valid if the terms dropped in the rotating wave approximation can be ignored for all pairs of coupled normal modes, i.e. this is the case in the present study.

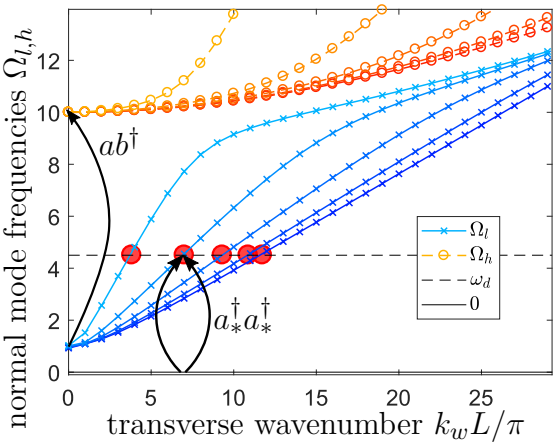


Figure 3.6: Normal mode frequencies as a function of wavenumber $w = k_w L/\pi$ for in-plane momentum k_w for a stack of ten junctions of length $L = 0.5$ (factor of ten smaller then in Fig. 3.2b) with the different normal mode frequencies of the two bands given by crosses and circles respectively. The large arrow indicates a transition of the type $ab^\dagger$ from a low frequency mode with normal mode frequency $\vec{\Omega}_{g^j_{w\sim 0}(l)}$ to a high frequency mode with normal mode frequency $\vec{\Omega}_{g^j_{w\sim 0}(h)}$ belonging to the high frequency band due to driving on the cooling sideband $2\omega_d = \vec{\Omega}_{g^j_{w\sim 0}(h)} - \vec{\Omega}_{g^j_{w\sim 0}(l)}$. The horizontal black dashed line is guide to the eye to identify potentially critical modes (red circles) occurring at intersection $\vec{\Omega}^*_{g^{j'}_{w'}(l)} \approx \omega_d$. The creation of pairs associated with $a_*^\dagger a_*^\dagger$ is indicated by two shorter arrows from 0.

3.4.3 Heating due to resonance catastrophes

Above we discussed the cooling limit for one pair of normal modes. However, all of the pairs share a common driving frequency ω_d, which can be made explicit by adding the argument $\mathcal{H}_w^{(j)} \to \mathcal{H}_w^{(j)}(\omega_d)$, such that Eq. (3.71) becomes

$$\mathcal{H}_w = \mathcal{H}_w^{(1)}(\omega_d) \otimes \mathcal{H}_w^{(2)}(\omega_d) \otimes \ldots \otimes \mathcal{H}_w^{(n_{junc}/2)}(\omega_d). \tag{3.82}$$

When increasing the junction size, the normal mode structure becomes more densely spaced and in general a single frequency ω_d can only drive the cooling sideband of at most a subgroup of pairs, but will be off-resonant for all other pairs, such that the RWA, leading to Eq. (3.78), is only justified for the subgroup of pairs for which $2\omega_d/\omega_p \approx \Omega_h - \Omega_l$. Other terms of the model Hamiltonian given in Eq. (3.76) can become resonant for all pairs due to the cooling of another pair of normal modes (see Fig. 3.6). The other terms contributing to the dynamics of the jth mode, which could be ignored previously in a rotating wave approximation valid for $2\omega_d/\omega_p \approx \Omega_h - \Omega_l$, are:

(i) For $\omega_d \approx \Omega_r$ with $r = l, h$, diagonal components of the coupling matrix in Eq. (3.76) become resonant, which are respectively given by

$$\mathcal{H}_w^{(j)} \approx -\cos\left(2\omega_d \tau/\omega_p\right)\Lambda_{ll}(a + a^\dagger)^2, \tag{3.83}$$

and

$$\mathcal{H}_w^{(j)} \approx -\cos\left(2\omega_d \tau/\omega_p\right)\Lambda_{hh}(b + b^\dagger)^2. \tag{3.84}$$

For resonant driving $\omega_d/\omega_p = \Omega_l$ terms such as $aa^\dagger$ and $a^\dagger a$ can be eliminated through a rotating wave approximation (correspondingly for Eq. (3.84) when we replace $a \to b$ and $\Omega_l \to \Omega_h$). Going into the rotating frames Eq. (3.83) (Eq. (3.84)) becomes identical to the parametric down conversion Hamiltonian given in Eq. (2.52). In Sec. 2.2.1, we show that in the presence of dissipation parametric instability can be suppressed it the dissipation is large enough. This is the main assumption we have to make in order to observe a cooling effect despite the presence of parametric instabilities at the same driving frequency. In this case the driving only leads to a finite increase of the thermal occupation of the respective normal mode $r = l, h$ belonging to the jth pair, which from Eq. (2.53) is given by

$$R^{(j,r)}_{\text{single}}(w) = \frac{\gamma'^2_r n(\Omega_r) + 2\Lambda^2_{rr} + 4n(\Omega_r)\Delta^2}{\gamma'^2_r - 4\Lambda^2_{rr} + 4\Delta^2}, \tag{3.85}$$

The heating only depends on the driving to damping ratio Λ_{ii}/γ_i with detuning $\Delta = \Omega_r - \omega_d$ and Boltzmann occupation factor $n(\Omega_r)$ with $r \in \{l, h\}$. For resonant driving $\omega_d/\omega_p = \Omega_{l,h}$, if the oscillator is connected so strongly to the bath that energy introduced by the driving mechanism is quickly dissipated away, i.e. $\gamma_i^2 > 4\Lambda_{ii}^2$ with $i = l, h$, a steady state can be achieved. Otherwise, if the driving is stronger then the disipation, the drive can increase the thermal occupation of the oscillator indefinitely. For driving on a higher resonance, i.e. $2\omega_d/\omega_p = \Omega_{l,h}$, Eq. (3.83) and Eq. (3.84) can lead to an enhanced effective Josephson coupling as studied in Ref. [43, 45] discussed in Sec. 2.2.2.

(ii) Off-diagonal components of the coupling matrix belonging to counter-rotating terms in Eq. (3.76), i.e. contributions from

$$-\cos\left(2\omega_d\tau/\omega_p\right)2\Lambda_{lh}(ab + a^\dagger b^\dagger). \tag{3.86}$$

These terms are resonantly excited for $2\omega_d/\omega_p = \Omega_l + \Omega_h$ and are associated with the heating sideband (discussed in Sec. 2.2.1, see Eq. (B.113)), where the drive excites the thermal occupation in both modes.

Terms of the form given in Eq. (3.86) are sufficiently far off-resonant to be ignored (see Fig. B.1). Therefore, the analytic expression for the cooling ratio agrees with the one obtained from the steady state of the linearised Eq. (3.65) in the low temperature, which is also confirmed numerically (see Fig. 3.14).

However, terms of the form given in Eq. (3.83) corresponding to a single parametrically driven harmonic oscillator can in general not be ignored, the associated resonance catastrophes are only suppressed by the larger damping rates of the corresponding modes due to in-plane dissipation (see Sec. 3.1.3 and Sec. 2.2.1). An exemplary situation is depicted in Fig. 3.6, where the monochromatic drive is tuned to the cooling sideband $2\omega_d = \vec{\Omega}_{g^j_{w\sim 0}(h)} - \vec{\Omega}_{g^j_{w\sim 0}(l)}$ of a coupled pair $(\vec{\Omega}_{g^j_{w\sim 0}(l)}, \vec{\Omega}_{g^j_{w\approx 0}(h)})$. The corresponding transition is indicated by the large black arrow in Fig. 3.6 corresponding to a transition between low momentum modes ($k_w \sim 0$). However, if $2\omega_d/\omega_p \approx 2\vec{\Omega}^*_{g^{j'}_{w'}(l)}$, the same driving frequency can become resonant with terms of the form Eq. (3.83) for another mode $\vec{\Omega}^*_{g^{j'}_{w'}(l)}$. Different

candidates for such a critical resonantly driven mode are highlighted by the red circles in Fig. 3.6. The corresponding transition is exemplary indicated by the two small black arrows in Fig. 3.6 at $k_{w'} \neq 0$. These types of resonances can in general not be avoided for long junctions with sufficiently smooth frequency dispersion curve or large stack sizes, where low-frequency modes branch out from the lower frequency band (see Fig. 3.2). These critical resonantly driven normal modes only have a steady state if the driving is sufficient weak in comparison to the damping rate $2\Lambda^*_{ll}(k_w) < \gamma^*_l(k_w)$ or the detuning is large enough (see Eq. (3.85)). If the material has very large damping rates γ^* for $k_w \neq 0$ due to in-plane dissipation and the driving scheme is chosen such that these modes are not driven strongly, it is possible to satisfy this requirement for all critical modes. As the corresponding critical modes are approximately a factor of 4.5 larger then the smallest normal mode frequencies $\min(\vec{\Omega})$, i.e. $\vec{\Omega}^*_{g^{j'}_{w\neq 0}(l)} \approx 4.5\min(\vec{\Omega})$ and they are already sufficiently high-frequency that their thermal occupation is relatively and any small heating effect can remain insignificant, e.g. a correction of the order $1/4.5^2$.

3.5 Simulations

3.5.1 Simplified linearised model

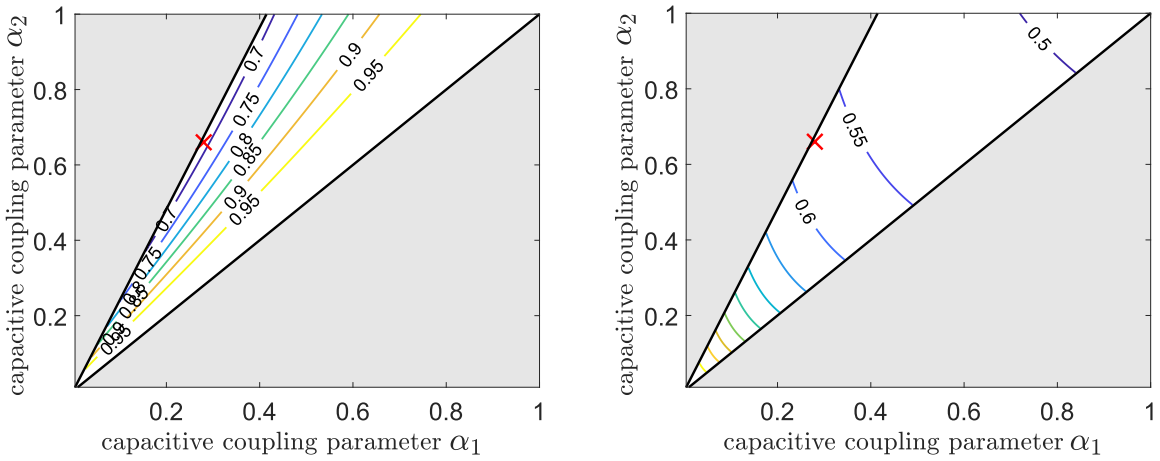
In the first part of this subsection, we study the cooling ratio of the phase quadrature of a short two-junction toy model as a function of capacitive coupling, damping rates and driving arrangement. We next study the cooling ratio obtained from the linearised regime given in Eq. (3.79) for different spatial modes with finite in-plane momentum in a finite stack of long junctions. To address all thermally occupied normal modes we replace the monochromatic driving pulse by a broadband pulse.

Individually addressable cooling sidebands To approximate the total cooling efficiency achievable in the presence of a broad band pulse, we assume that all modes have a narrow response to only a single monochromatic frequency tuned to their respective cooling sideband, i.e. the driving frequency for the jth mode is $2\omega_d^{(w,j)}/\omega_p = \vec{\Omega}_{g^j_w(h)} - \vec{\Omega}_{g^j_w(l)}$. In this case, the total Hamiltonian (3.82) can be approximated by individually addressable subspaces schematically shown in Fig. 3.5, i.e.

$$\mathcal{H}_w = \mathcal{H}_w^{(1)}(\omega_d^{(w,1)}) \otimes \mathcal{H}_w^{(2)}(\omega_d^{(w,2)}) \otimes ... \otimes \mathcal{H}_w^{(n_{junc}/2)}(\omega_d^{(w,n_{junc}/2)}). \tag{3.87}$$

This assumption of individual addressability requires the difference between $2\omega_d^{(w,j')}$ and $2\omega_d^{(w,j)}$ to be smaller then the linewidth of the driving response from Eq. (2.49) with the exact value depending on the driving strength. The cooling ratios obtained from this approximation provides an upper bound for the total cooling ratio with regard to additional slightly off-resonant driving. This is only valid in the absence of resonance catastrophes, which affect a few isolated modes shown in Fig. B.1, and strongly off-resonant driving of other normal modes. When concentrating on a specific subspace, we refer to the normal mode frequencies of the jth pair of momentum k_w, that is $(\vec{\Omega}_{g^j_w(l)}, \vec{\Omega}_{g^j_w(h)})$ simply as (Ω_l, Ω_h).

The splitting into subspaces from Fig. 3.5 survives for increasing k_w for $\epsilon(t)$-Model, though it breaks down for $J^C(t)$-Model for large k_w due to an overall decrease in the driving amplitude with increasing k_w in this case we restrict ourselves to two junction toy models.



(a) $\epsilon(t)$-Model from Eq. (3.32) with driving amplitudes $\nu_1 = 0$, $\nu_2 = 0.1$

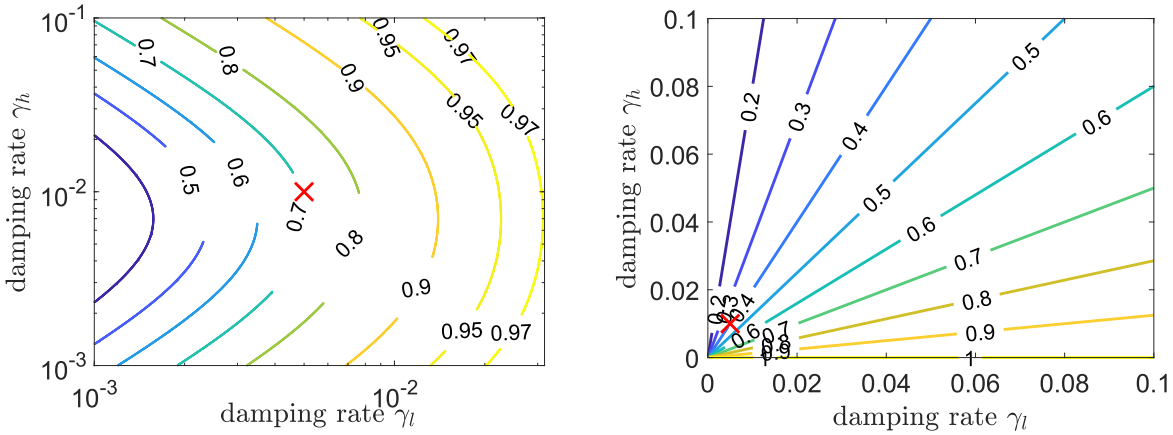
(b) $J^C(t)$-Model from Eq. (3.28) with driving amplitudes $A_1 = 0.15$, $A_2 = -0.15$

Figure 3.7: $\alpha_{1,2}$ dependence of the cooling ratio $R^{(1,l)}(0)$ from Eq. (3.79) of a two-junction toy model for **(a)** $\epsilon(t)$-Model from Eq. (3.32) **(b)** $J^C(t)$-Model from Eq. (3.28). Red crosses indicate $\alpha_1 = 0.28$, $\alpha_2 = 0.66$. The two grey triangular regions outside the black boundary are associated with non-physical values of $\alpha_{1,2}$ due to condition given in Eq. (3.52) (damping rates $\gamma_l = 0.005$, $\gamma_h = 0.01$).

Importance of capacitive coupling for short junctions The low-frequency band from Fig. 3.2 of the $k_w = 0$ mode has the highest thermal occupation (see discussion below Eq. (3.62)). Consequently, achieving a significant cooling efficiency in short junctions, where only the $k_w = 0$ mode is thermally occupied, is a prerequisite for the efficient cooling of long junctions.

We notice that the cooling of the spatially homogeneous mode corresponding to $k_w = 0$ is impossible in the absence of capacitive coupling, i.e. $\alpha_{1,2} \to 0$, as both mass matrix $\boldsymbol{\mathcal{M}}^{\phi}(\tau)$ and spring constant $\boldsymbol{\mathcal{K}}_0(\tau)$ from Eq. (3.45) are diagonal such that the off-diagonal elements of the coupling matrix Λ_{lh} are zero. In this case, any type of driving only leads to the diagonal parametric modulations of the form given in Eq. (3.83) and (3.84).

For $\epsilon(t)$-Mode from Eq. (3.32), the smallest cooling ratios $R^{(1,l)}(0)$ from Eq. (3.79) are achieved for a non-zero $\alpha_{1,2}$ close to the boundary $\alpha_2 \approx \alpha_1 D_l/D_h$ as shown in Fig. 3.7a, while for $J^C(t)$-Model from Eq. (3.28), the $\alpha_{1,2}$ dependence is more symmetric and maximised for large values of $\alpha_{1,2}$ as shown in Fig. 3.7b. The grey area corresponds to the restrictions on $\alpha_{1,2}$ given in Eq. (3.52) due to the assumption of identical superconducting sheets. In the following we use $\alpha_1 = 0.28$ and $\alpha_2 = 0.66$ as indicated by the red crosses in both Fig. 3.7a and Fig. 3.7b. This choice of $\alpha_{1,2}$ leads to relatively small coupling rates of $\Lambda_{lh}/\Omega_l \approx 0.004$ for $\epsilon(t)$-Model with driving amplitude $\nu_{1,2} = \pm 0.1$ and coupling rates of $\Lambda_{lh}/\Omega_l \approx 0.006$ for $J^C(t)$-Model with driving amplitudes $A_1 = -A_2 = 0.15$.



(a) $R^{(1,l)}(0)$ from Eq. (3.79) for $\epsilon(t)$-Model from Eq. (3.32) ***(b)*** Strong driving limit $R_{\text{strong}}(\gamma_l, \gamma_h)$ from Eq. (3.88)

Figure 3.8: Damping rate $\gamma_{l,h}$-dependence of the cooling ratio $R^{(1,l)}(0)$ obtained from Eq. (3.79) for a two junction toy model for **(a)** intermediate driving of $\epsilon(t)$-Model from Eq. (3.32)) with $\nu_1 = 0$ and $\nu_2 = 0.1$ **(b)** strong driving limit $\Lambda_{lh}^2 \gg \gamma_l\gamma_h/4$. The red cross indicates damping rates $\gamma_l = 0.005$ and $\gamma_h = 0.01$, which lead to a significant cooling already in the weak driving regime. **(a)** shows that an optimal value of γ_h for laser cooling exist, while a small γ_l is preferable. **(b)** $\gamma_{l,h}$ dependence of the cooling ratio $R^{(1,l)}(0)$ as obtained from Eq. (3.88) in the strong driving limit (capacitive coupling parameter $\alpha_1 = 0.28$, $\alpha_2 = 0.66$).

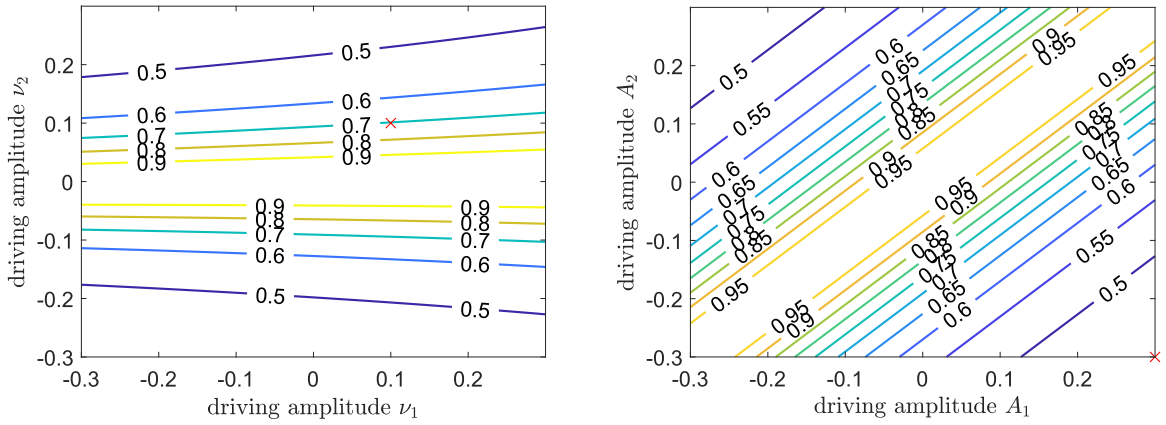
Homogeneous damping rates In absence of dissipation, the driving would periodically transport energy quanta back and forth between the high-and low-frequency mode, just as in Rabi oscillations. Dissipation introduces irreversibility into the system and allows for a net energy transfer from the low to the high-frequency junction. In Fig. 3.8a, the analytical cooling ratio $R^{(1,l)}(0)$ of the spatially uniform mode ($k_w = 0$) from Eq. (3.79) is shown as a function of the damping rates $\gamma_{l,h}$ of a two junction toy model. The driving strength is only intermediate, i.e. $\Lambda_{lh}^2 \sim \gamma_l\gamma_h/4$. A small γ_l is found to improve the cooling efficiency, as it ensures the coherence of the energy transport out of the low-frequency mode. As the noise effectively acts as a measurement [284], large dissipation disrupts the coherent transfer of the energy quanta to the high-frequency mode. The damping rate of the high-frequency mode γ_h is found to have an optimal value of approximately $\gamma_h \approx 0.01$ in this parameter regime. This optimal value corresponds to a sweet spot, where γ_h is not too low such that the quanta transferred from Ω_l-to Ω_h-oscillator are sufficiently quickly dissipated into the bath before they could be coherently transferred back to the low-frequency oscillator as in Rabi-oscillations. Additionally, a large γ_h is detrimental for cooling, as otherwise the populations are effectively frozen as in the quantum Zeno effect due to the strong coupling to the bath.

In the strong driving regime given by $\Lambda_{lh}^2 \gg \gamma_l\gamma_h/4$, but still restricted to $\Omega_l \gg \Lambda_{lh}$ by the approximation leading to Eq. (2.43), the cooling ratio becomes independent of the coupling parameter Λ_{lh}. It then solely depends on the damping rates $\gamma_{l,h}$ according to Eq. (2.50)

$$R_{\text{strong}}(\gamma_l, \gamma_h) = \frac{\gamma_l}{\gamma_l + \gamma_h} + \frac{\gamma_h}{\gamma_l + \gamma_h}\frac{\Omega_l}{\Omega_h}. \tag{3.88}$$

As the width of the system response from Eq. (2.49) and Eq. (B.122) depends on the damping

rate, the expression in Eq. (3.88) is formally only valid as long any other normal mode remains sufficiently detuned. The cooling ratios shown in Fig. 3.7a and Fig. 3.7b are obtained for relatively weak driving and do not saturate the cooling limit of $R_{\text{strong}}(0.005, 0.01) = 0.4$ obtained from Eq. (3.88). Increasing the driving strengths of the permittivity used in Fig. 3.7a would require to take higher harmonics of the driving terms of order $O(\nu_{1,2}^2)$ into account (see Eq. (3.34)). Ignoring the influence of higher harmonics and other normal modes, i.e. parametric modulations of the form given in Eq. (3.83) and (3.84) leading to a system response approximated by Eq. (B.122), the saturated cooling ratio from Eq. (3.88) is shown in Fig. 3.8b. The driving is so large that it always dominates over the dissipative dynamics of Ω_h. Consequently, the quantum Zeno effect is negligible on the driving timescale and the optimal value for γ_h has disappeared. In the strong driving regime, the cooling ratio is therefore optimised by a minimal γ_l and maximal γ_h, as long as the driving is sufficiently strong and γ_l much smaller than γ_h. In the following, we use damping rates $\gamma_l = 0.005$, $\gamma_h = 0.01$ (marked by the red cross in Figs. 3.8). The experimentally observed damping rates for YBCO [18] are considerably larger. However, we have now shown that in materials, where effects due to higher harmonics are suppressed, cooling is also possible for large damping rates leading to the expression given in Eq. (3.88). For larger damping rates, it is necessary to control the simultaneous response of all normal modes in the system.



(a) $\epsilon(t)$-Model (Eq. (3.32)) ($\nu_1 \neq 0$, $\nu_2 \neq 0$) ***(b)*** $J^C(t)$-Model (Eq. (3.28)) ($A_1 \neq 0$, $A_2 \neq 0$)

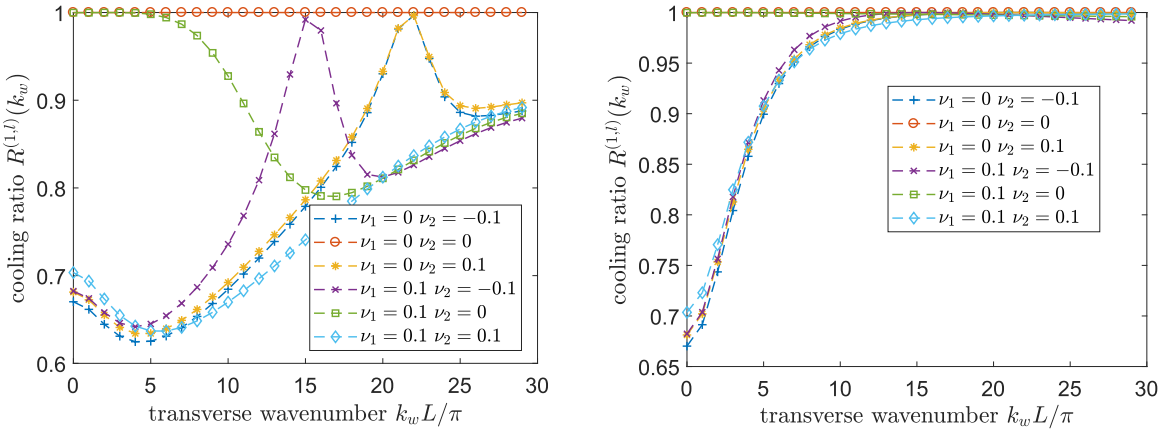
Figure 3.9: Cooling ratio $R^{(1,l)}(0)$ from Eq. (3.79) of the final driven vs initial thermal normal mode quadrature of the homogeneous mode $k_w = 0$ as a function of the driving amplitude for a two junction toy model for a **(a)** $\epsilon(t)$-Model from Eq. (3.32) **(b)** for $J^C(t)$-Model from Eq. (3.28) (capacitive coupling parameter $\alpha_1 = 0.28$, $\alpha_2 = 0.66$).

Relative driving amplitudes Though the driving is uniform along the stack it is allowed to differ in the l, h-type of junction from Fig. 3.1 as physically expected from the excitation of different phonon modes. The cooling efficiency not only depends on the type of driving and its amplitude but also the relative sign of the driving amplitudes $\nu_{1,2}$ (and $A_{1,2}$) in the respective two physical junctions defined in Sec. 3.1.4. In Figure 3.9a the cooling ratio $R^{(1,l)}(0)$ from Eq. (3.79) of the flat phase quadrature of a short two-junction toy model is given as a function of driving amplitudes $\nu_{1,2}$ for $\epsilon(t)$-Model. The smallest cooling ratio $R^{(1,l)}(0)$ is obtained by maximising the modulation amplitude ν_2 in the h-type of junction.

Restricting the driving to the h-type of physical junction from Fig. 3.1 (see Fig. A.10 with $\nu_1 = 0$ compared to Fig. A.9 with $\nu_1 = 0.1$) is found to reduce the driving amplitude $\Lambda^*_{ll}(k_w)$ of the form given in Eq. (3.83) and (3.84) of critical modes from Fig. 3.6 without significantly reducing the cooling efficiency from Fig. 3.9a.

For $J^C(t)$-Model, we find that out-of-phase driving $A_1 \neq A_2$ of the two physical junctions with respective driving amplitude $A_{1,2}$ is essential to achieve a significant cooling efficiency with the smallest cooling ratio obtained for anti-phase driving with $A_1 = -A_2$ as shown in Fig. 3.9b. For in-phase driving with $A_1 = A_2$, on the other hand, the time-dependent spring constant (Eq. (3.45)) is diagonalised through the normal mode transformation (see Eq. (3.49)) such the parametric modulation is only of the form given in Eq. (3.83) and (3.84), while pairs of normal modes are not coupled to each other, i.e. the amplitude Λ_{lh} in Eq. (3.78) is zero. This corresponds to driving of the form given in Eq. (3.83) and (3.83) leading to the effect observed in Ref. [43, 45].

We, therefore, find that for both $\epsilon(t)$-Model and $J^C(t)$-Model, the cooling efficiency and the type of modulation sensitively depends on the driving amplitudes in the physical junction. As discussed in Sec. 3.1.4, controlling the relative driving amplitude is only possible through selecting specific phonon modes. We, therefore, emphasize that finding a material with both the right driving amplitude and driving frequency of the phonon modes will most likely require some tuning and engineering of the material.



(a) Absence of in-plane dissipation $f = 0$ ***(b)*** In-plane dissipation $f = 1/3$

Figure 3.10: Cooling ratio $R^{(1,l)}(k_w)$ from Eq. (3.79) for $\epsilon(t)$-Model from Eq. (3.32) as a function of in-plane momentum k_w for two materials differing in the magnitude of the in-plane dissipation to c-axis dissipation rate f (exact definition below Eq. (3.64)) with **(a)** $f = 0$ **(b)** for $f = \frac{1}{3}$. For the material with a large in-plane dissipation rate as shown in **(b)** the cooling effect disappears for $k_w > 10$. (length $L = 0.5$, capacitive coupling parameters $\alpha_1 = 0.28$ and $\alpha_2 = 0.66$, damping rates $\gamma_l = 0.005$ and $\gamma_h = 0.01$)

Role of in-plane dissipation The diagonal components of the driving amplitude Λ^*_{ll} of the form given in Eq. (3.83) and (3.84) can lead to resonant driving $2\omega_d/\omega_p \approx 2\Omega^*_l$ of critical modes with frequency Ω^*_l. According to Eq. (3.85) the heating associated with these resonance catastrophes indicated in Fig. 3.6 is only negligible if the damping γ^*_l is larger

then the driving amplitude Λ^*_{ll} such that $2\Lambda^*_{ll} < \gamma^*_l/2$. In this case, energy introduced by the driving mechanism quickly dissipates into the heat bath.

For $\epsilon(t)$-Model, restricting the driving to the h-type of physical junction from Fig. 3.1 (see Fig. A.10 with $\nu_1 = 0$ compared to Fig. A.9 with $\nu_1 = 0.1$) reduces the driving amplitude $\Lambda^*_{ll}(k_w)$ without significantly reducing the cooling efficiency from Fig. 3.9a. For a material with negligible in-plane dissipation, the amplitudes $\Lambda^*_{ll}(k_w)$ responsible for the resonance catastrophes are in general larger than the smallest damping rate of the low-frequency mode, γ_l defined below Eq. (3.63). Consequently, for $f = 0$ the damping of the critical modes $\gamma^*_l = \gamma_l$ is not sufficient strong to avoid switching into a resistive state. The analytic expression of the hypothetical cooling ratio[14] $R^{(1,l)}(k_w)$ obtained from Eq. (3.79) and shown in Fig. 3.10a cannot be achieved.

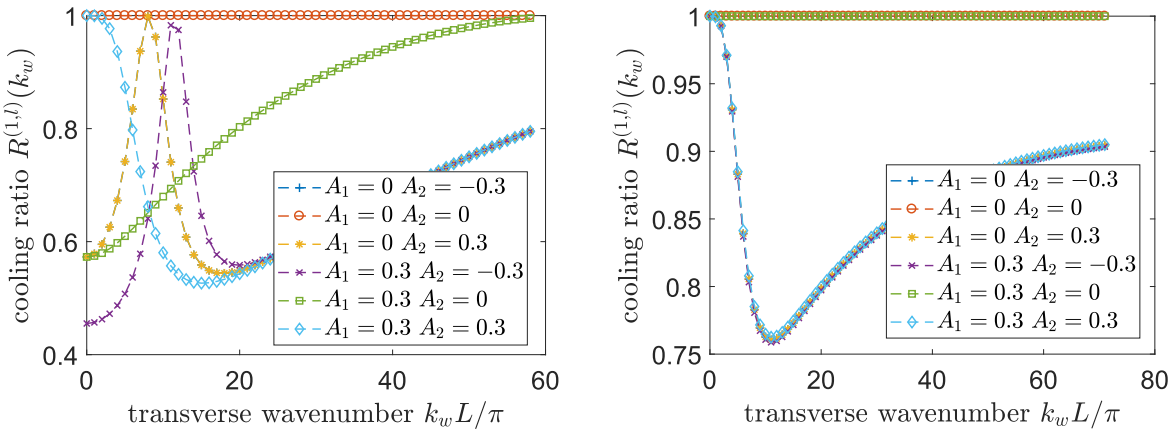
For materials with large in-plane quasi-particle currents, on the other hand, the effective decay rates $\gamma^*_l(k_w)$ of the critical modes are increased with in-plane momentum Fig. 3.4 such that $\gamma_l(k_w) \geq \gamma_l$. The relative size of in-plane to out-of-plane dissipation is estimated by the ratio f defined below Eq. (3.64). If only the high-frequency junction is driven, i.e. $\nu_1 = 0$ and $\nu_2 = 0.1$, a bilayer cuprate with $f \geq \frac{1}{3}$ satisfies $2\Lambda^*_{ll} < \gamma^*_l/2$ and is able to suppress heating. The corresponding cooling ratio $R^{(1,l)}(k_w)$ obtained from Eq. (3.79) is shown in Fig 3.10b for a material with $f = 1/3$. Due to the sensitive dependence of the cooling efficiency on damping rates, the in-plane dissipation has a detrimental effect on the cooling efficiency of modes with finite k_w. Though normal modes with finite in-plane momentum have a smaller thermal occupation than the spatially homogeneous modes, it is advantageous to choose a material with a small in-plane dissipation possible while still sufficiently suppressing heating of critically driven modes.

In $J^C(t)$-Model (Eq. (3.28)), the driving amplitude Λ^*_{ll} of the critical modes (see Fig. 3.6) is smaller than the smallest damping rate of the system dynamics, γ_l, for $\gamma_l = 0.005$ if $|A_{1,2}| \sim 0.3$. Finding a material with a small in-plane dissipation would in this case allow to cool large k_w-modes. The corresponding cooling ratio is shown in Fig. 3.11a. The dip in the cooling efficiency around $k^*_w L/\pi \approx 10$ arises around the location of the critical modes from Fig. 3.6. This effect is also accompanied by a reduction of the driving amplitude such that $\Lambda^*_{lh} \to 0$. From Fig. 3.11b, which shows the cooling ratio $R^{(1,l)}(k_w)$ from Eq. (3.79) for $J^C(t)$-Model in the absence of capacitive coupling, we see that at $k^*_w L/\pi \approx 10$ the minimal cooling ratio for a purely inductive cooling scheme is reached. The elimination of the cooling effect for $k^*_w L/\pi \approx 10$ in Fig. 3.11a seems to occur from a competition of capacitive and inductive coupling.

Relative driving amplitudes in the long junction regime for $J^C(t)$-Model from Eq. (3.28) From Figure 3.9b we know that the largest cooling efficiency in the short junction limit with a flat phase $k_w = 0$ is achieved for anti-phase driving (see Fig. 3.11a), while no cooling is achieved for in-phase driving. With increasing k_w the cooling ratio $R^{(1,l)}(k_w)$ from Eq. (3.79) becomes independent of the driving amplitude A_1 of the l-type of

[14] The analytical expression $R^{(1,l)}(k_w)$ obtained from Eq. (3.79) ignores resonance catastrophes, which lead to growth of the corresponding thermal occupations until the coupling between different modes cannot be ignored in the non-linear regime and the whole system switches into a resistive state.

junction. The overall cooling ratio is simultaneously reduced by the decrease in the relative gap between the normal mode frequencies of the two bands shown in Fig. 3.2 for a material with negligible in-plane dissipation. Modes with large normal mode frequencies do not have a large thermal occupation (see discussion below Eq. (3.62)).



(a) Negligible in-plane dissipation

(b) Negligible capacitive coupling

Figure 3.11: Cooling ratio $R^{(1,l)}(k_w)$ from Eq. (3.79) for $J^C(t)$-Model (Eq. (3.28)) as a function of in-plane momentum k_w for different driving amplitudes for **(a)** negligible in-plane dissipation in the presence of capacitive coupling (magnitude of in-plane dissipation $f = 0.01$ defined below Eq. (3.64), capacitive coupling parameter $\alpha_1 = 0.28$, $\alpha_2 = 0.66$) **(b)** for negligible capacitive coupling (capacitive coupling parameter are rescaled by a factor $s = 10^{-10}$ to $\alpha_1 = 0.28s$, $\alpha_2 = 0.66s$, magnitude of in-plane dissipation $f = 0.75$ defined below Eq. (3.64)). Modes beyond $k_wL/\pi \geq 15$ have a negligible thermal occupation. Cooling ratio $R^{(1,l)}(k_w)$ as a function of in-plane momentum k_w for different driving arrangement of critical current in the case of an extremely small capacitive coupling (length $L = 1.5$). **(a)** The data points for pluses and stars are overlapping.

In Fig. 3.11b, we show the cooling ratio for a material with significant in-plane dissipation $f = 0.75$ in the absence of capacitive coupling $\alpha_{1,2} \to 0$[15], that is purely inductive coupling. As expected, there is no cooling effect for the spatially homogeneous mode as the junctions decouple without the capacitive coupling and no energy transfer is possible. However, for modes with spatial dependence the cooling efficiency increases to its maximum value around $k_wL/\pi \approx 10$, which is the value where the cooling efficiency due to capacitive and inductive coupling goes to zero in Fig. 3.11a. This drop in cooling efficiency for intermediate wavenumbers in Fig. 3.11a arises from the competition of cooling due to capacitive and inductive coupling.

Length dependence In Eq. (3.79), we defined the cooling ratio as the ratio of the normal mode quadrature of the driven steady vs undriven thermal normal mode. To capture both flat and spatial excitations in one quantity, we define an effective cooling ratio of the total phase quadrature of the undriven initial thermal state at $\tau_{\text{init}} = 0$ and the one of the final

[15]The ratio of α_1/α_2 is kept fixed according to the restrictions posed by the assumption of identical superconducting sheets (see discussion above Eq. (3.10)).

steady state at $\tau_{\text{final}} = 1/\gamma_l$ as

$$R^r_{traj} = \frac{\int \text{avg}(\langle \vec{\phi}_r^\top \vec{\phi}_r \rangle_{\tau_{\text{final}}}) dx}{\int \text{avg}(\langle \vec{\phi}_r^\top \vec{\phi}_r \rangle_{\tau_{\text{init}}}) dx}, \tag{3.89}$$

where the integral leads to an average of the quadratures of the phases $\vec{\phi}_r$ in the $r = l, h$-type of junction from Fig. 3.1 over the whole junction length, $\langle \ldots \rangle$ corresponds to an expectation value obtained from the average over independent trajectories of the Langevin equation in Eq. (3.65). The optional average avg(...) over a time-interval of $1/\gamma_l$ allows speeding up convergence and reducing the number of trajectories needed. Averaging over time is only possible for negligible time dependence of the quadrature values.

Given that the largest thermal weight arises from phase fluctuation in the low frequency junction, the ratio R^l_{traj} in Eq. (3.89) can be approximated by replacing the phases in the low frequency junction $\vec{\phi}_l$ by $\vec{\phi}$. As common additional factors cancel in the ratio, we can replace $\vec{\phi}_r^\top \vec{\phi}_r$ by $\vec{\phi}^\top \boldsymbol{\mathcal{M}}^i_w \vec{\phi}$ in the cooling ratio R^l_{traj} from Eq. (3.89). Under the assumption of individually addressable subspaces from Eq. (3.87), the cooling ratio from Eq. (3.89) can be approximated as a ratio of the cooling ratios of the normal mode quadratures $R^{(j,l)}(k_w)$ from Eq. (3.79) weighted by the relative thermal occupation, as

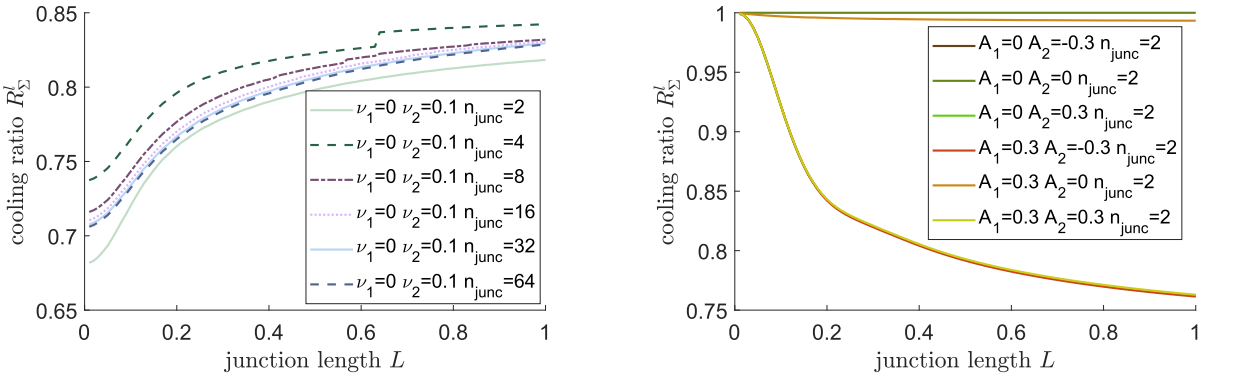
$$R^{(l)}_\Sigma = \frac{\sum\limits_{k_w,j} R^{(j,l)}(k_w) \left(\vec{\Omega}_{g^j_w(l)}\right)^{-2} (1+\delta_{w,0})/2}{\sum\limits_{k_w,j} \left(\vec{\Omega}_{g^j_w(l)}\right)^{-2} (1+\delta_{w,0})/2}, \tag{3.90}$$

where $\vec{\Omega}_{g^j_w(r)}$ defined below Fig. 3.5 is the normal mode frequency of the jth pair with in-plane momentum k_w, $\langle \ldots \rangle$ an average over multiple trajectories and the $\delta_{w,0}$-function taking into account the spatial structure of the modes. For the numerical simulations of the full non-linear equation in Sec. 3.5.2 given in Eq. (3.65). The results from both cooling ratio Eq. (3.90) and Eq. (3.89) agree well as shown in Fig. 3.14.

In Fig. 3.12a, the cooling ratio obtained from Eq. (3.90) is shown as a function of junction length L for different stack sizes. The additional normal mode structure present in larger junctions makes cooling less efficient when increasing the junction length from two junctions (bright green solid line) to four junctions (dark green dashed line) after which the cooling efficiency again increases with stack size. A small jump in the line corresponding to $n_{junc} = 4$ arises from the competition between capacitive and inductive coupling, which is only resolved at these length scales.[16] As the capacitive coupling is very small it is almost not visible in Fig. 3.2. For larger stacks, this bump splits and distributes over different modes, e.g. two smaller bumps in $n_{junc} = 8$. The long-junction regime is approached for $L \geq 0.5$, which

[16] The junction length determines the spacing between the discrete points in Fig. 3.2b. For a junction of length $L \approx 0.6$, the points are able to resolve the re-ordering due to the competition between capacitive and inductive coupling of the normal mode frequencies at very small k_w. More precisely, for $k_w = 0$ the low frequency mode increases with longitudinal momentum $q_z \approx 0$ (small arrow in Fig. 3.2b at $k_w = 0$) although for finite k_w the order is inverted (large arrow) (see also expert in Fig. A.2). For a small stack the discrete spacing of the normal modes leads to an abrupt transition resulting into a sharp bump, which becomes continuous for larger stack sizes as the discrete spacing becomes increasingly smoother.

correspond to the continuous limit where the discrete nature of the normal mode structure disappears, i.e. the markers in Fig. 3.2b become more densely spaced without changes to the overall shape of the normal mode structure otherwise. Increasing the junction size further does not modify the cooling limit as the whole spectrum only gets denser and the relative thermal occupation of all low-frequency modes, which can be cooled efficiently to those which cannot remains fixed. Because we can cool $k_w \neq 0$-mode, the cooling effect survives in the thermodynamic limit $L \to \infty$.



(a) $\epsilon(t)$-Model (Eq. (3.32)) for different stack sizes

(b) $J^C(t)$-Model (Eq. (3.28)) with negligible capacitive coupling

Figure 3.12: Length dependence of the total cooling ratio $R_\Sigma^{(l)}$ from Eq. (3.90) as a function of junction length L for **(a)** $\epsilon(t)$-Model (Eq. (3.32)) for different stack sizes ($\alpha_1 = 0.28$, $\alpha_2 = 0.66$, $f = 0.75$). **(b)** $J^C(t)$-Model (Eq. (3.28)) for two-junction toy model in the absence of capacitive coupling ($\alpha_1 = 0.28s$, $\alpha_2 = 0.66s$, $s = 10^{-10}$, $f = 0$)

Cooling due to purely inductive coupling achieved through a time-dependent critical current has a distinctively different dependence on the junction length. No cooling is possible in the short junction regime in the absence of capacitive coupling, the cooling efficiency increases with junction length and converges against 25% as shown in Fig. 3.12b in the absence of in-plane dissipation. A steady value of 10 percent survives even in the thermodynamic limit even in the presence of strong in-plane dissipation (not shown).

Including capacitive coupling leads to a significantly more complicated driving dependence as shown in Fig. 3.13. For in-phase driving the cooling effect is again purely inductive and increases with junction size, while for anti-phase driving the highest cooling efficiency is again achieved for the smallest junction, as the cooling efficiency of large k_w modes is suppressed here due to in-plane dissipation.

3.5.2 Simulations of full non-linear equations of motion

We now study the long-junction regime using the full non-linear equations from Eq. (3.65). The non-linear terms lead to interaction between different spatial modes, which no longer evolve independently as in Eq. (3.44). The system initially starts in a thermal state at time $\tau_{\text{init}} = 0$, at which point the driving is switched on continuously. In order to simultaneously address the cooling sideband of all spatial modes with a relevant thermal occupation, we

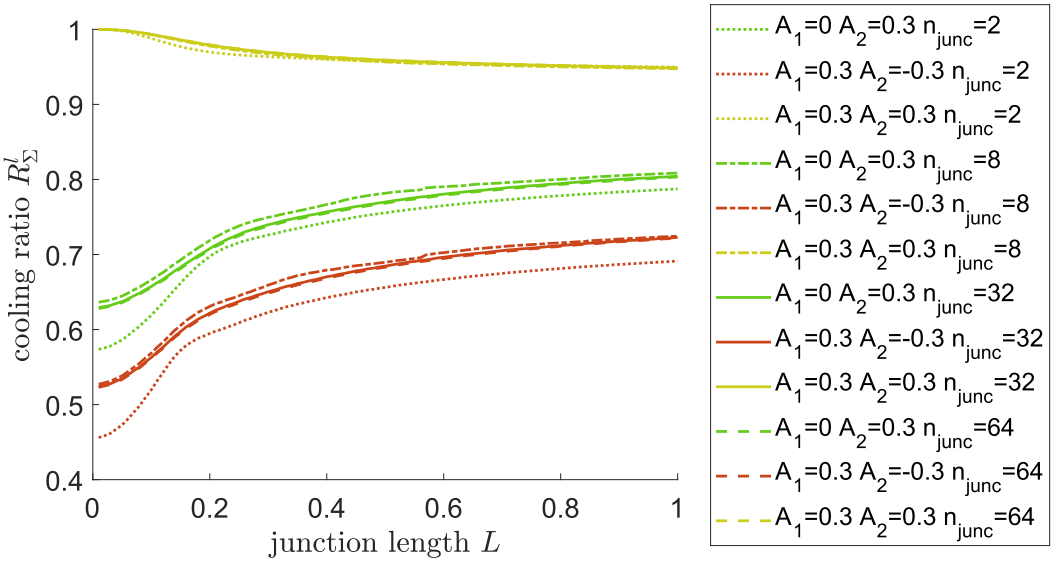


Figure 3.13: Length dependence of the total cooling ratio $R_\Sigma^{(l)}$ from Eq. (3.90) for different driving amplitudes of $J^C(t)$-Model (Eq. (3.28)) as a function of junction length L for stacks of 2 (dotted line), 8 (dashed dotted line), 32 (solid line) and 64 (dashed line) junctions for $(A_1, A_2) = (0, 0.3)$ (green line), anti-phase $(A_1, A_2) = (0.3, -0.3)$ (red line) and in-phase $(A_1, A_2) = (0.3, 0.3)$ (yellow line) ($\alpha_1 = 0.28$, $\alpha_2 = 0.66$, $f = 0.75$).

replace the monochromatic driving from Sec. 3.1.4 by a broadband pulse, i.e.

$$\cos\left(2\omega_d \tau/\omega_p\right) \to \sum_l^{N_l} \cos\left(2\omega_d^l \tau + \phi_l\right), \tag{3.91}$$

modelled in terms of N_l discrete frequencies $2\omega_d^l$ in the range $[7, 9.39]$. The large range of driving frequencies ensures that the system can be also cooled in the presence of reductions to the effective normal mode frequencies due to the presence of bias current (see Eq. (1.24)) and large thermal occupation. The discrete frequencies of the broadband pulse from Eq. (3.91) are separated by 0.02, which is slightly larger than the lower bound to the linewidth $\sim \gamma_l + \gamma_h$ of the cooling response from Eq. (2.49). As long as the spacing between the driving frequencies is larger than the cooling linewidth, the different contributions of a broadband pulse are expected to contribute independently. For $\phi_l = 0$, all frequency components of the pulse from Eq. (3.91) add up at $\tau \approx 0$ leading to a see-saw shaped pulse with an extremely steep peak. Such a kick might displace the phase to the extent that the system directly switches into a resistive state characterised by a finite voltage. To keep the effective magnitude of the pulse small at all times, we distort the pulse shape using random phases ϕ_l.

For $J^C(t)$-Model from Eq. (3.28) we find that the multi-frequency driving pulse does not lead to stable solutions even though the requirement for stable solutions in the presence of monochromatic driving from Eq. (2.53) is satisfied for any of frequency components of the broadband pulse from Eq. (3.91). We find that the maximum driving amplitude Λ_{hh} of parametric modulations of the form given in Eq. (3.84) of all possible pairs is $\Lambda_{hh}/\Omega_h \approx 0.04$ for $A_1 = -A_2 = 0.15$ ($\Lambda_{ll}/\Omega_l \approx 0.04$, $\Lambda_{lh}/\Omega_l = 0.01$). Given that the pulse consists

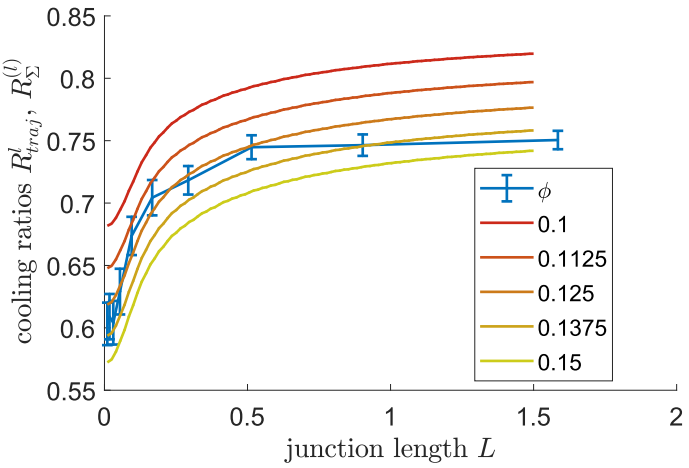


Figure 3.14: Cooling ratios of the total phase quadrature averaged over the junction length for a two junction toy model as a function of junction length L. The temperature $\mathcal{T} = 0.001$ is chosen low enough for all junction lengths, such that the cooling ratio R^l_{traj} from Eq. (3.89) (blue error bars labelled ϕ) and $R^{(l)}_\Sigma$ from Eq. (3.90) (red to yellow solid line labelled by driving strength ν_2) have the same systematic dependence (driving amplitudes $\nu_1 = 0$, $\nu_2 = 0.1$ from Eq. (3.32), magnitude of in-plane dissipation $f = 3/4$ defined below Eq. (3.64), $\mathcal{T} = 0.001$ using approximately 200 trajectories and averaging over a time interval of the order $1/\gamma_l$, errorbars from bootstrapping).

of approximately 120 different frequencies, the effective driving strength can be roughly estimated as $120\Lambda_{hh}/\Omega_h \approx 48$, which is much larger than $\Lambda^*_{hh} \approx 5.5$ obtained from the stability criteria of a monochromatic drive from Eq. (2.53). This rough estimate shows that the driving of the critical current leads to a very strong driving of the high-frequency mode and the independent mode approximation breaks down. This might also explain, why the cooling effect obtained in Ref. [43, 45] for driving of the critical current (see Sec. 2.2.2) is small compared to the parametric enhancement of the effective Josephson coupling arising from Λ_{hh}.

For $\epsilon(t)$-Model from Eq. (3.32), on the other hand, the maximum Λ_{hh} is approximately a factor of 10 smaller than for $J^C(t)$-Model as $\Lambda_{hh}/\Omega_h \approx 0.005$ ($\Lambda_{ll}/\Omega_l \approx 0.01$, $\Lambda_{lh}/\Omega_l = 0.008$) for $\nu_1 = \nu_2 = 0.1$. In the following, we do not pursue $J^C(t)$-Model further and only study $\epsilon(t)$-Model.

Length dependence The effective analytical cooling ratio $R^{(l)}_\Sigma$ of the normal mode quadrature from Eq. (3.90) increases with junction length L as shown by the solid lines in Fig. 3.14 for different driving amplitudes ν_2 (encoded by the color red to yellow).[17] This is not surprising as in Sec. 3.5.1 we found that the presence of in-plane dissipation and closing of the gap between different normal modes reduces the cooling efficiency for modes with large in-plane momentum. Using the broadband pulse from Eq. (3.91) of driving strength $\nu_2 = 0.1$, the cooling ratio R^l_{traj} defined in Eq. (3.89) increases with increasing junction length L from around 0.6 to 0.7 (Fig. 3.14). The error bars are obtained by applying statistics to 1000

[17] In Sec. 3.5.1, we showed that the driving of critical modes is reduced by setting $\nu_1 = 0$.

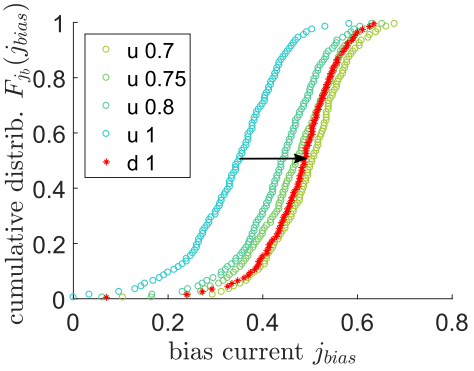
bootstrap samples from independent stochastic trajectories of the full non-linear Langevin equation from Eq. (3.65) using the broadband pulse from Eq. (3.91). The data points of the cooling ratio R^l_{traj} are parallel shifted with respect to the cooling ratio $R^{(l)}_\Sigma$ for the same driving amplitude $\nu_2 = 0.1$ (red solid line) and instead follow the curve $\nu_2 = 0.125$ (orange solid line) up to lengths $L \leq 0.5$. The parallel shift arises due to the assumption of individually addressable, resonantly driven subspaces from Sec. (3.82) used for obtaining $R^{(l)}_\Sigma$. The overlap of the cooling response due to the discrete driving frequencies of the multi-frequency driving pulse from Eq. (3.91) increases the effective driving amplitude for R^l_{traj}. For larger junction lengths $L > 0.5$ the cooling ratio R^h_{traj} converges to a plateau because normal modes with frequencies larger than the thermal cut-off frequency ω^c, defined below Eq. (3.62), are not thermally occupied. This thermal cut-off ω^c has not been oposed on the linearised model leading to $R^{(l)}_\Sigma$. Raising ω^c is associated with an increase in the system size and makes the simulations numerically more challenging, but does not introduce additional instabilities.

We numerically check that the heating of the high-frequency mode remains negligible in the full model. For the system parameters studied in Fig. 3.14, we find a heating ratio $R^h_{traj} \leq 3$ for phase quadrature in the h-type junction. This increase is negligible as the initial thermal occupation of the high-frequency mode is in the thermal state is of the order $\langle \vec{\phi}^2_h \rangle \sim \langle \vec{\phi}^2_l \rangle / 100$. However, the ratio R^h_{traj} for the h-type of junction depends on the averaging time in Eq. (3.89) for junctions $L > 0.01$ involving modes with $k_w \neq 0$. This time dependence is not found in the cooling ratio of the l-type of junction R^l_{traj}, which is independent of the averaging time used in the definition of R^l_{traj} from Eq. (3.89). This time dependence most likely arises from off-resonant parametric driving of high k_w-modes, which can periodically transfer energy between the momentum and position quadrature (see Fig. 4.2). For $\epsilon(t)$-Model the diagonal terms of the driving amplitude Λ_{rr} with $r = l, h$ leading to parametric modulations of the form given in Eq. (3.84), are significantly smaller than for $J^C(t)$-Model. Therefore, we do not expect a significant reduction of the effective Josephson interlayer coupling by the frequency redistribution mechanism proposed in Ref. [43, 45] for spatially homogeneous modes. More strongly driven spatial modes with large k_w, would not be probed in the optical response (Fig. 3.3a). However, when increasing both damping strength and driving strength both effects could potentially be observed simultaneously, which we do not investigate further as it would require to include higher harmonics in Eq. (3.34).

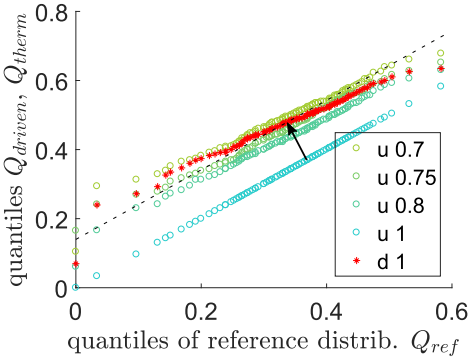
Switching current distribution

In the previous section, we only considered the low-temperature regime, where the non-linear terms of the Josephson potential do not play a role. At larger temperatures, the phase can escape the trapping potential shown in Fig. 1.2. The junction can be thermally activated from a superconducting state to a resistive state, characterised by a finite time-averaged voltage according to the generalised AC-Josephson relation from Eq. (3.3).

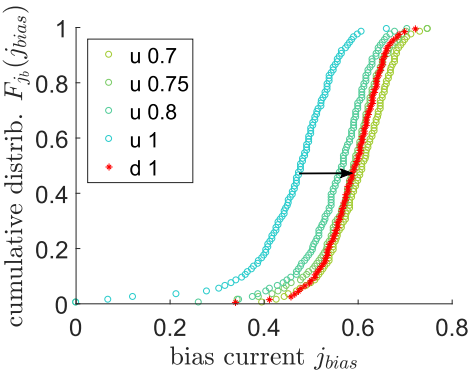
A reduction in the phase quadrature of the low-frequency junction is only useful for stabilising superconductivity if the cooling effect survives in the presence of a bias current. A reduction in the phase quadrature of the low-frequency junction is expected to be reflected in a shift of the switching current distribution [31, 43]. The switching current distribution



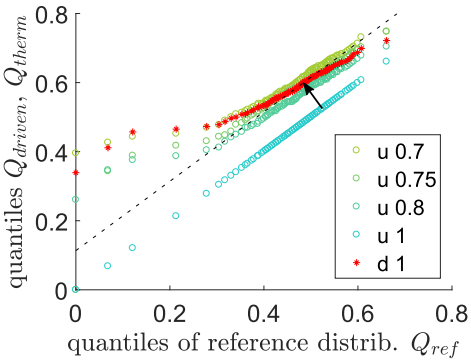
(a) Cumulative $F_{j_b}(j_{\text{bias}})$



(b) Q-Q plot



(c) Quantiles as a function of j_{bias}



(d) Q-Q plot

Figure 3.15: **(a)** & **(d)** Empirical cumulative distribution function $F_{j_b}(j_{\text{bias}})$ from Eq. (3.92) obtained for driven (red star shaped markers labelled d) and undriven (turquoise circular markers labelled u) systems at different temperatures $\mathcal{T}/\mathcal{T}_0 = (0.75, 0.75, 0.8, 1)$ as a function of the bias current j_{bias}. **(b)** & **(c)** Q-Q plot giving the quantiles of the switching current distribution $P_{\text{switch}}(j_b)$ for a driven system (Q_{driven}) and undriven system (Q_{therm}) vs the quantiles Q_{ref} of $P_{\text{switch}}(j_b)$ obtained for an undriven reference system at temperature $\mathcal{T}_0 = 0.0025$. Junction length $L = 2$, stack size $n_{\text{junc}} = 2$ for **(a)** & **(b)** and junction length $L = 0.5$, stack size $n_{\text{junc}} = 10$ for **(d)** & **(c)** and the labels are the same as in all figures (magnitude of in-plane dissipation $f = 3/4$ defined below Eq. (3.64), driving amplitudes $\nu_1 = 0$ and $\nu_2 = 0.1$ from Eq. (3.32)).

$P_{\text{switch}}(j_b)$ (see Sec. 1.1.3 and 2.1.2) is a distribution of the stochastic variable j_b corresponding to the bias current at which the junction becomes resistive. $P_{\text{switch}}(j_b)$ can be measured experimentally [78, 285–287]. Both width [78, 93, 288] (see Sec. 2.1.2) and mean value [10] (see Sec. 1.1.3) of $P_{\text{switch}}(j_b)$ have been used as measures of the system temperature.

Here, we empirically estimate $P_{\text{switch}}(j_b)$ by measuring j_b over 500 trajectories. Each trajectory corresponds to a realisation of Eq. (3.65) with the replacement Eq. (3.91) starting with a system initialised in a superconducting thermal state at temperature $\mathcal{T}$ with zero bias current. The bias current is linearly increased over a long time interval $\Delta\tau = 2\pi \times 10^3$ to the critical current $\mathcal{J}_l^C$ of the l-type junction. This interval has to be chosen long enough to ensure that the dynamics are independent of the ramp duration at every bias current [10].

It is apriori not guaranteed that $P_{\text{switch}}(j_b)$ of a driven system resembles $P_{\text{switch}}(j_b)$ of an undriven thermal system. To simplify the comparison, we use the cumulative distribution

function defined by

$$F_{j_b}(j_{\text{bias}}) = \int_{-\infty}^{j_{\text{bias}}} dj_b P_{\text{switch}}(j_b). \tag{3.92}$$

In Fig. 3.15a, we show $F_{j_b}(j_{\text{bias}})$ as a function of the bias current j_{bias} for both a driven (red stars labelled d) and undriven (turquoise diamonds labelled u) system at different temperatures $\mathcal{T} = (0.7, 0.75, 0.8, 1)\mathcal{T}_0$. We find that driving results in a shift of the distribution $F_{j_b}(j_{\text{bias}})$ to higher bias currents (as indicated by the black arrows). The resulting $F_{j_b}(j_{\text{bias}})$ of the driven system resembles the undriven reference distribution for a system initially at a lower temperature of $\mathcal{T} \simeq 0.75\mathcal{T}_0$ (middle of the green curves on the right). We obtain an effective 25% reduction in temperature in the long-junction regime $L = 2$ in agreement with the cooling ratio of 0.75 obtained in the linear regime from Fig. 3.14.

In Figure 3.15b we represent the same data used for Fig. 3.15a in terms of a Q-Q plot, which allows a more systematic comparison of different distributions. In the Q-Q plot, the quantiles[18] of the switching current distributions used for Fig. 3.15a are plotted against the quantiles of a reference distribution of an undriven system at temperature $\mathcal{T}_0 = 0.0025$. Both the quantiles of the driven (red star-shaped markers and labelled d) at temperature $\mathcal{T}_0$ and undriven distribution at temperatures $\mathcal{T} = (0.7, 0.75, 0.8, 1)\mathcal{T}_0$ (green diamond-shaped marker labelled u) are plotted versus the quantiles the undriven distribution of a system at $\mathcal{T}_0$. The distribution of the undriven system at temperature $\mathcal{T}_0$ lies trivially on the diagonal. We clearly see the shift of the whole distribution due to the driving. The distributions are further slightly tilted with respect to the diagonal (black dashed line is a guide to the eye), which effectively corresponds to a reduction in the width of the distribution as predicted for a system with a lower temperature.

The shift in the mean value and the tilt in the distribution are more easily recognisable for larger systems, i.e. either by increasing the stack size or junction length. With decreasing junction size, the decrease in the number modes and the associated narrowing in the system response leads to a decrease in the width of the switching distribution and the switching occurs at higher temperatures (measured in units proportional to the Josephson energy see Sec. 3.3). In Fig. 3.15d and 3.15c, we show the cumulative distribution function $F_{j_b}(j_{\text{bias}})$ from Eq. (3.92) and Q-Q-plot for a finite stack of ten junctions of length $L = 0.5$. The temperature used is relatively low resulting in some outliers, where the junction already switches into a resistive state in the absence of a bias current such that the cooling mechanism does not have time to suppress switches observed. The cooling effect of around 25% is approximately the same as obtained for the two-junction model of the same length from Fig. 3.14.

We find a decrease in the mean value of the switching current density with junction size, in agreement with Ref. [287][19]. Simultaneously, the width of the current distribution is found

[18] Given a probability p the quantile of a probability distribution $P(X)$ gives the value x such that the random variable X is smaller or equal x with probability p. The different quantiles divide $P(X)$ into intervals, such that the probability for a data point to lie in any of the intervals is equal. The quantiles are more closely spaced at peaks of the distribution.

[19] The authors in Ref. [287] observe an increase in the mean value of the total switching current with junction size. However, accounting for the area the mean switching current decreases with junction size.

to increase for longer junctions.

We attempted to obtain a systematic temperature dependence of the cooling effect using both linear interpolations of different reference temperatures and analytical expressions valid for short junction models. For all junctions up to the maximum $L = 2$ studied, we observe a cooling effect of roughly $20 - 30\%$ without any clear length dependence. Differences to analytic expressions obtained from the thermal activation of short Josephson junction are not surprising. In general, $P_{\text{switch}}(j_b)$ obtained for HTSC can differ from the thermal activation of a single short Josephson junction discussed in Sec. 1.1.3 due to the finite junction length and strong coupling between different junctions. Especially, for the bilayer, the l-type of junction shown in Fig. 3.1 become resistive much before the phases in the h-type of junction due to the difference in the maximal critical current of the two junctions. Measuring the temperature dependence of $P_{\text{switch}}(j_b)$ in $Bi_2Sr_2CaCu_2O_y$, Kitano et al. [286] observed an increase in the standard deviation of $P_{\text{switch}}(j_b)$ with decreasing temperature, which was attributed to re-trapping event not captured by simple thermal activation models.

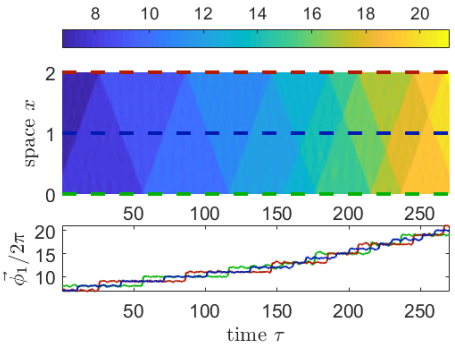
Sample trajectories

In Sec. 1.1.3, we described the transition of a short Josephson junction from a superconducting to resistive state as the thermally activated escape of a fictitious phase particle out of a trapping potential of the washboard potential. For underdamped junctions, the phase particle typically does not get re-trapped in any of the other minima of the periodic Josephson potential and reaches a constant velocity. The resulting resistive state is characterised by a net time-averaged voltage according to the generalised AC-Josephson relation from Eq. (3.5). The situation is more complicated in the long-junction regime, as there is effectively one fictitious phase particles for each k_w-mode. For a junction of length L, switching into a resistive state can be described as the thermal activation of approximately L/λ_J inductively coupled phase particles [287] with λ_J the Josephson penetration length from Eq. (2.15). Spatial dependence of the phase leads to a reduction of the effective activation barrier is reduced by $(\lambda_J/L)^d$ with $d = 1$ for a long junction and $d = 2$ for a junction of area $L \times L$ [286]. Qualitatively, with increasing junction size, the spatially uniform thermal activation becomes energetically unfavourable in comparison to a switch via a 2π kink [285, 287] (see also discussion in Sec. 3.6). The type of thermally activated switching into a resistive state is therefore expected to depend strongly on the length of the junction.

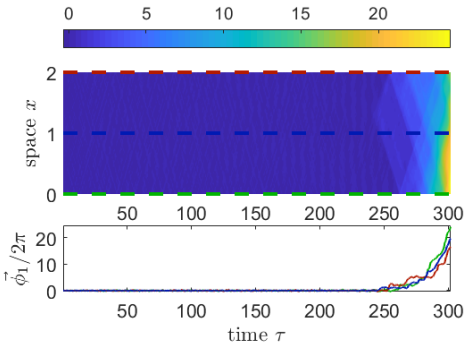
Long Josephson junctions allow for non-linear solitonic excitations of the phase. For a single junction of infinite length in absence of dissipation a soliton is given by wavepackets of the form [289]

$$\phi_{\pm}(x, \tau, u) = 4 \arctan\left[\exp\left(\pm \frac{x - u\tau}{\sqrt{1 - u^2}}\right)\right] \tag{3.93}$$

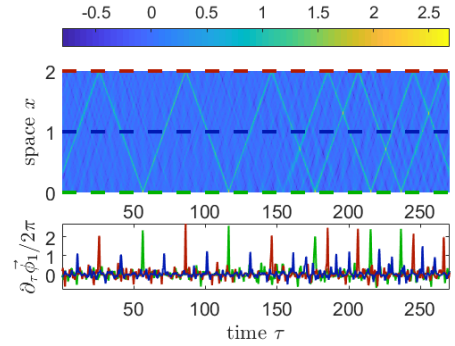
travelling at velocity u. Depending on the sign $\pm$, the phase increases or decreases by 2π along the junction. As spatial gradients in the phase are related to different signs of the associated magnetic field $\vec{B}^y(x)$ according Eq. 3.12, the two solutions $\pm$ are also referred to as fluxon and an anti-fluxon. Despite being non-linear solutions, solitons remain characteristically unaffected by collisions with each other as visible in Fig. 3.16.



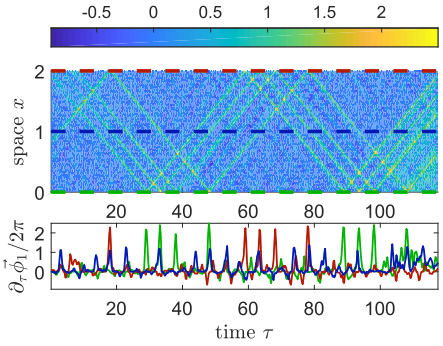
(a) $\vec{\phi}_1(x,\tau)/2\pi$ $j_{\text{bias}} = 0.3$, $\mathcal{T} = 0.004$



(b) $\partial_\tau\vec{\phi}_1(x,\tau)/2\pi$ $j_{\text{bias}} = 0.4$, $\mathcal{T} = 0.005$



(c) $\vec{\phi}_1(x,\tau)/2\pi$ $j_{\text{bias}} = 0.3$, $\mathcal{T} = 0.004$

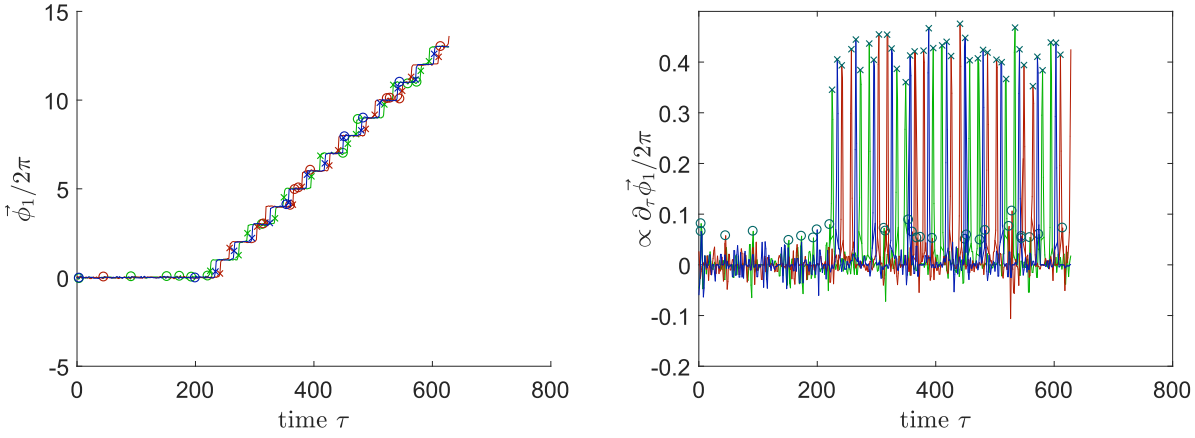


(d) $\partial_\tau\vec{\phi}_1(x,\tau)/2\pi$ $j_{\text{bias}} = 0.3$, $\mathcal{T} = 0.004$

Figure 3.16: Top panel respectively show the phase evolution $\vec{\phi}_1(x,\tau)/2\pi$ (**(a)** & **(b)**) and its time derivative $\partial_\tau\vec{\phi}_1(x,\tau)/2\pi$ (**(c)** & **(d)**) of the l-type junction from Fig. 3.1 as a function of time τ and spatial coordinate x. Each trajectory is obtained from Eq. (3.65) with the replacement Eq. (3.91). Bottom panel shows the same quantity at three different positions indicated by a dashed line of the same color in the top panel (same data in **(a)** and **(c)**, stack of two junctions of length $L = 2$, magnitude of in-plane dissipation $f = 3/4$ defined below Eq. (3.64), driving amplitudes $\nu_1 = 0$ and $\nu_2 = 0.1$ for $\epsilon(t)$-Model driving from Eq. (3.32), preprocessing using median filter over 3 data points).

In Figure 3.16, we show the phase evolution $\vec{\phi}_1(x,\tau)/2\pi$ and time derivative of the phase $\partial_\tau\vec{\phi}_1(x,\tau)/2\pi$ for a two-junction model of length $L = 2$ in the presence of a constant bias current. We observe both fluxons and anti-fluxon corresponding approximately to the $\pm$ in Eq. (3.93). While they pass each other undisturbed, they are inter-converted upon reflection at the boundary leading to a phase jump of approximately 4π at the boundaries (green and brown line) instead of only 2π in the middle of the junction (blue line). According to Eq. (3.5) and Eq. (3.12) moving solitons are associated with both electric and magnetic fields, which upon hitting the boundary leads to short electromagnetic pulses visible experimentally. The time-averaged voltage in Fig. (3.16), depends on the number of solitons present in the junction. In Fig. 3.16a and 3.16c, there is initial only one soliton present. At $\tau \approx 150$, a second soliton is excited at the system boundary, which leads to an increase of the time-averaged voltage by a factor of 2. We also find that solitons are not necessarily excited at the boundary. In Fig. 3.16b, we see the thermal excitation of a fluxon and anti-fluxon pair in the middle of the junction. The bias current drives the pair in opposite directions. They are quickly

joined by further solitons, which finally switch the junction into a resistive state. Fig. 3.16d shows multiple solitons accompanied by some additional ripples in the phase of the junction. Further spatial gradients of exemplary trajectories are given in Fig. A.11 range from trains of solitons (Fig. A.11a), soliton-antisoliton pairs (Fig. A.11b), single soliton propagating back and forth (Fig. A.11c) to a soliton radiating further solitons off (Fig. A.11d).

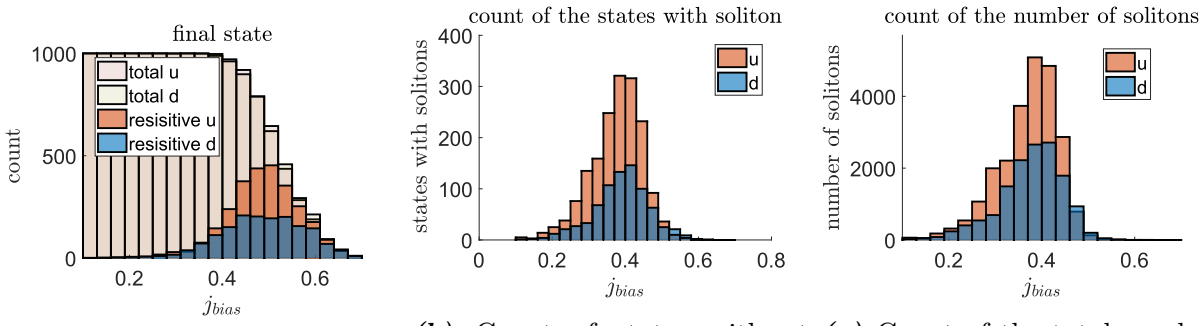


(a) $\vec{\phi}_1/2\pi$ ***(b)*** $\partial_\tau \vec{\phi}_1/2\pi$

Figure 3.17: Identification of solitons from trajectories as given in Fig. 3.16 based on jumps in the **(a)** phase by $\Delta\vec{\phi}/2\pi \approx 1 \pm 0.3$ over the width associated with peaks in the **(b)** time derivative of the phase. If the phase changes by . Color encodes the different locations $x = (1/4, 3/4, 1)L$ in the junction (bias current $j_{\text{bias}} = 0.15152$, temperature $\mathcal{T} = 0.002$).

Identification of solitons To automate the identification of solitons, we first pre-process using a median filter over 3 data points. This filter is known to conserve sharp edges as exemplarily shown for the phase evolution at three locations in Fig. 3.17. We see that the system remains in a superconducting state up to approximately $\tau = 200$ at which time we obtain a single soliton propagating back and forth. The corresponding gradients of the phase $\partial_\tau \vec{\phi}_1$ are shown in Fig. 3.17b. The markers indicate the position of peaks. Solitons are identified if over the respective peak width associated with these peaks the phase from Fig. 3.17a jumps by $\Delta\vec{\phi}/2\pi \approx 1 \pm 0.3$. Crosses in Fig. 3.17 indicate the identification of a soliton. Besides the thermal noise, there is a finite-size effect in small junctions, where the solitons could be distorted by the boundaries in either direction.

Histogram We now implement the algorithm from Fig. 3.17 to count the number of solitons present in a trajectory of fixed duration and fixed bias current exemplary shown Fig. 3.16. The phase is only allowed to grow up to $100 \cdot 2\pi$, i.e. it can contain anything between a maximum number of 100 solitons or a single soliton propagating back and forth 100 times after which the simulation is terminated. In Figures 3.18b and 3.18c, we respectively show histograms of the count of trajectories containing at least one soliton and the respective total number of solitons identified. Comparing the histograms in the presence of the driving mechanism (blue labelled $d = 1$) and the absence of the driving mechanism (red labelled $d = 0$), we clearly find a strong reduction of the number of resistive states in



(a) Type of final state

(b) Count of states with at least one solitons

(c) Count of the total number of solitons detected

Figure 3.18: Using a total of 5000 trajectories obtained from Eq. (3.65) initialised in a thermal state with different equally spaced initial bias currents between 0 and 0.7 we determine histograms for different system properties detected in the simulation time interval $\Delta\tau/2\pi = 100$ for both driven system (labelled d) and undriven one (labelled u). The driving is only switched on after an initial thermalisation phase without driving in which many of the junctions already slipped into an resistive state reduction of yellow counts in **(a)**. In **(a)** we show the histogram of the number of resistive and total (that is resistive and superconducting) as a function of the bias current. **(b)** Histogram for the counts of events in which one trajectory contains solitons. **(c)** Count of the number of solitons measured (soliton identified by $\Delta\vec{\phi}/2\pi \approx 1 \pm 0.3$ using algorithm from Fig. 3.17, $\mathcal{T} = 0.002$, $\epsilon(t)$-Model (Eq. (3.32), $\nu_1 = 0$, $\nu_2 = 0.1$, $L = 2$ $n_{\text{junc}} = 2$ $f = 3/4$)

Fig. 3.18a. Additionally, from Fig. 3.18b we find that the cooling mechanism leads to a reduction in the number of states that contain solitons. We also find that the total number of solitons is strongly suppressed (Fig. 3.18c).

The suppression of the excitation of thermal solitons can be understood as follows. In the linear regime, the spatially homogeneous bias current leads to a shift in the spatially homogeneous mode (see Sec.3.2. For a single Josephson junction this shift approximately reduces the effective Josephson plasma frequency by $\sqrt{\cos(\phi_0)}$ with $\phi^0 = \arcsin\left(J_{bias}/J_1^C\right)$ (see Sec. 3.2). More interestingly, the bias current also effectively lowers the excitation energy of the spatially homogeneous mode and tilts the washboard potential in Fig. 1.2. The tilt and shift amplify the non-linearity of the Josephson Junction (see also Eq. (2.18)). Therefore, the thermal excitation of homogeneous phase coupling to a large k_w modes can facilitate the excitation of thermal solitons. By reducing the phase fluctuation in the spatial homogeneous mode it is possible to suppress the switching into the resistive state. This effect relies on the spatial independence. For spatially dependent bias current, it becomes more important to cool those low momentum spatial modes, which have the same spatial dependence as the bias current. However, as we also effectively cool small momentum modes, we expect the cooling to survive in the presence of small spatial dependence of the bias current.

In order to numerically simulate large Josephson junctions in a reasonable amount of time, we are restricted to roughly $200/n_{junc}$ spatial modes for a stack of n_{junc} junctions. To keep the system sizes as small as possible, involving only a few thermally occupied modes, we require the dispersion of the normal mode frequencies to be very strong. For the regime studied, non-local Josephson electrodynamics can become relevant as the magnetic

field associated, for example, with a vortex can extend beyond the vortex core, leading to non-local phase influences on the vortices [252]. To ignore non-local electrodynamics (see also Appendix A.2.2) formally requires that the Josephson penetration length λ_J, which characterises typical spatial variations of the phase, is much larger than the c-axis London penetration length λ_c, i.e. $\lambda_c \ll \lambda_J$ [252], which characterises the typical spatial variations of the magnetic field. This requirement is not satisfied here, however, primarily we are only interested in thermal excitations associated with low frequencies. These include low-momentum normal modes as well as modes excited by parametric modulation. However, different to many studies of non-linear Josephson Junction, we do not excite modes directly through moving Josephson vortex lattices or by coupling external radiation to the phase of the superconducting order parameter. As the parametric drive only addresses modes with low in-plane momentum, local electrodynamics is justified for the purposes here. Highly non-linear dynamics such as solitons are only excited indirectly cooled through the cooling of low-frequency mode.

3.5.3 Summary of findings

A parametric cooling scheme was proposed for the cooling of long stacks of Josephson junctions, where the spatial dependence of the phase cannot be ignored. The driving due to the external coherent excitation of phonon modes is modelled as both time-dependent permittivity ($\epsilon(t)$-Model) and critical current ($J^C(t)$-Model). The proposed scheme has been investigated as a function of length, type of driving and system parameters. We identified a large parameter range, where laser cooling of phase fluctuations is feasible and derived the corresponding achievable cooling efficiency. The parametric cooling of short junctions relies on capacitive coupling independent of the type of driving. For long junctions, inductive coupling leads to non-diagonal parametric modulations for $J^C(t)$-Model, which allows cooling spatially inhomogeneous modes in the absence of capacitive coupling.

$J^C(t)$-Model drives potentially resonantly driven modes less strongly and therefore allows for cooling even for materials with small in-plane dissipation. The cooling efficiency of $J^C(t)$-Model and $\epsilon(t)$-Model shows distinct dependence on junction length and relative arrangements of the driving amplitude in the two physical junctions of the bilayer. For $\epsilon(t)$-Model, it is essential to drive the high-frequency junction, while for $J^C(t)$-Model anti-phase driving is essential to cool short junction. For cooling higher spatial modes, on the other hand, it is crucial to driving the high-frequency junction in both cases. $\epsilon(t)$-Model is found to be prone to resonance catastrophes, where the cooling sideband of the spatially homogeneous mode happens to excite spatially inhomogeneous modes resonantly. To reduce the associated heating, successful laser cooling of long junctions requires to avoid driving of the low-frequency junction. The heating can be additionally suppressed by choosing materials with substantial in-plane dissipation. However, an increase in in-plane dissipation negatively affects the cooling efficiency of high momentum modes, thus limiting the achievable cooling efficiency for a long junction.

The full non-linear equations were only investigated for $\epsilon(t)$-Model, as the driving of critical current was unstable in the presence of broadband pulses. The way the junctions

enters the resistive state was shown to depend on both junction length and bias current. For small junctions or high bias current, the phase slips homogeneously. For long junctions and low currents, an intermediate solitonic state involving thermally excited solitons was found, which can be characterised by small discrete voltage steps. The number of solitons was found to be suppressed by the cooling mechanism. We, therefore, find that the stabilisation of the low-momentum modes is sufficient to suppress highly non-linear dynamics, which is in agreement with the findings in Ref. [32]. In Ref. [290], it was found that pancake vortices, which are topological excitations in the superconducting phase, provide viscous friction for Josephson vortices. Being able to cool Josephson vortices might suggest reversely that it might be possible to also cool pancake vortices indirectly. The same authors also identified an attractive interaction of Josephson vortices with pancake vortices [291]. This finding suggests that it might be possible to cool thermally excited pancake vortices. These, which live in the superconducting plane. The infinitely thin junction along the y-axis assumed throughout this work, makes spatially in-homogeneous excitation along y very energetic such that they can be ignored. This model can therefore not capture topological excitation of the superconducting sheets, which are believed to play a role in a Kosterlitz-Thouless physics approaching the phase transition (see Sec. A.5). Therefore, describing topological excitations would require an extension of the model along the y axis. In essence, this is trivial and is not believed to change the physics qualitatively as in the linearized regime small excitations of the phase travelling along x and y direction are expected to evolve independently.

3.6 Switching between resistive, superconducting and soliton states

In Sec. 3.1.4, we model the excitation of phonon modes through infrared pulses as a parametric modulation of the permittivity or critical current. However, it is also possible to directly excite the gauge-invariant phase difference itself by directly coupling external THz radiation to the gauge-invariant phase [204, 292–294]. Weak radiation is used to probe the material response by measuring the reflectivity as schematically depicted in Fig. 3.3a, which reveals information about plasmon modes or the presence of a Josephson vortex lattice [295]. By increasing the radiation further, it is also possible to excite the inherently non-linear dynamics leading to the formation of solitons [293], the parametrically amplification of plasma waves [204] and generation of higher harmonics, which allow probing the otherwise optically silent striped phase [294].

The wavelengths used in these THz experiments are much larger than the typical junctions size. Consequently, external radiation can only efficiently couple to modes whose excitation can give rise to macroscopic electric fields across the junctions (see discussion in Sec. 3.2.1). The effect of the external radiation is to synchronise the dynamics in all junctions, reducing the problem to a single junction treatment.

Studying this regime in Ref. [32] for a monolayer cuprate, we show how strong THz pulses with controlled amplitude and frequency can switch between superconducting, resistive, and

solitonic states. In contrast to the work presented in this chapter, we focus on the low-temperature regime where thermal fluctuations are small such that thermal solitons are not playing a role in the dynamics. Any change in the macroscopic state is due to external driving. We also remain in the parameter regime where the validity of the mean-field model has been tested experimentally [296]. The effects of light-induced pair breaking as well as microscopic materials details should be negligible. Furthermore, for the short pulses employed, heating effects do not play a role.

Since the plasmon dispersion depends on the macroscopic state, the superconducting, resistive, and solitonic states reacts differently to external driving, thus creating parameter regimes in which only one transition responds to the pulse, while other excitation paths remain "dark". Therefore, tailored pulses can act as deterministic switches between macroscopic states. Roughly speaking, low-frequency driving destabilises high-voltage states, while high-frequency radiation can force the system into high-voltage states. This switching mechanism can be understood as a destabilisation of the centre-of-mass excitation of the Josephson phase, made possible by the highly non-linear nature of the light-matter coupling. The presence of an external bias current reduces the lowest order correction to the Hamiltonian given in Eq. (3.44) from quartic in $\delta\vec{\phi}$ in the absence of the bias current to cubic in the presence of a bias current, see Hamiltonian is given in Eq. (2.16). Therefore, the presence of a bias current allows to amplify the non-linear correction and thereby enhances the non-linear coupling between different modes of different in-plane momentum.[20] We find that a toy model consisting of only the lowest three spatial modes plus external driving already produces many of the features of the full simulation [32]. Our simple model gives rise to correct predictions not only for the excitation of the uniform resistive state but also for the highly localised moving soliton state where intuition could suggest a close connection to spatial modes with large in-plane momentum. However, our explanation is insufficient to predict the final state following the destabilisation. Comparing the control of deterministically excited soliton states in Ref. [32] with the suppression of thermal solitons found in Fig. 3.18, we see that the spatially homogeneous phase plays a major role in controlling the excitation of solitonic states. Physically, this observation is not unexpected as the bias current, is taken to be completely homogeneous throughout the long junction in both cases (see discussion close to Fig. 3.18).

Specific parameter regimes are identified in which the driving does not destroy the SC state, yet can destabilise the resistive state and thereby prohibit phase fluctuations from destroying the coherence between junctions. This type of driving might offer an unusual approach to laser cool or stabilise superconducting fluctuations. Different to the parametric cooling scheme such an approach would allow cooling of a monolayer material and does not rely on a very intricate model [32].

[20] This type of coupling mechanism is also exploited in the single junction sideband cooling scheme based on Ref. [78], as presented in Sec. 2.1.2.

3.7 Chapter summary

We proposed different schemes for cooling as well as controlling the phase dynamics in HTSC modelled as stacks of long Josephson Junctions. We explore both parametric driving and very strong THz radiation. We find that the cooling effect strongly depends on the type of modulation used. In fact, for modulation of the critical current, the cooling is found to arise even in the absence of capacitive coupling for long Josephson junctions. Cooling efficiency of 20% to 30% is achievable and visible as a reduction in the phase quadrature value as well as the measurable slipping current distribution. We find that though the driving scheme only efficiently cools low-momentum modes, it can also be used to suppress the generation of solitons in the junction, which dominate the switching mechanism for long junctions.

Chapter 4

Strongly driven open quantum systems

In the previous chapter, we presented a scheme for parametric cooling of phase fluctuations in long stacks of Josephson junctions through optical driving. The driving is sufficiently weak such that it does not influence the dissipation mechanism and driving is only added to the coherent part of the evolution. Consequently, driving and dissipation can be treated independently. However, with increasing driving strength, this assumption is expected to break down. This situation is similar to the one encountered in the ultrastrong coupling regime in circuit QED, where the coupling between two quantum subsystems can become so strong that it cannot be ignored on the cooling time-scales. The role of the strong classical driving field is taken by ultrastrong coupling to a second quantum system in QED.[1] Thermalising each decoupled subsystem in QED independently and adding the dominating coupling term afterwards would lead to spurious effects, e.g. the system might not relax to its ground state at zero temperature [178]. The weak coupling to the bath leads to transitions between the dressed states instead of the eigenstates of the decoupled Hamitlonian [178], here we will use similar ideas to solve the strongly driven system dynamics exactly and add the effect of the heat bath perturbatively, which goes beyond standard approximation allowing new physics to be discovered.

It is already known that strongly driven open quantum system can enter the intriguing regime of environment governed dynamics [237] (EGD). In the EGD regime, the system dynamics is predominantly determined by the details of the system-bath interaction [237]. However, in HTSC [297], as well as in many other condensed matter systems there exists no widely accepted microscopic model underlying the system-bath coupling. Directly observable manifestations of system-bath interactions such as decay and decoherence rates are often enough for the phenomenological description of a weakly driven system, e.g. as in the previous chapter. However, these quantities reveal little about the microscopic details of the system-bath interaction. The development of techniques that go beyond measuring decay and decoherence rates is, therefore, a highly desirable yet difficult task. A fascinating question is whether the environment-dependent dynamics in the regime of EGD can be employed

[1] It is possible to interpret the Floquet states associated with the time-periodic classical drive in terms of coupling the system to quantised radiation field in the classical large photon number limit [234, 241].

to infer microscopic details about the system-bath interaction. The main part of this chapter is therefore devoted to using strong driving to learn about the dissipation mechanism [298]. More explicitly, we show how strong parametric driving can be exploited to probe a harmonic oscillator for microscopic coupling parameter of the system-bath interactions.

In Sec. 4.2.1 we introduce our model of an isolated parametrically driven harmonic oscillator. The coupling operator between the system and a thermal heat bath is allowed to vary between position and momentum coupling. The corresponding driven quantum master equation is discussed in Sec. 4.2.3. In Sec. 4.3, we present our numerical findings on the coupling angle dependence for a range of temperatures and driving frequencies. In Sec. 4.4, we show that the coupling angle dependence can be absorbed into the spectral density of the heat bath. Parametric driving, therefore, provides a method to probe the spectral density of the heat bath. We conclude with an outlook on future work in Sec. 4.5.

4.1 Learning coupling mechanism to an environment

Given that solid-state systems are often "inaccessible", i.e. spectroscopic and scanning techniques are often restricted to the sample surface, and the fact that a phenomenological description in terms of decay rates is often sufficient to describe the decay towards an equilibrium state, it is not surprising that only very few schemes are known for studying dissipation processes in condensed matter. The ultra-high sensitivity of cavity optomechanical experiments allows calculating the slope of the local spectral density of a condensed matter heat bath by observing the non-Markovian behaviour of an optomechanical resonator coupled to it [299]. For weak coupling g compared to dissipation rate of the cavity κ, i.e. $g \ll \kappa$, the cavity light field adiabatically follows the random motion of the oscillator and therefore carries information about the environment of the mechanical oscillator. Carefully deconvolving all additional noise processes, it is possible to isolate the original noise acting on the mechanical oscillator alone. Implementation of this scheme for HTSC is expected to be challenging, as the expected quality factors for either a nano-electronic resonator circuit printed on top of HTSC or a cavity mode of the material coupled to an oscillating degree of freedom are significantly lower and it might not allow for the detection of THz radiation with sufficient precision.

An alternative approach for measuring the bath spectral density of the environment uses qubits as noise probes in combination with dynamical decoupling [300, 301]. The influence of multi-pulse sequences on the decoherence rate can be related to the spectral density of the underlying dephasing bath, which allows to reconstruct it. However, the initialisation procedure implicit in these protocols might not be possible for a range of condensed matter systems. Otherwise, the learning the bath spectral density might be possible through quantum process tomography [302].

These examples are either non-linear, accessible to quantum process tomography and state initialisation, driven or can be resolved with ultra-high precision, to learn about the microscopic details of the underlying coupling mechanism between system and bath. In the next section, we are going to focus on the effects driving can have on open quantum systems.

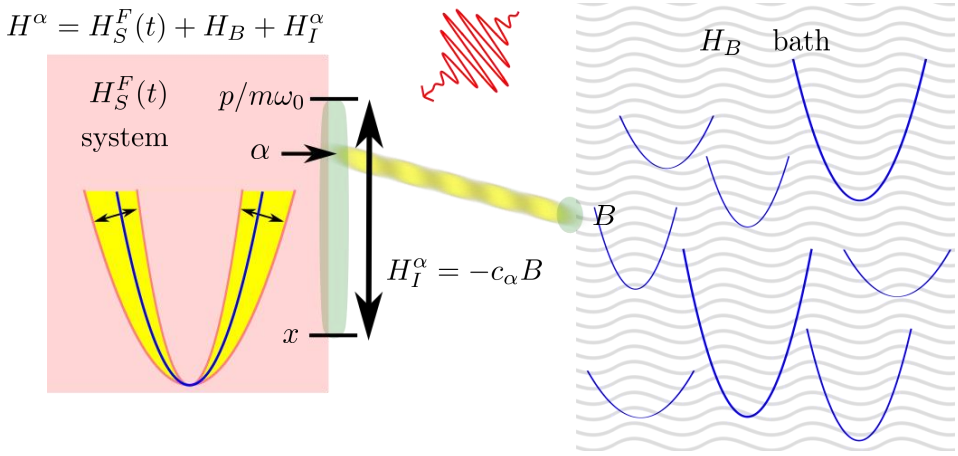


Figure 4.1: The system of interest is comprised of a parametrically driven harmonic oscillator and a bath of harmonic oscillators with Hamiltonians $H_{\mathrm{S}}^F(t)$ and H_{B}, respectively. The system-bath interaction is described by the interaction Hamiltonian H_I^α, where the parameter α allows one to continuously adjust the interaction from position ($\alpha = 0$) to momentum coupling ($\alpha = \pi/2$). The parametric driving affects both the system and dissipation mechanism as indicated by the red arrow.

4.2 Probing for dissipation mechanism through strong parametric driving

In the next subsection, we start with a discussion of the parametrically driven harmonic oscillator, which is coupled to the bath via a superposition of position and momentum operator. We then discuss the form of the Floquet Born-Markov master equation for the parametrically driven harmonic oscillator (also see Sec. 2.3), taking care to avoid an unjustified rotating wave approximation (see the rightmost panel of Fig. 2.6). We then show the results regarding the dependence of the steady-state values of the mean position and momentum quadrature as a function of system-bath coupling and temperature. We finish with a detailed discussion. This work was published in Ref. [298]

4.2.1 Single strongly parametrically driven harmonic oscillator

Incorporating strong driving in the presence of dissipation without the implementation of a mRWA turns out to be a formidable task for a general unbounded system. We will, therefore, restrict ourselves to the simplest possible case of a parametrically driven harmonic oscillator (see also discussion on page 16 for justification regarding HTSC). This situation is for example realised for the linearised version of the isolated Josephson Junctions or a stack where the phase in each junction moves uniformly and is captured by a Hamiltonian of the form given in Eq. (2.54).

Here we describe our theoretical model for a driven harmonic oscillator coupled to a

thermal bath.

4.2.2 Isolated system dynamics

We consider a harmonic oscillator with mass m and time-dependent frequency $\omega_F(t)$. The corresponding Hamiltonian is given by [303–309]

$$H_{\mathrm{S}}^F(t) = \frac{p^2}{2m} + \frac{1}{2}m\omega_F^2(t)x^2, \tag{4.1}$$

where the position and momentum operators x and p obey the canonical commutation relation $[x,p] = \mathrm{i}\hbar$. We assume that the oscillator frequency $\omega_F(t)$ is modulated periodically with frequency ω_L,

$$\omega_F^2(t) = \omega_0^2[1 + F\cos(\omega_L t + \phi_L)], \tag{4.2}$$

where F is the relative modulation amplitude.

Throughout this chapter, we assume that $F = 0$ for $t < 0$. It follows that the Hamiltonian in Eq. (4.1) reduces to an ordinary harmonic oscillator with frequency ω_0 and mass m for negative times. In our model, the driving amplitude is suddenly switched on at $t = 0$ and held at a constant value for $t > 0$. Note that the driving in Eq. (4.1) breaks the symmetry between position and momentum variables.

The time-dependent Schrödinger equation associated with the Hamiltonian in Eq. (4.1) can be solved [309–313],

$$\mathrm{i}\hbar\frac{\partial}{\partial t}\psi_n(x,t) = H_{\mathrm{S}}^F(t)\psi_n(x,t)\,. \tag{4.3}$$

The solutions $\psi_n(x,t)$ $(n = 0,1,2...)$ are described in Appendix B.2 and reduce to the familiar harmonic oscillator states for $F = 0$. It is possible to introduce generalized creation and annihilation operators that operate on the states $\psi_n(x,t)$ like in the undriven harmonic oscillator [230],

$$A(t)\,|\psi_n(t)\rangle = \sqrt{n}\,|\psi_{n-1}(t)\rangle\,, \tag{4.4a}$$

$$A^\dagger(t)\,|\psi_n(t)\rangle = \sqrt{n+1}\,|\psi_{n+1}(t)\rangle\,. \tag{4.4b}$$

Note that the operators A and $A^\dagger$ are time-dependent. Time-dependent Hamiltonians generally do not guarantee the validity of uncertainty relations and commutation relations [311]. However, the solution to the isolated system dynamics for our system Hamiltonian in Eq. (4.1) does not violate the uncertainty and commutation relations between canonical position and momentum operators [313].

We assume that the driven oscillator is weakly coupled to a heat bath of N harmonic oscillators with Hamiltonian

$$H_B = \sum_{r=1}^{N}\left(\frac{p_r^2}{2m_r} + \frac{1}{2}m_r\omega_r^2 x_r^2\right). \tag{4.5}$$

Here position and momentum operators of the rth oscillator with mass m_r and frequency ω_r are denoted by operators x_r and p_r, respectively.

System-bath coupling H_{I}^{α}

The coupling between the bath and system is described by the Hamiltonian

$$H_{\mathrm{I}}^{\alpha} = -c_{\alpha} B, \tag{4.6}$$

where the parameter α in the coupling operator

$$c_{\alpha} = \cos(\alpha) x + \sin(\alpha) \frac{p}{m\omega_0} \tag{4.7}$$

describes which degrees of freedom are coupled to the bath. Note that $c_{\alpha=0}$ corresponds to position coupling, and $c_{\alpha=\pi/2}$ realises momentum coupling [314–317].

The bath operator B in Eq. (4.6) is given by

$$B = \sum_{r=1}^{N} \kappa_r x_r \,, \tag{4.8}$$

and κ_r are coupling constants. The system-bath interaction Hamiltonian in Eq. (4.6) thus couples the system operator c_{α} to the position operators of the bath.

With the definitions in Eqs. (4.1), (4.5) and (4.6) we arrive at the total Hamiltonian for the driven oscillator coupled to the bath,

$$H^{\alpha} = H_S^F(t) + H_B + H_I^{\alpha} \,. \tag{4.9}$$

The driving breaks the symmetry between x and p operator.

4.2.3 Driven version of the Born-Markov master equation

We assume the coupling to the bath to be weak and describe the quantum dynamics of the reduced density operator of the system ρ by a Born-Markov master equation [196] (see Appendix B.3),

$$\dot{\rho} = -\frac{\mathrm{i}}{\hbar}\left[H_{\mathrm{S}}^F(t), \rho\right] + \mathcal{K}\rho, \tag{4.10}$$

where the first term describes the coherent evolution and $\mathcal{K}\rho$ accounts for the interaction with the heat bath at temperature T,

$$\mathcal{K}\rho = -\frac{1}{\hbar^2}\int_0^{\infty} \mathrm{d}\tau \mathrm{Tr}_B \left\{\left[H_{\mathrm{I}}^{\alpha}, \left[\tilde{H}_{\mathrm{I}}^{\alpha}(t-\tau, t), \rho_B \otimes \rho(t)\right]\right]\right\}. \tag{4.11}$$

Here

$$\rho_B = \exp\left(-\frac{H_B}{k_{\mathrm{B}}T}\right) / \mathrm{Tr}_B \left\{\exp\left(-\frac{H_B}{k_{\mathrm{B}}T}\right)\right\} \tag{4.12}$$

is the density operator of the bath in thermal equilibrium and k_B is Boltzmann's constant. The operator $\tilde{H}_\mathrm{I}^\alpha$ in Eq. (4.11) is defined as

$$\tilde{H}_\mathrm{I}^\alpha(t,t_0) = [U_S(t,t_0)U_B(t,t_0)]^\dagger H_\mathrm{I}^\alpha [U_S(t,t_0)U_B(t,t_0)], \tag{4.13}$$

where $U_B(t,t_0) = \exp[-(\mathrm{i}/\hbar)H_B(t-t_0)]$ describes the free evolution of the bath. The time evolution operator of the system is

$$U_S(t,t_0) = \begin{cases} \mathcal{T}_+ \exp\left(-\frac{\mathrm{i}}{\hbar}\int_{t_0}^{t} \mathrm{d}t' \left[H_\mathrm{S}^F(t')\right]\right), & t \geq t_0, \\ \mathcal{T}_- \exp\left(\frac{\mathrm{i}}{\hbar}\int_{t}^{t_0} \mathrm{d}t' \left[H_\mathrm{S}^F(t')\right]\right), & t < t_0, \end{cases} \tag{4.14}$$

where $\mathcal{T}_+$ and $\mathcal{T}_-$ are the chronological and anti-chronological time ordering operators, respectively.

Equation (4.11) can be evaluated for any system-bath interaction that justifies a Born-Markov approximation. In order to be specific, we assume that the heat bath exhibits an Ohmic spectral density with a Lorentz-Drude cutoff $\Omega \gg \omega_0$ [196], i.e.,

$$J(\omega) = \frac{1}{\pi}\gamma\omega m \frac{\Omega^2}{\Omega^2+\omega^2}, \tag{4.15}$$

where γ is the decay rate. This choice allows us to calculate the thermal correlation time of the bath explicitly and thus gives us full control over the validity of the Markov approximation. We find $\tau_B = \hbar/(2\pi k_B T)$ (see Appendix B.3), and all considered temperatures T in Sec. 4.3 are chosen such that $\tau_B \ll 1/\gamma$ as required by the Markov approximation. With these assumptions Eq. (4.11) can be written as (see Appendix B.3)

$$\begin{aligned} \mathcal{K}\rho = & \frac{1}{\hbar}\int_{-\infty}^{\infty} \mathrm{d}\omega J(\omega) n(\omega) \\ & \times \int_0^\infty \mathrm{d}\tau\, e^{\mathrm{i}\omega\tau} \left[\tilde{c}_\alpha(t-\tau,t)\rho, c_\alpha\right] + \text{H.c.}, \end{aligned} \tag{4.16}$$

where H.c. is the Hermitian conjugate and

$$n(\omega) = \frac{1}{e^{\hbar\omega/k_B T}-1} \tag{4.17}$$

is the Bose-Einstein distribution. The operator $\tilde{c}_\alpha$ is defined as

$$\tilde{c}_\alpha(t,t_0) = [U_\mathrm{S}(t,t_0)]^\dagger c_\alpha U_\mathrm{S}(t,t_0) \tag{4.18}$$

and depends on the driving amplitude F via the time evolution operator in Eq. (4.14). In order to simplify the master equation further we take advantage of the fact that there exists a complete set of solutions to the isolated system dynamics. The details of the derivation

are given in Appendix B.3. We find

$$\begin{aligned}\dot{\rho} = &-\frac{\mathrm{i}}{\hbar}\left[H_{\mathrm{S}}^{F}(t),\rho\right]\\ &+\Big\{\mathcal{S}_1^{\alpha}(t)\left[A(t)\rho A^{\dagger}(t)-A^{\dagger}(t)A(t)\rho\right]\\ &\quad+\mathcal{S}_2^{\alpha}(t)\left[A^{\dagger}(t)\rho A(t)-A(t)A^{\dagger}(t)\rho\right]\\ &\quad+\mathcal{S}_3^{\alpha}(t)\left[A(t)\rho A(t)-A(t)A(t)\rho\right]\\ &\quad+\mathcal{S}_4^{\alpha}(t)\left[A^{\dagger}(t)\rho A^{\dagger}(t)-A^{\dagger}(t)A^{\dagger}(t)\rho\right]\\ &\quad+\mathrm{H.c.}\Big\},\end{aligned} \tag{4.19}$$

where the time-dependent functions $\mathcal{S}_i^{\alpha}$ ($i\in\{1,2,3,4\}$) are defined in Appendix B.3 in terms of solutions to the system of a classical parametrically driven harmonic oscillator. In order to be consistent with the separation of time-scales required by the Markov approximation [196, 198,318], the definitions of $\mathcal{S}_i^{\alpha}$ ($i\in\{1,2,3,4\}$) involve a time average to exclude any dynamics faster than the bath response time [see Eq. (B.54)]. In this way we avoid tracking all the degeneracies in the Floquet eigenenergies [229,242]. This approach is similar the one used in Ref. [225], where a Fourier expansion of the density matrix elements in the basis of Floquet modes is used to set those elements of the Fourier expansion to zero, which correspond to ignoring transitions larger than a truncation frequency ω_{trunc} as described below Eq. (2.77).

We show in Sec. 4.3 that Eq. (4.19) can be approximated by a simpler master equation in the high-temperature regime, which we refer to as high-temperature master equation (HTME). The HTME is obtained by ignoring the driving term in Eq. (4.18) which results in

$$\tilde{c}_{\alpha}(t,t_0)\to e^{\frac{\mathrm{i}}{\hbar}H_{\mathrm{S}}^{0}(t-t_0)}c_{\alpha}e^{-\frac{\mathrm{i}}{\hbar}H_{\mathrm{S}}^{0}(t-t_0)}. \tag{4.20}$$

With this additional approximation, the HTME can be written as

$$\begin{aligned}\dot{\rho} = &-\frac{\mathrm{i}}{\hbar}\left[H_{\mathrm{S}}^{F}(t),\rho\right]\\ &+\Big\{\frac{\gamma}{2}n(\omega_0)\left[a^{\dagger}\rho,a\right]+\frac{\gamma}{2}(n(\omega_0)+1)\left[a\rho,a^{\dagger}\right]\\ &\quad+\frac{\gamma}{2}n(\omega_0)e^{\mathrm{i}2\alpha}\left[a^{\dagger}\rho,a^{\dagger}\right]\\ &\quad+\frac{\gamma}{2}(n(\omega_0)+1)e^{-\mathrm{i}2\alpha}\left[a\rho,a\right]+\mathrm{H.c.}\Big\},\end{aligned} \tag{4.21}$$

where $a^{\dagger}$ and a are the familiar creation and annihilation operators of the undriven harmonic oscillator.

4.3 Results

Here we present a systematic study of the quasi-steady state of the driven harmonic oscillator as a function of the external driving parameters, the temperature of the bath and the coupling angle α in the system-bath Hamiltonian. In a first step, we describe how we characterise

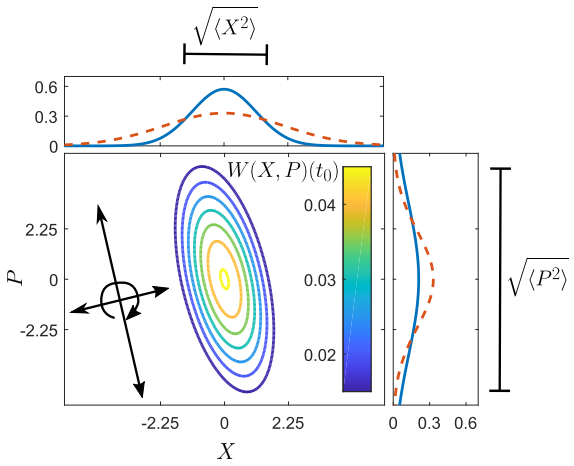


Figure 4.2: The central panel shows a snapshot of $W(X,P)$ at time $t_0 \gg 1/\gamma$. The black arrow next to the ellipse indicates its dynamics consisting of simultaneous squeezing and rotation. The top and right panel contain the resulting probability distributions of the quadratures X and P (solid blue line). The red dashed line in the side panels corresponds to the initial thermal state for $t < 0$. The width of the probability distribution is given by $\sqrt{\langle Y^2\rangle}$ with $Y = X, P$. Driving parameters are $b = 0.1$, $q = 0.5$ and $\zeta = 0.7$ as defined in the text.

the quasi-steady state of the oscillator in Sec. 4.3.1. The numerical results are shown in Sec. 4.3.2.

We introduce dimensionless parameters which are frequently used to characterise periodically driven systems [218, 319, 320]. For the specific model at hand, $b = (2\omega_0/\omega_L)^2$ is proportional to the ratio of natural and driving frequencies squared and $q = 2F\omega_0^2/\omega_L^2$ characterises the effective driving strength. We further define $\zeta = \hbar\omega_0/(k_B T)$, which is proportional to the inverse temperature. In order to be consistent with the Born-Markov approximation, we set the decay rate to $\gamma/\omega_0 = 0.02$ and only consider parameters $\zeta \leq 3$ such that $\tau_B \gamma = \zeta\gamma/(2\pi\omega_0) \ll 1$. Note that γ enters the master equation (Eq. (4.19)) implicitly via the spectral density in Eq. (4.15).

4.3.1 Observables

A descriptive way to illustrate the quantum state of the oscillator is given by the Wigner quasi probability distribution defined as [321, 322]

$$W(X,P)(t) = \frac{1}{\pi}\int_{-\infty}^{\infty} \langle X+Y|\rho(t)|X-Y\rangle e^{-2iPY/\hbar}\, dY\,. \tag{4.22}$$

In this equation, the density operator $\rho(t)$ is determined by Eq. (4.19) and X and P are dimensionless position and momentum operators, respectively,

$$X = \sqrt{\frac{m\omega_0}{\hbar}}x\,, \tag{4.23a}$$

$$P = \sqrt{\frac{1}{m\omega_0\hbar}}p\,. \tag{4.23b}$$

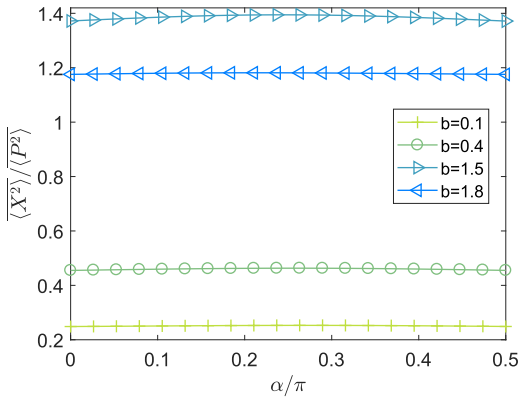


Figure 4.3: Ratio of the time averaged quadratures $\overline{\langle X^2\rangle}/\overline{\langle P^2\rangle}$ as a function of the coupling angle α and for different values of b. We have chosen $q = 0.5$, $\zeta = 10^{-4}$.

For $t < 0$ the system is in a thermal state, which corresponds to a circular quasi-probability distribution with equally sized position and momentum quadratures $\langle X^2\rangle$ and $\langle P^2\rangle$, respectively. Once the driving is switched on at $t = 0$, the shape of the Wigner function changes in time. A snapshot of $W(X,P)(t_0)$ at $t_0 \gg 1/\gamma$ is shown in Fig. 4.2. In contrast to the thermal distribution, $W(X,P)(t_0)$ has an elliptic shape with a tilted major axis. The value of $\langle X^2\rangle$ ($\langle P^2\rangle$) has decreased (increased) with respect to the thermal distribution. Even though this is just an example of the Wigner function at a particular point in time, the whole dynamics of $W(X,P)(t \gg 1/\gamma)$ can be described by an ellipse rotating around the origin with period $4\pi/\omega_L$. During one revolution the angular velocity of rotation changes in time, and the ellipse grows and shrinks along its major and minor axis.

The dynamics of $\{\langle X^2\rangle, \langle P^2\rangle, \langle XP+PX\rangle\}$ can be obtained from a closed set of equations since the total Hamiltonian H^α in Eq. (4.9) is quadratic and therefore preserves the Gaussian nature of the initial thermal state [323–328]. This set of equations is derived from the full master equation (4.19) and given in Appendix B.3.1. A similar closed set of equations can be obtained from the HTME in Eq. (4.21), and the corresponding results are denoted by $\langle \ldots\rangle_{\mathrm{HTME}}$. In the following we consider the steady-state regime $t \gg 1/\gamma$ and restrict our analysis to $\overline{\langle X^2\rangle}$ and $\overline{\langle P^2\rangle}$, where the bar indicates a time average over the interval $\Delta t \approx 1/\gamma \gg 2\pi/\omega_L$. It follows that $\sqrt{\overline{\langle X^2\rangle}}$ and $\sqrt{\overline{\langle P^2\rangle}}$ characterise the width of the time-averaged Wigner function in X and P, respectively.

4.3.2 Numerical results

Here we systematically investigate the dependence of $\overline{\langle X^2\rangle}$ and $\overline{\langle P^2\rangle}$ on the parameters b, ζ and α. In a first step, we find that the ratio $\overline{\langle X^2\rangle}/\overline{\langle P^2\rangle}$ is approximately independent of the coupling angle α as shown in Fig. 4.3. This ratio only depends on the driving frequency and strength, and is larger (smaller) than unity for $b > 1$ ($b < 1$). The shape of the time-averaged Wigner function thus deviates significantly from a circle in the presence of the parametric driving. The results in Fig. 4.3 correspond to the high-temperature limit $\zeta = 10^{-4}$. However, we find that the ratio $\overline{\langle X^2\rangle}/\overline{\langle P^2\rangle}$ is also approximately independent of ζ for the considered

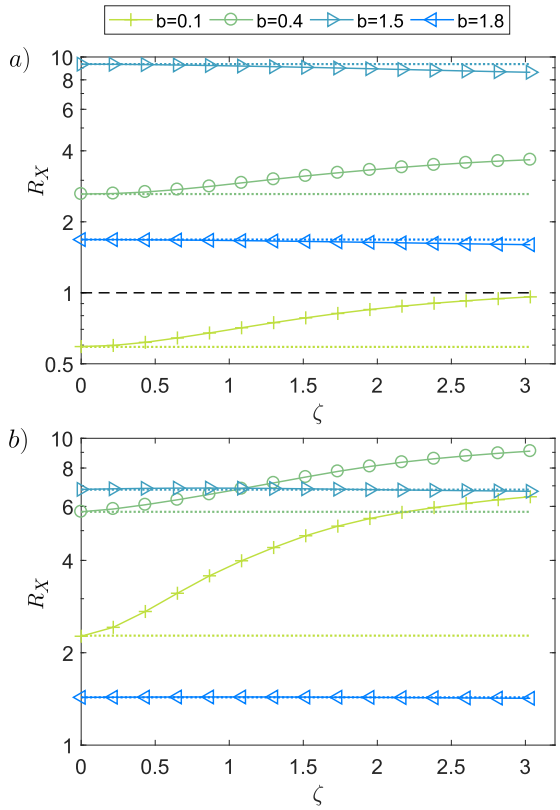


Figure 4.4: R_X as a function of inverse temperature ζ for $q = 0.5$, different driving frequencies and coupling angle a) $\alpha = 0$ and b) $\alpha = \frac{\pi}{2}$. Dotted lines of the same color indicate the results obtained from the evolution of the HTME. Dashed line at $R_X = 1$ in a) is a guide to the eye.

range of values $\zeta \in \left[10^{-4}, 3\right]$.

The previously discussed dependence of $\overline{\langle X^2 \rangle}$ and $\overline{\langle P^2 \rangle}$ allows us to restrict the following analysis to one of the two quadratures. We choose $\overline{\langle X^2 \rangle}$ and investigate its dependence on b, α and ζ by introducing the short-hand notation

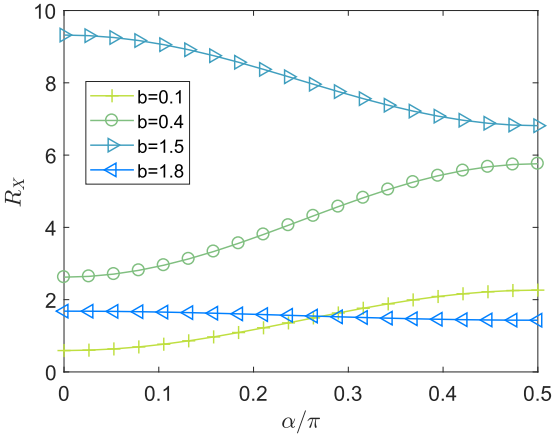
$$R_X = \overline{\langle X^2 \rangle} / \langle X^2 \rangle_{\text{thermal}}, \tag{4.24}$$

where $\langle X^2 \rangle_{\text{thermal}}$ is the undriven initial thermal value of $\overline{\langle X^2 \rangle}$. A value of $R_X > 1$ [$R_X < 1$] thus means that the driving enhances [reduces] the value of $\overline{\langle X^2 \rangle}$ compared to its thermal value.

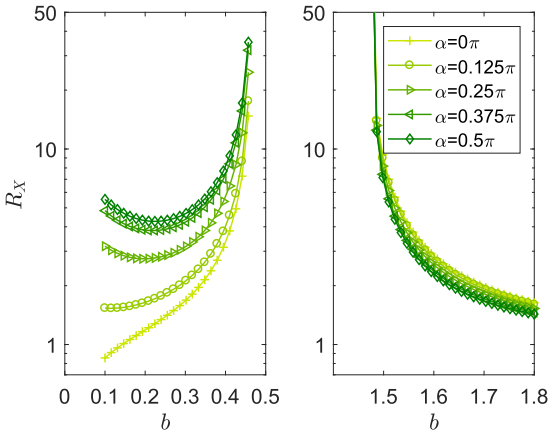
The dependence of R_X on ζ is shown in Figs. 4.4a) and b) for position and momentum coupling, respectively. Note that all values for R_X in Fig. 4.4 differ from unity and hence the parametric driving changes the value of $\overline{\langle X^2 \rangle}$ compared to $\langle X^2 \rangle_{\text{thermal}}$. Furthermore, we note that the results for R_X in Fig. 4.4 differ significantly for position and momentum coupling. Most prominently, $R_X > 1$ for all curves in Fig. 4.4b) (momentum coupling), while $R_X < 1$ for position coupling and$b = 0.1$. The reduction of $(R_X)_{\zeta \to 0}$ below unity for position coupling and fast driving ($b \ll 1$) has already been studied in Refs. [323,329–331]. In general, we find that R_X strongly increases with ζ for both coupling types if $b < 1$. On the other hand, R_X shows a much weaker dependence on ζ for $b > 1$. The value of $(R_X)_{b>1}$ slightly

decreases with ζ for position coupling and remains approximately constant for momentum coupling.

In order to illustrate the significance of the ζ-dependence of R_X, we show the results for $(R_X)_{\mathrm{HTME}}$ obtained via the HTME in Eq. (4.21) by the horizontal dotted lines in Fig. 4.4. Since they exhibit no ζ-dependence, the temperature dependence of R_X predicted by the full master equation is a direct consequence of the parametric driving on the system-bath coupling. The differences between the HTME and full master equation are most pronounced near $\zeta = 3$ and for $b = 0.1$. On the other hand, we find that R_X converges to $(R_X)_{\mathrm{HTME}}$ in the limit $\zeta \to 0$ which can be understood as follows. The thermal correlation time of the bath $\tau_B = \hbar/(2\pi k_B T)$ [196, 198] becomes much smaller than the typical timescale $\tau_S = \min(1/\omega_0, 1/\omega_L)$ of the system dynamics in the high-temperature limit. Consequently, the time-evolution of the system cannot influence the system-bath coupling.



(a) R_X as a function of coupling angle α for different values of b, driving strength $q = 0.5$ and inverse temperature $\zeta = 10^{-4}$.



(b) R_X as a function of inverse driving frequencies for different coupling angles α, driving strength $q = 0.5$ and inverse temperature $\zeta = 2$. The left and right panel correspond to driving above and below the resonance frequency, respectively.

Figure 4.5

Next we investigate the α-dependence of R_X in the high-temperature limit and for different driving frequencies. The results are shown in Fig. 4.5a. We observe an increase (decrease) of R_X with increasing α for $b < 1$ ($b > 1$). This behaviour is similar to the functional dependence of R_X on ζ and b shown in Fig. 4.4. We thus find that increasing α or ζ leads to qualitatively comparable effects. Most importantly, R_X shows a strong dependence on α for $b = 0.4$ and $b = 1.5$. Since R_X is monotonously increasing (decreasing) for $b = 0.4$ ($b = 1.5$), one can determine the coupling angle α by comparing $\overline{\langle X^2 \rangle}$ to $\langle X^2 \rangle_{\mathrm{thermal}}$. Note that the α-dependence of the results in Fig. 4.5a is a direct consequence of the counter-rotating terms $\propto e^{\pm 2i\alpha}$ in the HTME in Eq. (4.21).

In order to identify the parameter regime with the strongest α-dependence, we move away from the high-temperature limit and show R_X as a function of b for different values of α in Fig. 4.5b. Here the left and right panels correspond to the parameter range $b < 0.5$

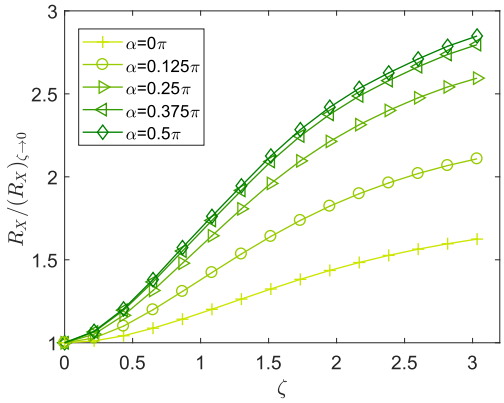


Figure 4.6: $R_X/(R_X)_{\zeta\to 0}$ as a function of ζ for $b = 0.1$, $q = 0.5$ and different values of α. The values of $(R_X)_{\zeta\to 0}$ can be obtained from the $b = 0.1$ curve in Fig. 4.5a.

and $b > 1.45$, respectively. For values closer to $b = 1$ the solutions become unstable and no steady-state can be achieved. Figure 4.5b shows that R_X exhibits the strongest dependence on α for $b \approx 0.1$. In particular, note that the range of the R_X values from $\alpha = 0$ to $\alpha = \pi/2$ is larger than in the corresponding curve for $b = 0.1$ in Fig. 4.5a due to the different ζ values.

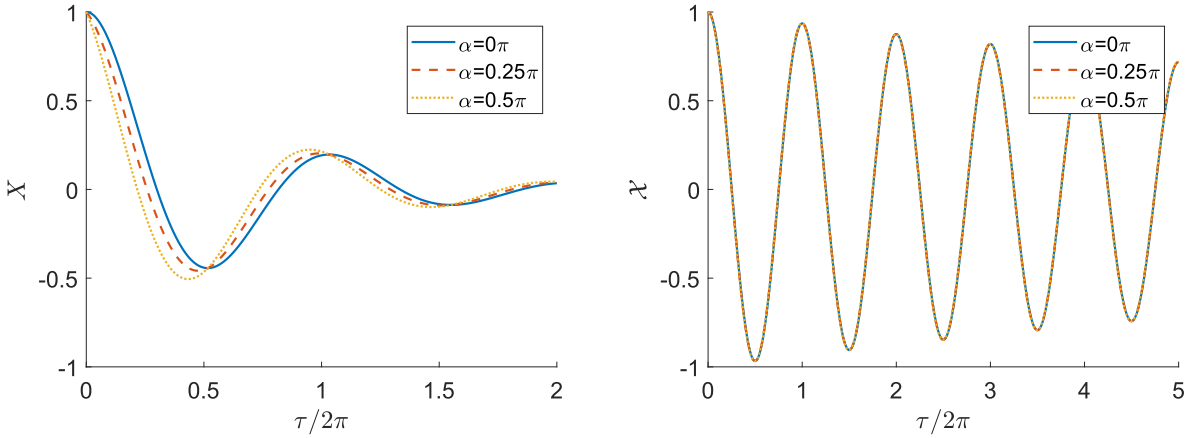
Finally, we focus on $b = 0.1$ and investigate the ζ-dependence of R_X for different values of α. We find that R_X increases relative to its $\zeta \to 0$ value for all considered values of α as shown in Fig. 4.6. The relative increase with ζ is the largest for $\alpha = \pi/2$ and the smallest for $\alpha = 0$. Furthermore, we find that small changes in α change the ζ-dependence of $R_X/(R_X)_{\zeta\to 0}$ most significantly near $\alpha = 0$.

Two conclusions can be drawn from the results in Fig. 4.6. First, increasing the value of ζ increases the spread of R_X with α. It thus becomes easier to determine α via a comparison of $\overline{\langle X^2\rangle}$ and $\langle X^2\rangle_{\text{thermal}}$ for smaller temperatures of the bath. Second, the difference of the ζ-dependence of R_X for various choices of α opens up a second route to determining α. For example, one could increase ζ by a given factor and measure the corresponding increase in R_X. According to Fig. 4.6, this increase is a unique function of α. Note that this approach works best for small α where the ζ-dependence of R_X is most sensitive to changes in α.

4.4 Discussion of α-dependence

The strong α dependence of the results in Sec. 4.3 is a direct consequence of the driving. In order to see this, we note that the full master equation (4.19) reduces to the HTME in Eq. (4.21) in the case of an undriven system ($F = 0$). Since only the counter-rotating terms exhibit an α dependence, all α dependent terms are of the order of γ/ω_0 for $F = 0$. In the regime of weak system-bath coupling $\gamma/\omega_0 \ll 1$ considered here, the α dependence is negligibly small. It is thus justified to perform a rotating-wave approximation [196] in the HTME which completely removes the α dependence and reduces the HTME to the standard quantum optical master equation. With this approximation, the density operator and hence all expectation values are independent of α in the undriven regime.

Note that the approximate α independence in the absence of the driving is not only a feature of our quantum model described in Sec. 4.2.1, but extends to the corresponding classical model if $\gamma/\omega_0 \ll 1$.



(a) $\gamma/\omega_0 = 0.5$ ***(b)*** $\gamma/\omega_0 = 0.02$

Figure 4.7: A deflected ($X(0) = 1$ and $P(0) = 1$) classical harmonic oscillator with distinct damping rates γ undergoing damping described by Eq. (4.25a) and (4.25b) for $\alpha = 0, \pi/4, \pi/2$.

The equations of motion for the classical, dimensionless position and momentum variables $\mathcal{X}$ and $\mathcal{P}$ for $F = 0$ are (Eq. (B.84) and Eq. (B.85))

$$\frac{d\mathcal{X}}{d\tau} = -\frac{\gamma}{\omega_0}\sin^2(\alpha)\mathcal{X} + \mathcal{P}\left(1 + \frac{\gamma}{2\omega_0}\sin(2\alpha)\right), \tag{4.25a}$$

$$\frac{d\mathcal{P}}{d\tau} = -\frac{\gamma}{\omega_0}\cos^2(\alpha)\mathcal{P} - \mathcal{X}\left(1 - \frac{\gamma}{2\omega_0}\sin(2\alpha)\right), \tag{4.25b}$$

where we ignored noise terms and introduced $\tau = t\omega_0$. These equations coincide with the equations of motion for $\langle X\rangle$ and $\langle P\rangle$ derived from the HTME, and all α dependent terms are proportional to γ/ω_0. The classical motion thus only exhibits a significant α dependence for extremely strong damping of the order of $\gamma \approx \omega_0$, which is outside the parameter range considered here.

Having established that the strong α dependence of our results is a consequence of the driving, we now investigate its origin in more detail. According to [237], our results are a manifestation of EGD which can be explained in terms of quasi-degeneracies of the Floquet eigenenergies of the quantum problem. Due to the infinite number of Floquet eigenenergies in our problem, this section aims to give an alternative and more intuitive picture for the strong α-dependence of our results.

To this end we show in Appendix B.3.2 that the total Hamiltonian H^α in Eq. (4.9) is unitarily equivalent to

$$\mathcal{H}^\alpha = H_{\mathrm{S}}^F(t) + H_{\mathrm{B}} + \mathcal{H}_{\mathrm{I}}^\alpha + H_{\mathrm{shift}}, \tag{4.26}$$

where $H_{\mathrm{S}}^F(t)$ and H_{B} remain unchanged and H_{shift} is given in Appendix B.3.2. The latter term describes small shifts of the bath and system frequencies and will be neglected in the following.

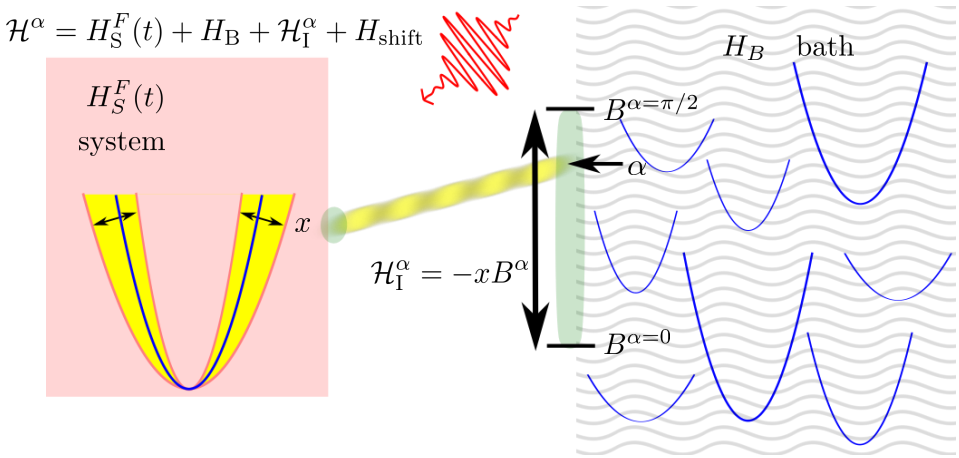


Figure 4.8: Different to Fig. 4.1, where the dipole operator of the system is tuned by α, here we show an equivalent model obtained through a canonical transformation. Here the system-bath interaction is described by the interaction Hamiltonian $\mathcal{H}_I^\alpha$, where the parameter α allows one to continuously adjust the bath dipole operator from $B^{\alpha=0}$ to $B^{\alpha=\pi/2}$ as indicated by the lever, which results into an α dependent bath spectral density.

The transformed interaction Hamiltonian $\mathcal{H}_I^\alpha$ is given by

$$\mathcal{H}_I^\alpha = -xB^\alpha, \tag{4.27}$$

where

$$B^\alpha = \sum_{r=1}^{N} \kappa_r \left(\cos(\alpha) x_r - \frac{\sin(\alpha)}{m_r \omega_0} p_r \right). \tag{4.28}$$

In contrast to H_I^α in Eq. (4.6), the system-bath coupling in $\mathcal{H}_I^\alpha$ is mediated by the position coordinate of the oscillator coupled to an α-dependent superposition of position and momentum operators of the bath modes. In this way, the α-dependence has been entirely moved from the coupling operator to the bath as shown in Fig. 4.8.

Following the steps in Appendix B.3 we derive a master equation for the density operator ρ_U from the transformed Hamiltonian $\mathcal{H}^\alpha$, see Appendix B.3.2. we have explicitly verified that ρ_U and ρ lead to the same results for all parameters investigated in Sec. 4.3.2. In the derivation of the master equation for ρ_U, the linear superposition of bath operators in Eq. (4.28) gives rise to an α-dependent spectral density

$$J^\alpha(\omega) = J(\omega) \left[\cos(\alpha)^2 + \left(\frac{\omega}{\omega_0} \right)^2 \sin^2(\alpha) \right], \tag{4.29}$$

which is the product of the Ohmic spectral density $J(\omega)$ in Eq. (4.15) and an α-dependent function. We show $J^\alpha(\omega)$ for the two extreme cases $\alpha = 0$ and $\alpha = \pi/2$ in Fig. 4.9. While $J^0(\omega)$ and $J^{\pi/2}(\omega)$ are identical at $\omega = \pm\omega_0$, they differ significantly for $|\omega| \neq \omega_0$.

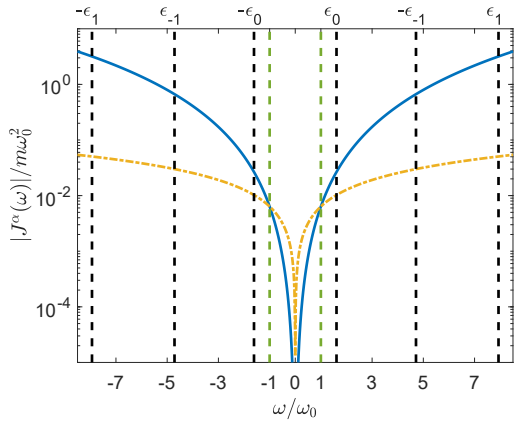


Figure 4.9: The dash-dotted yellow (solid blue) line corresponds to the bath spectral density $J^{\alpha=0}(\omega)$ $[J^{\alpha=\pi/2}(\omega)]$. The green dashed vertical lines mark the undriven system frequency $\pm\omega_0$. The scaled Floquet quasi-frequencies $\epsilon_r = (\mu + r\omega_L)/\omega_0$ for $q = 0.5$ and $b = 0.1$ are indicated by black dashed vertical lines.

We are now in a position to understand the α-dependence of the results in Sec. 4.3.2. In general, the system-bath interaction is determined by the values of $J^\alpha(\omega_c)$ at the characteristic frequencies ω_c of the classical solution of the undamped harmonic oscillator [see Appendix B.3.2 for details]. We have found that all observables in Sec. 4.3.2 are independent of α for an undriven oscillator. In this case, the resonance frequency ω_0 is the only characteristic frequency involved in the system dynamics. However, the spectral density in Eq. (4.29) satisfies $J^\alpha(\pm\omega_0) = J(\pm\omega_0)$ for all α, and hence the system-bath interaction is independent of α. This picture changes significantly if the driving is switched on. The driving leads to new characteristic frequencies $\omega_c = \pm\mu + r\omega_L$, with $r \in \mathbb{Z}$ and where μ is the quasi-frequency of the Floquet spectrum closest to ω_0 of the underlying classical model of a driven but undamped harmonic oscillator. Naturally, these excitations of the heat bath at multiples of the driving frequency [237, 242, 244] mentioned also below Eq. (2.72) can be suppressed by driving the bath at higher frequencies than the cutoff frequency of the bath, i.e. $\Omega_c \ll \omega_L$. In Fig. 4.8, this would correspond to an increase in the distance between the characteristic frequencies ω_c to the extent that the bath only responds at a single frequency (this cutoff is very high in Fig. 4.8). According to condition (II) discussed in Sec. 2.3.1 based on Ref. [225], in this regime, the state reduces to an effective Floquet-Gibbs state.

Since the spectral density J^α depends strongly on α for $|\omega| > \omega_0$ [see Fig. 4.9], the parametric driving leads to α-dependent results.

We have shown that parametric driving of a harmonic oscillator coupled to a heat bath allows one to distinguish between different microscopic models for the system-bath interaction. More specifically, we have considered a bath with an Ohmic spectral density that couples to a linear superposition of the position and momentum degrees of freedom of the oscillator. This superposition is parametrised via the coupling angle α which allows one to continuously change the character of the coupling from position to momentum coupling. We have systematically investigated the dependence of the time-averaged expectation values of $\overline{\langle X^2\rangle}$ and $\overline{\langle P^2\rangle}$ on the driving parameters, temperature T of the bath and α. While $\overline{\langle X^2\rangle}/\overline{\langle P^2\rangle}$ is approximately independent of α and T, we have shown that $R_X = \overline{\langle X^2\rangle}/\langle X^2\rangle_{\text{thermal}}$ shows

a strong dependence on temperature and on the coupling angle α. This dependence on the coupling angle could be used to determine α by measuring $\overline{\langle X^2 \rangle}$ ($\langle X^2 \rangle_{\text{thermal}}$ in the presence (absence) of the parametric driving. We have found that R_X exhibits the strongest dependence on α for large driving frequencies $\omega_L \gg \omega_0$ and for bath temperatures with $k_B T \leq \hbar\omega_0$. In this regime, R_X also displays a characteristic dependence on inverse temperature for each value of α, thus offering an additional route to determine the value of α in the interaction Hamiltonian. We obtained our results within the framework of a master equation in the Born-Markov approximation that accounts for the modification of the system-bath interaction due to the parametric driving. In order to be consistent with the Markov approximation, we describe the time evolution of the reduced density operator of the oscillator on a coarse-grained time axis with resolution Δt, where Δt is much smaller than $1/\gamma$ and much larger than the bath correlation time. We compare our results to a simpler master equation that neglects the influence of the driving on the dissipative part and where all counter-rotating terms are kept. We find that this HTME agrees with the full master equation in the high-temperature limit where $\hbar\omega_0 \ll k_B T$, but deviates significantly otherwise. This can be understood as follows: For short bath correlation times, i.e. high temperatures, the driven system does not change much during the correlation time and can, for the purpose of determining the thermal noise, be considered static [332], though there are still contributions from counter-rotating terms. This situation changes when the frequency of the modulation becomes comparable to the bath correlation time, allowing for interference between the dynamics induced by the drive and the environment [333, 334]. We thus conclude that the influence of the parametric driving on the system-bath coupling must be considered in general.

The α-dependence of our results can be understood within the general framework of EGD introduced in [237], where the dependence of the system dynamics on the coupling operator is explained in terms of quasi-degeneracies of the Floquet spectrum. In addition, we have provided a complementary and intuitive explanation of the α-dependence of our results by applying a unitary transformation to the total system-bath Hamiltonian. In this transformed picture, the position variable of the oscillator couples to an α-dependent superposition of bath variables which results in an α-dependent spectral density J^α. Since the system-bath coupling is determined by the values of J^α at the Floquet quasi-frequencies associated with the parametric driving, the density operator obtained from this master equation depends on α if the system is driven.

4.5 Future work

These results open up several directions for future investigations. The explanation of the α-dependence of our results via the unitarily equivalent model giving rise to an α-dependent spectral density shows that strong parametric driving allows one to probe an unknown spectral density if the microscopic coupling mechanism between the system and the bath is known.

Furthermore, this approach could be extended to investigate systems with several com-

peting dissipation mechanisms or to the non-Markovian regime of strong damping which is often encountered in solid-state materials [335, 336]. This could either be achieved by using the Feynman-Vernon path integral formalism [323, 337] or the stochastic Liouville-von Neumann equation [338]. Alternatively, it is possible to simplify the non-Markovian dynamics to effective Markovian dynamics. For example, by including an auxiliary system into the system, such that the combined dynamics of both is again Markovian [339]. Or alternatively, by using augmented density operator containing information about the system history [340] such that the influence functional [341], which contains all information about the bath property, reduces to Markovian dynamics. This approach requires the bath spectral density to be sufficiently smooth that only a short system history is required. This restriction has to some extent be eased in Ref. [342], by exploiting an efficient representation of the propagator in terms of an operator acting on a matrix product states, allowing the exact numerical simulations of systems with longer bath correlation times. This formalism is therefore particularly convenient as matrix products states are often used for the study of strongly correlated and interacting electron systems.

Eventually, an improved understanding of system-bath interactions paves the way to control and engineer their quantum dynamics via strong driving. For example, cooling of a driven harmonic oscillator coupled to a non-Markovian bath can be achieved via optimal control techniques [328, 343]. This could allow one to prepare the oscillator in non-classical, squeezed states [344–347].

An alternative approach suggested by the findings in this work would be based on introducing gaps in the bath spectral density such as to suppress specific transitions, which otherwise lead to heating [217].

Up to now a lot of interesting exotic states have only been stabilised in a pre-thermal state, where the Magnus expansion does not converge and the system eventually heats up to infinite temperature (see Sec. 2.3). In order to go beyond metastable states, it is, therefore, necessary to understand and design the dissipation such as to reach interesting steady-states. The energy filter proposed for suppressing photon-assisted tunnelling in the interaction with an electronic reservoir [227]. The necessarily structured bath spectral density would make a full non-Markovian treatment necessary in general.

The present work focused on the steady-state regime. However, currently, the laser intensities necessary to produce non-linear effects are only implemented in pulsed operation [36]. A steady-state operation competing with dissipative dynamics in continuous operation with lower laser intensities could be achievable in a cavity implementation as proposed for arrays of cavities consisting of Josephson junction array covered by gold plates [186, 274].

4.6 Chapter summary

In this chapter, we considered the paradigmatic example for system-bath interactions comprised of a parametrically driven oscillator, weakly coupled to a thermal bath. We show that strong parametric driving of a quantum harmonic oscillator coupled to a thermal bath allows

one to distinguish between different microscopic models for the oscillator-bath coupling. We consider a bath with an Ohmic spectral density and a model where the system-bath interaction can be tuned continuously between position and momentum coupling via the coupling angle α. We derive a master equation for the reduced density operator of the oscillator in Born-Markov approximation and investigate its quasi-steady state as a function of the driving parameters, the temperature of the bath and the coupling angle α. We find that the driving introduces a strong dependence of the time-averaged variance of position and momentum on these parameters. In particular, we identify parameter regimes that maximise the α dependence and provide an intuitive explanation of our results. We showed that strong parametric driving can be used as a method to learn about smooth spectral densities. However, aiming at engineering dissipative dynamics for condensed matter systems, the presence of non-Markovianity arising from structured environment seems unavoidable.

Chapter 5

Conclusion and Outlook

In this thesis, we study the interplay between driving and dissipation for a phenomenological model of a high-temperature superconductor. Following two background chapters (Chapter 1 and Chapter 2), we propose a parametric cooling scheme for bilayer stacks of capacitively and inductively coupled long Josephson Junction model in Chapter 3. This model treats the superconducting phase difference classically and ignores any effect due to discrete energy levels. Though, the cooling scheme only effectively addresses low momentum modes, the cooling effect survives in the long junction regime. We also showed that cooling is possible in the presence of high momentum modes as arising through the excitation of Josephson vortices. However, these modes are only treated approximately as we do not account for non-local electrodynamics. In order for the cooling effect of the phase quadrature to enhance superconductivity, it needs to allow to stabilise superconductivity at higher temperatures. As we cannot describe the superconducting to normal state phase transitions in our model, we only showed that the parametric cooling scheme allows to suppress switches from the superconducting to a resistive state. We have further ignored spatial excitation along the y-axis, which should play a role approaching the phase transition through the excitation of in-plane pancake vortices as discussed in Appendix A.5.

In Chapter 3, the driving amplitude was assumed to be weak in comparison to the undriven system frequencies. In Chapter 4, we studied a parametrically driven harmonic oscillator to understand the influence stronger driving can have in the presence of dissipative dynamics. Interpolating the coupling operator between position and momentum operator is found to be related to modifications in the bath spectral density, which can be distinguished through the driving mechanism. We studied a smooth bath spectral density, in agreement with the Born-Markov approximation. Our results indicate that by selectively designing gaps in the bath spectral density it is possible to suppress specific transition frequencies in the interaction between system and bath and thereby steer the system. Pursuing this bath further it might ultimately allow for engineering dissipative dynamics as in cold atoms and quantum optics. In these atomic systems, our understanding of the system-bath coupling is so accurate that it can be used to control and engineer these interactions (Appendix B.8). In this way, the role of dissipation and decoherence can be transformed from a detrimental effect [348] into a wanted feature as shown, e.g. in [349–355]. In general such a treatment would, however, require a full non-Markovian treatment going beyond the formalism derived

here. The ultimate goal for such work should be stabilise a driven many-body model in an exotic many-body state. As we discussed in Chapter 2, the Floquet-Markov master equation can be simplified through a partial secular approximation as long as an energy gap in the spectrum of the Floquet quasi-energies projected onto the first Brillouin zone survives in the thermodynamic limit. However, any such treatment will be challenging as it requires an exact solution to the isolated system dynamics, which is in general numerically only possible for small system sizes.

Appendix A

Josephson Electrodynamics

This Appendix contains detailed derivations of the Josephson electrodynamics used in Sec. 2.1.3 and Chapter 3 starting from Maxwell's equation and Josephson relations. The basic assumptions behind modelling the Josephson electrodynamics of a bilayer cuprate as a stack of alternating Josephson junctions (shown in Fig. 3.1 and Fig. A.1) are discussed in Sec. 1 and Sec. 3.1.

A.1 Modified Josephson relation including capacitive coupling

We start by outlining the derivation of the capacitive coupling relation from Eq. (3.5) following Machida and Sakai [192], which results into an equation of motion for the gauge invariant phase difference ϕ_M from Eq. (3.1).

A.1.1 Capacitive coupling

As discussed at the beginning of Sec. 3.1, we assume the number of superconducting pairs to be constant inside the superconducting sheets, i.e. the amplitude of the macroscopic order parameter from Eq. (1.6) is constant. The resulting wave-dynamics of the phase of the order parameter in the mth superconducting layers is given by [192]

$$\frac{\Phi_0}{2\pi}\partial_t\varphi_m = -\left(\Theta_m + \frac{1}{e}\mu_m\right), \tag{A.1}$$

where Φ_0 is the magnetic flux quanta and the expression in the bracket corresponds to the electro-chemical potential consisting of the sum of the corresponding scalar potential Θ_m and chemical potential μ_m. The electro-chemical potential is taken to be constant inside the junction such that $\partial_z\partial_t\varphi_m = 0$ for a gauge-choice $\partial_t A_m^z = 0$ [192]. A shift $\delta\mu_m$ in the chemical potential μ_m along the z-axis (see Fig. A.1) of the mth superconducting layer induces a charge density ρ_m. The charge density is related to the superconducting phase φ_m

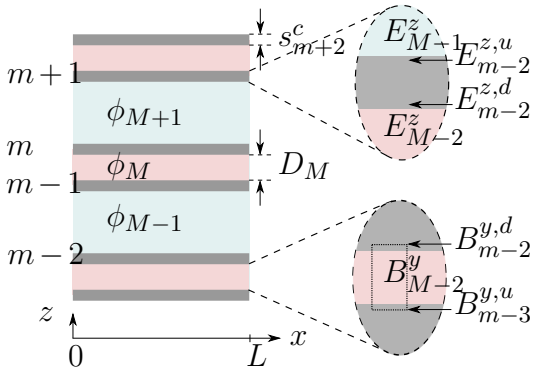


Figure A.1: Model for a stack of bilayer cuprates with thin grey regions indicating the superconducting layers of thickness s^c and the coloured areas representing the two different insulators. The mth superconducting layer and all fields and physical quantities directly associated with it are labelled by lower case m. The Mth insulator between the two superconducting layers $(m, m-1)$, forming a Josephson junction, and the corresponding properties and fields are indexed by a capital M, e.g. thickness D_M and gauge invariant phase difference ϕ_M of a superconductor. The top magnification of the $m+1$ superconducting sheet distinguishes the electric field in z-direction E^z at the upside (u) and downside (d) of the sheets and the fields in the adjacent insulator. The bottom magnification shows a dotted rectangular path across an insulating sheet used in the derivation of the inductive coupling and the associated notation for the magnetic field in y-direction B^y.

and the scalar potential Θ_m in the mth superconducting layer as [192]

$$\rho_m = -\frac{\epsilon_0 \epsilon^s_m}{\lambda^{(D)2}_{c,m}} \left(\Theta_m + \frac{\Phi_0}{2\pi} \partial_t \varphi_m \right), \tag{A.2}$$

where ϵ_0 the vacuum permittivity, ϵ^s_m is the dielectric constant and $\lambda^{(D)}_{c,m}$ is the Debye screening length in the mth superconducting layer. The charge density induces a gradient in the electric field E^z_m along the z-axis according to Gauss law

$$\partial_z E^z_m = \frac{\rho_m}{\epsilon_0 \epsilon^s_m}, \tag{A.3}$$

Taking ∂_z of this expression together with Eq. (A.2), $\partial_z \partial_t \varphi_m = 0$ from below Eq. (A.1) and using $E^z_m = -\partial_t A^z_m - \partial_z \Theta_m$ with vector potential A^z_m we obtain a screening relation for the electric field inside the superconducting sheets [192]

$$\partial^2_z E^z_m = \frac{1}{\lambda^{(D)2}_{c,m}} E^z_m. \tag{A.4}$$

Solutions to Eq. (A.4) inside the mth superconducting layer of thickness s^c_m are given by

$$E^z_m(z - z_0) = E^{z,d}_m \cosh\left(\frac{z - z_0}{\lambda^{(D)}_{c,m}} \right) + \frac{E^{z,u}_m - E^{z,d}_m \cosh\left(s^c_m / \lambda^{(D)}_{c,m} \right)}{\sinh\left(s^c_m / \lambda^{(D)}_{c,m} \right)} \sinh\left(\frac{z - z_0}{\lambda^{(D)}_{c,m}} \right), \tag{A.5}$$

where $E^z_m = \{E^{z,d}_m, E^{z,u}_m\}$ are the electric fields at the down and upside of the superconducting layer, i.e. $z - z^0_m = \{0, s^c_m\}$ (see top magnification in Fig. A.1). Physically, the electric

field given in Eq. (A.5) only decays over the Debye screening length $\lambda_{c,m}^{(D)}$. If $\lambda_{c,m}^{(D)}$ is large compared to the thickness s_m^c of the superconducting layers, the electric field penetrates into neighbouring layers and induces screening charges there, giving rise to the capacitive coupling between different junctions. Neglecting any sheet charges at the boundary between the mth superconducting layer and the adjacent Mth and $M+1$th insulating sheet, and using the continuity of the displacement field we obtain

$$E_M^z = \frac{\epsilon_m^s E_m^d}{\epsilon_M(x,t)}, \tag{A.6}$$

and

$$E_{M+1}^z = \frac{\epsilon_m^s E_m^u}{\epsilon_{M+1}(x,t)}, \tag{A.7}$$

at the lower and upper boundary shown in the top magnification in Fig. A.1. The driving of a phonon mode from Sec. (3.1.4) is modelled as a time-dependent permittivity in the insulating layers as ($\epsilon(t)$-Model see Eq. (3.32))

$$\epsilon_M(x,t) = \epsilon_M \left[1 + \nu_M \frac{1}{2}\left(1+\cos\left(2k_d x\right)\right)\frac{1}{2}\left(1-\cos\left(2\omega_d t\right)\right)\right], \tag{A.8}$$

where ϵ_M is the undriven permittivity taken to be equal for all layers and ν_M is the amplitude of small modulation of the permittivity in the Mth insulators arising from a driven phonon mode with wavevector k_d. Using these expressions together with Eq. (A.5) and Gauss law from Eq. (A.3) culminates in an expression for the charge density at the downside

$$\rho_m^d = \epsilon_0 \frac{\epsilon_{M+1}(x,t)E_{M+1}^z - \epsilon_M(x,t)\cosh\left(s_m^c/\lambda_{c,m}^{(D)}\right)E_M^z}{\lambda_{c,m}^{(D)}\sinh\left(s_m^c/\lambda_{c,m}^{(D)}\right)}, \tag{A.9}$$

and upside

$$\rho_m^u = \epsilon_0 \frac{\epsilon_{M+1}(x,t)E_{M+1}^z\cosh\left(s_m^c/\lambda_{c,m}^{(D)}\right) - \epsilon_M(x,t)E_M^z}{\lambda_{c,m}^{(D)}\sinh\left(s_m^c/\lambda_{c,m}^{(D)}\right)} \tag{A.10}$$

of the mth superconducting layer (see Fig. A.1). Combining the shift $\delta\mu_m$ in the chemical potential μ_m due to the presence of a charge density ρ_m with a dynamical equation for the order parameter as a function of the electrochemical potential, $e\Theta_m + \mu_m$, where Θ_m is the scalar potential, Machida and Sakai [192] obtain

$$\frac{\Phi_0}{2\pi}\partial_t\phi_M = -\frac{{\lambda_{c,m}^{(D)}}^2}{\epsilon_0\epsilon_m^s}\rho_m + \frac{{\lambda_{c,m-1}^{(D)}}^2}{\epsilon_0\epsilon_{m-1}^s}\rho_{m-1} + \int_{z_{m-1}}^{z_m} E_m^z\,dz. \tag{A.11}$$

This generalised Josephson relation describes the coupling of the gauge invariant phase difference ϕ_M from Eq. (3.1) to the electric field E_m^z along the z axis. The first and second term on the right hand side of Eq. (A.11) explicitly contain the influence from the charge density induced by a shift in chemical potential in the neighbouring superconducting layers. Using the charge densities from Eq. (A.9) and (A.10) in the generalised Josephson relation from Eq. (A.11) gives

$$\frac{\Phi_0}{2\pi}\partial_t\phi_M = s_{M,M-1(t)}^{(C,d)}E_{M-1}^z + D_M^C(t)E_M^z + s_{M+1,M}^{(C,u)}(t)E_{M+1}^z, \tag{A.12}$$

where the diagonal $D_M^C(t)$ and the off-diagonal capacitive couplings $s_{M+1,M}^{(C,u)}(t)$ and $s_{M+1,M}^{(C,d)}(t)$ for identical superconducting layers, i.e. $s^c = s_m^c$, $\epsilon^s = \epsilon_m^s$ and $\lambda_c^{(D)} = \lambda_{c,m}^{(D)}$, are

$$\begin{aligned} D_M^C(t) &= D_M + 2\epsilon_M(x,t)\cosh s^c/\lambda_c^{(D)} r^c, && \text{(A.13)} \\ s_{M+1,M}^{(C,u)}(t) &= -\epsilon_{M+1}(x,t) r^c, && \text{(A.14)} \\ s_{M,M-1}^{(C,d)}(t) &= -\epsilon_{M-1}(x,t) r^c. && \text{(A.15)} \end{aligned}$$

The Debye screening length is absorbed into a new time independent length-scale $r^c = \frac{\lambda_c^{(D)}}{\epsilon^s \sinh\left(s^c/\lambda_c^{(D)}\right)}$. To increase the similiarity to the monolayer and bilayer models studied in Ref. [121, 193, 256], it is convenient to characterise the capacitive coupling strength by the capacitive coupling constants α_M defined in terms of the time independent expressions for D_M^C and $s_M^{(C,i)}$ with $i = u, d$ as

$$\frac{\alpha_{M+1}}{2\alpha_{M+1}+1} = -\frac{s_{M,M-1}^{(C,d)}}{D_{M-1}^C} = \frac{\epsilon_{M-1} r^c}{D_{M-1}^C} = -\frac{s_{M+1,M}^{(C,u)}}{D_{M+1}^C} = \frac{\epsilon_{M+1} r^c}{D_{M+1}^C}, \tag{A.16}$$

where we explicitly assume a bilayer material such that every second insulator has the same physical parameters, i.e. $\epsilon_{M+1} = \epsilon_{M-1}$ and $D_{M-1}^C = D_{M+1}^C$. Introducing the tridiagonal matrix

$$\mathbf{C}(x,t)\boldsymbol{\epsilon}^{-1}(x,t) = \mathbf{C}\boldsymbol{\epsilon}^{-1} + \mathbf{D}\left(\boldsymbol{\epsilon}^{-1}(x,t) - \boldsymbol{\epsilon}^{-1}\right), \tag{A.17}$$

allows to express Eq. (A.12) in a more compact form using the basis defined around Eq. (3.4) as

$$\frac{\Phi_0}{2\pi}\partial_t \vec{\phi} = \mathbf{C}(x,t)\vec{E}^z. \tag{A.18}$$

Using Eq. (A.8), it is possible to approximate Eq. (A.17) to first order in the driving strength ν as

$$\mathbf{C}(x,t)\boldsymbol{\epsilon}^{-1}(x,t) = \mathbf{C}\boldsymbol{\epsilon}^{-1} - \frac{1}{2}\mathbf{D}\boldsymbol{\nu}\boldsymbol{\epsilon}^{-1}\frac{1}{2}\left(1+\cos\left(2k_d x\right)\right)\left(1-\cos\left(2\omega_d t\right)\right) + O(\nu^2), \tag{A.19}$$

while the contribution from the undriven matrix is given by

$$\mathbf{C}\boldsymbol{\epsilon}^{-1} = r^c\left(\boldsymbol{\alpha}^{-1} - \boldsymbol{\Delta}\right). \tag{A.20}$$

This undriven part of the capacitive coupling matrix becomes identical to the one used in Ref. [193] for $s^c/\lambda_c^{(D)} \to 0$ such that $\cosh\left(s^c/\lambda_c^{(D)}\right) \to 2$, i.e. Eq. (3.10)

$$\frac{\Phi_0}{2\pi}\partial_t \vec{\phi} = \left(\boldsymbol{I} - \boldsymbol{\Delta}\boldsymbol{\alpha}\right)\vec{V}, \tag{A.21}$$

where we defined voltages $\vec{V} = \mathbf{D}\vec{E}$ across each junction.

A.1.2 Ampère's law relating phase to magnetic field

In Sec. 3.1.4, we argued that external driving of a phonon mode can be modelled as either a time permittivity $\epsilon_M(t)$ as in Eq. (A.8) following the motivation from Ref. [31] or a time-dependent critical current density $J_M^C(t)$ as in Ref. [43, 45]. The c-axis current density is then given by

$$J_M^z(t) = \sigma E_M^z + J_M^C(t)\sin\phi_M \tag{A.22}$$

consists of a quasi-particle current proportional to conductivity σ (first term) and a supercurrent part proportional to the critical current density $J_M^C(t)$ (second term). Substituting Eq. (A.22) and Eq. (A.18) into Ampère's law

$$\partial_x B_M^y = \partial_t\left(\frac{\epsilon_M(x,t)}{c^2}E_M^z\right) + \mu_0 J_M^z(t), \tag{A.23}$$

results into a relation between the magnetic field and phase of the form

$$\partial_x \mathbf{B}^y = \frac{\Phi_0}{2\pi}\frac{\boldsymbol{\epsilon}(x,t)}{c^2}\mathbf{C}^{-1}(x,t)\partial_t^2\vec{\phi} + \mu_0\boldsymbol{J}^C(t)\sin(\vec{\phi}) + \frac{\Phi_0}{2\pi c^2}\left[\partial_t\left(\boldsymbol{\epsilon}(x,t)\mathbf{C}^{-1}(x,t)\right) + \frac{\boldsymbol{\sigma}}{\epsilon_0}\mathbf{C}^{-1}(x,t)\right]\partial_t\vec{\phi}, \tag{A.24}$$

where $\boldsymbol{\epsilon}(x,t)$, $\boldsymbol{J}^C(t)$ and $\boldsymbol{\sigma}$ are diagonal matrices containing the values of the corresponding physical quantities. The term on the left, containing $\partial_x B_M^y$ will be shown to be responsible for inductive coupling, while the first on the right is responsible for capacitive coupling. The remaining terms arise from Josephson current, displacement current and quasi-particle current along the c-axis respectively. The third term has the form of a damping term with a time-dependent damping rate, which is only present for a driven system and can even change sign. For a consistent Hamiltonian formulation, it can arise due to a time-dependent effective mass. This term is effectively ignored in Ref. [31] as the "Ampère's law" used there only contains the time derivative of the electric field instead of the displacement field. Therefore, the driven equations of motion used in the following do not reduce to the expressions in Ref. [31] even in the short junction limit and for $\alpha = \alpha_{1,2}$. The driving term used in Ref. [31] could instead arise from a very intricate form of time-dependent critical current. The fourth term arising from a quasi-particle current is a more conventional damping term.

A.2 Derivation of inductive coupling in terms of supercurrent difference

In this Section, we start by relating the magnetic field to the screening current following Ref. [117]. We go beyond the standard derivation of the coupled sine-Gordon equation from Eq. (3.19), by including displacement current and quasi-particle current in x-direction in addition to superconducting screening current. Keeping these terms results into an equation of motion for a second field $\vec{S}$ from Eq. (3.23) proportional to the difference in screening current across the junction. The additional damping term due to in-plane dissipation [255, 259] is believed to play an essential role in the synchronisation of the junctions and vortex lattice motion [255,259]. However, this term is often overlooked in favour of a simpler coupled sine-Gordon equation as given in Eq. (3.19).

To relate the gradient in the phase difference to the magnetic field, it is sufficient to consider the magnetic flux $\Phi = \oint_{\Sigma} \vec{A} \cdot d\vec{\ell} = \int_{\Sigma_l} \vec{B}^y \cdot d\vec{l}$, over a surface Σ enclosed by a rectangular path Σ_l across the insulating layer as shown in the lower magnification in Fig. A.1. The components of the path parallel to the layers are just inside the superconducting sheets. Replacing the x component of the vector potential $\vec{A}^x$ in favour of the Ginzburg-Landau expression of the screening current [10, 252]

$$J_m^{s,x} = \frac{1}{\mu_0 \lambda^2} \left(\frac{\Phi_0}{2\pi} \partial_x \varphi_m - A_m^x \right), \tag{A.25}$$

where λ is the bulk London penetration length and the z component of the vector potential $\vec{A}^z$ by the definition of ϕ_M from Eq. (3.1) gives the interaction between $\partial_x \phi_M$ and the screening current in the adjacent superconducting sheets as [117]

$$\frac{\Phi_0}{2\pi} \partial_x \phi_M = D_M B_M^y + \mu_0 \lambda^2 \left(J_m^{s,x,d} - J_{m-1}^{s,x,u} \right), \tag{A.26}$$

where $i = u$ ($i = d$) in $J_m^{s,x,i}$ indicates the up (down)side of the corresponding superconducting sheet. This expression can be written more compactly as

$$\frac{\Phi_0}{2\pi} \partial_x \phi_M = D_M B_M^y + \frac{\Phi_0}{2\pi} \left(q_m^d - q_{m-1}^u \right), \tag{A.27}$$

where $q_m = \partial_x \varphi_m - \frac{2\pi}{\Phi_0} A_m^x$ is the in plane momentum [253] in the mth superconducting layer, which is proportional to the superconducting current [126, 255]

$$J_m^{s,x} = \frac{\Phi_0}{2\pi \mu_0 \lambda^2} q_m, \tag{A.28}$$

where λ is the bulk London penetration depth. The second field is proportional to the difference in in plane momentum across the insulating layer.

The x component of Ampère's law inside the superconducting sheets yields

$$-\partial_z B_m^y = \mu_0 J_m^{d,x} + \mu_0 J_m^{s,x} + \mu_0 J_m^{q,x}, \tag{A.29}$$

where the current along the superconducting sheets is divided into three components. Firstly, the superconducting screening current given by Eq. (A.25). Secondly, the small displacement current

$$J_m^{d,x} = \epsilon_0 \epsilon_{ab} \partial_t E_m^x = \epsilon_0 \epsilon_{ab} \frac{\Phi_0}{2\pi} \partial_t^2 q_m, \tag{A.30}$$

where we used the first London equation $E_m^x = \frac{\Phi_0}{2\pi} \partial_t q_m$ [126]. This term gives rise to the kinetic term of the second field but is very small and can be neglected for all relevant frequencies [119, 255, 259]. Thirdly, the in-plane quasi-particle current $J_m^{q,x}$ [121, 255, 259–262] given by

$$J_m^{q,x} = \sigma_{ab} E_m^x = \sigma_{ab} \frac{\Phi_0}{2\pi} \partial_t q_m. \tag{A.31}$$

Equation A.29 reduces to an equation of motion for in-plane momentum q_m, i.e.

$$-\frac{2\pi}{\Phi_0} \partial_z B_m^y = \mu_0 \epsilon_0 \epsilon_{ab} \partial_t^2 q_m + \frac{1}{\lambda^2} q_m + \mu_0 \sigma_{ab} \partial_t q_m. \tag{A.32}$$

The definition of $\partial_z B_m^y$ in Eq. (A.32) for a bilayer model is trickier then for a monolayer. Applying Ampère's law to the superconducting sheets, ∂_z can be replaced by a discrete derivative across a single superconducting sheet distinguishing between up (u) and downside (d), i.e.

$$\partial_z B_m^y = \frac{1}{s^c}\left(B_m^{y,u} - B_m^{y,d}\right) = \frac{1}{s^c}\left(B_{M+1}^y - B_M^y\right), \tag{A.33}$$

where we used the continuity of the magnetic field (Eq. (A.27)) in across the insulator-superconductor interface. This expression can also be obtained from a zeroth order expansion of the $B_m^y(z,t)$ field obtained in Ref. [117], which is a good approximation as $\frac{s^c}{\lambda} \ll 1$.

A.2.1 Equation of motions of supercurrent difference

The second field could be chosen proportional to the in-plane momentum or screening current as in Ref. [67, 68] or magnetic field as in Ref. [126]. However, the model studied there considers infinitely thin superconducting sheet and more importantly a monolayer. This simplifies the interpretation of discrete derivatives, in a way that is not trivially extendible to a bilayer model. Here, we are, however, considering a bilayer model of finite thickness and further also include capacitive coupling such that we cannot follow their derivation. We instead use the difference in the in plane momentum across the insulating layers multiplied by s^c as the second, dimensionless field, that is

$$S_M = s^c\left(q_m^d - q_{m-1}^u\right). \tag{A.34}$$

Equation A.27 allows to re-express this field in terms of the magnetic field inside the insulating layers as

$$\vec{S} = s^c\left(\partial_x\vec{\phi} - \frac{2\pi}{\Phi_0}\mathbf{D}\vec{B}^y\right), \tag{A.35}$$

Evaluating the difference of Eq. (A.32) across the Mth insulator and replacing the magnetic field using Eq. (A.35) and the in plane momentum using $S_M = s^c(q_m^d - q_{m-1}^u)$ gives

$$\mu_0\epsilon_0\epsilon_{ab}\partial_t^2\vec{S} + \mu_0\sigma_{ab}\partial_t\vec{S} + \frac{1}{\lambda^2}\mathbf{L}\mathbf{D}^{-1}\vec{S} + \mathbf{\Delta}\mathbf{D}^{-1}\partial_x\vec{\phi} = 0, \tag{A.36}$$

where replacing the bulk London penetration length λ by the in-plane London penetration length λ_{ab} by $\lambda = \lambda_{ab}\sqrt{s^c/D}$ [252] gives

$$\mathbf{L} = \frac{\lambda_{ab}^2}{D}\left(\boldsymbol{\eta}^{-1} - \mathbf{\Delta}\right) \tag{A.37}$$

characterised by the inductive coupling strength $\boldsymbol{\eta} = \frac{\lambda_{ab}^2}{D}\mathbf{D}^{-1}$ [194]. Using Eq. (A.35) for the last two terms in Eq. (A.36) gives

$$\mu_0\epsilon_0\epsilon_{ab}\partial_t^2\vec{S} + \mu_0\sigma_{ab}\partial_t\vec{S} + \frac{2\pi}{\Phi_0}\frac{s_c}{\lambda^2}\left(\frac{\Phi_0}{2\pi}\partial_x\vec{\phi} - \mathbf{L}\vec{B}^y\right) = 0. \tag{A.38}$$

The term in the bracket is the inductive coupling relation used in Eq. (3.12). The first term can be ignored as it is of order $\frac{\epsilon_{ab}}{\epsilon}\frac{1}{\gamma_d\gamma^2}$, with $\gamma_d = \frac{D}{s^c}$ is the ratio of the thickness of typical

insulator to superconducting sheet, $\gamma_c = \frac{\lambda_c}{D}$ is the ratio of the London penetration depth to the thickness of typical insulator, $\gamma = \frac{\lambda_c}{\lambda_{ab}}$ is the anisotropy factor given by the ratio of c to in-plane London penetration depth λ_{ab} with $\gamma_d = \frac{D}{s^c}$ is the ratio of the thickness of typical insulator to superconducting sheet, $\gamma_c = \frac{\lambda_c}{D}$ is the ratio of the London penetration depth to the thickness of typical insulator. It is kept in the following section to achieve a Hamiltonian consisting of two fields $\vec{\phi}$ and $\vec{S}$ instead of only $\vec{\phi}$ as in Eq. (3.19).

The second term corresponding to in-plane dissipation is the dominant dissipation mechanism for spatially non-uniform excitations such as Josephson lattices in very anisotropic stacks [121, 255, 259–262]. While the tiny displacement current term can be neglected for all relevant purposes, the in-plane dissipation current is only included as a first order correction to the adiabatic elimination [258].

We now replace $\vec{S}$ in Eq. (A.38) with the help of Eq. (A.35), while neglecting damping terms an order $\frac{1}{\gamma}$ smaller than the rest. In this approximation, the leading order terms of the in-plane dissipation term leads to an additional term $\mu_0 \frac{\Phi_0}{2\pi} \lambda^2 \sigma_{ab} \partial_t \partial_x \vec{\phi}$ in the dimension-full sine-Gordon equation or equivalently to the replacement

$$\partial_x^2 \vec{\phi} \to \left(\frac{\epsilon_{ab}}{\epsilon} \frac{\gamma_{ab}}{\gamma_d \gamma^2} \partial_\tau + 1 \right) \partial_x^2 \vec{\phi}, \tag{A.39}$$

with $\gamma_{ab} = \frac{\sigma_{ab}}{\epsilon_0 \epsilon_{ab} \omega_p}$ for the dimensionless one (Eq. (3.19)). We model noise terms phenomenologically by assuming a large heat bath consisting of weakly interacting phonon modes. We only use the form and values of the noise term to motivate an additional increase in the damping rate due to in-plane dissipation for spatially inhomogeneous modes.

A.2.2 Non-local Josephson electrodynamics

The Josephson electrodynamics described by the coupled sine-Gordon equation given in Eq. (3.19) is purely local. To ignore non-local contribution to the Josephson electrodynamics for a single junction requires that the ratio $\lambda_J/\lambda \gg 1$ is large [273]. In this case, any variation of the phase, characterised by the Josephson penetration length λ_J, are smooth over the length-scale associated with variation in the magnetic field, characterised by the London penetration length λ, and any non-local terms can be approximated by local ones. For a layered Josephson junction, local Josephson electrodynamics is only a good approximation if $\lambda_J/\lambda_c \gg 1$ [252], which is even smaller than λ_J/λ as $\lambda_c/\lambda = \gamma \gamma_d^{1/2} \gg 1$.

A.3 Hamiltonian for phase difference and supercurrent difference

In this Section we are going to define the Hamiltonian giving rise to the non-dissipative parts of Eq. (A.24) and Eq. (A.36). The driving introduced damping term in Eq. (A.24) is included in this formulation, as it is not of dissipative origin. However, as we are ignoring in-plane dissipation, the adiabatic elimination of the second field is trivial and the resulting

Hamiltonian reduces to the single field Hamiltonian given in Eq. (3.15). Here, keep the second field to provide a more symmetric full Hamiltonian and relate its different terms to the energies in the system.

The total Hamiltonian can be separated into the two parts describing the dynamics of the two fields $\vec{\phi}$ and $\vec{S}$ and their coupling as

$$\mathcal{H} = \mathcal{H}_\phi^{(1)} + \mathcal{H}_\phi^{(2)} + \mathcal{H}_S + \mathcal{H}_{\text{int}}. \tag{A.40}$$

All terms can be related to the energy densities in the system. In the short junction regime any spatial dependence can be ignored the corresponding quadratic Hamiltonian of a capacitively coupled stack of short Josephson junctions for a junction of area A_{area} in the xy-plane is given by

$$\mathcal{H}_\phi^{(1)} = \frac{1}{L}\int_0^L dx \frac{1}{2}\vec{p}^\top \mathbf{M}^\phi(x,t)^{-1}\vec{p} + \frac{\Phi_0}{2\pi}A_{\text{area}}\mathbf{J}^C\left(1-\cos(\vec{\phi})\right). \tag{A.41}$$

The conjugate variable to the $\vec{\phi}$ field, $\vec{p} = \mathbf{M}^\phi(x,t)\partial_t\vec{\phi}$, is proportional to the electric field in the insulating sheets with mass

$$\mathbf{M}^\phi(x,t) = A_{\text{area}}\left(\frac{\Phi_0}{2\pi}\right)^2 \epsilon_0 \boldsymbol{\epsilon}(x,t)\mathbf{C}^{-1}(x,t), \tag{A.42}$$

where the time and spatially parts of the mass are inherited from the drive. This trivially satisfy the first Hamilton equation $\frac{\mathrm{d}\vec{\phi}}{\mathrm{d}t} = \frac{\partial\mathcal{H}}{\partial\vec{p}}$ as $\mathcal{H}_\phi^{(1)}$ is the only term of the Hamiltonian containing the kinetic term $\vec{p}$. An additional contribution due to a gradient in the phase is given by

$$\mathcal{H}_\phi^{(2)} = \frac{1}{L}\int_0^L dx \frac{1}{2\mu_0}A_{\text{area}}\left(\frac{\Phi_0}{2\pi}\right)^2 \partial_x\vec{\phi}^\top\mathbf{D}^{-1}\partial_x\vec{\phi}. \tag{A.43}$$

The conjugate variable to $\mathbf{S}$ is the momentum $\vec{b} = \mathbf{M}^S\partial_t S$, with the mass matrix given by

$$\mathbf{M}^S = -A_{\text{area}}\frac{\epsilon_0\epsilon_{ab}}{s^c}\left(\frac{\Phi_0}{2\pi}\right)^2\boldsymbol{\Delta}^{-1}. \tag{A.44}$$

The corresponding Hamiltonian of the $\vec{S}$ field in the short junction regime is given by

$$\mathcal{H}_S = \frac{1}{L}\int_0^L dx \frac{1}{2}\vec{b}^\top\mathbf{M}^{S^{-1}}\vec{b} + A_{\text{area}}\frac{1}{2}\frac{c^2}{\epsilon_{ab}\lambda^2}\vec{S}^\top\mathbf{M}^S\mathbf{L}\mathbf{D}^{-1}\vec{S}. \tag{A.45}$$

where $\mathbf{L}$ is given by a tridiagonal matrix,

$$\mathbf{L} = \frac{\lambda_{ab}^2}{D}\left(\boldsymbol{\eta}^{-1} - \boldsymbol{\Delta}\right), \tag{A.46}$$

characterised by the inductive coupling strength $\boldsymbol{\eta}^{-1} = \frac{D}{\lambda_{ab}^2}\boldsymbol{D}$. As conjugate variable the first Hamilton equation $\frac{\mathrm{d}\vec{S}}{\mathrm{d}t} = \frac{\partial\mathcal{H}_S}{\partial\vec{b}}$ is trivially satisfied. The kinetic part corresponds the x component of the electric field density, derived from displacement current along the superconducting sheets. This term is usually neglected in the adiabatic approximation, allowing

the **S** field to be replaced in the equation of motions, resulting into the coupled sine Gordon equation as presented in [192]. Keeping the kinetic part of **S**, however, allows a more elegant, symmetric and physically insightful picture.

The interaction part of the Hamiltonian contains the linear coupling of the two fields to each other, as

$$\mathcal{H}_{\text{int}} = A_{\text{area}} \frac{1}{L} \int_0^L dx \frac{1}{2\mu_0 s^c} \left(\frac{\Phi_0}{2\pi}\right)^2 \left(\vec{\phi}^\top \mathbf{D}^{-1} \partial_x \vec{S} - \vec{S}^\top \mathbf{D}^{-1} \partial_x \vec{\phi}\right). \tag{A.47}$$

This term contains a spatial derivative in x direction, therefore in the short junction regime $\mathcal{H}_{\text{int}} \to 0$ and the dynamics of the $\vec{\phi}$ and $\vec{S}$ is separately determined by $\mathcal{H}_\phi^{(1)}$ and $\mathcal{H}_S$ respectively.

Origin of each term in Hamiltonian The potential energy term in Eq. (A.41) corresponds to the Josephson potential, while the kinetic term in $\mathcal{H}_\phi^{(1)}$ can be expressed in terms of z component of the electric field energy using Eq. (3.5)

$$A_{\text{area}} \frac{1}{L} \int_0^L dx \frac{1}{2} \epsilon_0 \vec{E^z}^\top \boldsymbol{\epsilon}(x,t) \mathbf{C}(x,t) \vec{E^z} = A_{\text{area}} \frac{1}{L} \int_0^L dx \frac{1}{2} \vec{V}^\top \mathbf{C}_{cap}(x,t) \vec{V}, \tag{A.48}$$

with capacitance $\mathbf{C}_{cap}(x,t) = A_{\text{area}} \epsilon_0 \boldsymbol{D}^{-1} \boldsymbol{\epsilon}(x,t) \mathbf{C}(x,t) \boldsymbol{D}^{-1}$ and voltage $\vec{V} = \boldsymbol{D} \vec{E^z}$.

The physical origin for the first (kinetic) term in $\mathcal{H}_S$ in Equation A.45 is the displacement current $J_m^{d,x} = \epsilon_0 \epsilon_{ab} \partial_t E_m^x$ in x direction from Eq. (A.30). Using the first London equation [126]

$$E_m^x = \frac{\phi_0}{2\pi} \partial_t q_m, \tag{A.49}$$

the kinetic energy term can again be rewritten as the electric energy of the x component of the electric field

$$A_{\text{area}} \frac{1}{L} \int_0^L dx \frac{1}{2} \epsilon_0 \epsilon_{ab} s^c \vec{E^x}^\top \vec{E^x}. \tag{A.50}$$

by approximately cancelling the finite difference across the insulating layer δ with the inverse of the 2nd order discrete derivative, i.e. $\boldsymbol{\Delta}^{-1} \sim -\delta^\top \delta$.

The magnetic energy is given by

$$A_{\text{area}} \frac{1}{L} \int_0^L dx \frac{1}{2\mu_0} \vec{B}^\top \mathbf{D} \vec{B}, \tag{A.51}$$

which involves both fields. Using Eq. (A.35) it can be shown to arise from the first term of the potential energy (first term of **L**) in $\mathcal{H}_S$, $\mathcal{H}_\phi^{(2)}$ and the interaction term $\mathcal{H}_{\text{int}}$. The remaining second much smaller ($\eta \ll 1$) contribution to the potential energy in $\mathcal{H}_S$ due to the second term in **L** has the form of a small inductive term,

$$A_{\text{area}} \frac{1}{L} \int_0^L dx \frac{1}{2} \mu_0 s^c \lambda^2 \left(J^{\vec{s},x}\right)^\top J^{\vec{s},x}. \tag{A.52}$$

The different terms in the Hamiltonian to the electromagnetic and Josephson energies of the system.

Adiabatic elimination The Hamiltonian in Eq. (A.40) can be reduced to the form given in Eq. (3.15) after an adiabatic elimination of the time dependent current differrence $\partial_t \vec{S}$ in Eq. (A.38) such that $\vec{S}$ instantaneously adapts to gradients such that

$$\vec{S}^{(0)} = s^c \left(\mathbf{L} - \mathbf{D}\right) \mathbf{L}^{-1} \partial_x \vec{\phi}, \tag{A.53}$$

which is the zeroth order adiabatic elimination [258]. Ignoring the kinetic term in Eq. (A.45), we obtain

$$\mathcal{H}^{(0)} = \mathcal{H}_{\phi}^{(1)} + A_{\text{area}} \frac{1}{L} \int_0^L dx \frac{1}{2\mu_0} \left(\frac{\Phi_0}{2\pi}\right)^2 \partial_x \vec{\phi}^{\top} \mathbf{L}^{-1} \partial_x \vec{\phi}, \tag{A.54}$$

where we ignore the driving in the following. In dimensionless units with energy measured in units of $\frac{\Phi_0}{2\pi} A_{\text{area}} \mathbf{J}^C$ the Hamiltonian is given by

$$\mathcal{H}(\tau) = \frac{1}{L} \int_0^L dx \frac{1}{2} \vec{p}^{\top} \boldsymbol{\mathcal{M}}^{\phi^{-1}} \vec{p} + \left[\boldsymbol{\mathcal{J}}^C \left(1 - \cos(\vec{\phi})\right) - \mathbf{j}_{bias} \vec{\phi}\right] + \frac{1}{2} \frac{\gamma^4 \gamma_d}{\gamma_c^2} \partial_x \vec{\phi}^{\top} \boldsymbol{\mathcal{L}}^{-1} \partial_x \vec{\phi}, \tag{A.55}$$

where $\vec{p} = \boldsymbol{\mathcal{M}}^{\phi} \partial_\tau \vec{\phi}$ is the dimensionless momentum of the $\vec{\phi}$ field with the dimensionless mass $\boldsymbol{\mathcal{M}}^{\phi} = \frac{D}{\epsilon r^c} \boldsymbol{\mathcal{C}}^{-1}$, $\gamma_d = \frac{D}{s^c}$ is the ratio of the thickness of typical insulator to superconducting sheet, $\gamma_c = \frac{\lambda_c}{D}$ is the ratio of the London penetration depth to the thickness of typical insulator, $\gamma = \frac{\lambda_c}{\lambda_{ab}}$ is the anisotropy factor given by the ratio of c to in-plane London penetration depth λ_{ab}.

Dropping the non-linear terms in the Josephson potential makes it possible to obtain a Hamiltonian of an opto-mechanical form, which is formally equivalent to the Hamiltonian used in Ref. [31]. However, the Hamiltonian defined in Ref. [31] cannot be rigorously compared even in the short junction regime as it is missing terms from Ampère's law. 3.14, where the time-dependent permittivity leads to two terms, $\epsilon_0(\partial_t \epsilon_M(t)) E_M^z + \epsilon_0 \epsilon_M(t) \partial_t E_M^z$, the first of which was not taken into account in the derivation presented in Ref. [31].

Alternative expression The time dependence of the mass generates a time dependent coupling in the form of a damping term,

$$\boldsymbol{\gamma}_{disp}(x,\tau) = \frac{2\omega_d}{\omega_p} \sin\left(\frac{2\omega_d}{\omega_p}\tau\right) \frac{1}{2} \left(1 + \cos\left(2k_d x\right)\right) \boldsymbol{\mu} \boldsymbol{\mathcal{C}}(x,\tau)^{-1}. \tag{A.56}$$

which leads to Eq. (3.39). The mass can be recast as

$$\boldsymbol{\mathcal{M}}^{\phi}(x,\tau)^{-1} = \left[\boldsymbol{\mathcal{P}}_i^C - \boldsymbol{\mathcal{P}}_t^C \left(1 - \cos\left(\frac{2\omega_d}{\omega_p}\tau\right)\right) \frac{1}{2} \left(1 + \cos\left(2k_d x\right)\right)\right] \left(\boldsymbol{\mathcal{J}}^C\right)^{-1}, \tag{A.57}$$

The inductive coupling coupling matrix is then given by

$$\boldsymbol{\mathcal{P}}^L(x,\tau) = \frac{\gamma^4 \gamma_d}{\gamma_c^2} \left[\boldsymbol{\mathcal{P}}_i^C - \boldsymbol{\mathcal{P}}_t^C \left(1 - \cos\left(2\frac{\omega_d}{\omega_p}\tau\right)\right) \frac{1}{2} \left(1 + \cos\left(2k_d x\right)\right)\right] \left(\boldsymbol{\mathcal{J}}^C\right)^{-1} \boldsymbol{\mathcal{L}}^{-1}. \tag{A.58}$$

A.4 Analytic expressions

A.4.1 Transformation matrix

As the time independent part of the mass $\boldsymbol{\mathcal{M}}_i$ is a positive definite matrix, it can be diagonalised by the orthogonal block-diagonal matrix $\mathbf{V}$, i.e.

$$\boldsymbol{\mathcal{M}}_i = \mathbf{V}\mathbf{m}_i\mathbf{V}^\top, \tag{A.59}$$

where $\mathbf{m}_i$ is a diagonal matrix containing the positive mass eigenvalues.

Constructing a transformation $\mathbf{W} = \mathbf{V}\mathbf{m}_i^{-1/2}$, results in $\mathbf{W}^\top\boldsymbol{\mathcal{M}}_i\mathbf{W} = \mathbf{I}$. This transformation conserves the symmetry of $\mathbf{K}' = \mathbf{W}^\top\mathbf{K}\mathbf{W}$. Therefore we can diagonalise $\mathbf{K}'$ as

$$\mathbf{K}' = \mathbf{G}\boldsymbol{\Omega}^2\mathbf{G}^\top, \tag{A.60}$$

where $\boldsymbol{\Omega}^2$ is a diagonal matrix containing the time averaged frequencies squared of the two oscillators, which are the eigenvalues of $\boldsymbol{\mathcal{M}}_i^{-1}\mathbf{K}$.

The similarity transformation matrix used to diagonalise the Hamiltonian is than given by

$$\mathbf{P} = \mathbf{W}\mathbf{G}\bar{\mathbf{m}}_i^{1/2} = \mathbf{V}\mathbf{m}_i^{-1/2}\mathbf{G}\bar{\mathbf{m}}_i^{1/2}, \tag{A.61}$$

with the different symbols defined below. In general this transformation is not orthogonal, but it is still orthogonal with respect to the mass as metric. Consequently, it decouples the equation of motions of the different normal modes and conserves the commutation relation defined by the Poisson bracket [265].

A.4.2 Diagonalising Hamiltonian for spatially inhomogeneous driving

Only keeping linear terms in $\vec{\phi}$ field and performing the spatial integral, the different k_n are only coupled for spatially inhomogeneous driving, i.e. for $k_d \neq 0$. We therefore expect the total linearised Hamiltonian to satisfy $\mathcal{H} = \sum_{n,m}\mathcal{H}(n,m)$, where

$$\mathcal{H}(n,m) = \frac{1}{2}\vec{p}_n^\top\boldsymbol{\mathcal{M}}^\phi(n,m,\tau)^{-1}\vec{p}_m + \frac{1}{2}\vec{\phi}_n^\top\boldsymbol{\mathcal{K}}(n,m)\vec{\phi}_m, \tag{A.62}$$

with spring constant matrix

$$\boldsymbol{\mathcal{K}}(n,m) = \left(\boldsymbol{\mathcal{J}}^C + k_n^2\frac{\gamma^4}{\gamma_c^2\gamma_d}\boldsymbol{\mathcal{L}}^{-1}\right)\delta_{n,m}(1+\delta_{n,0})/2, \tag{A.63}$$

$$\boldsymbol{\mathcal{M}}^{-1}(n,m,\tau) = \frac{1}{L}\int dx\boldsymbol{\mathcal{M}}^\phi(x,\tau)^{-1}\cos(k_n x)\cos(k_m x) \tag{A.64}$$

Expanding the mass matrix in terms of the spatial modes, i.e.

$$\boldsymbol{\mathcal{M}}(n,m,\tau) = \frac{1}{L}\int dx\boldsymbol{\mathcal{M}}^\phi(x,\tau)\cos(k_n x)\cos(k_m x), \tag{A.65}$$

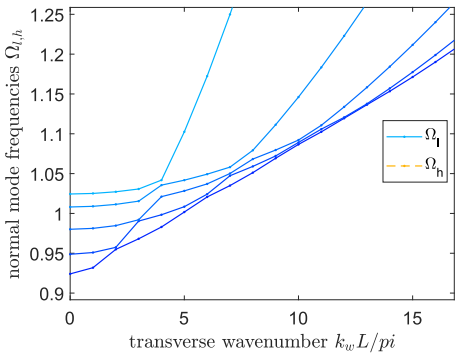


Figure A.2: Excerpt of the dispersion of the normal mode frequencies showing the competition between capacitive and inductive coupling for $\mathbf{\Omega}_l(w)$ leading to reordering of the normal modes. The wavenumber only takes integer values w and lines are only a guide to the eye.

We explicitly pull out the time dependence of the mass matrix by introducing to constant blockdiagonal matrices $\boldsymbol{\mathcal{M}}^i(n,m) = \boldsymbol{\mathcal{M}}(n,m,\frac{\pi}{2}\frac{\omega_p}{2\omega_d})$ and

$$\boldsymbol{\mathcal{M}}^t(n,m) = -\boldsymbol{\mathcal{J}}^C \left(\boldsymbol{\mathcal{P}}_i^C\right)^{-1} \boldsymbol{\mathcal{P}}_t^C \left(\boldsymbol{\mathcal{P}}_i^C\right)^{-1} \frac{1}{L}\int \frac{1}{2}(1+\cos(k_d x))\cos(k_n x)\cos(k_m x)dx. \quad \text{(A.66)}$$

such that $\boldsymbol{\mathcal{M}}(n,m,\tau) = \boldsymbol{\mathcal{M}}^i(n,m) + \boldsymbol{\mathcal{M}}^t(n,m)\cos\left(\frac{2\omega_d}{\omega_p}\tau\right) + O(\nu^2)$. Reshaping the modes dependence into a matrix, i.e. the set of matrices $\{\mathbf{A}(n,m)\}$ becomes

$$\mathbf{A} = \begin{pmatrix} \mathbf{A}(0,0) & \mathbf{A}(0,1) & \cdots \\ \mathbf{A}(1,0) & \mathbf{A}(1,1) & \cdots \\ \vdots & \vdots & \ddots \end{pmatrix}, \quad \text{(A.67)}$$

and similarly the set of vectors $\{\vec{v}(n)\}$ becomes

$$\vec{v} = \begin{pmatrix} \vec{v}(0) \\ \vec{v}(1) \\ \vdots \end{pmatrix}. \quad \text{(A.68)}$$

For spatially dependent driving the spatial modes are coupled already through linear terms and have to be solved simultaneously, i.e. the matrices for the nth mode are replaced by larger matrices containing all modes simultaneously, e.g. $\mathbf{P}_n \to \mathbf{P}$, $\mathbf{K}_n \to \mathbf{K}$, $\bar{\mathbf{m}}_n^i \to \bar{\mathbf{m}}^i$, $\mathbf{\Omega}_n^2 \to \mathbf{\Omega}^2$, $\vec{Q}_n \to \vec{Q}$ and $\vec{\bar{Q}}_n \to \vec{\bar{Q}}$.

A.4.3 Spatial structure of normal modes for finite stack

The spatial arrangement of the different eigenvectors becomes more complicated with increasing w. In Fig. A.3 and A.4 (in the Appendix) the lowest (blue and red respectively)

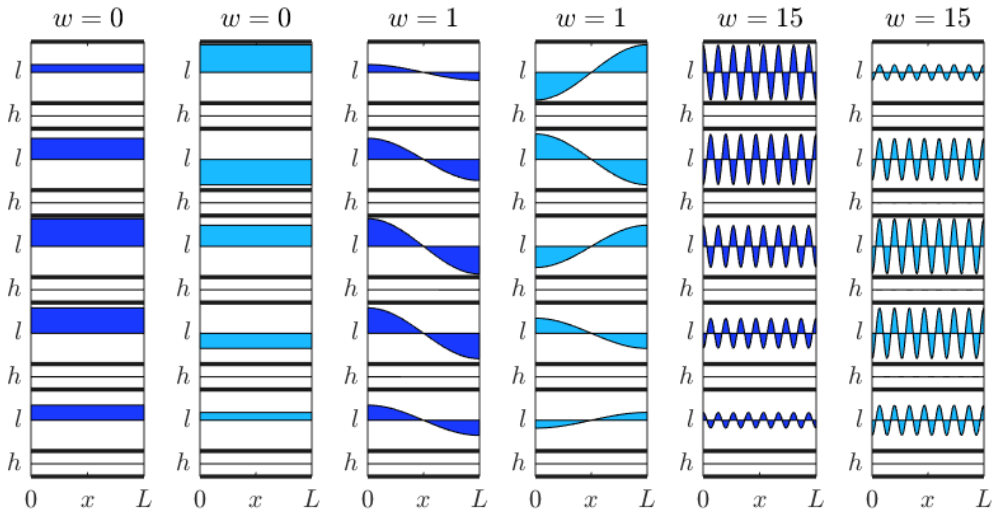


Figure A.3: Spatial arrangement of eigenvectors corresponding to highest (turquoise) and lowest (blue) normal mode of $\Omega_l(w)$ branch for different k_w corresponding to $w = 0, 1, 15$ for a stack of ten junction. Parameters given in Sec. 3.2.1.

and highest (turquoise and yellow respectively) eigenvectors of the low $\Omega_l(w)$ and high $\Omega_h(w)$ frequency branch are shown for different $k_w = w\pi/L$ corresponding to $w = 0, 1, 15$. This arrangement can be understood using a plasma wave ansatz of the form $\vec{\phi} \propto e^{i(k_z z + k_w x - \omega t)}$ with in-plane (out-of) plane momentum k_w (k_z). Ignoring the complexity of the bilayer model by going into the continuous limit such that 2nd order finite differences $\boldsymbol{\Delta}$ can be approximated as derivatives ∂_z^2 and ignoring terms $O(\frac{1}{\eta_{l,h}})$, the dispersion curves of the corresponding continuous model are approximated as

$$\omega^2(k_w, k_z) \approx \frac{\epsilon r^c}{D}\left(\boldsymbol{\alpha}^{-1} + k_z^2\right)\left(\mathrm{diag}(\boldsymbol{\mathcal{J}}^C) + \frac{k_w^2}{k_z^2}\frac{\gamma^4}{\gamma_c^2\gamma_d}\right). \tag{A.69}$$

Firstly, for the homogeneous mode $w = 0$ or $k_w = 0$, the lowest and highest frequency mode of $\boldsymbol{\Omega}_l(w = 0)$ are approximately in-phase ($k_z \approx 0$) and out-of-phase (maximum k_z) as visible in Fig. A.3 by focussing on the excitation in the l junction. For $w = 15$, on the other hand the in-phase oscillation corresponding to $k_z \approx 0$ (turquise) become the most energetic, i.e. the second term in the second bracket dominates over the k_z dependence in the first bracket. This shows the competition between capacitive and inductive coupling leads to a reordering of the normal mode frequencies already for very small k_w as inductively coupling is order of magnitudes larger [192].

For the finite stack consisting of 20 junctions, it is only visible in a close up of the $k_w = 0$ from Fig. 3.2b. The spatial structure of the normal modes characterised by approximate values for q and k_w determines, which modes couple to each other once the driving is switched on. The spatial arrangement of the modes in a finite stack of ten Josephson junction agrees with the expectation from the continuous model. The spatial arrangement of the highest (yellow) and lowest (blue) frequency mode is for example shown for $k_w = 0$ in the left and middle panel of Fig. A.5 with both modes corresponding to $q \approx 0$.

For finite in-plane momentum k_w, the highest frequency mode of the low-frequency branch

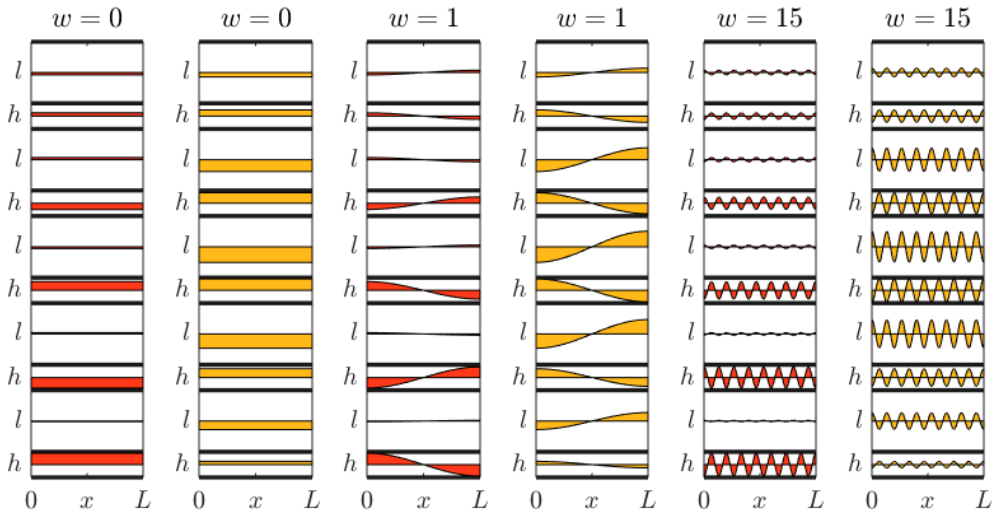


Figure A.4: Spatial arrangement of eigenvectors corresponding to highest (yellow) and lowest (red) normal mode of $\Omega_h(w)$ branch for different k_w corresponding to $w = 0, 1, 15$. Parameters given in Sec. 3.2.1.

(turquoise) corresponds to $q \approx 0$, each bilayer moves in phase. This observation is in agreement with the expectation that this mode converges against $\omega^{(+,-)}(k_w)$ with $q = 0$. The lowest frequency mode (dark blue) for $k_w \neq 0$ in Fig. 3.2b on the other hand corresponds to high q in agreement with Ref. [277] (see Fig. 3.2b). The frequency dependence on q is therefore inverted going from $k_w = 0$ to a small but finite $k_w \neq 0$. This reordering of the normal mode frequencies arises from the competition between the capacitive and inductive coupling and occurs already at very small k_w, as inductively coupling magnitudes larger than capacitive coupling [192].

A.4.4 Definition of cooling ratios

The expression for the cooling ratio from Eq. (3.90) can be transformed to real space. As the thermal occupation of the high-frequency mode remains small at all times, the quadrature values of the low-frequency normal modes are approximately equal to the total quadrature $\langle \vec{Q}_w^\top \vec{Q}_w \rangle$. Choosing $\bar{\mathbf{m}}_w^i$ equal to the identity (see discussion around Eq. (3.47)), we obtain from Eq. (3.46) that $\vec{Q}_w^\top \vec{Q}_w = \vec{\phi}_w^\top \boldsymbol{\mathcal{M}}_w^i \vec{\phi}_w$. We therefore obtain that the cooling ratio from Eq. (3.90) for is approximately equal to a whole stack of final ($\tau \to \infty$) and initial ($\tau_{\text{init}} = 0$) phase quadratures[1] weighted by the mass matrix $\boldsymbol{\mathcal{M}}_w^i$ is given by

$$\bar{R}_\Sigma^{(r)} = \frac{\int dx \langle \vec{\phi}_r^\top(x) \boldsymbol{\mathcal{M}}_w^i \vec{\phi}_r(x) \rangle_{\tau \to \infty}}{\int dx \langle \vec{\phi}_r^\top(x) \boldsymbol{\mathcal{M}}_w^i \vec{\phi}_r(x) \rangle_{\tau_{\text{init}}=0}}. \tag{A.70}$$

with $\vec{\phi}_{r=l,h}(x)$[2] as a vector formed from the phase in the l-and h-type of junction (see Fig. 3.1). $\langle \ldots \rangle$ denotes a thermal average. The expression for the cooling ratio from

[1] The phase averages to the equilibrium position, i.e. $\langle \delta\vec{\phi} \rangle = 0$.

[2] $\langle \vec{\phi}_l^\top \vec{\phi}_l \rangle = \langle \vec{\phi}^\top \vec{\phi} \rangle$

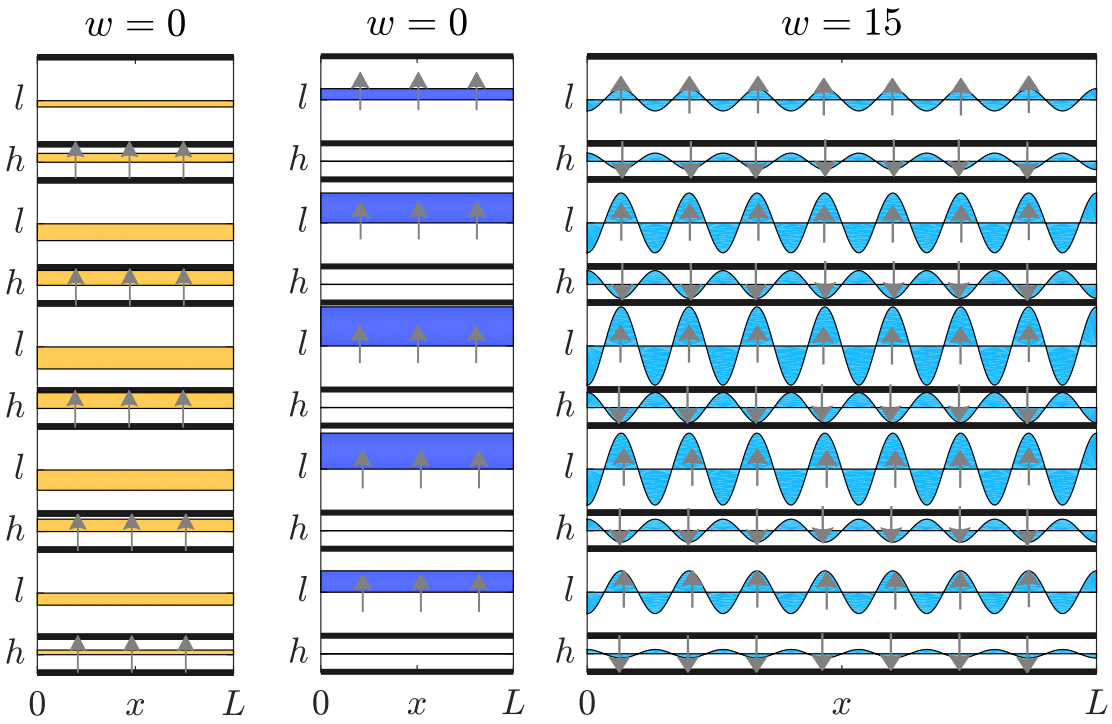


Figure A.5: The eigenstate structure of the phase for selected modes as indicated by black lines. The shaded area below them is just a visual help for the identification of the equilibrium position using the same colour code as for the twenty junction stack in Fig. 3.2b. Thick black lines indicated the superconducting sheet. The three separate copies of the ten junction stack of length $L = 0.4$ correspond to different spatial modes $w = 0, 15$ with the junction type labelled by l and h. The grey arrows show the expectation from the continuous model for the uniform motion of the unit cells for $\Omega^{(+,-)^2}(q = 0)$. Considering a unit cell, the high-frequency mode also contains an out of phase component from the low-frequency junction. The highest frequency component of the low-frequency branch approaches the transverse optical frequency ω_T, which corresponds to out of phase fluctuation.

Eq. (A.70) is good real space approximation of Eq. (3.90). Different to Eq. (3.89) it includes the mass matrix as a metric.

A.4.5 Solving for physical parameters in a two-junction toy model

Debye screening length $\lambda_c^{(D)}$ In the capacitive coupling the thickness appears as a ratio with respect to the Debye screening length, i.e. $\frac{s^c}{\lambda_c^{(D)}}$. From Equation A.13 and A.16 this ratio is determined in terms of the free parameters α_1 and α_2 as

$$\cosh\left(\frac{s^c}{\lambda_c^{(D)}}\right) = \left(\frac{D_l}{D_h}\frac{\epsilon_h}{\epsilon_l} - \frac{\frac{\alpha_2}{2\alpha_2+1}}{\frac{\alpha_1}{2\alpha_1+1}}\right)\frac{1}{2\frac{\alpha_2}{2\alpha_2+1}\left(\frac{D_l}{D_h}\frac{\epsilon_h}{\epsilon_l}-1\right)}, \tag{A.71}$$

where we explicitly kept the permittivity of each insulating layer to allow the comparison with the work done in [356].

As $\cosh(x) \geq 1$ in order to satisfy this equation the right hand side of Equation A.71 has to be larger then 1. This can be shown to lead to the restriction

$$\alpha_1 > \frac{D_h}{D_l}\frac{\epsilon_l}{\epsilon_h}\alpha_2, \tag{A.72}$$

placing a lower bound on the region for possible $\alpha_{1,2}$ values. In [192] s^c is estimated to be comparable to or even larger then $\lambda_c^{(D)}$ even for intrinsic Josephson junction. For $\epsilon_l = \epsilon_h$ such values correspond to the $\alpha_2 \approx \alpha_1$, while a small thickness compared to Debye screening length would rather correspond to $\alpha_1 \approx \frac{D_h}{D_l}\alpha_2$.

Permittivity in superconductor ϵ_s While the permittivity in the insulating layer and along the *ab* plane is taken to be 5, the permittivity in the superconducting sheets is determined by the external parameters $\alpha_{1,2}$. From the definition of r^c above Eq. (A.13) and Eq. (A.16), we obtain

$$\epsilon^s = \frac{\lambda_c^{(D)}}{\sinh\left(\frac{s^c}{\lambda_c^{(D)}}\right)}\frac{2\alpha_M+1}{\alpha_M}\frac{\epsilon_M}{D_M^C}. \tag{A.73}$$

For completeness Equation A.73 can be used to determine

$$r^c = \frac{\alpha_1\alpha_2}{\epsilon}\frac{D_l - D_h}{\alpha_2 - \alpha_1}, \tag{A.74}$$

where again $\epsilon_l = \epsilon_h = \epsilon$.

Effective insulating layer thickness D_M^C Dividing Equation A.13 by D_M^C and using A.16, we obtain

$$D_M^C = \frac{D_M}{1 - \frac{2\alpha_M}{2\alpha_M+1}\cosh\left(\frac{s^c}{\lambda_c^{(D)}}\right)}, \tag{A.75}$$

for the effective insulating layer thickness for capacitive coupling D_M^C in dependence of the Debye screening length obtained in the previous section. The effective insulating layer thickness for capacitive coupling D_M^C is expected to be positive. Therefore the denominator is expective to be positive, which restricts possible choices for $\alpha_{1,2}$.

Using Equation A.71 it can be shown that $D_M^C > 0$ for both choices $M = \{l, h\}$, when

$$\alpha_1 < \alpha_2, \tag{A.76}$$

placing an upper bound on the region for possible $\alpha_{1,2}$ values.

Frequency $\varpi_{l,h}$ The normal mode frequencies are fixed by experimental values. Introducing a function

$$h(\alpha_1, \alpha_2) = 1 + 2\alpha_2 + 2\alpha_1 + 3\alpha_1\alpha_2, \tag{A.77}$$

the frequencies $\varpi_{l,h}$ are defined to lowest two order in $r = \frac{\Omega_l}{\Omega_h} \approx \frac{1}{10}$ by

$$\varpi_l^2 = \Omega_l^2 \frac{1+2\alpha_2}{h(\alpha_1,\alpha_2)} + O(r^4), \tag{A.78}$$

and

$$\varpi_h^2 = \Omega_h^2 \frac{1}{1+2\alpha_2} - \frac{\Omega_l^2 \alpha_1\alpha_2}{(1+2\alpha_2)h(\alpha_1,\alpha_2)} + O(r^3), \tag{A.79}$$

respectively.To obtain driving independent normal mode frequencies we use

$$\varpi_l^2 = \Omega_l^2 \frac{1+2\alpha_2}{h(\alpha_1,\alpha_2)} \left[1 - \frac{1}{h(\alpha_1,\alpha_2)} \left(\frac{\eta_h}{2}\frac{\alpha_1\alpha_2}{1+2\alpha_2} + \frac{\eta_l}{2}(1+2\alpha_2)\right)\right] + O(r^4), \tag{A.80}$$

and

$$\varpi_h^2 = \Omega_h^2 \frac{1}{1+2\alpha_2}\left(1 - \frac{\eta_h}{2(1+2\alpha_2)}\right) - \frac{\Omega_l^2\alpha_1\alpha_2}{(1+2\alpha_2)h(\alpha_1,\alpha_2)} + \frac{\Omega_h^2\eta_h^2}{4(1+2\alpha_2)^3} + O(r^3), \tag{A.81}$$

Analytical cooling ratio as a function of driving strength

Cooling of momentum quadratures To stabilise superconductivity from switching into a resistive state, we only require to cool the phase quadrature and not necessarily the momentum quadrature. Nevertheless, in Figure A.12 we have also included the cooling ratio of the momentum quadrature (dashed orange line and markers labelled by p) obtained by respectively replacing $\vec{\phi}(\boldsymbol{x})$ by $\vec{p}(\boldsymbol{x})$ in the expression for R^l_{traj} from Eq. (3.89) (orange errorbars) and by replacing $\vec{Q}_w$ by $\mathfrak{P}_w$ in the expression for $R^{(l)}_\Sigma$ from Eq. (3.90) (dashed line for driving strength $\nu_2 = 0.125$). According to the classical equipartition theorem (Appendix B.7), any thermally occupied degree of freedom carries the same energy such that $\langle\vec{\mathfrak{P}}_w^2\rangle = \bar{\boldsymbol{m}}_w^i \frac{k_B T^r}{E_J}\mathcal{T}$. Both quadratures are simply related by $\langle\vec{Q}_w^2\rangle = \boldsymbol{\Omega}^{-2}(k_w)\langle\vec{\mathfrak{P}}_w^2\rangle$ and therefore cooled by the same ratio $R^{(j,l)}(k_w)$ from Eq. (3.79). Therefore, spatial modes with frequencies just below the cutoff ω^c still contribute to the cooling ratio though the corresponding position quadrature is negligibly small. The apparent difference between the cooling ratio of the blue and red curves is therefore only an artefact due to distinct weights assigned to different contributions, while in fact both quadratures are cooled by the same ratio.

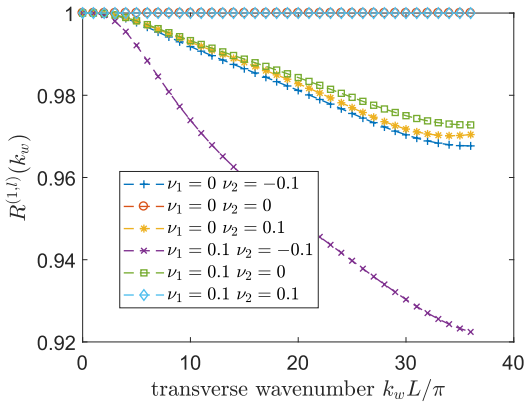


Figure A.6: Cooling ratio $R^{(1,l)}(k_w)$ from Eq. (3.79) for $\epsilon(t)$-Model (Eq. (3.32)) as a function of wavenumber $w = k_w L/\pi$ for different driving arrangement of permittivity in the case of an extremely small capacitive coupling (length $L_0 = 0.5$, $\alpha_1 = 0.28s$, $\alpha_2 = 0.66s$, $s = 10^{-10}$, $\gamma_l = 0.005$, $\gamma_h = 0.01$, $f = \frac{1}{3}$).

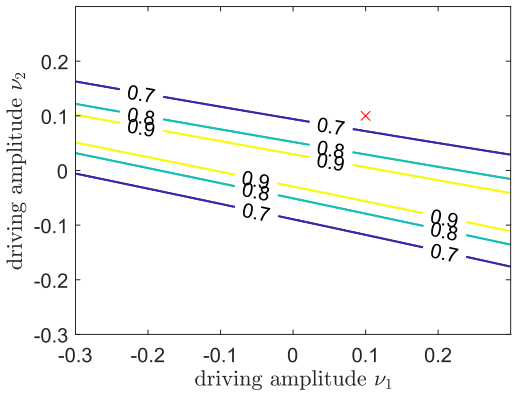


Figure A.7: Cooling ratio $R^{(1,l)}(k_w)$ from Eq. (3.79) of the final driven vs initial thermal normal mode quadrature of the in-homogeneous mode $w = 10$ for $\epsilon(t)$-Model (Eq. (3.32)) ($L = 0.5$).

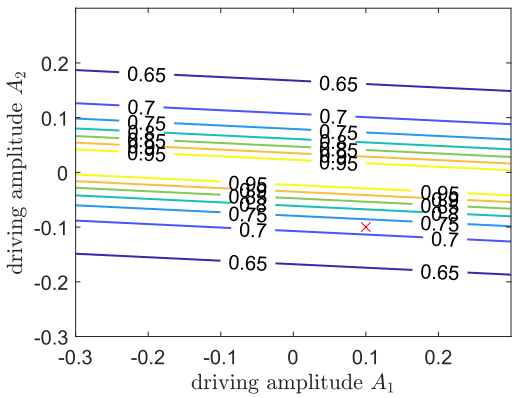


Figure A.8: Cooling ratio $R^{(1,l)}(k_w)$ from Eq. (3.79) of the final driven vs initial thermal normal mode quadrature of the in-homogeneous mode $w = 10$ for $J^C(t)$-Model (Eq. (3.28)) ($L = 0.5$).

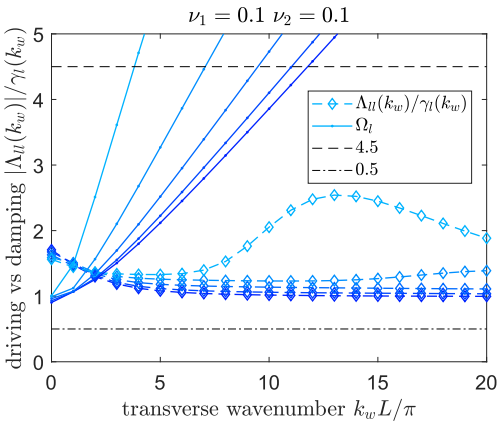


Figure A.9: Damping rates $\gamma(k_w)$ and driving strength $\Lambda_{ll}(k_w)$ for $\nu_1 = 0.1$ and $\nu_2 = 0.1$ for $\epsilon(t)$-Model (Eq. (3.32)) (length $L_0 = 0.5$, $\alpha_1 = 0.28$, $\alpha_2 = 0.66$, $f = 0.75$).

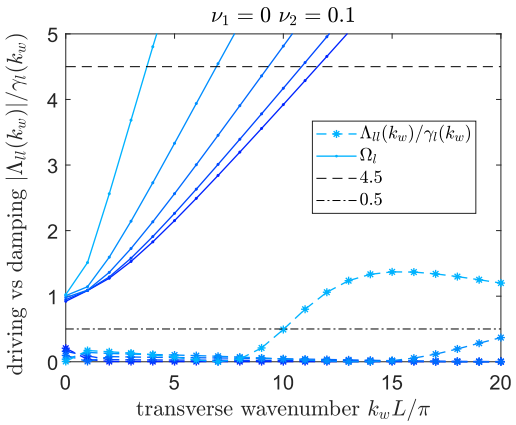


Figure A.10: Damping rates $\gamma(k_w)$ and driving strength $\Lambda_{ll}(k_w)$ for $\nu_1 = 0$ and $\nu_2 = 0.1$ for $\epsilon(t)$-Model (Eq. (3.32)) (length $L_0 = 0.5$, $\alpha_1 = 0.28$, $\alpha_2 = 0.66$, $f = 0.75$).

A.5 Approaching the phase transition

The generalisation of the parametric cooling scheme to a higher dimension is a first step towards describing a true phase transition. However, the current model does not allow very high energy in plane excitations such as vortices. These are topological features occurring in the superconducting phase of 2D thin films of conventional superconductors [138]. At the centre of these vortices, the amplitude of the order parameter is suppressed $|\psi(\vec{r})| \to 0$, while the phase increases by an integer m of 2π as

$$\oint \varphi(\vec{r})\, dl = 2\pi m, \tag{A.82}$$

where the integration is performed in a loop around the vortex core.

As the energy of an isolated [138] vortex diverges in the thermodynamic limit, they are usually excited as vortex-anti-vortex pairs (Fig. A.13). The strong gradients associated with the phase winding around the vortex core lead to strong in-plane screening currents causing vortices in the same layer to exert a Lorentz force on each other. Close to the transition temperature, the 2D thin film screening length becomes larger then the system size such that the logarithmic part of the resulting interaction potential dominates [138,357]. In this limit, the minimisation of the free energy is governed by a delicate interplay of the interaction energy and entropy associated with vortices, leads to a type of Berezinskii-Kosterlitz-Thouless (BKT) transition in the thermodynamic limit. The resulting creation of vortices and unbinding of vortex-antivortex pairs gives rise to a finite resistance.

A.5.1 XY model

The standard model to capture such a BKT transition is the XY model given by

$$H_{XY} = -\sum_{i \neq j} J_{ij}^{ab} \cos(\varphi_i - \varphi_j). \tag{A.83}$$

Physically, this model corresponds to a two-dimensional array of superconducting islands connected by Josephson junction with critical current J_{ij}^{ab}, where ij correspond to the spatial indices.

The intrinsically layered structure of HTSC makes the idea of BKT transitions very compelling. There are indications in support of such a transition in HTSC, ranging from a finite frequency conductivity [56, 358], Nernst effect [359] to nonlinear magnetization [360].

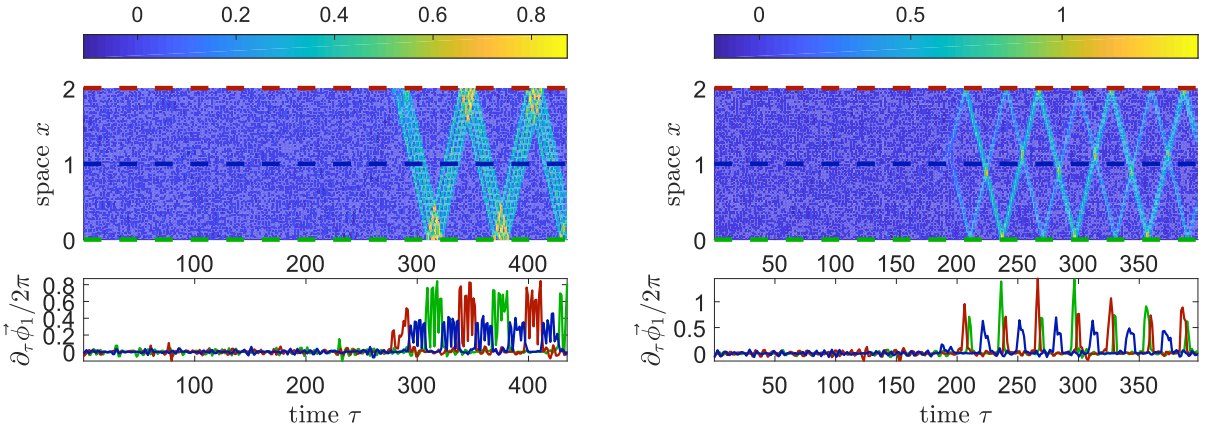
A 3D extension to the XY model including an additional weak coupling across the planes appears to account for some 3D critical scaling behaviour observed in Ref. [361–364]. The presence of an interlayer coupling J_c smoothens the in-plane vortex divergence [139]. Modulation of J_c should, therefore, influence the transition [365]. In the electro-dynamical model of Josephson junction, the two-dimensional cupper-oxide planes are treated as conventional superconductors. While this is a good approximation in the low-temperature regime, such a model cannot capture the phase transition in HTSC. The reduction of the phase to zero $|\psi(\vec{r})| \to 0$ in conventional superconductors is associated with the reduction of the superconducting gap. Reducing the gap to zero inside of vortex cores would require an enormous large energy in HTSC. Consequently, only a few of these cores could be excited above T_c, which has not been observed experimentally [366]. Scanning tunnelling microscope experiments of the vortex core in HTSC [132, 133] instead show that the superconducting gap survives. Finding a cooling mechanism around the critical temperature will, therefore, require to make a connection to the underlying material. The problem of vortex energy has for example been addressed using an SU(2) slave boson theory [104]. An effective XY model for such an approach has been developed in Ref. [366], where both SC pairing and phase are modelled. A simulation of the phase transition might therefore always include a competing order or additional fields motivated by the underlying structure [366].

The first step in the study of the interaction between vortices and the gauge invariant phase would be to manually introduce vortices created by a magnetic field or thermally excited pairs in the model of Josephson junction following the rather involved treatment in Ref. [260]. Such an approach does not describe the excitation of the vortex-antivortex pair, but only their unbinding. As the vortices live in the superconducting phase instead of the gauge invariant phase difference, a canonical transformation [257] of the short junction Hamiltonian to a frame focussing on the superconducting phase instead of the phase difference is advantageous, as it avoids singularities in the equation of motions [260]. The cost of this transformation would be a more involved driving term. There exist no optimal frame for the representation of both vortices and driving, one favouring the simulation of the gauge invariant phase difference of the Josephson junction, while the other the one of the superconducting phase in each layer.

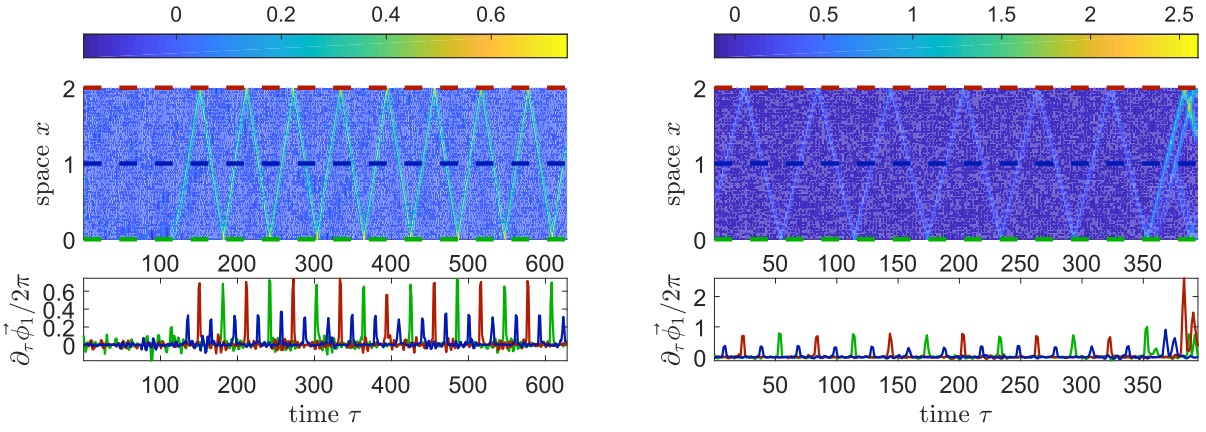
Dividing the cuprates into independently thermalised stacks of short junctions, the singularity of the vortex core is restricted to islands in between. The vortex creation could then be investigated in a modified version of a 3D XY model consisting of Josephson junction array of capacitively coupled Josephson junction as shown in Fig. A.14 coupled in an XY fashion.

In a 2D XY model the vortex core energy is $\propto J_{ab}$ [138]. However, there are indications

that the vortex core energy deviates from the XY prediction in the case of HTSC [104, 127, 138, 139]. By mapping a 3D-XY model to a sine Gordon model, this has been analysed under renormalisation group flow in Ref. [127, 139]. The interlayer coupling parameter J_c leads to smoothing out of the superfluid-density jump as observed in the experiment, while upon increasing the vortex energy the superfluid-density jump was increased above the T_{BKT}. There are therefore strong reasons to include variable vortex energy in a simulation of HTSC. It could for example also be that an underlying competing phase to determines the vortex core energy, and the coupling of a driving field could, therefore, be also pictured to modify this energy completely changing the dynamics of the phase indirectly.



(a) $j_{\text{bias}} = 0.40902$ ***(b)*** $j_{\text{bias}} = 0.3982$



(c) $j_{\text{bias}} = 0.19739$ ***(d)*** $j_{\text{bias}} = 0.41263$

Figure A.11: Time derivative of the phase $\partial_\tau \vec{\phi}_1(x,\tau)/2\pi$ for the low frequency junction as a function of time τ and spatial coordinate x obtained from a trajectory of Eq. (3.65) with the replacement Eq. (3.91). Bottom panel shows the same quantity at three different positions in the junction, whose respective location in the junction is encoded by a dashed line of the same color in the top panel. Fewer datapoints used then in Fig. 3.16, the spatial averaging over 3 datapoints has a larger effect (stack of two junctions of length $L = 2$, magnitude of in-plane dissipation $f = 3/4$ defined below Eq. (3.64), driving amplitudes $\nu_1 = 0$ and $\nu_2 = 0.1$ for $\epsilon(t)$-Model driving from Eq. (3.32),$\mathcal{T} = 0.002$).

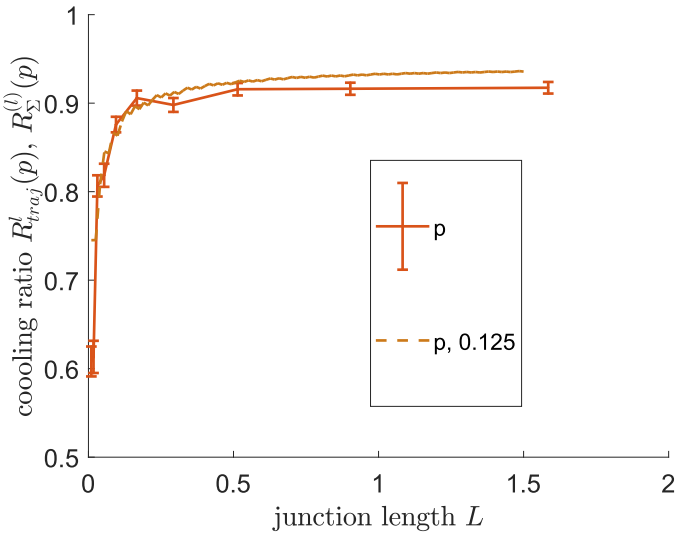


Figure A.12: Cooling ratios for the momentum quadrature obtained from the expressions for R^l_{traj} and $R^{(l)}_\Sigma$ by respectively replacing the phase $\vec{\phi}$ by its conjugate momentum $\vec{p}$ (orange error bar labelled p) and $\vec{Q}$ by $\mathfrak{P}$ (orange dashed line labelled p and by driving amplitude $\nu_2 = 0.125$). In this case the cooling ratio is reduced as high-frequency modes with negligible position quadratures all contribute equally (driving amplitudes $\nu_1 = 0$, $\nu_2 = 0.1$ from Eq. (3.32), magnitude of in-plane dissipation $f = 3/4$ defined below Eq. (3.64), $\mathcal{T} = 0.001$ using approximately 200 trajectories and averaging over a time interval of the order $1/\gamma_l$, errorbars from bootstrapping).

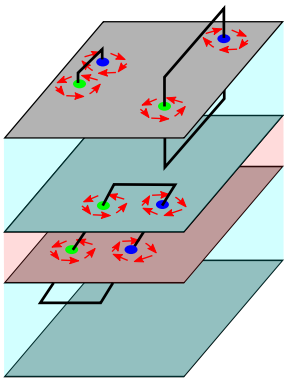


Figure A.13: Vortex anti-vortex pairs sitting in the superconducting grey sheets are represented by green and blue dots respectively. A couple of different pairs are shown with black vortex tubes connecting them to simplify the categorisation.

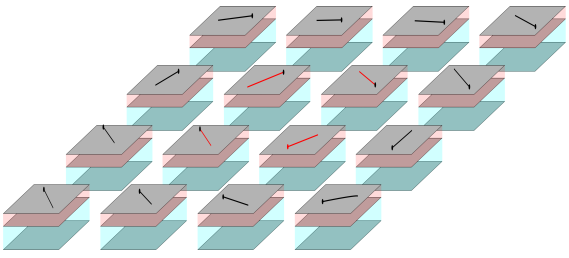


Figure A.14: Array of stacks of short junction coupled in an XY model like fashion allowing for a vortex in between the junctions.

Appendix B

Open quantum system

B.1 Quantum treatment of a single Josephson junction

In this Appendix, we consider the coherent dynamics governed by a quantised version of Eq. (1.20). Promoting the phase operator $\hat{\phi}$ and its conjugate momentum $p_\phi/\hbar \to \hat{n}$ to operators, where $\hat{n}$ is the number of Cooper pairs such that $[\hat{n}, \hat{\phi}] = -\mathrm{i}$ we obtain a Hamiltonian of the form [10, 95, 367]

$$\mathcal{H}_\phi = E_C \hat{n}^2 + U(\hat{\phi}), \quad U(\hat{\phi}) = -E_J \cos(\hat{\phi}) - \frac{\hbar I_{bias} \hat{\phi}}{2e}, \tag{B.1}$$

where we defined the charging energy as $E_C = \frac{(2e)^2}{2C} = \frac{\hbar^2}{2m_\phi}$ in terms of the mass $m_\phi = \left(\frac{\hbar}{2e}\right)^2 C$ for a junction of capacitance $C = \epsilon_0 \epsilon_r A_{\text{area}}/D$ for a junction of area A_{area}, thickness D and relative permittivity ϵ_r [69]. In general, a good basis choice depends on the relative magnitude of the effective Josephson coupling energy $E_J = \frac{\hbar I^C}{2e}$. The discussion of quantum versus classical treatment can be separated into two regimes according to the damping strength [95]. In the overdamped regime, the phase is strongly damped and consequently well-defined with little uncertainty leading to classical phase dynamics. In the underdamped regime, on the other hand, quantum effects cannot be ignored apriori [95]. Spreading of the wavepacket happens on time scales $\frac{\hbar}{E_C} \propto C$ determined by the kinetic energy of the phase particle E_C. However, below the damping induced phase transition, superconductivity can be still observed as a non-equilibrium state for all relevant time-scales [69]. In the steady state, however, the duality between momentum and position means that an underdamped phase dynamics corresponds to a classical overdamped dynamics for its conjugate variable leading to well-defined quasi-charge, which can have observable effects such as Bloch oscillation [368].

Diagonalisation of linearised Hamiltonian In the absence of a bias current, keeping only terms quadratic in $\hat{\phi}^2$ we obtain from Eq. (B.1) dropping constant energy shifts [10]

$$\mathcal{H}_\phi = E_C \hat{n}^2 + \frac{E_J}{2} \hat{\phi}^2, \tag{B.2}$$

which can be diagonalised using annihilation operator

$$\hat{b} = \sqrt{\frac{E_J}{2\hbar\omega_0}}\hat{\phi} + \mathrm{i}\sqrt{\frac{\hbar\omega_0}{2E_J}}\hat{n}, \tag{B.3}$$

$$\hat{b}^\dagger = \sqrt{\frac{E_J}{2\hbar\omega_0}}\hat{\phi} - \mathrm{i}\sqrt{\frac{\hbar\omega_0}{2E_J}}\hat{n}, \tag{B.4}$$

with $V = A_{\text{area}}D$ Josephson plasma frequency ω_0

$$\omega_0^2 = 2E_C E_J/\hbar^2, \tag{B.5}$$

such that the Hamiltonian is quantized as

$$\mathscr{H}_\phi = \hbar\omega_0\left(\hat{b}^\dagger\hat{b} + \frac{1}{2}\right), \tag{B.6}$$

Diagonalisation of linearised Hamiltonian for long cavity We next consider the diagonalisation of the linearised Hamiltonian from Eq. 2.18) for a long Josephson junction containing the first three spatial modes. The canonical variable of the wth mode is given by $n_w = \frac{1+\delta_{w,0}}{2}\frac{E_J}{\hbar\omega_0^2}\frac{d\phi_w}{dt}$ with Dirac delta $\delta_{w,0}$ coming from the spatial overlap which changes the effective mass of the mode such that the Poisson bracket evaluates as $\{n_w, \phi_w\} = -1$. We can promote both canonical variables to operators $n_w \to \hat{n}_w$ and $\phi_w \to \hat{\phi}_w$ such that $[\hat{n}_w, \hat{\phi}_w] = -\mathrm{i}$ and we obtain annihilation operator for the spatially homogeneous mode

$$\hat{b}_w = \sqrt{\frac{E_J\Omega_w}{2\hbar\omega_0^2}\frac{1+\delta_{w,0}}{2}}\hat{\phi}_w + \mathrm{i}\sqrt{\frac{\hbar\omega_0^2}{2E_J\Omega_w}\frac{2}{1+\delta_{w,0}}}\hat{n}_w, \tag{B.7}$$

where the normal mode frequency of Ω_w with $\Omega_0^2 = \omega_0^2\cos(\phi^0)$ and $\Omega_1^2 = \omega_1^2 = \omega_0^2[\cos(\phi_0) + \lambda_J^2 k_1^2]$ and the corresponding creation operator $\hat{b}_w^\dagger$ given as the Hermitian conjugate, such that the uncoupled part of the Hamiltonian diagonalises as

$$\mathscr{H}_\phi = \hbar\Omega_w\left(\hat{b}_w\hat{b}_w + \frac{1}{2}\right) + \mathscr{H}_{\text{int}}. \tag{B.8}$$

Collective degree of freedom in JJ A selection of noise processes acting on conventional Josephson Junction has been studied from first principles in an imaginary time path integral formulation in Ref. [69]. Starting from a microscopic model Hamiltonian of the BCS or normal metal, the auxiliary collective bosonic field appears after a Hubbard-Stratonovich transformation [69, 81]. Tracing out the microscopic electronic degree of freedom firstly gives this field its physical interpretation as the superconducting phase difference and secondly introduces dissipative non-local contributions to the action of the path integral. The symmetry of these dissipative actions depends on whether the dissipation process is due to an Ohmic shunt or quasi-particle tunnelling, which can have physical consequences for the charge transport or induce phase transition at zero temperature in ultra-small Josephson Junction governed by quantum mechanics(Sec. B.1).

For Ohmic dissipation, the dissipative part of the action is quadratic, which is also what is expected for phenomenological Caldeira Leggett model describing the thermalisation in terms of coupling to a bath of harmonic oscillator [318]. For quasi-particle tunnelling, on the other hand, the action contains a trigonometric function. As a consequence of the surviving symmetry, quasi-particle tunnelling only reduces the translational symmetry of the underlying Josephson Junction from 2π as it would be if only pairs of charges tunnel to 4π as in the presence of single particles, while Ohmic dissipation destroys the translational symmetry. For small phase deviation, the dissipative part of both actions becomes quadratic such that the translational symmetry is destroyed in both cases. Physically, this corresponds to a regime, where the difference between discrete vs continuous charge transport disappears leading to the Caldeira Leggett type of coupling. The non-linearity of the action and its physical consequences on charge transport might, therefore, allow distinguishing between different dissipation mechanism. These two dissipation processes are of course not the only ones. Other studies consider for example the role of anomalous dissipation [369] and electromagnetic environment [98].

Together with the dissipation induced phase transition discussed in next subsection, which relies on charge and phase being conjugate variables, these effects due to the non-linearity of the underlying Josephson Junction correspond to another approach for learning about the dissipative dynamics. As we are only considering linearised junctions, these effects will not be present in the model studied here.

Dissipation induced phase transition in JJ Both dissipation due to Ohmic resistance and quasi-particle tunnelling, can induce phase transition at zero temperature. Intuitively, the phase transition can be understood as follows. For ultrasmall Josephson Junction, the capacitance is so low that the capacitive coupling energy becomes of the same order of the Josephson coupling energy $E_J \approx E_C$. In this case a full quantum mechanical treatment is necessary, where number difference of Cooper pairs $\hat{n}$ and phase operator $\hat{\phi}$ are treated as conjugate quantities, i.e. $[\hat{n}, \hat{\phi}] = -\mathrm{i}$ (Appendix. B.1). As conjugate variables, charge and phase cannot both be well-defined due to Heisenberg uncertainty relation. Therefore, in the absence of dissipation an initially localised wavefunction corresponding to the initial well-defined phase, spreads over the junction leading to a well-defined charge as the conjugate degree of freedom, i.e. the charge. A charge sitting on the junction blocks the next one from entering, and any superconducting response is destroyed due to Coulomb blockade. Equivalently, while a well-defined phase as expected for a classical variable gives rise to a superconducting current $J^C \sin(\phi)$, quantum fluctuations, which are necessarily present when the charge is fixed, can average the associated current to zero $\sin(\phi) \to 0$. By suppressing quantum fluctuations, which are destructive for superconductivity, dissipation can localise the phase and therefore be used to stabilise superconductivity [69, 98–102]. In fact, in the absence of dissipation, superconductivity can therefore only be observed as a non-equilibrium effect [69]. In the presence of Ohmic dissipation alone this phase transition is expected to be independent of the ratio E_C/E_J between the energy corresponding to capacitive coupling E_C and Josephson coupling E_J. For quasi-particle tunnelling, on the other hand, the critical damping required for a phase transition is small in the tight binding limit ($E_C/E_J \ll 1$) and increases with E_C/E_J (decreasing capacitance). These expectations are in good agreement

with experimental observation [100], and a similar superconductor-insulator transition has also been observed in arrays of Josephson Junctions [370].

Cooling schemes based on discrete energy levels Choosing the system parameters such that the spacing of the energy levels is sufficiently large in comparison to the non-linearity of the Josephson potential, it is possible to selectively address only the lowest two or three energy levels using voltage, magnetic fields, currents and microwave radiation. Due to the anharmonicity of the Josephson potential, the other energy levels remain sufficiently detuned from the drive, and the system reduces to an artificial two or three-level atom depending on the circuit design and driving frequencies involved [348, 371]. The resulting superconducting qubits are currently considered as one of the most promising architectures for quantum computing. Thanks to the discrete energy level structure, methods from atomic physics can be translated to these artificial atoms [371]. For example, electronic circuits can be built such as to coherently couple artificial atoms based on Josephson junctions to a single mode cavity field [6, 372], which allows atom and field to coherently exchange energy leading to Rabi oscillation of frequency Ω. Such interaction has been realised in a variety of superconducting qubit infrastructures see Ref. [373–377]. A requirement to observe the coherent energy exchange between superconducting qubit and cavity mode in the form of Rabi oscillations is that the Rabi frequency determined by the coupling is larger than the damping rate of both cavity and the superconducting qubit. Thanks to small mode volume of a transmission line resonator, the coupling g can enter the strong coupling regime $g > \gamma, \kappa$, where it is larger than the decay rates of both the artificial atom γ (the superconducting qubit) and the cavity κ (transmission line resonator) [377] or even the ultrastrong coupling regime with g a significant fraction of the atom transition frequency ω_0 [177, 378], and where the counter-rotating terms in the light-matter coupling have to be included.

B.2 Numerical exact solution of a parametrically driven harmonic oscillator

Here we describe the solutions $\psi_n(x,t)$ to the time-dependent Schrödinger equation in Eq. (4.3) following the apporach in [312, 313] that is based on dynamical invariants [307, 379]. We write the solutions as

$$\psi_n(x,t) = \frac{1}{\sqrt{2^n n!}} \left(\frac{m\omega_I}{\pi \hbar g_-(t)} \right)^{\frac{1}{4}} e^{-\mathrm{i}\frac{g_0(t)}{2\hbar g_-(t)}x^2} e^{-\mathrm{i}\Lambda(t)(n+\frac{1}{2})} e^{-\frac{m\omega_I}{2\hbar g_-(t)}x^2} H_n\left(\sqrt{\frac{m\omega_I}{\hbar g_-(t)}} x \right), \quad \text{(B.9)}$$

where

$$\Lambda(t) = \int_0^t \mathrm{d}t' \frac{\omega_I}{g_-(t')}, \quad \text{(B.10)}$$

is a global phase,

$$\omega_I = \frac{1}{m}\sqrt{g_+(t)g_-(t) - g_0^2(t)}, \quad \text{(B.11)}$$

is a time-independent constant frequency and H_n are the Hermite polynomials of degree n. The functions $g_+(t)$, $g_+(t)$ and $g_+(t)$ in Eq. (B.9) are defined as

$$g_+(t) = m^2 \dot{f}_1(t)\dot{f}_2(t), \tag{B.12a}$$

$$g_0(t) = -\frac{m}{2}[\dot{f}_1(t)f_2(t) + f_1(t)\dot{f}_2(t)], \tag{B.12b}$$

$$g_-(t) = f_1(t)f_2(t), \tag{B.12c}$$

where $f_i(t)$ $(i \in \{1,2\})$ are two linearly independent solutions of the classical harmonic oscillator. These functions obey

$$\ddot{f}_i(t) + \omega^2(t) f_i(t) = 0, \tag{B.13}$$

and we impose the initial condition $f_i(0) = 1$ at $t = 0$ and require $f_1(t) = f_2(t)^*$. For $t < 0$ where the driving is absent we thus find $f_{1,2}(t<0) = e^{\pm \mathrm{i}\omega_0 t}$, and consequently $g_0(t<0) = 0$. Furthermore, as $g_-(t<0) = 1$ the chosen initial conditions result in $\omega_I = \omega_0$ such that $\psi_n(x,t)$ reduces to the harmonic oscillator eigenstates. These states form an orthogonal basis and the states $\psi_n(x,t)$ remain orthogonal for $t \geq 0$, i.e. $\langle \psi_n(t) \rangle \psi_m(t) = \delta_{n,m}$ as the time dependence of the argument $\frac{m\omega_I}{\hbar g_-(t)}$ of the integral in the equal time norm can be eliminated by a change of variables. It follows that the states $|\psi_n(t)\rangle$ in Eq. (B.9) span a complete basis at all times.

We define generalised creation and annihilation operators $A^\dagger$ and A that act on the states $|\psi_n(t)\rangle$ as described in Eq. (4.4). The annihilation operator is given by [230]

$$A(t) = \frac{1}{\sqrt{2}} \left[\sqrt{\frac{m\omega_0}{\hbar}} h_1(t) x + \sqrt{\frac{1}{\hbar m \omega_0}} h_2(t) p \right], \tag{B.14}$$

and the complex functions $h_1(t)$ and $h_2(t)$ are defined as

$$h_1(t) = \exp(\mathrm{i}\Lambda(t)) \sqrt{\frac{\omega_I}{\omega_0 g_-(t)}} \left(1 + \mathrm{i}\frac{g_0(t)}{m\omega_I}\right), \tag{B.15a}$$

$$h_2(t) = \mathrm{i} \exp(\mathrm{i}\Lambda(t)) \sqrt{\frac{\omega_0 g_-(t)}{\omega_I}}. \tag{B.15b}$$

Since $[x,p] = \mathrm{i}\hbar$ and $h_1(t)h_2^*(t) - h_1^*(t)h_2(t) = -2\mathrm{i}$, the equal-time commutation relation $\left[A(t), A^\dagger(t)\right] = 1$ is satisfied.

B.3 Derivation of the Born-Markov master equation

Derivation for weak coupling for both driven and undriven systems In this subsection we derive the integral differential master equation used in Sec. 4, which perturbatively captures the coupling to a reservoir. While we explicitly state the time dependence of the system Hamiltonian, this treatment does not differ significantly from the one for a time-independent Hamiltonian as found for example in Ref. [196].

The coupling to the bath also introduces a small renormalization of the system potential, which is compensated by the additional term in the system Hamiltonian,

$$H^c = x^2 \sum_r \frac{\kappa_r^2}{2 m_r \omega_r^2}, \tag{B.16}$$

which however will be treated as a small perturbation to the interaction term, i.e.

$$H_I^{\alpha,c} = H_I^{\alpha} + H^c. \tag{B.17}$$

The combined density operator for system and bath, $\rho_{tot}(t)$, is taken to separable at t_0, i.e. $\rho_{tot}(t_0) = \rho(t_0) \otimes \rho_B$. Using the evolution operator for the decoupled bath

$$U_B(t, t_0) = \exp\left(-\frac{\mathrm{i}}{\hbar} H_B(t - t_0)\right). \tag{B.18}$$

The total evolution for decoupled system and bath is given by $U_0(t, t_0) = U_{Sys}(t, t_0)U_B(t, t_0)$ The van Neumann equation for the total density operator in interaction picture $\tilde{\rho}_{tot}(t) = U_0^{\dagger}(t, t_0)\rho_{tot}(t)U_0(t, t_0)$ is given by

$$\mathrm{i}\hbar \frac{d\tilde{\rho}_{tot}(t)}{dt} = [\tilde{H}_I^{\alpha,c}(t), \tilde{\rho}_{tot}(t)]. \tag{B.19}$$

Integrating Equation B.19, we obtain

$$\tilde{\rho}_{tot}(t) = \tilde{\rho}_{tot}(t_0) - \frac{\mathrm{i}}{\hbar} \int_{t_0}^{t} ds \left[\tilde{H}_I^{\alpha,c}(s), \tilde{\rho}_{tot}(s)\right], \tag{B.20}$$

which after substitution into Equation B.19 leads to

$$\frac{d\tilde{\rho_{tot}}(t)}{dt} = -\frac{\mathrm{i}}{\hbar} \left[\tilde{H}_I^{\alpha,c}(t), \tilde{\rho}_{tot}(t_0)\right] - \frac{1}{\hbar^2} \int_{t_0}^{t} ds [\tilde{H}_I^{\alpha,c}(t), \left[\tilde{H}_I^{\alpha,c}(s), \tilde{\rho}_{tot}(s)\right]]. \tag{B.21}$$

Performing a trace over the bath, i.e. $\tilde{\rho}(t) = \mathrm{tr}_B\{\tilde{\rho}_{tot}(t)\}$, leads to

$$\frac{d\tilde{\rho}(t)}{dt} = -\frac{\mathrm{i}}{\hbar} \mathrm{tr}_B\{\left[\tilde{H}_I^{\alpha,c}(t), \tilde{\rho}_{tot}(t_0)\right]\} - \frac{1}{\hbar^2} \int_{t_0}^{t} ds\, \mathrm{tr}_B\{\tilde{H}_I^{\alpha,c}(t), \left[\tilde{H}_I^{\alpha,c}(s), \tilde{\rho}_{tot}(s)\right]\}. \tag{B.22}$$

In the following we outline the standard arguments for Born-Markov treatment. The third assumption is not used in this case, but added for completeness.

Assumption 1 (Weak coupling- Born approximation for undriven system) *The bath and system are only weakly coupled, such that the influence of the system on the bath is small. The density matrix of the bath is assumed to be unaffected by the system leading to*

$$\tilde{\rho}_{tot}(t) \approx \tilde{\rho}(t) \otimes \tilde{\rho}_B. \tag{B.23}$$

This factorising of the dynamics of the bath and system is not strictly necessary. It can be avoided in the derivation of the same master equation based on projection operator technique [200].

Possible excitation in the bath are then taken to decay fast enough, such that they remain unresolved leading to

$$\frac{d\tilde{\rho}(t)}{dt} = -\frac{\mathrm{i}}{\hbar} \mathrm{tr}_B\{\left[\tilde{H}_I^{\alpha,c}(t), \tilde{\rho}_{tot}(t_0)\right]\} - \frac{1}{\hbar^2} \int_{t_0}^{t} ds\, \mathrm{tr}_B\{\left[\tilde{H}_I^{\alpha,c}(t), \left[\tilde{H}_I^{\alpha,c}(s), \tilde{\rho}(s) \otimes \tilde{\rho}_B\right]\right]\}. \tag{B.24}$$

We simplify this expression further by implementing the Markov approximation, i.e.

$$\tilde{\rho}(s) \to \tilde{\rho}(t), \tag{B.25}$$

which still does not lead to a Markovian master equation due to the dependence on the system preparation at t_0. By substituting s by $t-s$ and letting the upper limit go to infinity, we obtain

$$\frac{d\tilde{\rho}(t)}{dt} = -\frac{\mathrm{i}}{\hbar}\,\mathrm{tr}_B\{\left[\tilde{H}_I^{\alpha,c}(t), \tilde{\rho}_{tot}(t_0)\right]\} - \frac{1}{\hbar^2}\int_0^\infty ds\,\mathrm{tr}_B\{\left[\tilde{H}_I^{\alpha}(t), \left[\tilde{H}_I^{\alpha}(t-s), \tilde{\rho}(t)\otimes\tilde{\rho}_B\right]\right]\}, \tag{B.26}$$

where we ignore the small shift in the interaction due $\tilde{H}^c(t)$ in the second term on the right hand side.

Assumption 2 (Markov approximation for undriven system) *The Markov approximation requires the thermal correlation time $\tau_B = \frac{\hbar}{2\pi k_B T}$, where k_B is the Boltzmann constant and T the temperature, to be much shorter then the time scale over which the system varies appreciably that is the relaxation time of the system $\tau_R = \frac{1}{\gamma}$, where γ is the decay rate, i.e.*

$$\tau_B \ll \tau_R, \quad or \quad \gamma \ll \frac{2\pi k_B T}{\hbar}. \tag{B.27}$$

Assumption 3 (Potential rotating wave approximation for undriven system) *The rotating wave approximation for an undriven underdamped harmonic oscillator requires that the intrinsic time of the system evolution $\tau_S \sim |\omega' - \omega|^{-1}$, which for an undriven harmonic oscillator can be estimated as $\tau_S \sim \omega_0^{-1}$, satisfies*

$$\tau_S \ll \tau_R, \quad or \quad \gamma \ll \omega_0. \tag{B.28}$$

This can be satisfied for the recovery time of the system under investigation, which is taken to be $\tau_R = \frac{1}{\gamma} \approx \frac{100}{\omega_0}$. In the usual derivation of the quantum-optical master equation, the Lindblad form of the equation is only ensured by using the rotating wave approximation. It allows ignoring rapidly oscillating terms such as $\exp(\mathrm{i}(\omega' - \omega)t)$ for $\omega = \omega'$, where ω and ω' are levels of the system.

Revising the conditions leading to the Markov and Born approximation for a driven system Above we have only given the Born-Markov approximation for an undriven system, which is only a valid approximation as long as the driving is sufficiently weak. In this subsection we outline the condition for the Born-Markov approximation as derived in Ref. [242].

Equation B.23 is effectively assuming that the bath does not introduce any memory effects into the system, ignoring higher order correlations where the interaction with the bath depends on the interaction at a previous point in time.

Assuming $\kappa_n = \kappa$ independent of n (first Markov approximation), which will implicitly be implemented by the white noise approximation, we simplify the interaction Hamiltonian to

$$H_{int} = -\kappa x R, \tag{B.29}$$

where R only acts on the bath operators $R = \sum_n x_n$, and x only on the system operators. The bath correlation

$$G(\tau) = \mathrm{tr}_B\{\tilde{R}(t)\tilde{R}(t-\tau)\rho_B\} \tag{B.30}$$

is only nonzero if $\tau \ll \tau_B$. The dissipative term $\mathcal{K}\rho(t)$ provides an estimate for the relevant timescale over which the density operator is changed by the coupling to the heat bath. Substituting the expression for H_{int} into

$$\mathcal{K}\rho(t) = -\frac{1}{\hbar^2}\int_0^\infty ds\, \mathrm{tr}_B\{H_{int}\tilde{H}_{int}(t-s,t)(\rho(t)\otimes\rho_B) - \tilde{H}_{int}(t-s,t)(\rho(t)\otimes\rho_B)H_{int} + \mathrm{H.c.}\}, \tag{B.31}$$

We obtain

$$\mathcal{K}\rho(t) = -\frac{\kappa^2}{\hbar^2}\int_0^\infty ds\{G(s)\,[x\tilde{x}(t-s,t)\rho(t) - \tilde{x}(t-s,t)\rho(t)x] + \mathrm{H.c.}\}, \tag{B.32}$$

Approximating the integrand as a piecewise constant function of value evaluated at $s = 0$ for $s \in [0, \tau_B]$ and zero otherwise, the rate of change at which $\rho(t)$ changes is then estimated as

$$\Gamma_2 = \kappa^2\tau_B\,\langle x^2\rangle\,\langle R^2\rangle, \tag{B.33}$$

which requires the integrand to be constant over τ_B, i.e. requiring the driving to be slow enough such that it does not introduce any fast dynamics into the system $\frac{1}{\omega_L} \gg \tau_B$. The resulting condition for the Markov approximation is

$$\tau_B\Gamma_2 \ll 1, \tag{B.34}$$

which is shown in Ref. [242] to be a sufficient condition for the Born approximation. By estimating the rate corresponding to the lowest order correction due to the factorisation of the density matrix in the next higher order term as

$$\Gamma_4 = \kappa^4\tau_B^3\,\langle x^4\rangle\,\langle B^2\rangle^2. \tag{B.35}$$

This is smaller than Γ_2 and therefore already fulfilled by Eq. B.34.

Here we discuss the derivation of the master equation in Sec. 4.2.2. My approach builds on the work presented in [230], but considers a more general system-bath coupling does not use the Floquet basis states and employs the weakest possible rotating-wave approximation in order to be consistent with the Born-Markov approximation.

In a first step we re-write the dissipative term $\mathcal{K}\rho$ in Eq. (4.11) as follows [196, 229, 242] (for a derivation of this term see Sec. B.3),

$$\mathcal{K}\rho = \frac{1}{\hbar^2}\int_0^\infty \mathrm{d}\tau\left(\frac{\mathrm{i}}{2}D(\tau)[c_\alpha, \{\tilde{c}_\alpha(t-\tau,t),\rho\}] - \frac{1}{2}D_1(\tau)[c_\alpha,[\tilde{c}_\alpha(t-\tau,t),\rho]]\right), \tag{B.36}$$

where $\{Q,W\} = QW + WQ$ is the anti-commutator for operators Q, W and we introduced following [196] the dissipation kernel

$$D(\tau) = \mathrm{i}\,\langle[B,\tilde{B}(-\tau)]\rangle = \mathrm{i}\left[B,\tilde{B}(-\tau)\right], \tag{B.37}$$

and the noise kernel

$$D_1(\tau) = \langle\{B, \tilde{B}(-\tau)\}\rangle\,. \tag{B.38}$$

We find

$$D(\tau) = 2\,\hbar \int_0^\infty \mathrm{d}\omega J(\omega) \sin\omega\tau\,, \tag{B.39a}$$

$$D_1(\tau) = 2\,\hbar \int_0^\infty \mathrm{d}\omega J(\omega) \coth(\,\hbar\omega/2k_BT) \cos\omega\tau\,, \tag{B.39b}$$

and

$$J(\omega) = \sum_{n=1}^{N} \frac{\kappa_n^2}{2m_n\omega_n} \delta(\omega - \omega_n) \tag{B.40}$$

is the spectral density. As described in the main text we assume that $J(\omega)$ is Ohmic with a Lorentz-Drude cutoff as given in Eq. (4.15). The longest thermal correlation time is then given by [196] $\tau_B = \max[\,\hbar/(2\pi k_BT), \Omega^{-1}]$. We set $\Omega = 10^5\omega_0$ such that for all considered parameters $\tau_B = \hbar/(2\pi k_BT)$. With the identities $J(\omega) = -J(-\omega)$ as well as $-n(-\omega) = n(\omega) + 1$ we obtain Eq. (4.16).

The solution of the master equation (4.10) with $\mathcal{K}\rho$ as in Eq. (4.16) is greatly simplified by projecting it onto the states $|\psi_n(t)\rangle$ which solve the full Schrödinger equation of the driven oscillator. The matrix elements of the density operator of the system in this basis are denoted by

$$\rho_{nm}(t) = \langle\psi_n(t)|\,\rho(t)\,|\psi_m(t)\rangle\,, \tag{B.41}$$

and evolve only due to the system-bath coupling. We find

$$\dot{\rho}_{nm}(t) = \sum_{k,l} \Big[\bar{C}^\alpha_{nk}(t)\rho_{kl}(t)C^\alpha_{lm}(t) - C^\alpha_{nk}(t)\bar{C}^\alpha_{kl}(t)\rho_{lm}(t)\Big] + \text{H.c.}, \tag{B.42}$$

where

$$C^\alpha_{nm}(t) = \langle\psi_n(t)|\,c_\alpha\,|\psi_m(t)\rangle\,, \tag{B.43a}$$

$$\bar{C}^\alpha_{nm}(t) = \frac{1}{\hbar}\int_{-\infty}^{\infty} \mathrm{d}\omega\, J(\omega)n(\omega) \int_0^\infty \mathrm{d}\tau\, e^{\mathrm{i}\omega\tau} C^\alpha_{nm}(t-\tau)\,. \tag{B.43b}$$

In order to evaluate these matrix elements, we express the coupling operator c_α in Eq. (4.7) in terms of the generalised creation and annihilation operators $A(t)$ and $A^\dagger(t)$,

$$c_\alpha = s_1^\alpha(t)A^\dagger(t) + s_2^\alpha(t)A(t), \tag{B.44}$$

where

$$s_1^\alpha(t) = \mathrm{i}\sqrt{\frac{\hbar}{2m\omega_0}}\,[\sin(\alpha)h_1(t) - \cos(\alpha)h_2(t)] \tag{B.45}$$

is a complex-valued function and $s_2^\alpha(t) = [s_1^\alpha(t)]^*$. The matrix element in Eq. (B.43a) thus reads

$$C^\alpha_{nm}(t) = s_1^\alpha(t)A^\dagger_{nm} + s_2^\alpha(t)A_{nm}, \tag{B.46}$$

and the time-independent matrix elements of the creation and annihilation operators are given by

$$A^\dagger_{nm} = \langle \psi_n(t)| A^\dagger(t) |\psi_m(t)\rangle = \sqrt{m+1}\delta_{n,m+1}\,, \tag{B.47a}$$
$$A_{nm} = \langle \psi_n(t)| A(t) |\psi_m(t)\rangle = \sqrt{m}\delta_{n,m-1}\,. \tag{B.47b}$$

Next we discuss the evaluation of $\bar{C}_{nm}$ in Eq. (B.43b).

With the help of Eq. (B.46), we find

$$\bar{C}^\alpha_{nm}(t) = \bar{s}^\alpha_1(t)A^\dagger_{nm} + \bar{s}^\alpha_2(t)A_{nm}, \tag{B.48}$$

where

$$\bar{s}^\alpha_i(t) = \frac{1}{\hbar}\int_{-\infty}^{\infty} \mathrm{d}\omega\, J(\omega)n(\omega)\int_0^\infty \mathrm{d}\tau\, e^{\mathrm{i}\omega\tau} s^\alpha_i(t-\tau)\,. \tag{B.49}$$

In order to evaluate Eq. (B.49), we choose a sufficiently large time interval $\left[t_i, t_f\right]$ of length $T_{if} = t_f - t_i$ to avoid artefacts from the Gibbs effect [380] and represent s^α_i in terms of the first N_k terms of its discrete Fourier series,

$$s^\alpha_i(t_i < t < t_f) \approx \sum_{k=-k_{\max}}^{k_{\max}} \mathcal{F}[s^\alpha_i](\omega_k)e^{\mathrm{i}w_k t}\,. \tag{B.50}$$

Here $w_k = \frac{2\pi k}{T_{if}}$ are the discrete frequencies with integer index k, $k_{\max} = \frac{N_k - 1}{2}$ and the Fourier coefficients $\mathcal{F}[s^\alpha_i](\omega_k)$ are defined as

$$\mathcal{F}[s^\alpha_i](\omega_k) = \frac{1}{T_{if}}\int_{t_i}^{t_f} s^\alpha_i(t)e^{-\mathrm{i}w_k t}\,\mathrm{d}t\,. \tag{B.51}$$

The expansion in Eq. (B.50) allows us to evaluate the integrals in Eq. (B.49). We find

$$\bar{s}^\alpha_i(t) = \frac{\pi}{\hbar}\sum_{k=-k_{\max}}^{k_{\max}} J(w_k)n(w_k)e^{\mathrm{i}w_k t}\mathcal{F}[s^\alpha_i](\omega_k)\,, \tag{B.52}$$

where we employed the identity $\int_0^\infty \mathrm{d}t e^{\mathrm{i}\omega t} = \pi\delta(\omega) + P(\mathrm{i}/\omega)$ and neglected the principal part.

We now return to the master equation (B.42). Substituting Eqs. (B.46) and (B.48) in Eq. (B.42) results in a differential equation for ρ_{nm} with time-dependent coefficients $s^\alpha_i(t)\bar{s}^\alpha_j(t)$. In order to be consistent with the Born-Markov approximation we average these time-dependent terms over the correlation time of the bath τ_B times a constant factor f. In order to make sure that the bath cannot introduce any dynamics faster than τ_B, we set $f = 10$ in Eq. (B.54). This is necessary since the Markov approximation assumes that the

system does not evolve appreciably over this time scale. We find

$$\begin{aligned}\dot{\rho}_{nm}(t) = \sum_{k,l} \Big\{ & \mathcal{S}_1^\alpha(t) \left[A_{nk}\rho_{kl}A_{lm}^\dagger - A_{nk}^\dagger A_{kl}\rho_{lm} \right] \\ & + \mathcal{S}_2^\alpha(t) \left[A_{nk}^\dagger \rho_{kl} A_{lm} - A_{nk}A_{kl}^\dagger \rho_{lm} \right] \\ & + \mathcal{S}_3^\alpha(t) \left[A_{nk}\rho_{kl}A_{lm} - A_{nk}A_{kl}\rho_{lm} \right] \\ & + \mathcal{S}_4^\alpha(t) \left[A_{nk}^\dagger \rho_{kl} A_{lm}^\dagger - A_{nk}^\dagger A_{kl}^\dagger \rho_{lm} \right] \\ & \Big\} + \text{H.c.}\,, \end{aligned} \tag{B.53}$$

where

$$\mathcal{S}_1^\alpha(t) = \frac{1}{f\tau_B} \int_{t-f\tau_B}^{t} \mathrm{d}t' \bar{s}_2^\alpha(t') s_1^\alpha(t')\,, \tag{B.54a}$$

$$\mathcal{S}_2^\alpha(t) = \frac{1}{f\tau_B} \int_{t-f\tau_B}^{t} \mathrm{d}t' \bar{s}_1^\alpha(t') s_2^\alpha(t')\,, \tag{B.54b}$$

$$\mathcal{S}_3^\alpha(t) = \frac{1}{f\tau_B} \int_{t-f\tau_B}^{t} \mathrm{d}t' \bar{s}_2^\alpha(t') s_2^\alpha(t')\,, \tag{B.54c}$$

$$\mathcal{S}_4^\alpha(t) = \frac{1}{f\tau_B} \int_{t-f\tau_B}^{t} \mathrm{d}t' \bar{s}_1^\alpha(t') s_1^\alpha(t')\,. \tag{B.54d}$$

By converting Eq. (B.53) into an operator-valued equation we obtain Eq. (4.19) in the main text.

B.3.1 Master equation for an undriven system

The standard quantum opto-mechanical master equation used in Sec. 3.5 and Sec. 2.1.3 derived in the absence or a very weak drive is obtained by using $A(t) \to e^{\mathrm{i}\omega_0 t}a$, $A\dagger(t) \to e^{-\mathrm{i}\omega_0 t}a^\dagger$, $s_1^\alpha(t) = e^{\mathrm{i}\omega_0 t}\frac{\hbar/2m\omega_0}{=}(s_2^\alpha(t))^*$. The off-resonant terms $\mathcal{S}_{3,4}^\alpha(t) = 0$ disappear through the filtering operation equivalent to a rotating wave approximation.

Closed set of equations of motions for full master equation A closed set of differential equations for the components of the the vector $\boldsymbol{v} = (\langle X^2\rangle, \langle P^2\rangle, \langle XP + PX\rangle)^\intercal$ with position-momentum correlator $D = XP + XP$ can be derived from the full master equation and is given by

$$\begin{aligned}\frac{d}{dt}v_1 = \omega_0 v_3 + \Big\{ & -\mathrm{i}v_1 \left[h_1(h_2^* S_1^\alpha + h_2 S_3^\alpha) + h_1^*(h_2 S_2^\alpha + h_2^* S_4^\alpha) \right] \\ & \frac{-\mathrm{i}v_3 + 1}{2} \left[h_2(h_2^* S_1^\alpha + h_2 S_3^\alpha) + h_2^*(h_2 S_2^\alpha + h_2^* S_4^\alpha) \right] + \text{h.c.} \Big\}, \end{aligned} \tag{B.55}$$

$$\frac{d}{dt}v_2 = -\frac{\omega^2(t)}{\omega_0}v_3 + \Big\{iv_2\left[h_2(h_1^*S_1^\alpha + h_1S_3^\alpha) + h_2^*(h_1S_2^\alpha + h_1^*S_4^\alpha)\right] + \frac{iv_3+1}{2}\left[h_1(h_1^*S_1^\alpha + h_1S_3^\alpha) + h_1^*(h_1S_2^\alpha + h_1^*S_4^\alpha)\right] + \text{h.c.}\Big\}, \quad \text{(B.56)}$$

and

$$\frac{d}{dt}v_3 = 2\omega_0 v_2 - 2\frac{\omega^2(t)}{\omega_0}v_1 + \Big\{\mathrm{i}v_1\left[h_1(h_1^*S_1^\alpha + h_1S_3^\alpha) + h_1^*(h_1S_2^\alpha + h_1^*S_4^\alpha)\right] - \mathrm{i}v_2\left[h_2(h_2^*S_1^\alpha + h_2S_3^\alpha) + h_2^*(h_2S_2^\alpha + h_2^*S_4^\alpha)\right] - \frac{1}{2}\left[(h_1^*h_2 + h_2^*h_1)(S_1^\alpha + S_2^\alpha) + 2h_1h_2S_3^\alpha + 2h_1^*h_2^*S_4^\alpha\right] - v_3\left[S_1^\alpha - S_2^\alpha\right] + \text{h.c.}\Big\}. \quad \text{(B.57)}$$

In case of the HTME, we obtain

$$\frac{d\boldsymbol{v}}{dt} = M_i^\alpha \boldsymbol{v} + A_w \cos(\omega_L t) M_t \boldsymbol{v} + \boldsymbol{I}_\alpha\,, \quad \text{(B.58)}$$

where

$$M_i^\alpha = \begin{pmatrix} -2\gamma\sin^2(\alpha) & 0 & \frac{\gamma}{2}\sin(2\alpha) + \omega_0 \\ 0 & -2\gamma\cos^2(\alpha) & \frac{\gamma}{2}\sin(2\alpha) - \omega_0 \\ \gamma\sin(2\alpha) - 2\omega_0 & \gamma\sin(2\alpha) + 2\omega_0 & -\gamma \end{pmatrix}$$

determines the isolated system dynamics,

$$M_t = \begin{pmatrix} 0 & 0 & 0 \\ 0 & 0 & -\omega_0 \\ -2\omega_0 & 0 & 0 \end{pmatrix} \quad \text{(B.59)}$$

accounts for the external driving and

$$\boldsymbol{I}_\alpha = [2n(\omega_0)+1]\gamma \begin{pmatrix} \sin^2(\alpha) \\ \cos^2(\alpha) \\ -\sin(2\alpha) \end{pmatrix} \quad \text{(B.60)}$$

is the inhomogeneity in Eq. (B.58).

B.3.2 Unitary transformation to $\mathscr{H}^\alpha$

The unitary transformation relating the total Hamiltonian H^α to $\mathscr{H}^\alpha$ in Eq. (4.26) is given by

$$U = e^{-\frac{\mathrm{i}}{\hbar}\frac{\sin(\alpha)}{\omega_0}x\sum_r \kappa_r x_r}\,. \quad \text{(B.61)}$$

This transformation leaves the position operators of the system and bath unchanged, i.e., $x_r = U^\dagger x_r U$ and $x = U^\dagger x U$. However, the momentum operators transform as

$$U^\dagger p_r U = p_r - \frac{\sin(\alpha)}{\omega_0}\kappa_r x, \quad \text{(B.62a)}$$

$$U^\dagger p U = p - \frac{\sin(\alpha)}{\omega_0}\sum_{r=1}^{N}\kappa_r x_r\,. \quad \text{(B.62b)}$$

The term $\mathcal{H}_{\text{shift}}$ in Eq. (4.26) is given by

$$\mathcal{H}_{\text{shift}} = \left[\frac{1}{2\omega_0^2}\sum_{r=1}^{N}\frac{\kappa_r^2}{m_r}x^2 - \frac{1}{2m\omega_0^2}\left(\sum_{r=1}^{N}\kappa_r x_r\right)^2\right]\sin^2(\alpha)\,. \tag{B.63}$$

Master equation resulting from $\mathcal{H}^\alpha$ Following the steps in Appendix B.3, the transformed Hamiltonian $\mathcal{H}^\alpha$ gives rise to the following master equation,

$$\begin{aligned}\dot{\rho}_U =& -\frac{\mathrm{i}}{\hbar}\left[H_{\mathrm{S}}^F(t),\rho_U\right]\\ &+\Big\{\mathcal{U}_1^\alpha(t)\left[A(t)\rho_U A^\dagger(t) - A^\dagger(t)A(t)\rho_U\right]\\ &\quad+\mathcal{U}_2^\alpha(t)\left[A^\dagger(t)\rho_U A(t) - A(t)A^\dagger(t)\rho_U\right]\\ &\quad+\mathcal{U}_3^\alpha(t)\left[A(t)\rho_U A(t) - A(t)A(t)\rho_U\right]\\ &\quad+\mathcal{U}_4^\alpha(t)\left[A^\dagger(t)\rho_U A^\dagger(t) - A^\dagger(t)A^\dagger(t)\rho_U\right]\\ &\quad+\text{H.c.}\Big\}\,,\end{aligned} \tag{B.64}$$

where the operators A are the same as in Appendix B.3 and

$$\mathcal{U}_1^\alpha(t) = \frac{1}{f\tau_B}\int_{t-f\tau_B}^{t}\mathrm{d}t'\bar{u}_2^\alpha(t')u_1(t')\,, \tag{B.65a}$$

$$\mathcal{U}_2^\alpha(t) = \frac{1}{f\tau_B}\int_{t-f\tau_B}^{t}\mathrm{d}t'\bar{u}_1^\alpha(t')u_2(t')\,, \tag{B.65b}$$

$$\mathcal{U}_3^\alpha(t) = \frac{1}{f\tau_B}\int_{t-f\tau_B}^{t}\mathrm{d}t'\bar{u}_2^\alpha(t')u_2(t')\,, \tag{B.65c}$$

$$\mathcal{U}_4^\alpha(t) = \frac{1}{f\tau_B}\int_{t-f\tau_B}^{t}\mathrm{d}t'\bar{u}_1^\alpha(t')u_1(t')\,. \tag{B.65d}$$

As in Appendix B.3, τ_B is the bath correlation time and $f = 10$. The function u_1 in Eq. (B.65) is given by

$$u_1(t) = -\mathrm{i}\sqrt{\frac{\hbar}{2m\omega_0}}h_2(t)\,, \tag{B.66}$$

where $h_2(t)$ is defined in Eq. (B.15) and only depends on the parameters of the classical parametric oscillator. Furthermore, $u_2(t) = [u_1(t)]^*$ and

$$\bar{u}_i^\alpha(t) = \frac{1}{\hbar}\int_{-\infty}^{\infty}\mathrm{d}\omega\, J^\alpha(\omega)n(\omega)\int_0^\infty \mathrm{d}\tau\, e^{\mathrm{i}\omega\tau}u_i(t-\tau)\,, \tag{B.67}$$

where J^α given in Eq. (4.29). By calculating the discrete Fourier transform $\mathcal{F}[u_i]$ of u_i and neglecting principle value integrals analogous to Eq. (B.52), Eq. (B.67) can be written as

$$\bar{u}_i^\alpha(t) \approx \frac{\pi}{\hbar}\sum_{k=-k_{\max}}^{k_{\max}} J^\alpha(w_k)n(w_k)e^{\mathrm{i}w_k t}\mathcal{F}[u_i](\omega_k)\,. \tag{B.68}$$

Since $u_1 \propto h_2$ and $u_2 \propto h_2^*$, Eq. (B.68) shows that the system-bath interaction is determined by the spectral density $J^\alpha(w_k)$ evaluated at the characteristic frequencies $\omega_k = \omega_c$ of the classical harmonic oscillator solutions.

B.4 General Floquet Born-Markov master equation

Here we give an alternative expression for the Floquet Markov master equation, which does not specialised on the case of a parametrically driven harmonic oscillator. Using the $T_L = \frac{2\pi}{\omega_L}$-periodicity of the Floquet modes $\{|\phi_\alpha(t)\rangle\}$ in Eq. (2.67), the dipole operators in Eq. (B.42) can in general be expanded in terms of a Fourier series as [236]

$$C^\alpha_{lm}(t) = \sum_k e^{\mathrm{i}\Delta_{nmk}t} C^\alpha_{nmk}, \tag{B.69}$$

with frequency difference from Eq. (2.71)

$$\Delta_{\alpha,\beta,k} = \mu_\alpha - \mu_\beta + k\omega_L, \tag{B.70}$$

and Fourier expansion coefficients

$$C^\alpha_{nmk} = \frac{1}{T_L}\int_0^{T_L} dt e^{-\mathrm{i}k\omega_L t} \langle\phi_n(t)| c_\alpha |\phi_m(t)\rangle . \tag{B.71}$$

Using the expansion Eq. (B.43b) simplifies to

$$\bar{C}^\alpha_{nm}(t) = \sum_{k'} \frac{\pi}{\hbar} J(\Delta_{n,m,k'}) n(\Delta_{n,m,k'}) C^\alpha_{nmk'} e^{\mathrm{i}\Delta_{n,m,k'}t}, \tag{B.72}$$

where we employed the identity $\int_0^\infty \mathrm{d}t e^{\mathrm{i}\omega t} = \pi\delta(\omega) + P(\mathrm{i}/\omega)$ and neglected the principal part. We now derive an equation of motion for matrix elements expressed in terms of Floquet modes (see Eq. (2.64))

$$\bar{\rho}_{nm}(t) = \langle\phi_n(t)| \rho(t) |\phi_m(t)\rangle . \tag{B.73}$$

Substituting Eq. (B.69) and Eq. (B.72) into Eq. (B.42) keeping only terms with $k \neq -k'$ in the product of the two sums from Eq. (B.72) into Eq. (B.42), i.e. the partial secular approximation discussed on page 50, we obtain [236, 237, 242]

$$\dot{\bar{\rho}}_{nm}(t) = -\mathrm{i}(\mu_n - \mu_m)\bar{\rho}_{nm}(t) + \sum_{\delta,\beta} \mathcal{R}_{nm\delta\beta}\bar{\rho}_{\delta\beta}(t), \tag{B.74}$$

with

$$\mathcal{R}_{nm\delta\beta} = \Gamma^+_{n\delta m\beta} + \Gamma^-_{n\delta m\beta} - \delta_{\beta m}\sum_k \Gamma^+_{k\delta kn} - \delta_{\delta n}\sum_k \Gamma^-_{kmk\beta}, \tag{B.75}$$

and using $C^\alpha_{\beta\delta(-r)} = \left(C^\alpha_{\delta\beta r}\right)^*$ we obtain [237]

$$\Gamma^+_{nm\delta\beta} = \frac{\pi}{\hbar}\sum_r J(\Delta_{n,m,r}) n(\Delta_{n,m,r}) C^\alpha_{nmr}\left(C^\alpha_{\delta\beta r}\right)^*, \tag{B.76}$$

$$\Gamma^-_{nm\delta\beta} = \frac{\pi}{\hbar}\sum_r J(\Delta_{\delta,\beta,r}) n(\Delta_{\delta,\beta,r}) C^\alpha_{nmr}\left(C^\alpha_{\delta\beta r}\right)^*. \tag{B.77}$$

The different rates of the master equation given in Eq. (B.74) are time-independent as they have effectively been averaged over one driving period (Eq. (B.71)) [242].

B.5 Quantum Langevin equation

Unitary transformation on system operators leading to $H'^{F}_{\mathbf{S}}(t)$ The undriven harmonic oscillator is an example for a self dual system. While this self-duality is in general broken by the coupling to the bath, the duality with a different experimental setup can be exploited [95, 368]. The undriven part of the system Hamiltonian corresponding to a simple harmonic oscillator is therefore preserved under a simple rotation in phase-space

$$H'^{F}_{\mathrm{S}}(t) = \frac{p'^2}{2m} + \frac{1}{2}m\omega_F^2(0)x'^2 + \frac{1}{2}m\left(\omega_F^2(t) - \omega_F^2(0)\right)\left(\cos(\alpha)x' - \sin(\alpha)\frac{p'}{m\omega_0}\right)^2. \tag{B.78}$$

where x', p' are the new position and momentum coordinates obtained from a canonical transformation of the form

$$x' = \cos(\alpha)x + \sin(\alpha)\frac{p}{m\omega_0}, \tag{B.79}$$

$$p' = \cos(\alpha)p - \sin(\alpha)m\omega_0 x. \tag{B.80}$$

This choice is convenient as it reduces the interaction Hamiltonian from Eq. 4.6 to position coupling

$$H'^{\alpha}_{\mathrm{I}} = -x'B. \tag{B.81}$$

Evolution of undriven system largely independent of α The system-bath coupling is therefore unitary equivalent to position coupling to the bath in the absence of a drive. Without complete control over the generation of initial states, it is therefore not possible to distinguish between the different types of coupling to the bath.

Here, we construct a toy model of the dissipation process of the total undriven Hamiltonian $H' = H'^{F}_{\mathrm{S}}(0) + H'^{\alpha}_{\mathrm{I}} + H_B$. While the classical limit of the quantum Langevin equation can be directly derived from first principle for the present Hamiltonian [198, 381] it is simpler to motivate our choice through the canonical transformation above. Ignoring the noise part, from Eq. B.78 for position coupling we expect a classical Langevin equation of the form

$$\frac{dp'}{dt} = -m\omega_0^2 x' - \gamma p', \tag{B.82}$$

with

$$\frac{dx'}{dt} = \frac{p'}{m}. \tag{B.83}$$

From this we obtain the Hamilton equation+damping term in the original coordinates as

$$\frac{dx}{dt} = -\gamma\sin^2(\alpha)x + \frac{p}{m}\left(1 + \frac{\gamma}{2\omega_0}\sin(2\alpha)\right), \tag{B.84}$$

similarly for position coordinate we obtain

$$\frac{dp}{dt} = -\gamma\cos^2(\alpha)p - m\omega_0^2 x\left(1 - \frac{\gamma}{2\omega_0}\sin(2\alpha)\right). \tag{B.85}$$

Eq. B.84 and Eq. B.85 correspond to Eq. 4.25a and Eq. 4.25b in the main text.

Above we motivated the form of the damping term in the classical Langevin equation using a shortcut in the derivation of the Langevin equation based on the canonical transformation into position coupling. Here, we directly derive the full Hamiltonian following the standard quantum Langevin treatment [198, 381]. The Heisenberg equation of the system are given by

$$\frac{dx}{dt} = \frac{p}{m} - \frac{\sin(\alpha)}{m\omega_0}B, \tag{B.86}$$

$$\frac{dp}{dt} = -m\omega_0^2 x + \cos(\alpha)B, \tag{B.87}$$

and for the bath

$$\frac{dx_r}{dt} = \frac{p_r}{m_r}, \tag{B.88}$$

$$\frac{dp_r}{dt} = \kappa_r c_\alpha - m_r\omega_r^2 x_r. \tag{B.89}$$

A formal solution to the bath equation of motion is given by

$$x_r(t) = x_r(t_0)\cos(\omega_r t) + \frac{p_r(t_0)}{m_r\omega_r}\sin(\omega_r t) + \frac{\kappa_r}{m_r\omega_r^2}c_\alpha(t) - \frac{\kappa_r}{m_r\omega_r^2}\int_{-\infty}^{t} dt' \cos(\omega_r(t-t'))\dot{c}_\alpha(t'), \tag{B.90}$$

with initial condition $x_r(t_0)$ and $p_r(t_0)$ as can be easily verified by substituting this expression into the equation of motion of the bath operators

$$m_r\frac{d^2x_r}{dt^2} = \kappa_r c_\alpha - m_r\omega_r^2 x_r. \tag{B.91}$$

From Eq. B.86 and B.87 we obtain

$$\frac{dc_\alpha}{dt} = \cos(\alpha)\frac{p}{m} - \omega_0\sin(\alpha)x, \tag{B.92}$$

which is independent of the bath operators, exactly as expected using the definition of the canonical momentum. After a sufficient long time $t \gg 0$ the bath operator becomes independent of the initial condition. The total dipole operator of the bath $B = \sum_r \kappa_r x_r$ given by

$$B = F(t) - \int_{-\infty}^{t} dt' g(t-t')\left(\cos(\alpha)\frac{p(t')}{m} - \omega_0\sin(\alpha)x(t')\right) \tag{B.93}$$

can be decomposed into a noise term

$$F(t) = \sum_r \frac{\kappa_r^2}{m_r\omega_r^2}c_\alpha(t), \tag{B.94}$$

and damping term

$$g(t) = \sum_r \frac{\kappa_r^2}{m_r\omega_r^2}\cos(\omega_r t)\Theta(t). \tag{B.95}$$

Substituting these expressions into Eq. B.86 and Eq. B.87 gives the most general quantum Langevin equation. We now approximate this expression further. Going into the continuum limit the damping term $g(t)$ becomes

$$g(t) = \int_0^\infty d\omega \cos(\omega_r t)\Theta(t)G(\omega)\frac{dn(\omega)}{d\omega}, \tag{B.96}$$

where $G(\omega_r) = \kappa_r^2$. We now perform the first Markov approximation [198] letting $G(\omega)\frac{dn(\omega)}{d\omega} = \frac{2\gamma}{\pi}m$,

$$g(t) = 2\gamma m\delta(t). \tag{B.97}$$

We dropped the $\Theta(t)$ as it is implicit in the integral limits of Eq. B.93, which reduces to

$$B = F(t) - \gamma\left(\cos(\alpha)\frac{p}{m} - \omega_0 \sin(\alpha)x\right). \tag{B.98}$$

Eq. B.86 and Eq. B.87 are then given by

$$\frac{dx}{dt} = \frac{p}{m} - \frac{\sin(\alpha)}{m\omega_0}F(t) + \frac{\sin(\alpha)}{\omega_0}\gamma\left(\cos(\alpha)\frac{p}{m} - \omega_0\sin(\alpha)x\right), \tag{B.99}$$

$$\frac{dp}{dt} = -m\omega_0^2 x + \cos(\alpha)F(t) - \cos(\alpha)\gamma\left(\cos(\alpha)p - m\omega_0\sin(\alpha)x\right), \tag{B.100}$$

B.6 Parametric cooling for two coupled springs

Here, we present some of the derivations used to obtain the expression in Sec. 2.1.3.

Rotating wave approximation In the following we assume that the frequency associated with the undriven oscillators are much larger than the ones arising due to the driving, i.e. $\Omega_r \gg \Lambda_{rs}$ for any choice $r, s = l, h$. The fast evolution goverened by the undriven oscillator $\mathcal{H}^u_{sys}$ can be transformed out by going to the interaction picture defined by the unitary

$$U_I(t, t_0) = e^{-\mathrm{i}\mathcal{H}^u_{sys}(t-t_0)/\hbar}. \tag{B.101}$$

An arbitrary operator A is than transformed as $A_I(t) = U_I^\dagger(t, t_0)AU_I(t, t_0)$ and the new Hamiltonian governing the whole system dynamics in the interaction picture is $\mathcal{H}^{d,I}_{sys}(t) = U_I^\dagger(t, t_0)\mathcal{H}^d_{sys}(t)U_I(t, t_0)$. The remaining evolution due to the driving can then be treated as a perturbation. Any off-resonant terms, which are still oscillating fast in this picture, cannot contribute to the dynamics as they effectively average out on the relevant time-scales of the evolution. For the annihilation and creation operator we obtain $a_r^I(t)$ and $a_r^{I\dagger}(t)$ this can be easily solved leading to $a_r^I(t) = e^{-\mathrm{i}\Omega_r t}a_r$ and $a_r^{I\dagger}(t) = e^{\mathrm{i}\Omega_r t}a_r^\dagger$ respectively, which explicitly separates out the fast evolution due to the undriven system dynamics. Depending on the driving frequency chosen, different terms survive in the rotating wave approximation (RWA).

Evolution of expectation values for cooling sideband Here, we consider the cooling limit, when the two coupled parameteric oscillator are approximately driven on their cooling sideband such that $\Delta\omega_{diff} = 2\omega_d - (\Omega_h - \Omega_l)$ is approximately zero and counter-rotating terms $a_l^\dagger a_h^\dagger$ and $a_l a_h$ are dropped to make the expressions less cumbersome but can be trivially included in the presentation below, as the Hamiltonian in Eq. (2.37) is time independent. The full expressions are used for the figures in the main text. We are interested in the equation of motions of the expectation value of an operator D, given by $\frac{d\langle D\rangle}{dt} = \mathrm{tr}(D\dot{\rho})$.

Using this relation to find the equation of motion of

$$\vec{u}^{\top}(t) = \left(\langle a_l^{\dagger} a_l\rangle, \langle a_h^{\dagger} a_h\rangle, \langle a_l^{\dagger} a_h\rangle, \langle a_h^{\dagger} a_l\rangle\right)^{\top}, \tag{B.102}$$

using $\Lambda_{hl}(t) = \Lambda_{hl}\exp(2\mathrm{i}\omega_d t)$ we obtain

$$\frac{d\vec{u}(t)}{dt} = \begin{pmatrix} -\gamma_l & 0 & \mathrm{i}\Lambda_{hl}(t) & -\mathrm{i}\Lambda_{hl}^*(t) \\ 0 & -\gamma_h & -\mathrm{i}\Lambda_{hl}(t) & \mathrm{i}\Lambda_{hl}^*(t) \\ \mathrm{i}\Lambda_{hl}^*(t) & -\mathrm{i}\Lambda_{hl}^*(t) & -\frac{\gamma_l+\gamma_h}{2} - \mathrm{i}(\Omega_h - \Omega_l) & 0 \\ -\mathrm{i}\Lambda_{hl}(t) & \mathrm{i}\Lambda_{hl}(t) & 0 & -\frac{\gamma_l+\gamma_h}{2} + \mathrm{i}(\Omega_h - \Omega_l) \end{pmatrix} \vec{u}(t) + \begin{pmatrix} \gamma_l n(\Omega_l) \\ \gamma_h n(\Omega_h) \\ 0 \\ 0 \end{pmatrix}. \tag{B.103}$$

This equation can be further simplified in the rotating picture $\vec{u} = \mathbf{R}(t)\tilde{\vec{u}}(t)$ going into the interaction picture using the rotation matrix,

$$\mathbf{R}(t) = \begin{pmatrix} 1 & 0 & 0 & 0 \\ 0 & 1 & 0 & 0 \\ 0 & 0 & e^{-\mathrm{i}2\omega_d t} & 0 \\ 0 & 0 & 0 & e^{\mathrm{i}2\omega_d t} \end{pmatrix}, \tag{B.104}$$

rotating at $2\omega_d = \Omega_h - \Omega_l + \Delta\omega_{diff}$ with detuning $\Delta\omega_{diff}$. The equation of motion become

$$\frac{d\tilde{\vec{u}}(t)}{dt} = \begin{pmatrix} -\gamma_l & 0 & \mathrm{i}\Lambda_{hl} & -\mathrm{i}\Lambda_{hl}^* \\ 0 & -\gamma_h & -\mathrm{i}\Lambda_{hl} & \mathrm{i}\Lambda_{hl}^* \\ \mathrm{i}\Lambda_{hl}^* & -\mathrm{i}\Lambda_{hl}^* & -\frac{\gamma_l+\gamma_h}{2} + \mathrm{i}\Delta\omega_{diff} & 0 \\ -\mathrm{i}\Lambda_{hl} & \mathrm{i}\Lambda_{hl} & 0 & -\frac{\gamma_l+\gamma_h}{2} - \mathrm{i}\Delta\omega_{diff} \end{pmatrix} \tilde{\vec{u}}(t) + \begin{pmatrix} \gamma_l n(\Omega_l) \\ \gamma_h n(\Omega_h) \\ 0 \\ 0 \end{pmatrix}, \tag{B.105}$$

which can be solved for a steady state value, $\frac{d\tilde{\vec{u}}(t)}{dt} = 0$. Following [31], introducing $\eta = \frac{\zeta}{\gamma_l \chi}$ with $\chi = 1 + \zeta\frac{(\gamma_l+\gamma_h)}{\gamma_l\gamma_h}$

$$\zeta = \frac{|\Lambda_{hl}|^2(\gamma_l+\gamma_h)}{{\Delta\omega_{diff}}^2 + {(\gamma_l+\gamma_h)^2}/{4}}, \tag{B.106}$$

we obtain the steady state values of the first two entries as

$$\tilde{u}_1 = n(\Omega_l) - \eta\left(n(\Omega_l) - n(\Omega_h)\right), \tag{B.107}$$

and

$$\tilde{u}_2 = n(\Omega_h) + \left(n(\Omega_l) - n(\Omega_h)\right)\left(1 - \frac{1}{\chi} - \eta\right) \tag{B.108}$$

with the cooling (heating) strength is characterised by a Lorentzian as

$$\eta = \frac{|\Lambda_{lh}|^2(\gamma_h+\gamma_l)/\gamma_l}{\Delta\omega_{diff}^2 + \left(\frac{\Lambda}{2}\right)^2}, \tag{B.109}$$

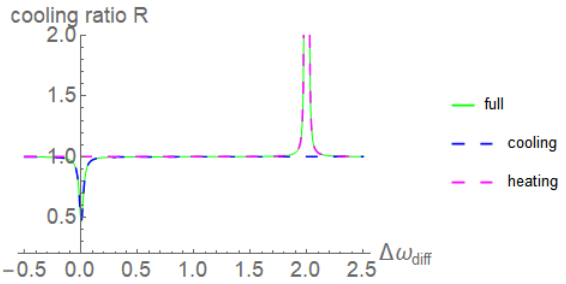
with width

$$\Lambda = \sqrt{\frac{(\gamma_h+\gamma_l)^2\left(4|\Lambda_{lh}|^2 + \gamma_h\gamma_l\right)}{\gamma_h\gamma_l}}. \tag{B.110}$$

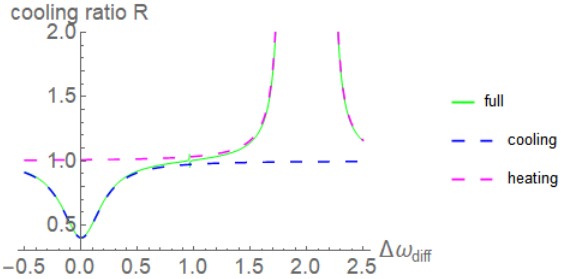
The cooling ratio monotonously decreases with the driving strength as shown in Fig. 2.4a as a function of driving strength and damping rate γ_h, where an increase in the driving

strength always leads to a larger cooling ratio, while the γ_h dependence is more intricate due to the competition between quantum-Zeno effect and efficient energy dissipation.

It is possible to solve for the steady state of the expectation values given in Eq. (2.45) governed by the master equation Eq. (2.43) with the coherent dynamics determined by the full Hamiltonian Eq. (2.37) (see for example Ref. [382]) as captured by the green line in Fig. B.1. However, the analytic expressions are cumbersome and the agreement with the approximation for the respective side-bands from Eq. (2.46) (blue dashed line in Fig. B.1)) and Eq. (2.53) (pink dashed line in Fig. B.1)) good.



(a) Intermediate driving regime ($\Lambda_{lh} = 0.01$)



(b) Strong driving regime depending approximately only on the ratio γ_l/γ_h ($\Lambda_{lh} = 0.1$).

Figure B.1: **(a)** and **(b)** Cooling ratio $R = \tilde{u}_1/n(\Omega_l)$ as a function of detuning $\Delta\omega_{\text{diff}}$ showing the cooling ($\Delta\omega_{\text{diff}} = 0$) and heating sideband ($\Delta\omega_{\text{diff}} = 2$) obtained from the solution to Eq. (2.43) for coherent dynamics determined by the full Hamiltonian (2.45) (green solid line labelled full). The solution for cooling-sideband from Eq. (2.46) and heating-sideband from Eq. (2.53) are shown as blue and pink dashed line labelled cooling and heating respectively with ($\Omega_l = 1$, $\Omega_h = 10$, $\gamma_h = 0.01$, $\gamma_l = 0.005$).

Resonant Energy Exchange Parametric cooling can be described as resonant energy exchange [31, 283]. As discussed there, using a transformation

$$\hat{\mathbf{U}} = \exp\left(\frac{-\mathrm{i}\hat{A}t}{\hbar}\right), \qquad \hat{A} = -2\hbar\omega_d a^\dagger a, \tag{B.111}$$

the time dependence in the modulation can be eliminated, i.e.

$$\mathscr{H}_n = \hbar(\Omega_h + \Delta\omega_{diff})a^\dagger a + \hbar\Omega_h b^\dagger b + \hbar\left(\Lambda_{lh}^* a b^\dagger + \Lambda_{lh} a^\dagger b\right), \tag{B.112}$$

such that the frequencies of the two oscillators only differ by the detuning from the resonance $\Delta\omega_{diff} = 2\omega_d - (\Omega_h - \Omega_l)$. The parametric modulation therefore allows resonant quanta transfer between the two oscillators.

Heating sideband Setting $\Delta\omega_{\text{diff}} = 2\Omega_l$ the system becomes resonant with the heating sideband such that $2\omega_d = \Omega_h + \Omega_l$, i.e. drive quanta can be converted to energy quanta of both the low and high frequency oscillator and the steady state population of the low frequency oscillator increases as

$$\tilde{u}_1/n(\Omega_l) = (1 + \eta_{\text{heating}}(\Delta\omega_{\text{diff}})) + \eta_{\text{heating}}(\Delta\omega_{\text{diff}})n(\Omega_h)/n(\Omega_l), \tag{B.113}$$

with

$$\eta_{\text{heating}}(\Delta\omega_{diff}) = \frac{|\Lambda_{lh}|^2 \frac{(\gamma_h+\gamma_l)}{\gamma_l}}{\text{sign}(\gamma_h\gamma_l - 4|\Lambda_{lh}|^2)\left(\Lambda_{\text{heating}}/2\right)^2 + \left(\Delta\omega_{diff} - 2\Omega_l\right)^2}, \tag{B.114}$$

where

$$\Lambda_{\text{heating}} = \sqrt{\frac{(\gamma_h+\gamma_l)^2\left(|\gamma_h\gamma_l - 4|\Lambda_{lh}|^2|\right)}{\gamma_h\gamma_l}}. \tag{B.115}$$

For weak driving $\gamma_h\gamma_l > 4|\Lambda_{lh}|^2$, the $\eta_{\text{heating}}(\Delta\omega_{diff})$ has the shape of a Lorentzian with width Λ_{heating}. However, when increasing the driving strength further, the weak driving approximation breaks down and a more elaborate model is required. Any use of this function in that regime should therefore be taken with a grain of salt. But this solution is already indicating that with increasing driving strength the width decreases up to $\gamma_h\gamma_l \leq 4|\Lambda_{lh}|^2$, where the functions obtains two poles at $\Delta\omega = 2\Omega_l \pm \Lambda_{\text{heating}}/2$. In this strong coupling regime, the exact form of this function is not valid, i.e. this function predicts even cooling inside the unstable region in the middle of the two poles. However, it gives an estimate that if the driving becomes too large the system can even becomes unstable on the cooling sideband.

Evolution of expectation values for parametrically driven harmonic oscillator Here we are interested in the analytical expression for the steady state for the thermal occupation of a single parametrically driven oscillator as studied in Sec. 2.2.1.

We define $a_r^\dagger(t)$ and $a_r(t)$ as solutions to the Heisenberg equation for the creation and annihilation operator in the absence of dissipative processes and $[X_1(t), Y_1(t)] = \frac{\mathrm{i}}{2}$. For resonant driving $\Delta = 0$, the quadrature operators $X_r(t) = (a_r(t) + a_r^\dagger(t))/2$ and $Y_r(t) = (a_r(t) - a_r^\dagger(t))/2\mathrm{i}$ grow and shrink as $X_r(t) = X_r(0)e^{\Lambda_{rr}t}$ and $Y_r(t) = Y_r(0)e^{-\Lambda_{rr}t}$ [383]. The corresponding density matrix ρ is conveniently represented in terms of the Wigner function [321, 322], which is a quasi-probability distribution defined in Eq. (4.22). The Wigner function for an initial undriven thermal state is described by a circular ellipse. Switching the drive on leads to a distortion into an ellipse, whose width along the minor and major axis is characterised by the dispersion of the two quadratures given by $\Delta(A) = \sqrt{\langle A^2\rangle - \langle A\rangle^2}$ for an operator A, i.e. the ellipse exponentially stretches and shrinks along the two quadratures. In the Schrödinger picture, the ellipse additionally rotates with a period $2\pi/\omega_0 = 2\pi/\omega_d$.

Starting from the master equation of the rth oscillator from Eq. (2.43) letting $\Omega_r \to \Omega_0$ and dropping the label r one can derive a closed expression for the equation of motions of the expectation values of all components of the vector $\vec{u} = (\langle a^\dagger a\rangle, \langle aa\rangle, \langle a^\dagger a^\dagger\rangle)^\top$. For small detuning from resonance $\Delta = \Omega_0 - \omega_d$ we obtain

$$\frac{d\vec{u}}{dt} = \mathbf{A}(t)\vec{u} + \bar{\mathbf{A}}\vec{u} + \mathbf{B}(t), \tag{B.116}$$

where

$$\mathbf{A}(t) = \begin{pmatrix} -\gamma & \mathrm{i}\Lambda(t) & -\mathrm{i}\Lambda^*(t) \\ -2\mathrm{i}\Lambda^*(t) & -\gamma & 0 \\ 2\mathrm{i}\Lambda(t) & 0 & -\gamma \end{pmatrix}, \tag{B.117}$$

and

$$\bar{\mathbf{A}} = \begin{pmatrix} 0 & 0 & 0 \\ 0 & -2\mathrm{i}\Omega_0 & 0 \\ 0 & 0 & 2\mathrm{i}\Omega_0 \end{pmatrix}, \tag{B.118}$$

and

$$\mathbf{B}(t) = \begin{pmatrix} \gamma n(\Omega_0) \\ -\mathrm{i}\Lambda^*(t) \\ \mathrm{i}\Lambda(t) \end{pmatrix}. \tag{B.119}$$

This equation can be further simplified in the rotating picture $\vec{u} = \mathbf{R}(t)\tilde{\vec{u}}(t)$ by introducing a rotation matrix, rotating at $2\omega_d = 2(\Omega_0 + \Delta)$

$$\mathbf{R}(t) = \begin{pmatrix} 1 & 0 & 0 \\ 0 & e^{-2\mathrm{i}(\Omega_0+\Delta)t} & 0 \\ 0 & 0 & e^{2\mathrm{i}(\Omega_0+\Delta)t} \end{pmatrix}. \tag{B.120}$$

Using $\frac{d\vec{R}}{dt} = \vec{R}\bar{\mathbf{A}}$, and defining $\Lambda_d = e^{2\mathrm{i}(\omega_d-\Omega_0)t-2\mathrm{i}\Delta t}\Lambda(t) = \Lambda_0 e^{\mathrm{i}\Phi}$, we obtain

$$\frac{d\tilde{\vec{u}}(t)}{dt} = \begin{pmatrix} -\gamma & \mathrm{i}\Lambda_d & -\mathrm{i}\Lambda_d^* \\ -2\mathrm{i}\Lambda_d^* & -\gamma + 2\mathrm{i}\Delta & 0 \\ 2\mathrm{i}\Lambda_d & 0 & -\gamma - 2\mathrm{i}\Delta \end{pmatrix} \tilde{\vec{u}}(t) + \begin{pmatrix} \gamma n(\Omega_0) \\ -\mathrm{i}\Lambda_d^* \\ \mathrm{i}\Lambda_d \end{pmatrix}. \tag{B.121}$$

We can find the steady state $\frac{d\tilde{\vec{u}}(t)}{dt} = 0$, i.e.

$$\tilde{\vec{u}} = \frac{1}{\gamma^2 - 4\Lambda_0^2 + 4\Delta^2} \begin{pmatrix} \gamma^2 n(\Omega_0) + 2\Lambda_0^2 + 4n(\Omega_0)\Delta^2 \\ (-\mathrm{i}\gamma + 2\Delta)\Lambda_0 e^{-\mathrm{i}\Phi}(1 + 2n(\Omega_0)) \\ (\mathrm{i}\gamma + 2\Delta)\Lambda_0 e^{\mathrm{i}\Phi}(1 + 2\ n(\Omega_0)) \end{pmatrix} \tag{B.122}$$

Parametric amplification Exploiting the non-linearity of the Josephson potential in the presence of strong pump pulses, parametric amplification of Josephson plasma waves has been experimentally realised in monolayer cuprates [204]. According to the AC-Josephson relation $\frac{\Phi_0}{2\pi D}\dot{\phi} = E(t)$, applying an oscillating electric field $E(t) = E_0 \sin(\omega_0 t)$ of amplitude E_0 in resonance with the Josephson plasma frequency ω_0 leads to oscillating in the phase difference as $\phi_{\mathrm{pump}}(t) = \phi_0 \cos(\omega_0 t)$ with amplitude $\phi_0 = -\frac{2eD}{\hbar\omega_0}$. A probe pulse applied to the system sees an effective parametric modulation of the Josephson plasma frequency at twice the plasma frequency

$$\omega_{JP}^2 = \omega_0^2 \cos(\phi_{\mathrm{pump}}(t)) = \omega_0^2 \left(1 - \frac{1}{4}\phi_0^2(1 + \cos(2\omega_0 t))\right). \tag{B.123}$$

The presence of the strong pump pulses combined with the non-linearity of the Josephson potential therefore leads to a parametric amplification of Josephson plasma waves of the probe pulse [204].

Linear Response Instead of measuring the current response to an external field, we measure the electric field response determined by the Josephson relation

$$\frac{\Phi_0}{2\pi}\dot{\phi} = \frac{\Phi_0}{2\pi} m_\phi^{-1} p_\phi = Eb, \tag{B.124}$$

to an external current $I^{ex} = I_0 \cos(\omega_d t + \theta)$ oscillating at a single frequency ω_d as in Ref. [43]. Taking the Fourier transform of the standard linear response function $\langle j(\tau)\rangle = \int d\tau' \sigma(\tau,\tau') E(\tau')$, we obtain

$$\langle j(\omega)\rangle = \int d\omega' \sigma(\omega,-\omega') E(\omega'), \tag{B.125}$$

where the conductivity contains off-diagonal terms due to the breaking of the time translational invariance, i.e.

$$\sigma(\omega,-\omega') = \frac{1}{2\pi}\int d\tau \frac{1}{2\pi}\int d\tau' e^{\mathrm{i}(\omega\tau+\omega'\tau')}\sigma(\tau,\tau'). \tag{B.126}$$

The conductivity used to determine effective Josephson coupling strength is then defined as

$$\sigma(\omega_d) = \sigma(\omega_d,-\omega_d) = \frac{I^{ex}(\omega_d)}{\delta\langle E(\omega_d)\rangle}. \tag{B.127}$$

B.7 Fluctuation-dissipation theorem

The fluctuation theorem characterises the linear response of a system to an external force by its equilibrium fluctuation.

Langevin equation For the work presented in Sec. blabla we use the classical Langevin formalism [179, 384, 385]. This treatment can be generalised to an arbitrary number of dynamical variables. Following [179], the Langevin equations can be expressed in terms of a vector $\vec{y}$ containing the dynamical variables as

$$\dot{\vec{y}} = \boldsymbol{\Xi}\vec{y} + \vec{F}(t), \tag{B.128}$$

where the matrix $\boldsymbol{\Xi}$ contains both deterministic and dissipative terms depending on the system. The average of the external stochastic forcing $F(t)$ taken over an ensemble, as indicated by $\langle\rangle$, satisfies

$$\langle F_i(t)\rangle = 0. \tag{B.129}$$

The strength of the Markovian noise is determined by the correlation

$$\langle F_i(t)F_j(t')\rangle = 2B_{ij}\delta(t-t'), \tag{B.130}$$

where B_{ij} are the indices of the matrix $\mathbf{B}$. These properties define a Langevin equation. We additionally assume that $F_i(t)$ is a Gaussian process, i.e. Eq. (3.62) defines Gaussian white noise. Consequently, the stochastic process is completely defined by Eq. (B.129) and Eq. (3.62) [385], allowing a Fokker-Planck representation of the process, convenient for smaller system sizes.

Formally integrating Eq. (B.128) we obtain

$$\vec{y}(t) = e^{\mathbf{\Xi} t}\vec{y}(0) + \int_0^t ds e^{(t-s)\mathbf{\Xi}}\vec{F}(s). \tag{B.131}$$

This solution allows to determine $\mathbf{B}$ in terms of the expected thermal expectation values of $\vec{y}$, in order to achieve the expected thermalisation for the system [179]. For example, for the case of a single harmonic oscillator of position x and momentum coordinate p, the dynamical variables are combined into $\vec{y} = (x,p)^\intercal$. The corresponding equation of motion is then described by

$$\mathbf{\Xi} = \begin{pmatrix} 0 & \frac{1}{m} \\ -m\omega^2 & -\gamma \end{pmatrix}, \tag{B.132}$$

and the only nonzero element of the matrix $\mathbf{B}$ is $B_{22} = m\gamma k_B T$. This leads to a steady state quadrature in agreement with the equipartition theorem given by $\langle x^2\rangle_{therm} = \frac{k_B T}{m\omega_0^2}$ and $\langle p^2\rangle_{therm} = m k_B T$. Consequently, $B_{22} = \gamma\langle p^2\rangle_{therm} = \gamma m^2\omega_0^2\langle x^2\rangle_{therm}$, where the temperature has been absorbed by the definition of the thermal expectation values.

Fokker-Plank formalism It is possible to express the linear Equation B.128 as a Fokker-Planck equation and evolve the probability distributions underlying the paths itself. The Fokker-Planck equation of the system [385] is given by

$$\frac{\partial}{\partial t}P(\vec{z},t) = -\sum_{i,j}\Xi_{ij}\frac{\partial}{\partial z_i}\left(z_j P(\vec{z},t)\right) + \frac{1}{2}\sum_{i,j}\Gamma_{ij}\frac{\partial^2}{\partial z_i z_j}P(\vec{z},t), \tag{B.133}$$

where $P(\vec{z},t)$ is a probability density. This equation can be used to simulate the second order moments directly [385] as

$$\partial_t\langle z_k z_l\rangle = \sum_i \Xi_{k,i}\langle z_i z_l\rangle + \sum_i \Xi_{l,i}\langle z_k z_i\rangle + \Gamma_{k,l}, \tag{B.134}$$

which is convenient for the purpose of analysing the EQM itself and simulation of small junction size as performed in the next section.

B.8 Engineering of dissipative dynamics

Engineering of dissipative dynamics in cold atoms and quantum optics To provide the necessary link with one of the main goals of the thesis, the transfer of methods from atomic and laser physics to condensed matter systems, we start with an overview over engineering dissipative dynamics in cold atoms and quantum optics. In these systems, our understanding of the system-bath coupling is so accurate that it can be used to control and engineer these interactions. In this way, the role of dissipation and decoherence can be transformed from a detrimental effect [348] into a wanted feature as shown, e.g. in [349–355]. At the end of the chapter, we close the arc by outlining possible challenges and opportunities for engineering of dissipative dynamics encountered in condensed matter systems.

In this section, we are going to start with a discussion of coherent control and knowledge of system-bath interaction, as two ingredients needed for engineering dissipative dynamics in

cold atoms and quantum optics. Next, we are going to give an overview of different schemes proposed for engineering dissipative dynamics.

Coherent control The dynamics of the atoms driven by an external light source depends strongly on the character of the source. For broadband radiation sufficiently detuned from atomic transitions, the dynamics are well described by rate equations [263, 386]. Coherent control [387], on the other hand, has been made possible by strong macroscopic light sources with frequencies close to atomic transitions. Such monochromatic radiation can be described by classical field as produced by a laser source described by an electric field of the form

$$\vec{E}_e(0,t) = \mathscr{E}_0 \cos(\omega_L t + \phi(\vec{r})), \tag{B.135}$$

where ω_L is the frequency, $\mathscr{E}_0$ the amplitude and $\phi(\vec{r})$ a spatially dependent phase. The corresponding dynamics is well described by standard optical Bloch equation [263, 386] with the classical light field leading to coherent Rabi oscillations between atomic energy levels at Rabi frequency $\Omega = -\frac{1}{\hbar}\vec{d}\cdot\mathscr{E}_0$, while the presence of the quantum field leads to spontaneous decay. Treating both dissipation and driving is only justified if the driving is sufficiently weak such that it can be ignored on time scales associated with the correlation time τ_c of vacuum fluctuations $\Omega \ll \tau_c^{-1}$ [386]. We implicitly made this assumption in the previous chapters.

Knowledge of system-bath interaction Accurate models for the interaction between a quantum system and its environment have been vital for the success of quantum optics and cold atom systems. They have paved the way for revolutionising methods such as laser cooling [388] and are essential for quantum technologies, where decoherence effects need to be as small as possible.

One of the fundamentals of the success in cold atoms has been the careful effort to ensure that the powerful machinery developed for the description of open quantum systems in quantum optics, based on Born-Markov and rotating wave approximation (RWA) (see Sec. B.3), remains valid in this many body setting [389]. The exact considerations are setup specific, but can be roughly summarised as [353, 389]:

- Good thermal isolation of the system, such that the system-bath coupling is very small (Born).
- A memoryless bath (Markov), which requires that the reservoir correlation times are much shorter than the characteristic time scales of the system evolution. A Markov master equation can also be derived in the presence of strong coupling to the bath [196]. In cold atoms, the Markov approximation can, for example, be justified if particles lost in collisional events are kicked out before they interact again with the lattice. In quantum optics, light emitted from a cavity should not be reabsorbed. The Lindblad equation can also be shown to arise in the limit of repeated continuous quantum interaction [390].

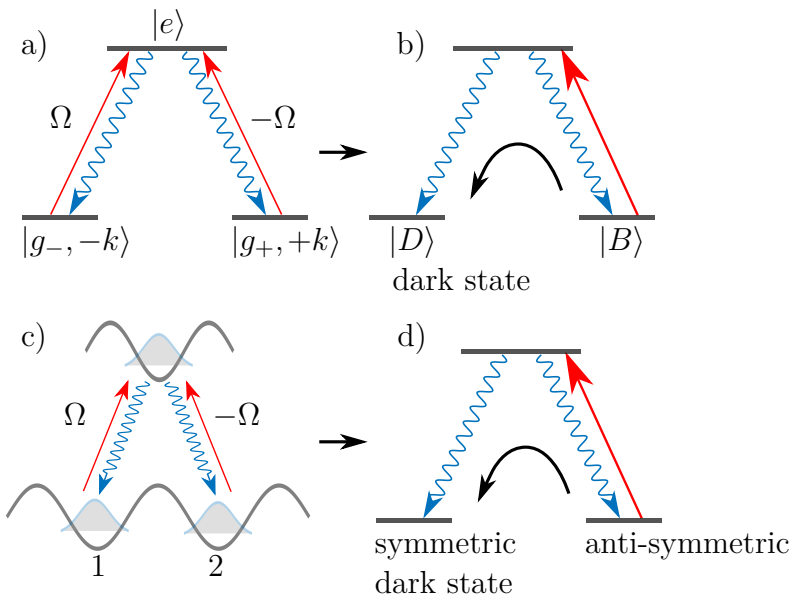


Figure B.2: a) Depiction of a simplified version of the subrecoil laser cooling scheme described in [391]. Two beams with Rabi frequencies $\pm\Omega$ are used to excite the anti-symmetric superposition $|B\rangle$ of atoms in ground states $|g_\pm,\pm k\rangle$ with opposite momentum k, i.e. $|B\rangle \approx |g_+,+k\rangle - |g_-,-k\rangle$. b) The dark state $|D\rangle \approx |g_+,+k\rangle + |g_-,-k\rangle$, on the other hand, is decoupled from the drive. The spontaneous decay from the auxiliary state $|e\rangle$ leads to the net result of an optical pumping from state $|B\rangle$ to state $|D\rangle$. c) Schematic of the cold atom implementation from [353] for two lattice sites. Driving with spatially dependent Rabi frequencies of alternating sign $\pm\Omega$ and the spontaneous decay of quasi-particles into a Bose-Einstein condensate leads to dissipative locking of adjacent sites. d) Net effect of both schemes is a transfer of population from anti-symmetric to symmetric states.

- Large band gaps (RWA) to ensure that only large energies are involved in the dissipative dynamics.

The design of dissipation processes is made possible due to the unique control of depth and geometries of lattices, tunable interaction and single atom addressability.

Engineering dissipative dynamics While von Neumann entropy cannot change under a purely unitary evolution, an initially mixed quantum states $\rho(t)$ can be purified in an open quantum system, i.e. $\partial_t \mathrm{tr}(\rho^2(t)) < 1$. An example for purification is schematically shown on the right of Fig. B.2 for a three level atom. Population in the pure steady-state $|D\rangle$ is decoupled from the pump, but can be populated through spontaneous emission, i.e. leading to $\rho(t) \xrightarrow{t\to\infty} |D\rangle\langle D|$. This final state can be identified as a dark state, which is an eigenstate of the jump operator with zero eigenvalues, i.e. it is annihilated by the Lindblad operator c_α as $c_\alpha|D\rangle = 0$ [354].

This situation is realised in subrecoil laser cooling [391,392], which has first been achieved in a Λ-system shown in a) and b) of Fig. B.2. Two Rabi frequencies of opposite sign, $\pm\Omega$, couple the anti-symmetric superposition $|B\rangle \sim |g_+,+k\rangle - |g_-,-k\rangle$ of the two degenerate electronic ground states $|g_\pm,\pm k\rangle$ of the atom with opposite momentum $\pm k$, to an excited auxiliary level $|e,0\rangle$ [391]. The symmetric superposition $|D\rangle \sim |g_+,+k\rangle + |g_-,-k\rangle$ on the

other hand remains non-absorbing to the two-photon Raman process. The net effect of this process is to pump population from an anti-symmetric state into a symmetric one. By replacing the internal electronic levels of the atom with an external degree of freedoms such as lattice sites, the subrecoil laser cooling scheme has been translated into a cold atom setup [353] and microcavity arrays [393]. Quasi-local jump operators, i.e. operators acting only on neighbouring sites, annihilate antisymmetric superposition and recycles them into symmetric ones as shown in c) and d) of Fig. B.2. The net effect is dissipative locking of adjacent atoms, creating long-range order and eventually a Bose-Einstein condensate (BEC) in the absence of interaction between the atoms. While locally acting Lindblad operators are often destructive, the coherence from the drive is inherited by the jump operators.

In fact, any pure state can be constructed as the unique steady-state of a dissipative process, though the jump operators might not always be quasi-local [394]. It is therefore not surprising that a variety of other dissipative processes have been proposed for the generation of dark states with exciting properties, starting from η-condensates [353], cooling of Kitaev toric code state [354], generation of noon states inside bimodal cavity via two-photon loss mechanism [350] as well as generalisation to dark spaces, e.g. Tonks-Girardeau gas of polaritons [349]. Particularly interesting for HTSC is the dissipative pairing into a dark state with the same d-wave symmetry as the conjectured ground state of a doped Fermi-Hubbard model, which is thought to be a minimum description of cuprate HTSC [44, 395].

Reservoir engineering can be further used to induce a new type of phase transition [351, 352], to generate non-reciprocal dynamics [396] by matching coherent interaction with its dissipative counterpart or even exploited as a resource in quantum computation and quantum-state engineering [355]. In Ref. [397], the concept of dark states has been extended to non-Hermitian "dark" Hamiltonian, where it is shown to allow for the generation of persistent coherent oscillations between disjoint sectors of the Hilbert space as a form of dissipation induced persistent long-time coherent dynamics.

Engineering of dissipative dynamics in condensed matter systems Many of the methods from the previous section cannot be translated to the "messier" condensed matter system because of a lack of control and addressability. However, recent advances in THz technology are beginning to change this, improving the selective control of low-energy degree of freedoms in condensed matter system.

In this section, we start with a general discussion of dissipation processes in condensed matter systems and then outline schemes for learning the spectral function of the bath. We give an overview of coherent control of quantum materials made possible by advances in THz technology, followed by a sketch of Floquet theory as a tool for studying periodically driven system. We next discuss Floquet-Markov Master equation (FFM) for the study of open driven quantum system as well as the regime of environment governed dynamics.

Many of the methods from the previous section cannot be translated to the "messier" condensed matter system because of a lack of control and addressability. However, recent advances in THz technology are beginning to change this, improving the selective control of low-energy degree of freedoms in condensed matter system.

Condensed matter systems are very different from atomic physics setup in the sense that there exists no clear boundary between system and environment. Low-energy degree of freedom of interest, i.e. the system, are merged with all other components of the system, which effectively act as its heat bath. This leads to a couple of fundamental problems but also limits the available tools for designing or at least combating the noise processes.

Specific experimental setups are very clean and accessible for probing, such as quantum point contacts [398–400], nanostructure and impurities. A good understanding of the noise processes in these system has allowed to combat them beyond simple cryogenic cooling. In the case of qubits based on silicon vacancy colour centres in diamond, for example, measures to increase decoherence lifetime range from material design [401–404] and dynamical decoupling [405–408], which allows for reducing magnetic and electric field noise, to inducing strain, which allows for probing and ultimately mitigating the decoherence effect due to thermal phonons [409]. However, in general, it is not possible to isolate individual components of the condensed matter system. Consequently, the source of noise is not always apparent, e.g. in HTSC resistivity and Nernst effect are not correlated close to the superconductor-insulator transition, as it would be expected if they both originated from the motion of vortices as in conventional superconductors [297]. In these cases it less clear, how one would go about combating the noise.

Applying a finite voltage across a Josephson junction leads to oscillating current according to the AC-Josephson relation Eq. (1.19). This effect can be used for the generation of THz light. The power achieved from a single junction is however quite low [410]. Using a stack of Josephson junction instead opens the possibility to achieve much larger powers scaling with the square of the total number of junctions [411]. The main problem with achieving these powers is achieving mutual phase locking of the junctions. While artificial junctions suffer from parameter irregularities, this is overcome by intrinsic Josephson junctions such as high-temperature superconductor [121, 412].

We have also not addressed the observation from Ref. [60], where it was observed that by replacing the trilayer vs bilayer structure no enhancement of HTSC was observed.

Significant progress in the clean fabrication of materials, the ultrastrong coupling regime has been realised in a variety of experimental setups ranging from optomechanics, superconducting circuits, organic molecules to Landau polaritons [177]. There also exist theoretical work regarding superconductors in cavities, ranging from cavity mediated superconductivity-photon pairing [413] to the conversion of Bologiubov quasi-particles into cavity photons [414]. Therefore, cavity might allow dressing the electrons participating in the formation of superconductivity such as to stabilise superconductivity and destroy competing orders. The underlying idea of first moving to a frame, which treats the coupled system exactly and then adding the dissipation perturbatively, is equivalent to the approach we present in Sec. 4 for treating strong driving.

Interesting with regard to engineering open quantum system in condensed matter, such a cavity implementation in the ultrastrong coupling regime would lead to the dressing of the Josephson plasmon by the quantum field. In fact, for better-understood materials, such as sandwiched 2D electron gases, vacuum Rabi splitting of collective cyclotron resonance

has been already observed in Ref. [415] in the ultra-strong coupling and large cooperativity regime. The ultrastrong coupling regime also allows to modify the dissipative dynamics, as shown by the breakdown of the Purcell effect [416] observed in Ref. [415] due to the relative importance of the diamagnetic term in the ultrastrong coupling regime. Light emitted by coherent radiation from cyclotron resonances cannot leave the cavity and re-excites the cyclotron resonances, such as to suppress the usually dominating collective superradiance decay [417]. The experimental feasibility of ultrastrong coupling in 2D electron gas has lead to a variety of proposals and theoretical work for other types of systems [177, 413, 414, 418, 419]. Additionally, the same group has now also observed Dicke cooperativity in the form of matter-matter interaction- [420] by replacing the light in the conventional Dicke model with a magnon mode, which might allow the engineering of phase transitions.

As a harmonic oscillator as studied in this thesis is an unbound system with equally spaced quasi-energies, this system is plagued by quasi-degeneracies in the Floquet spectrum, when projected to the first Brillouin zone. Given that the harmonic oscillator is one of the simplest models imaginable, it might therefore at first seem that the study of a more complex system such as an interacting electron system should be out of the question. However, this is not necessarily true. Fermions can be transformed into spin operators using Jordan-Wigner transformation [82]. They are therefore naturally bounded due to Pauli exclusion principle. For small system sizes, there exists an interesting parameter regime, where a Brillouin zone can be chosen such that there are no quasi-energies close to the boundaries. In these cases solving for the steady-state reduces to solving a linear equation.

This is, for example, the case for inter-band driving of the Fermi-Hubbard model for specific ratios between driving amplitude to frequency, where the dynamic is governed by superexchange [44]. However, it is not clear that the gap in the quasi-energy spectrum survives in the thermodynamic limit. As the FBM requires an exact solution of the Floquet basis of the isolated driven interacting system, the size of the system is strongly restricted. Reaching the thermodynamic limit might be virtually impossible. To approach larger system sizes of interacting system, it might, therefore, be necessary to further simplify or approximate the dynamics, for example through the use of non-Hermitian effective Hamiltonian, which essentially ignores the recycling terms in the master equation. Using a non-Hermitian approach [421], the interplay between dissipation due to losses to higher band and quasi-resonant driving of a two-band Bose-Hubbard system can lead to the generation of robust entangled states. Particular systems, such as quadratic quasi-free fermions with boundary dissipation undergoing periodic kicking, have been efficiently treated in terms of discrete Lyapunov equation [422]. Even analytical results based on quasilocal conservation laws have been derived for particular integrable lattice models with boundary dissipation based on a Trotterisation of integrable open system dynamics [423].

Besides making the system more complex by including interactions, it would also be interested to study more complex heat baths [424].

This situation differs significantly from the design of local dissipative Lindblad operators in cold atom systems, where excellent control over the system and design of dissipation processes, allows ensuring the validity of the Born-Markov approximation. Starting from a microscopic Hamiltonian, interesting dark states can be achieved by the design of quasi-local

Lindblad operators [353]. For condensed matter systems, the use of strong driving, material design, stress-induced changes in the heat bath as well as dressing collective dynamics with cavity field, already moves in the direction of engineering dissipative dynamics in condensed matter systems.

Bibliography

[1] Suresh V. Garimella, Amy S. Fleischer, Jayathi Y. Murthy, Ali Keshavarzi, Ravi Prasher, Chandrakant Patel, Sushil H. Bhavnani, R. Venkatasubramanian, Ravi Mahajan, Y. Joshi, Bahgat Sammakia, Bruce A. Myers, Len Chorosinski, Martine Baelmans, Prabhu Sathyamurthy & Peter E. Raad. *IEEE Trans. Components Packag. Technol.*, **31**, 4 (2008) 801–815.

[2] M. Mitchell Waldrop. *Nature*, **530**, 7589 (2016) 144–147.

[3] Philip Ball. *Nature*, **492**, 7428 (2012) 174–176.

[4] SIA. "2015 International Technology Roadmap for Semiconductors (ITRS)". Technical report, Semiconductor Industry Association (2015).

[5] Stefano Ambrogio, Pritish Narayanan, Hsinyu Tsai, Robert M. Shelby, Irem Boybat, Carmelo di Nolfo, Severin Sidler, Massimo Giordano, Martina Bodini, Nathan C. P. Farinha, Benjamin Killeen, Christina Cheng, Yassine Jaoudi & Geoffrey W. Burr. *Nature*, **558**, 7708 (2018) 60–67.

[6] M H Devoret & R J Schoelkopf. *Science*, **339**, 6124 (2013) 1169–74.

[7] McLeod James. "D-Wave's quantum computers can save energy, solve climate change'" (2018).

[8] Stephen J Blundell. "Superconductivity: A Very Short Introduction". Oxford University Press (2009).

[9] Coalition for the Commercial Application of Superconductors. "Superconductivity Present and Future Applications" (2014).

[10] Michael Tinkham. "Introduction to Superconductivity". Dover, 2 edition (1996).

[11] D N Basov & Andrey V Chubukov. *Nat. Phys.*, **7** (2011) 272.

[12] M R Norman. *Reports Prog. Phys.*, **79**, 7 (2016) 074502.

[13] Yuan Cao, Valla Fatemi, Ahmet Demir, Shiang Fang, Spencer L. Tomarken, Jason Y. Luo, Javier D. Sanchez-Yamagishi, Kenji Watanabe, Takashi Taniguchi, Efthimios Kaxiras, Ray C. Ashoori & Pablo Jarillo-Herrero. *Nature*, **556**, 7699 (2018) 80–84.

[14] N. W. Ashcroft. *Phys. Rev. Lett.*, **21**, 26 (1968) 1748–1749.

[15] A. P. Drozdov, M. I. Eremets, I. A. Troyan, V. Ksenofontov & S. I. Shylin. *Nature*, **525**, 7567 (2015) 73–76.

[16] Maddury Somayazulu, Muhtar Ahart, Ajay K. Mishra, Zachary M. Geballe, Maria Baldini, Yue Meng, Viktor V. Struzhkin & Russell J. Hemley. *Phys. Rev. Lett.*, **122**, 2 (2019) 027001.

[17] D Fausti, R I Tobey, N Dean, S Kaiser, A Dienst, M C Hoffmann, S Pyon, T Takayama, H Takagi & A Cavalleri. *Science*, **331**, 6014 (2011) 189–191.

[18] W Hu, S Kaiser, D Nicoletti, C R Hunt, I Gierz, M C Hoffmann, M Le Tacon, T Loew, B Keimer & A Cavalleri. *Nat. Mater.*, **13**, 7 (2014) 705–711.

[19] M Mitrano, A Cantaluppi, D Nicoletti, S Kaiser, A Perucchi, S Lupi, P Di Pietro, D Pontiroli, M Riccò, S R Clark, D Jaksch & A Cavalleri. *Nature*, **530** (2016) 461.

[20] D. Nicoletti, D. Fu, O. Mehio, S. Moore, A. S. Disa, G. D. Gu & A. Cavalleri. *Phys. Rev. Lett.*, **121**, 26 (2018) 267003.

[21] Matteo Rini, Ra'anan Tobey, Nicky Dean, Jiro Itatani, Yasuhide Tomioka, Yoshinori Tokura, Robert W Schoenlein & Andrea Cavalleri. *Nature*, **449**, 7158 (2007) 72–74.

[22] R I Tobey, D Prabhakaran, A T Boothroyd & A Cavalleri. *Phys. Rev. Lett.*, **101**, 19 (2008) 197404.

[23] R Mankowsky, B Liu, S Rajasekaran, H Y Liu, D Mou, X J Zhou, R Merlin, M Först & A Cavalleri. *Phys. Rev. Lett.*, **118**, 11 (2017) 116402.

[24] M. Först, R. I. Tobey, H. Bromberger, S. B. Wilkins, V. Khanna, A. D. Caviglia, Y.-D. Chuang, W. S. Lee, W. F. Schlotter, J. J. Turner, M. P. Minitti, O. Krupin, Z. J. Xu, J. S. Wen, G. D. Gu, S. S. Dhesi, A. Cavalleri & J. P. Hill. *Phys. Rev. Lett.*, **112**, 15 (2014) 157002.

[25] M. Först, A. Frano, S. Kaiser, R. Mankowsky, C. R. Hunt, J. J. Turner, G. L. Dakovski, M. P. Minitti, J. Robinson, T. Loew, M. Le Tacon, B. Keimer, J. P. Hill, A. Cavalleri & S. S. Dhesi. *Phys. Rev. B*, **90**, 18 (2014) 184514.

[26] T. F. Nova, A. Cartella, A. Cantaluppi, M. Först, D. Bossini, R. V. Mikhaylovskiy, A. V. Kimel, R. Merlin & A. Cavalleri. *Nat. Phys.*, **13**, 2 (2017) 132–136.

[27] A. D. Caviglia, R. Scherwitzl, P. Popovich, W. Hu, H. Bromberger, R. Singla, M. Mitrano, M. C. Hoffmann, S. Kaiser, P. Zubko, S. Gariglio, J.-M. Triscone, M. Först & A. Cavalleri. *Phys. Rev. Lett.*, **108**, 13 (2012) 136801.

[28] M. Först, A. D. Caviglia, R. Scherwitzl, R. Mankowsky, P. Zubko, V. Khanna, H. Bromberger, S. B. Wilkins, Y.-D. Chuang, W. S. Lee, W. F. Schlotter, J. J. Turner, G.ÂăL. Dakovski, M. P. Minitti, J. Robinson, S. R. Clark, D. Jaksch, J.-M. Triscone, J. P. Hill, S. S. Dhesi & A. Cavalleri. *Nat. Mater.*, **14**, 9 (2015) 883–888.

[29] M Först, K R Beyerlein, R Mankowsky, W Hu, G Mattoni, S Catalano, M Gibert, O Yefanov, J N Clark, A Frano, J M Glownia, M Chollet, H Lemke, B Moser, S P Collins, S S Dhesi, A D Caviglia, J.-M. Triscone & A Cavalleri. *Phys. Rev. Lett.*, **118**, 2 (2017) 027401.

[30] Mengkun Liu, Harold Y. Hwang, Hu Tao, Andrew C. Strikwerda, Kebin Fan, George R. Keiser, Aaron J. Sternbach, Kevin G. West, Salinporn Kittiwatanakul, Jiwei Lu, Stuart A. Wolf, Fiorenzo G. Omenetto, Xin Zhang, Keith A. Nelson & Richard D. Averitt. *Nature*, **487**, 7407 (2012) 345–348.

[31] Samuel Jonathan Denny, Stephen R. Clark, Yannis Laplace, Andrea Cavalleri & Dieter Jaksch. *Phys. Rev. Lett.*, **114** (2015) 137001.

[32] Frank Schlawin, Anastasia S. D. Dietrich, Martin Kiffner, Andrea Cavalleri & Dieter Jaksch. *Phys. Rev. B*, **96**, 6 (2017) 064526.

[33] Andrea Cavalleri. *Contemp. Phys.*, **59**, 1 (2018) 31–46.

[34] D Nicoletti, E Casandruc, Y Laplace, V Khanna, C R Hunt, S Kaiser, S S Dhesi, G D Gu, J P Hill & A Cavalleri. *Phys. Rev. B*, **90**, 10 (2014) 100503.

[35] S Kaiser, C R Hunt, D Nicoletti, W Hu, I Gierz, H Y Liu, M Le Tacon, T Loew, D Haug, B Keimer & A Cavalleri. *Phys. Rev. B*, **89**, 18 (2014) 184516.

[36] Daniele Nicoletti & Andrea Cavalleri. *Adv. Opt. Photonics*, **8**, 3 (2016) 401.

[37] N Peter Armitage. *Nat. Mater.*, **13**, 7 (2014) 665–666.

[38] Zachary M Raines, Valentin Stanev & Victor M Galitski. *Phys. Rev. B*, **91**, 18 (2015) 184506.

[39] R Höppner, B Zhu, T Rexin, A Cavalleri & L Mathey. *Phys. Rev. B*, **91**, 10 (2015) 104507.

[40] Michael Knap, Mehrtash Babadi, Gil Refael, Ivar Martin & Eugene Demler. *Phys. Rev. B*, **94**, 21 (2016) 214504.

[41] Aavishkar A Patel & Andreas Eberlein. *Phys. Rev. B*, **93**, 19 (2016) 195139.

[42] M. A. Sentef, A. F. Kemper, A. Georges & C. Kollath. *Phys. Rev. B*, **93**, 14 (2016) 144506.

[43] Jun-ichi Okamoto, Andrea Cavalleri & Ludwig Mathey. *Phys. Rev. Lett.*, **117**, 22 (2016) 227001.

[44] J. R. Coulthard, S. R. Clark, S. Al-Assam, A. Cavalleri & D. Jaksch. *Phys. Rev. B*, **96**, 8 (2017) 085104.

[45] Jun-ichi Okamoto, Wanzheng Hu, Andrea Cavalleri & Ludwig Mathey. *Phys. Rev. B*, **96**, 14 (2017) 144505.

[46] Mehrtash Babadi, Michael Knap, Ivar Martin, Gil Refael & Eugene Demler. *Phys. Rev. B*, **96**, 1 (2017) 014512.

[47] M Först, R. I. Tobey, H Bromberger, S. B. Wilkins, V Khanna, A. D. Caviglia, Y.-D. Chuang, W. S. Lee, W. F. Schlotter, J. J. Turner, M. P. Minitti, O Krupin, Z. J. Xu, J. S. Wen, G. D. Gu, S. S. Dhesi, A Cavalleri & J. P. Hill. *Phys. Rev. Lett.*, **112**, 15 (2014) 157002.

[48] Dante M Kennes, Eli Y Wilner, David R Reichman & Andrew J Millis. *Nat. Phys.*, **13**, 5 (2017) 479–483.

[49] Achilleas Lazarides, Arnab Das & Roderich Moessner. *Phys. Rev. Lett.*, **112**, 15 (2014) 150401.

[50] Luca D'Alessio & Marcos Rigol. *Phys. Rev. X*, **4**, 4 (2014) 041048.

[51] Tomotaka Kuwahara, Takashi Mori & Keiji Saito. *Ann. Phys. (N. Y).*, **367** (2016) 96–124.

[52] R. Mankowsky, A. Subedi, M. Först, S. O. Mariager, M. Chollet, H. T. Lemke, J. S. Robinson, J. M. Glownia, M. P. Minitti, A. Frano, M. Fechner, N. A. Spaldin, T. Loew, B. Keimer, A. Georges & A. Cavalleri. *Nature*, **516**, 7529 (2014) 71–73.

[53] Tao Wu, Hadrien Mayaffre, Steffen Krämer, Mladen Horvatić, Claude Berthier, W. N. Hardy, Ruixing Liang, D. A. Bonn & Marc-Henri Julien. *Nature*, **477**, 7363 (2011) 191–194.

[54] Tom Timusk & Bryan Statt. *Reports Prog. Phys.*, **62**, 1 (1999) 61–122.

[55] V. J. Emery & S. A. Kivelson. *Nature*, **374**, 6521 (1995) 434–437.

[56] J Corson, R Mallozzi, J Orenstein, J N Eckstein & I Bozovic. *Nature*, **398**, 6724 (1999) 221–223.

[57] R. D. Averitt, G. Rodriguez, A. I. Lobad, J. L. W. Siders, S. A. Trugman & A. J. Taylor. *Phys. Rev. B*, **63**, 14 (2001) 140502.

[58] M. Magnuson, T. Schmitt, V. N. Strocov, J. Schlappa, A. S. Kalabukhov & L.-C. Duda. *Sci. Rep.*, **4**, 1 (2015) 7017.

[59] R. Höppner, B. Zhu, T. Rexin, A. Cavalleri & L. Mathey. *Phys. Rev. B*, **91**, 10 (2015) 104507.

[60] W. Hu, D. Nicoletti, A. V. Boris, B. Keimer & A. Cavalleri. *Phys. Rev. B*, **95**, 10 (2017) 104508.

[61] Matthias C Hoffmann & József András Fülöp. *J. Phys. D. Appl. Phys.*, **44**, 8 (2011) 083001.

[62] S. O. Valenzuela, W. D. Oliver, D. M. Berns, K. K. Berggren, L. S. Levitov & T. P. Orlando. *Science*, **314**, 5805 (2006) 1589–1592.

[63] M. Grajcar, S. H. W. van der Ploeg, A. Izmalkov, E. Il'ichev, H.-G. Meyer, A. Fedorov, A. Shnirman & Gerd Schön. *Nat. Phys.*, **4**, 8 (2008) 612–616.

[64] K. Inomata, S. Sato, Koji Nakajima, A. Tanaka, Y. Takano, H. B. Wang, M. Nagao, H. Hatano & S. Kawabata. *Phys. Rev. Lett.*, **95**, 10 (2005) 107005.

[65] X. Y. Jin, J. Lisenfeld, Y. Koval, A. Lukashenko, A. V. Ustinov & P. Müller. *Phys. Rev. Lett.*, **96**, 17 (2006) 177003.

[66] Thilo Bauch, Tobias Lindström, Francesco Tafuri, Giacomo Rotoli, Per Delsing, Tord Claeson & Floriana Lombardi. *Science*, **311**, 5757 (2006) 57–60.

[67] Sergey Savel'ev, A L Rakhmanov & Franco Nori. *Phys. Rev. Lett.*, **98**, 7 (2007) 77002.

[68] Sergey Savel'ev, A O Sboychakov, A L Rakhmanov & Franco Nori. *Phys. Rev. B*, **77**, 1 (2008) 14509.

[69] Gerd Schön & A D Zaikin. *Phys. Rep.*, **198**, 5 (1990) 237–412.

[70] J. Q. You, Yu-xi Liu & Franco Nori. *Phys. Rev. Lett.*, **100**, 4 (2008) 047001.

[71] Adam Mann. *Nature*, **475**, 7356 (2011) 280–282.

[72] L Ozyuzer, A E Koshelev, C Kurter, N Gopalsami, Q Li, M Tachiki, K Kadowaki, T Yamamoto, H Minami, H Yamaguchi, T Tachiki, K E Gray, W.-K. Kwok & U Welp. *Science*, **318**, 5854 (2007) 1291 LP – 1293.

[73] Xiao Hu & Shi-Zeng Lin. *Supercond. Sci. Technol.*, **23**, 5 (2010) 053001.

[74] Ulrich Welp, Kazuo Kadowaki & Reinhold Kleiner. *Nat. Photonics*, **7**, 9 (2013) 702–710.

[75] Tomio Koyama, Hideki Matsumoto, Masahiko Machida & Kazuo Kadowaki. *Phys. Rev. B*, **79**, 10 (2009) 104522.

[76] A. E. Koshelev. *Phys. Rev. B*, **78**, 17 (2008) 174509.

[77] Masashi Tachiki, Shouta Fukuya & Tomio Koyama. *Phys. Rev. Lett.*, **102**, 12 (2009) 127002.

[78] J. Hammer, M. Aprili & I. Petković. *Phys. Rev. Lett.*, **107**, 1 (2011) 017001.

[79] John Bardeen. *Phys. Rev. Lett.*, **1**, 11 (1958) 399–400.

[80] James F. Annett. "Superconductivity, Superfluids and Condensates". Number May. Oxford University Press (2004).

[81] Alexander. Altland & Ben D. Simons. "Condensed Matter Field Theory." Cambridge University Press (2010).

[82] Piers Coleman. "Introduction to Many-Body Physics". Cambridge University Press, Cambridge (2015).

[83] Giovanni A.C. Ummarino. "Eliashberg Theory". In "Emergent Phenom. Correl. Matter", chapter 13, page 520. Forschungszentrum Jülich (2013).

[84] Philip Phillips. "Advanced Solid State Physics". Cambridge University Press, Cambridge (2012).

[85] Lev P. Gor'kov. *Sov. Phys. J. Exp. Theor. Phys.*, **36**, 9 (1959) 1364–1367.

[86] L.D. Landau. "On the theory of superconductivity". In Dirk ter Haar, editor, "Collect. Pap. L.D. Landau", pages 546–568. Pergamon (1965).

[87] B. D. Josephson. *Phys. Lett.*, **1**, 7 (1962) 251–253.

[88] B. D. Josephson. *Rev. Mod. Phys.*, **46**, 2 (1974) 251–254.

[89] John M. Martinis & Kevin Osborne. "Superconducting Qubits and the Physics of Josephson Junctions" (2004).

[90] Richard P. (Richard Phillips) Feynman, Robert B. Leighton & Matthew L. (Matthew Linzee) Sands. "The Feynman lectures on physics". Addison-Wesley Pub. Co (1963).

[91] D Rogovin & Marlan O Scully. *Ann. Phys. (N. Y).*, **88**, 2 (1974) 371–396.

[92] Antonio Barone & Paterno Gianfranco. "Physics and applications of Josephson effect" (1982).

[93] T.A. Fulton & L.N. Dunkleberger. *Phys. Rev. B*, **9**, 11 (1974) 4760–4769.

[94] A Wallraff, T Duty, A Lukashenko & A V Ustinov. *Phys. Rev. Lett.*, **90**, 3 (2003) 37003.

[95] W. Guichard & F. W. J. Hekking. *Phys. Rev. B*, **81**, 6 (2010) 064508.

[96] John M. Martinis, Michel H. Devoret & John Clarke. *Phys. Rev. Lett.*, **55**, 15 (1985) 1543–1546.

[97] Vinay Ambegaokar, Ulrich Eckern & Gerd Schön. *Phys. Rev. Lett.*, **48**, 25 (1982) 1745–1748.

[98] M. H. Devoret, D. Esteve, H. Grabert, G.-L. Ingold, H. Pothier & C. Urbina. *Phys. Rev. Lett.*, **64**, 1824.

[99] Albert Schmid. *Phys. Rev. Lett.*, **51**, 17 (1983) 1506–1509.

[100] J. S. Penttilä, Ü. Parts, P. J. Hakonen, M. A. Paalanen & E. B. Sonin. *Phys. Rev. Lett.*, **82**, 5 (1999) 1004–1007.

[101] Gil Refael, Eugene Demler, Yuval Oreg & Daniel S. Fisher. *Phys. Rev. B*, **68**, 21 (2003) 214515.

[102] Henry C. Fu, Alexander Seidel, John Clarke & Dung-Hai Lee. *Phys. Rev. Lett.*, **96**, 15 (2006) 157005.

[103] J G Bednorz & K A Müller. *Zeitschrift für Phys. B Condens. Matter*, **64**, 2 (1986) 189–193.

[104] Patrick A. Lee, Naoto Nagaosa & Xiao Gang Wen. *Rev. Mod. Phys.*, **78**, 1 (2006) 17—-85.

[105] P W Anderson, Z.-X. Shen, D. S. Dessau, D. S. Marshall, C. H. Park, P. Fournier & A. Kapitulnik. *Science*, **235**, 4793 (1987) 1196–8.

[106] J. Orenstein. *Science*, **288**, 5465 (2000) 468–474.

[107] Haoxiang Li, Xiaoqing Zhou, Stephen Parham, Theodore J. Reber, Helmuth Berger, Gerald B. Arnold & Daniel S. Dessau. *Nat. Commun.*, **9**, 1 (2018) 26.

[108] Tilman Esslinger. *Annu. Rev. Condens. Matter Phys.*, **1**, 1 (2010) 129–152.

[109] Daniel Greif, Thomas Uehlinger, Gregor Jotzu, Leticia Tarruell & Tilman Esslinger. *Science*, **340**, 6138 (2013) 1307–1310.

[110] Russell A Hart, Pedro M Duarte, Tsung-Lin Yang, Xinxing Liu, Thereza Paiva, Ehsan Khatami, Richard T Scalettar, Nandini Trivedi, David A Huse & Randall G Hulet. *Nature*, **519** (2015) 211.

[111] Matthew A Nichols, Lawrence W Cheuk, Melih Okan, Thomas R Hartke, Enrique Mendez, T Senthil, Ehsan Khatami, Hao Zhang & Martin W Zwierlein. *Science*, **363**, 6425 (2019) 383–387.

[112] Peter T Brown, Debayan Mitra, Elmer Guardado-Sanchez, Reza Nourafkan, Alexis Reymbaut, Charles-David Hébert, Simon Bergeron, A.-M. S Tremblay, Jure Kokalj, David A Huse, Peter Schauß & Waseem S Bakr. *Science*, **363**, 6425 (2019) 379–382.

[113] Anthony J. Leggett. *Nat. Phys.*, **2**, 3 (2006) 134–136.

[114] L Benfatto, A Toschi, S Caprara & C Castellani. *Phys. Rev. B*, **64**, 14 (2001) 140506.

[115] R. Kleiner, F. Steinmeyer, G. Kunkel & P. Müller. *Phys. Rev. Lett.*, **68**, 15 (1992) 2394–2397.

[116] R. Kleiner, P. Müller, H. Kohlstedt, N. F. Pedersen & S. Sakai. *Phys. Rev. B*, **50**, 6 (1994) 3942–3952.

[117] S Sakai, P Bodin & N F Pedersen. *J. Appl. Phys.*, **73**, 5 (1993) 2411–2418.

[118] S. Sakai, A. V. Ustinov, H. Kohlstedt, A. Petraglia & N. F. Pedersen. *Phys. Rev. B*, **50**, 17 (1994) 12905–12914.

[119] L. N. Bulaevskii, M. Zamora, D. Baeriswyl, H. Beck & John R. Clem. *Phys. Rev. B*, **50**, 17 (1994) 12831.

[120] L. Bulaevskii, D. Domínguez, M. Maley, A. Bishop & B. Ivlev. *Phys. Rev. B*, **53**, 21 (1996) 14601–14610.

[121] L. N. Bulaevskii & A. E. Koshelev. *Phys. Rev. Lett.*, **99**, 5 (2007) 057002.

[122] Shizeng Lin & Xiao Hu. *Phys. Rev. Lett.*, **100**, 24 (2008) 247006.

[123] Yoshihiko Nonomura. *Phys. Rev. B*, **80**, 14 (2009) 140506.

[124] Shizeng Lin & Xiao Hu. *Phys. Rev. B*, **79**, 10 (2009) 104507.

[125] H. B. Wang, S. Guénon, B. Gross, J. Yuan, Z. G. Jiang, Y. Y. Zhong, M. Grünzweig, A. Iishi, P. H. Wu, T. Hatano, D. Koelle & R. Kleiner. *Phys. Rev. Lett.*, **105**, 5 (2010) 057002.

[126] A E Koshelev & I Aranson. *Phys. Rev. B*, **64**, 17 (2001) 174508.

[127] L. Benfatto, C. Castellani & T. Giamarchi. *Phys. Rev. B*, **77**, 100506.

[128] A G Loeser, Z.-X. Shen, D S Dessau, D S Marshall, C H Park, P Fournier & A Kapitulnik. *Science*, **273**, 5273 (1996) 325 LP – 329.

[129] H. Ding, T. Yokoya, J. C. Campuzano, T. Takahashi, M. Randeria, M. R. Norman, T. Mochiku, K. Kadowaki & J. Giapintzakis. "Spectroscopic evidence for a pseudogap in the normal state of underdoped high-Tc superconductors" (1996).

[130] A G Loeser, Z.-X. Shen, M C Schabel, C Kim, M Zhang, A Kapitulnik & P Fournier. *Phys. Rev. B*, **56**, 21 (1997) 14185–14189.

[131] A V Fedorov, T Valla, P D Johnson, Q Li, G D Gu & N Koshizuka. *Phys. Rev. Lett.*, **82**, 10 (1999) 2179–2182.

[132] I Maggio-Aprile, Ch. Renner, A Erb, E Walker & Ø Fischer. *Phys. Rev. Lett.*, **75**, 14 (1995) 2754–2757.

[133] Ch. Renner, B Revaz, K Kadowaki, I Maggio-Aprile & Ø. Fischer. *Phys. Rev. Lett.*, **80**, 16 (1998) 3606–3609.

[134] Y J Uemura, G M Luke, B J Sternlieb, J H Brewer, J F Carolan, W N Hardy, R Kadono, J R Kempton, R F Kiefl, S R Kreitzman, P Mulhern, T M Riseman, D Ll. Williams, B X Yang, S Uchida, H Takagi, J Gopalakrishnan, A W Sleight, M A Subramanian, C L Chien, M Z Cieplak, Gang Xiao, V Y Lee, B W Statt, C E Stronach, W J Kossler & X H Yu. *Phys. Rev. Lett.*, **62**, 19 (1989) 2317–2320.

[135] V. J. Emery & S. a. Kivelson. *Phys. Rev. Lett.*, **74**, 16 (1995) 3253–3256.

[136] E. W. Carlson, S. a. Kivelson, V. J. Emery & E. Manousakis. *Phys. Rev. Lett.*, **83**, 3 (1999) 612—-615.

[137] L Benfatto, S Caprara, C Castellani, A Paramekanti & M Randeria. *Phys. Rev. B*, **63**, 17 (2001) 174513.

[138] Jorge V Jose. "40 years of Berezinskii-Kosterlitz-Thouless theory". World Scientific, Singapore (2013).

[139] L. Benfatto, C. Castellani & T. Giamarchi. *Phys. Rev. Lett.*, **98**, 11 (2007) 117008.

[140] Y. L. Loh & E. W. Carlson. *Phys. Rev. B*, **75**, 13 (2007) 132506.

[141] John Bardeen. *Rev. Mod. Phys.*, **34**, 4 (1962) 667–681.

[142] G. M. Eliashberg. *JETP Lett.*, **11**, 3 (1970) 114.

[143] B. I. Ivlev, S. G. Lisitsyn & G. M. Eliashberg. *J. Low Temp. Phys.*, **10**, 3-4 (1973) 449–468.

[144] Kenneth E. Gray. "Nonequilibrium Superconductivity, Phonons, and Kapitza Boundaries". Springer (1981).

[145] A H Dayem & J J Wiegand. *Phys. Rev.*, **155**, 2 (1967) 419–428.

[146] F. S. Bergeret, P. Virtanen, T. T. Heikkilä & J. C. Cuevas. *Phys. Rev. Lett.*, **105**, 11 (2010) 117001.

[147] Pauli Virtanen, Tero T. Heikkilä, F. Sebastián Bergeret & Juan Carlos Cuevas. *Phys. Rev. Lett.*, **104**, 24 (2010) 247003.

[148] Philip B. Allen. *Phys. Rev. Lett.*, **59**, 13 (1987) 1460–1463.

[149] A. A. Schafgans, C. C. Homes, G. D. Gu, Seiki Komiya, Yoichi Ando & D. N. Basov. *Phys. Rev. B*, **82**, 10 (2010) 100505.

[150] Martin Dressel & George Gruner. "Electrodynamics of Solids". Cambridge University Press, Cambridge (2002).

[151] D. N. Basov & T. Timusk. *Rev. Mod. Phys.*, **77**, 2 (2005) 721–779.

[152] S. D. Brorson, R. Buhleier, I. E. Trofimov, J. O. White, Ch. Ludwig, F. F. Balakirev, H.-U. Habermeier & J. Kuhl. *J. Opt. Soc. Am. B*, **13**, 9 (1996) 1979.

[153] D. J. Wineland & Wayne M. Itano. *Phys. Rev. A*, **20**, 4 (1979) 1521–1540.

[154] T.W. Hänsch & A.L. Schawlow. *Opt. Commun.*, **13**, 1 (1975) 68–69.

[155] Claude N. CohenâĂŘTannoudji & William D. Phillips. *Phys. Today*, **43**, 10 (1990) 33–40.

[156] E. S. Shuman, J. F. Barry & D. DeMille. *Nature*, **467**, 7317 (2010) 820–823.

[157] S. Truppe, H. J. Williams, M. Hambach, L. Caldwell, N. J. Fitch, E. A. Hinds, B. E. Sauer & M. R. Tarbutt. *Nat. Phys.*, **13**, 12 (2017) 1173–1176.

[158] Markus Aspelmeyer, Tobias J. Kippenberg & Florian Marquardt. *Rev. Mod. Phys.*, **86**, 4 (2014) 1391–1452.

[159] Galina Nemova & Raman Kashyap. *Reports Prog. Phys.*, **73**, 8 (2010) 86501.

[160] T J Kippenberg & K J Vahala. *Opt. Express*, **15**, 25 (2007) 17172–17205.

[161] V. B. Braginskii & A. B. Manukin. "Ponderomotive effects of electromagnetic radiation", volume 25. American Institute of Physics (1967).

[162] V.B. Braginskii, A.B. Manukin & M. Yu. Tikhonov. *J. Exp. Theor. Phys.*, **31**, 5 (1970) 829.

[163] P. F. Cohadon, A. Heidmann & M. Pinard. *Phys. Rev. Lett.*, **83**, 16 (1999) 3174–3177.

[164] Tal Carmon, Hossein Rokhsari, Lan Yang, Tobias J. Kippenberg & Kerry J. Vahala. *Phys. Rev. Lett.*, **94**, 22 (2005) 223902.

[165] T. J. Kippenberg, H. Rokhsari, T. Carmon, A. Scherer & K. J. Vahala. *Phys. Rev. Lett.*, **95**, 3 (2005) 033901.

[166] O Arcizet, P-F Cohadon, T Briant, M Pinard & a Heidmann. *Nature*, **444**, 7115 (2006) 71–74.

[167] Mo Li, W. H. P. Pernice, C. Xiong, T. Baehr-Jones, M. Hochberg & H. X. Tang. *Nature*, **456**, 7221 (2008) 480–484.

[168] M. S. Kang, A. Nazarkin, A. Brenn & P. St. J. Russell. *Nat. Phys.*, **5**, 4 (2009) 276–280.

[169] C. K. Law. *Phys. Rev. A*, **51**, 3 (1995) 2537–2541.

[170] Law. *Phys. Rev. A, At. Mol. Opt. Phys.*, **49**, 1 (1994) 433–437.

[171] a. a. Clerk, M. H. Devoret, S. M. Girvin, Florian Marquardt & R. J. Schoelkopf. *Rev. Mod. Phys.*, **82**, 2 (2010) 1155–1208.

[172] Crispin W. Gardiner & Peter Zoller. "Quantum noise". Springer (2004).

[173] Florian Marquardt, Joe P. Chen, A. A. Clerk & S. M. Girvin. *Phys. Rev. Lett.*, **99**, 9 (2007) 093902.

[174] I. Wilson-Rae, N. Nooshi, W. Zwerger & T. J. Kippenberg. *Phys. Rev. Lett.*, **99**, 9 (2007) 093901.

[175] I. Wilson-Rae, N. Nooshi, J. Dobrindt, T. J. Kippenberg & W. Zwerger. *New J. Phys.*, **10**, 9 (2008) 095007.

[176] J. M. Dobrindt, I. Wilson-Rae & T. J. Kippenberg. *Phys. Rev. Lett.*, **101**, 26 (2008) 263602.

[177] Anton Frisk Kockum, Adam Miranowicz, Simone De Liberato, Salvatore Savasta & Franco Nori. *Nat. Rev. Phys.*, **1**, 1 (2019) 19–40.

[178] Félix Beaudoin, Jay M. Gambetta & A. Blais. *Phys. Rev. A*, **84**, 4 (2011) 043832.

[179] R Zwanzig. "Nonequilibrium statistical mechanics", volume 54. Oxford University Press (2001).

[180] Michel Le Bellac, Fabrice Mortessagne & G. George Batrouni. "Equilibrium and non-equilibrium statistical thermodynamics" (2004).

[181] A. Schliesser, R. Rivière, G. Anetsberger, O. Arcizet & T. J. Kippenberg. *2008 Conf. Quantum Electron. Laser Sci. Conf. Lasers Electro-Optics, CLEO/QELS*, pages 415–419.

[182] A Schliesser, R Rivière, G Anetsberger, O Arcizet & T J Kippenberg. *Nat. Phys.*, **4** (2008) 415.

[183] Simon Gröblacher, Klemens Hammerer, Michael R. Vanner & Markus Aspelmeyer. *Nature*, **460**, 7256 (2009) 724–727.

[184] J. D. Teufel, T. Donner, Dale Li, J. W. Harlow, M. S. Allman, K. Cicak, A. J. Sirois, J. D. Whittaker, K. W. Lehnert & R. W. Simmonds. *Nature*, **475**, 7356 (2011) 359–363.

[185] J. D. Teufel, Dale Li, M. S. Allman, K. Cicak, A. J. Sirois, J. D. Whittaker & R. W. Simmonds. *Nature*, **471**, 7337 (2011) 204–208.

[186] Y Laplace, S. Fernandez-Pena, S Gariglio, J M Triscone & A Cavalleri. *Phys. Rev. B*, **93**, 7 (2016) 075152.

[187] M. V. Fistul & a. V. Ustinov. *Phys. Rev. B - Condens. Matter Mater. Phys.*, **75**, 21 (2007) 214506.

[188] K. Enpuku, K. Yoshida & F. Irie. *J. Appl. Phys.*, **52**, 1 (1981) 344–351.

[189] Mario Salerno, E Joergensen & M R Samuelsen. *Phys. Rev. B*, **30**, 5 (1984) 2635–2639.

[190] S. Pagano, M. P. Soerensen, R. D. Parmentier, P. L. Christiansen, O. Skovgaard, J. Mygind, N. F. Pedersen & M. R. Samuelsen. *Phys. Rev. B*, **33**, 1 (1986) 174–182.

[191] G. Rotoli, G. Costabile & R. D. Parmentier. *Phys. Rev. B*, **41**, 4 (1990) 1958–1968.

[192] Masahiko Machida & Shigeki Sakai. *Phys. Rev. B*, **70**, 14 (2004) 144520.

[193] Tomio Koyama. *J. Phys. Soc. Japan*, **71**, 12 (2002) 2986–2993.

[194] Tomio Koyama. *Phys. Rev. B*, **68**, 22 (2003) 224505.

[195] M Machida & T Koyama. *Phys. Rev. B*, **70**, 2 (2004) 24523.

[196] Heinz-Peter Breuer & Francesco Petruccione. "The Theory of Open Quantum Systems". Oxford University Press (2002).

[197] Crispin Gardiner & Peter Zoller. "The Quantum World of Ultra-Cold Atoms and Light Book III: Ultra-Cold Atoms". WORLD SCIENTIFIC (EUROPE) (2017).

[198] C.W. Gardiner & P. Zoller. "Quantum noise". Springer, New York, 2nd enlarg edition (2000).

[199] Ching-Kit Chan, Guin-Dar Lin, Susanne F. Yelin & Mikhail D. Lukin. *Phys. Rev. A*, **89**, 4 (2014) 042117.

[200] Ángel Rivas, A Douglas K Plato, Susana F Huelga & Martin B Plenio. *New J. Phys.*, **12**, 11 (2010) 113032.

[201] Leonard. Mandel & Emil. Wolf. "Optical coherence and quantum optics". Cambridge University Press (1995).

[202] Robert W. Boyd. "Nonlinear optics". Academic Press (2008).

[203] Ananda Roy & Michel Devoret. *Phys. Rev. B*, **98**, 4 (2018) 045405.

[204] S. Rajasekaran, E. Casandruc, Y. Laplace, D. Nicoletti, G. D. Gu, S. R. Clark, D. Jaksch & A. Cavalleri. *Nat. Phys.*, **12**, 11 (2016) 1012–1016.

[205] Beilei Zhu, Rexin Tobias & Mathey Ludwig. *Zeitschrift für Naturforsch. A*, **71** (2016) 921.

[206] Ivana Kovacic, Richard Rand & Si Mohamed Sah. *Appl. Mech. Rev.*, **70**, 2 (2018) 20802–20822.

[207] Gerald D. Mahan. "Many-Particle Physics". Springer, 3 edition (2000).

[208] Felix Binder, Sai Vinjanampathy, Kavan Modi & John Goold. *Phys. Rev. E*, **91**, 3 (2015) 032119.

[209] Cyril Elouard, David A. Herrera-Martí, Maxime Clusel & Alexia Auffèves. *npj Quantum Inf.*, **3**, 1 (2017) 9.

[210] Anatoli Polkovnikov. *Ann. Phys. (N. Y).*, **326**, 2 (2011) 486–499.

[211] Anatoli Polkovnikov. *Phys. Rev. Lett.*, **101**, 22 (2008) 220402.

[212] Anatoli Polkovnikov & Vladimir Gritsev. *Nat. Phys.*, **4** (2008) 477.

[213] Arnab Das & Bikas K Chakrabarti. *Rev. Mod. Phys.*, **80**, 3 (2008) 1061–1081.

[214] Simon A Weidinger & Michael Knap. *Sci. Rep.*, **7** (2017) 45382.

[215] Achilleas Lazarides, Arnab Das & Roderich Moessner. *Phys. Rev. E*, **90**, 1 (2014) 012110.

[216] Luca D'Alessio & Anatoli Polkovnikov. *Ann. Phys. (N. Y).*, **333** (2013) 19–33.

[217] Thomas Bilitewski & Nigel R. Cooper. *Phys. Rev. A*, **91**, 3 (2015) 033601.

[218] Marin Bukov, Luca D'Alessio & Anatoli Polkovnikov. *Adv. Phys.*, **64**, 2 (2015) 139–226.

[219] Roberta Citro, Emanuele G. Dalla Torre, Luca D'Alessio, Anatoli Polkovnikov, Mehrtash Babadi, Takashi Oka & Eugene Demler. *Ann. Phys. (N. Y).*, **360** (2015) 694–710.

[220] Netanel H. Lindner, Gil Refael & Victor Galitski. *Nat. Phys.*, **7**, 6 (2011) 490–495.

[221] M. Aidelsburger, M. Atala, M. Lohse, J. T. Barreiro, B. Paredes & I. Bloch. *Phys. Rev. Lett.*, **111**, 18 (2013) 185301.

[222] Marcos Rigol, Vanja Dunjko & Maxim Olshanii. *Nature*, **452**, 7189 (2008) 854–858.

[223] Peter Reimann. *Phys. Rev. Lett.*, **101**, 19 (2008) 190403.

[224] Pranjal Bordia, Henrik Lüschen, Ulrich Schneider, Michael Knap & Immanuel Bloch. *Nat. Phys.*, **13**, 5 (2017) 460–464.

[225] Tatsuhiko Shirai, Juzar Thingna, Takashi Mori, Sergey Denisov, Peter Hänggi & Seiji Miyashita. *New J. Phys.*, **18**, 5 (2016) 053008.

[226] Hossein Dehghani, Takashi Oka & Aditi Mitra. *Phys. Rev. B*, **90**, 19 (2014) 195429.

[227] Karthik I. Seetharam, Charles-Edouard Bardyn, Netanel H. Lindner, Mark S. Rudner & Gil Refael. *Phys. Rev. X*, **5**, 4 (2015) 041050.

[228] R. Graham & R. Hubner. *Ann. Phys. (N. Y).*, **234**, 2 (1994) 300–315.

[229] R. Blümel, A. Buchleitner, R. Graham, L. Sirko, U. Smilansky & H. Walther. *Phys. Rev. A*, **44**, 7 (1991) 4521–4540.

[230] Sigmund Kohler, Thomas Dittrich & Peter Hänggi. *Phys. Rev. E*, **55**, 1 (1997) 300–313.

[231] Heinz-Peter Breuer & Francesco Petruccione. *Phys. Rev. A*, **55**, 4 (1997) 3101–3116.

[232] Brecht Donvil. *J. Stat. Mech. Theory Exp.*, **2018**, 4 (2018) 043104.

[233] M. G. Floquet. *Ann. Sci. l'É.N.S.*, **12** (1883) 47–88.

[234] Jon H. Shirley. *Phys. Rev.*, **138**, 4B (1965) B979–B987.

[235] Peter Hänggi. "Driven quantum systems". In T. Dittrich, Peter Hänggi, G.-L. Ingold, B. Kramer, G. Schön & W. Zwerger, editors, "Quantum Transp. Dissipation", chapter 5. Wiley (1997).

[236] Milena Grifoni & Peter Hänggi. *Phys. Rep.*, **304**, 5 (1998) 229–354.

[237] S. Gasparinetti, P. Solinas, S. Pugnetti, R. Fazio & J. P. Pekola. *Phys. Rev. Lett.*, **110**, 15 (2013) 150403.

[238] Lucas Verney, Raphaël Lescanne, Michel H. Devoret, Zaki Leghtas & Mazyar Mirrahimi. *Phys. Rev. Appl.*, **11**, 2 (2019) 024003.

[239] Ya. B. Zel'Dovich & Ya. B. *Sov. Phys. JETP, Vol. 24, p.1006*, **24** (1967) 1006.

[240] A G Fainshtein, N L Manakov & L P Rapoport. *J. Phys. B At. Mol. Phys.*, **11**, 14 (1978) 2561–2577.

[241] André Eckardt & Egidijus Anisimovas. *New J. Phys.*, **17**, 9 (2015) 093039.

[242] Daniel W. Hone, Roland Ketzmerick & Walter Kohn. *Phys. Rev. E*, **79**, 5 (2009) 051129.

[243] Yiying Yan, Zhiguo Lü & Hang Zheng. *Phys. Rev. A*, **90**, 5 (2014) 053850.

[244] Matthias Langemeyer & Martin Holthaus. *Phys. Rev. E*, **89**, 1 (2014) 012101.

[245] Tatsuhiko Shirai, Takashi Mori & Seiji Miyashita. *Phys. Rev. E*, **91**, 3 (2015) 030101.

[246] Walter Kohn. *J. Stat. Phys.*, **103**, 3/4 (2001) 417–423.

[247] Tim Langen, Sebastian Erne, Remi Geiger, Bernhard Rauer, Thomas Schweigler, Maximilian Kuhnert, Wolfgang Rohringer, Igor E Mazets, Thomas Gasenzer & Jörg Schmiedmayer. *Science*, **348**, 6231 (2015) 207 LP – 211.

[248] Florian Lange, Zala Lenarčič & Achim Rosch. *Nat. Commun.*, **8** (2017) 15767.

[249] Florian Lange, Zala Lenarčič & Achim Rosch. *Phys. Rev. B*, **97**, 16 (2018) 165138.

[250] Zala Lenarčič, Florian Lange & Achim Rosch. *Phys. Rev. B*, **97**, 2 (2018) 024302.

[251] R. Mankowsky, M. Först, T. Loew, J. Porras, B. Keimer & A. Cavalleri. *Phys. Rev. B*, **91**, 9 (2015) 094308.

[252] Sergey Savel'ev, V A Yampol'skii, A L Rakhmanov & Franco Nori. *Reports Prog. Phys.*, **73**, 2 (2010) 026501.

[253] S. N. Artemenko & S. V. Remizov. *J. Exp. Theor. Phys. Lett.*, **66**, 12 (1997) 853–859.

[254] Ajay Kumar Saxena. "High-Temperature Superconductors". Springer Series in Materials Science 125 (2010).

[255] A E Koshelev. *Phys. Rev. B*, **62**, 6 (2000) R3616—-R3619.

[256] T. Koyama & M. Tachiki. *Phys. Rev. B*, **54**, 22 (1996) 16183–16191.

[257] Masahiko Machida & Tomio Koyama. *Supercond. Sci. Technol.*, **20**, 2 (2007) S23.

[258] N.G. Van Kampen. *Phys. Rep.*, **124**, 2 (1985) 69–160.

[259] Shi-Zeng Lin & Xiao Hu. *Phys. Rev. B*, **86**, 5 (2012) 054506.

[260] L N Bulaevskii, D Domínguez, M P Maley, A R Bishop, Ophelia K C Tsui & N P Ong. *Phys. Rev. B*, **54**, 10 (1996) 7521–7535.

[261] Yu. I Latyshev, A E Koshelev & L N Bulaevskii. *Phys. Rev. B*, **68**, 13 (2003) 134504.

[262] A. E. Koshelev. *Phys. Rev. B*, **76**, 5 (2007) 054525.

[263] Claude Cohen-Tannoudji, Jacques. Dupont-Roc & Gilbert. Grynberg. "Photons and atoms : introduction to quantum electrodynamics". Wiley (1989).

[264] Guang S. He. "Nonlinear Optics and Photonics". Oxford University Press, 1 edition (2015).

[265] Oliver Johns. "Analytical Mechanics for Relativity and Quantum Mechanics". Oxford University Press (2005).

[266] Jürgen Struckmeier & Claus Riedel. *Phys. Rev. E*, **64**, 2 (2001) 026503.

[267] Mark (Anthony Mark) Fox. "Optical properties of solids". Oxford University Press, 2nd edition (2010).

[268] T. Pereg-Barnea, P. J. Turner, R. Harris, G. K. Mullins, J. S. Bobowski, M. Raudsepp, Ruixing Liang, D. A. Bonn & W. N. Hardy. *Phys. Rev. B*, **69**, 18 (2004) 184513.

[269] D R Harshman, L F Schneemeyer, J V Waszczak, G Aeppli, R J Cava, B Batlogg, L W Rupp, E J Ansaldo & D Ll. Williams. *Phys. Rev. B*, **39**, 1 (1989) 851–854.

[270] D Winkler, Y M Zhang, P Å. Nilsson, E A Stepantsov & T Claeson. *Phys. Rev. Lett.*, **72**, 8 (1994) 1260–1263.

[271] D. Munzar, C. Bernhard, A. Golnik, J. Humlcek & M. Cardona. *Solid State Commun.*, **112** (1999) 365–369.

[272] M. Machida, T. Koyama & M. Tachiki. *Phys. Rev. Lett.*, **83**, 22 (1999) 4618–4621.

[273] A. Gurevich. *Phys. Rev. B*, **46**, 5 (1992) 3187–3190.

[274] Y. Laplace & A. Cavalleri. *Adv. Phys. X*, **1**, 3 (2016) 387–411.

[275] Guillaume Ducournau. *Nat. Photonics*, **12**, 10 (2018) 574–575.

[276] T. Harter, S. Muehlbrandt, S. Ummethala, A. Schmid, S. Nellen, L. Hahn, W. Freude & C. Koos. *Nat. Photonics*, **12**, 10 (2018) 625–633.

[277] Filippo Alpeggiani & Lucio Claudio Andreani. *Phys. Rev. B*, **88**, 17 (2013) 174513.

[278] D. van der Marel & a. Tsvetkov. *Czechoslov. J. Phys.*, **46**, SUPPL. 6 (1996) 3165–3168.

[279] D van der Marel & A A Tsvetkov. *Phys. Rev. B*, **64**, 2 (2001) 24530.

[280] S. J. Berkowitz, W. J. Skocpol, P. M. Mankiewich, R. H. Ono, N. Missert, P. A. Rosenthal & L. R. Vale. *J. Appl. Phys.*, **76**, 2 (1994) 1337–1339.

[281] A. O. Sboychakov, Sergey Savel'ev, A. L. Rakhmanov & Franco Nori. *Europhys. Lett.*, **80**, 1 (2007) 17009.

[282] A. O. Sboychakov, Sergey Savel'ev & Franco Nori. *Phys. Rev. B*, **78**, 13 (2008) 134518.

[283] S P Vyatchanin. *Sov. Phys. Dokl.*, **22** (1977) 321.

[284] Crispin Gardiner & Peter Zoller. "The Quantum World of Ultra-Cold Atoms and Light Book I: Foundations of Quantum Optics", volume Volume 2. Imperial College Press (2014).

[285] M G Castellano, G Torrioli, C Cosmelli, A Costantini, F Chiarello, P Carelli, G Rotoli, M Cirillo & R L Kautz. *Phys. Rev. B*, **54**, 21 (1996) 15417–15428.

[286] Haruhisa Kitano, Kensuke Ota & Atsutaka Maeda. *Supercond. Sci. Technol.*, **20**, 2 (2007) S68.

[287] Gil-Ho Lee & Hu-Jong Lee. *Phys. C Supercond.*, **470**, Supplement 1 (2010) S815 – S816.

[288] A. Wallraff, A. Lukashenko, C. Coqui, A. Kemp, T. Duty & A. V. Ustinov. *Rev. Sci. Instrum.*, **74**, 8 (2003) 3740–3748.

[289] D W McLaughlin & a C Scott. *Phys. Rev. A*, **18** (1978) 1652–1680.

[290] A. E. Koshelev. *Phys. Rev. B*, **68**, 9 (2003) 094520.

[291] A. E. Koshelev. *Phys. Rev. Lett.*, **83**, 1 (1999) 187–190.

[292] A. Dienst, HoffmannM. C., D. Fausti, PetersenJ. C., S. Pyon, TakayamaT., TakagiH. & CavalleriA. *Nat Phot.*, **5**, 8 (2011) 485–488.

[293] A Dienst, E Casandruc, D Fausti, L Zhang, M Eckstein, M Hoffmann, V Khanna, N Dean, M Gensch, S Winnerl, W Seidel, S Pyon, T Takayama, H Takagi & A Cavalleri. *Nat. Mater.*, **12**, 6 (2013) 535–41.

[294] S Rajasekaran, J Okamoto, L Mathey, M Fechner, V Thampy, G D Gu & A Cavalleri. *Science*, **359**, 6375 (2018) 575–579.

[295] Sergey Savel'ev, A. L. Rakhmanov & Franco Nori. *Phys. Rev. Lett.*, **94**, 15 (2005) 157004.

[296] Sergey Savel'ev, A L Rakhmanov, V A Yampol'skii & Franco Nori. *Nat Phys*, **2**, 8 (2006) 521–525.

[297] C. Capan, K. Behnia, Z. Z. Li, H. Raffy & C. Marin. *Phys. Rev. B*, **67**, 10 (2003) 100507.

[298] Anastasia S. D. Dietrich, Martin Kiffner & Dieter Jaksch. *Phys. Rev. A*, **98**, 1 (2018) 012122.

[299] S. Gröblacher, A. Trubarov, N. Prigge, G. D. Cole, M. Aspelmeyer & J. Eisert. *Nat. Commun.*, **6** (2015) 7606.

[300] Gonzalo A. Álvarez & Dieter Suter. *Phys. Rev. Lett.*, **107**, 23 (2011) 230501.

[301] Tatsuro Yuge, Susumu Sasaki & Yoshiro Hirayama. *Phys. Rev. Lett.*, **107**, 17 (2011) 170504.

[302] M. Mohseni, A. T. Rezakhani & D. A. Lidar. *Phys. Rev. A*, **77**, 3 (2008) 032322.

[303] C. F. Lo. *Phys. Rev. A, At. Mol. Opt. Phys.*, **43**, 1 (1991) 404–409.

[304] C. F. Lo. *Phys. Rev. A*, **47**, 1 (1993) 115–118.

[305] M. Sebawe Abdalla & R. K. Colegrave. *Phys. Rev. A*, **48**, 2 (1993) 1526–1531.

[306] Célia M. A. Dantas, I. A. Pedrosa & B. Baseia. *Phys. Rev. A*, **45**, 3 (1992) 1320–1324.

[307] Jeong-Young Ji, Jae Kwan Kim & Sang Pyo Kim. *Phys. Rev. A*, **51**, 5 (1995) 4268–4271.

[308] Ding Sheng, R. D. Khan, Zhang Jialun & Shen Wenda. *Int. J. Theor. Phys.*, **34**, 3 (1995) 355–368.

[309] Dae-Yup Song. *J. Phys. A. Math. Gen.*, **32**, 18 (1999) 3449–3456.

[310] Kyu Hwang Yeon, Kang Ku Lee, Chung In Um, Thomas F. George & Lakshmi N. Pandey. *Phys. Rev. A*, **48**, 4 (1993) 2716–2720.

[311] Chung-In Um, Kyu-Hwang Yeon & Thomas F. George. *Phys. Rep.*, **362**, 2 (2002) 63–192.

[312] Jeong-Young Ji, Jae Kwan Kim, Sang Pyo Kim & Kwang-Sup Soh. *Phys. Rev. A*, **52**, 4 (1995) 3352–3355.

[313] I. A. Pedrosa. *Phys. Rev. A*, **55**, 4 (1997) 3219–3221.

[314] H. Kohler & F. Sols. *Phys. A Stat. Mech. its Appl.*, **392**, 9 (2013) 1989–1993.

[315] Jing-Dong Bao & Yi-Zhong Zhuo. *Phys. Rev. E*, **71**, 1 (2005) 010102.

[316] A J Leggett. *Phys. Rev. B*, **30**, 3 (1984) 1208–1218.

[317] Alessandro Cuccoli, Andrea Fubini, Valerio Tognetti & Ruggero Vaia. *Phys. Rev. E*, **64**, 6 (2001) 066124.

[318] Ulrich Weiss. "Quantum Dissipative Systems". World Scientific Publishing Co. Pte. Ltd., Singapore, 2 edition (1999).

[319] D. Leibfried, R. Blatt, C. Monroe & D. Wineland. *Rev. Mod. Phys.*, **75**, 1 (2003) 281–324.

[320] M. Abramowitz & I. A. Stegun. "Handbook of Mathematical Functions with Formulas, Graphs, and Mathematical Tables". National Bureau of Standards Applied Mathematics Series, U.S. Government Printing Office, Washington, D.C. (1972).

[321] E. Wigner. *Phys. Rev.*, **40**, 5 (1932) 749–759.

[322] Anatoli Polkovnikov. *Ann. Phys. (N. Y).*, **325**, 8 (2010) 1790–1852.

[323] Christine Zerbe & Peter Hänggi. *Phys. Rev. E*, **52**, 2 (1995) 1533–1543.

[324] Yair Rezek & Ronnie Kosloff. *New J. Phys.*, **8**, 5 (2006) 83–83.

[325] J. Eisert & M. M. Wolf. "Gaussian quantum channels". In "Quantum Inf. with Continous Var. Atoms Light", pages 23–42. Imperial College Press (2007).

[326] Fernando Galve, Leonardo A. Pachón & David Zueco. *Phys. Rev. Lett.*, **105**, 18 (2010) 180501.

[327] K. W. Chang & C. K. Law. *Phys. Rev. A*, **81**, 5 (2010) 052105.

[328] R. Schmidt, A. Negretti, J. Ankerhold, T. Calarco & J. T. Stockburger. *Phys. Rev. Lett.*, **107**, 13 (2011) 130404.

[329] R Blatt, P Zoller, G Holzmüller & I Siemers. *Zeitschrift für Phys. D Atoms, Mol. Clust.*, **4**, 2 (1986) 121–126.

[330] Christine Zerbe, Peter Jung & Peter Hänggi. *Phys. Rev. E*, **49**, 5 (1994) 3626–3635.

[331] S. Arnold, J. H. Li, S. Holler, A. Korn & A. F. Izmailov. *J. Appl. Phys.*, **78**, 6 (1995) 3566–3571.

[332] S. Mukamel, I. Oppenheim & John Ross. *Phys. Rev. A*, **17**, 6 (1978) 1988–1998.

[333] M P Silveri, J A Tuorila, E V Thuneberg & G S Paraoanu. *Reports Prog. Phys.*, **80**, 5 (2017) 056002.

[334] Jian Li, M.P. Silveri, K.S. Kumar, J.-M. Pirkkalainen, A. Vepsäläinen, W.C. Chien, J. Tuorila, M.A. Sillanpää, P.J. Hakonen, E.V. Thuneberg & G.S. Paraoanu. *Nat. Commun.*, **4**, 1 (2013) 1420.

[335] Heinz-Peter Breuer, Elsi-Mari Laine, Jyrki Piilo & Bassano Vacchini. *Rev. Mod. Phys.*, **88**, 2 (2016) 021002.

[336] Inés de Vega & Daniel Alonso. *Rev. Mod. Phys.*, **89**, 1 (2017) 015001.

[337] R.P Feynman & F.L Vernon. *Ann. Phys. (N. Y).*, **24** (1963) 118–173.

[338] Jürgen T. Stockburger & Hermann Grabert. *Phys. Rev. Lett.*, **88**, 17 (2002) 170407.

[339] D. Tamascelli, A. Smirne, S.âĂŁF. Huelga & M.âĂŁB. Plenio. *Phys. Rev. Lett.*, **120**, 3 (2018) 030402.

[340] Nancy Makri & Dmitrii E. Makarov. *J. Chem. Phys.*, **102**, 11 (1995) 4600–4610.

[341] R.P. Feynman & F.L. Vernon. *Ann. Phys. (N. Y).*, **281**, 1-2 (2000) 547–607.

[342] A. Strathearn, P. Kirton, D. Kilda, J. Keeling & B. W. Lovett. *Nat. Commun.*, **9**, 1 (2018) 3322.

[343] Rebecca Schmidt, Selina Rohrer, Joachim Ankerhold & Jürgen T Stockburger. *Phys. Scr.*, **T151**, T151 (2012) 014034.

[344] Saleh Rahimi-Keshari, Thomas Kiesel, Werner Vogel, Samuele Grandi, Alessandro Zavatta & Marco Bellini. *Phys. Rev. Lett.*, **110**, 16 (2013) 160401.

[345] Krishna Kumar Sabapathy. *Phys. Rev. A*, **93**, 4 (2016) 042103.

[346] Hong-Bin Chen, Clemens Gneiting, Ping-Yuan Lo, Yueh-Nan Chen & Franco Nori. *Phys. Rev. Lett.*, **120**, 3 (2018) 030403.

[347] Arvind, N. Mukunda & R. Simon. *Phys. Rev. A*, **56**, 6 (1997) 5042–5052.

[348] Yuriy Makhlin, Gerd Schön & Alexander Shnirman. *Rev. Mod. Phys.*, **73**, 2 (2001) 357–400.

[349] M. Kiffner & M. J. Hartmann. *Phys. Rev. A*, **81**, 2 (2010) 021806.

[350] Martin Kiffner, Uwe Dorner & Dieter Jaksch. *Phys. Rev. A*, **85**, 2 (2012) 023812.

[351] Sebastian Diehl, Andrea Tomadin, Andrea Micheli, Rosario Fazio & Peter Zoller. *Phys. Rev. Lett.*, **105**, 1 (2010) 015702.

[352] M. Höning, M. Moos & M. Fleischhauer. *Phys. Rev. A*, **86**, 1 (2012) 013606.

[353] S. Diehl, A. Micheli, A. Kantian, B. Kraus, H. P. Büchler & P. Zoller. *Nat. Phys.*, **4**, 11 (2008) 878–883.

[354] Markus Müller, Sebastian Diehl, Guido Pupillo & Peter Zoller. *Adv. At. Mol. Opt. Phys.*, **61** (2012) 1–80.

[355] Frank Verstraete, Michael M. Wolf & J. Ignacio Cirac. *Nat. Phys.*, **5**, 9 (2009) 633–636.

[356] S J Denny, S R Clark, Y Laplace, A Cavalleri & D Jaksch. *Phys. Rev. Lett.*, **114**, 13 (2015) 137001.

[357] John R Clem. *Phys. Rev. B*, **43**, 10 (1991) 7837–7846.

[358] A Rüfenacht, J.-P. Locquet, J Fompeyrine, D Caimi & P Martinoli. *Phys. Rev. Lett.*, **96**, 22 (2006) 227002.

[359] Yayu Wang, Lu Li & N P Ong. *Phys. Rev. B*, **73**, 2 (2006) 24510.

[360] Lu Li, Yayu Wang, M J Naughton, S Ono, Yoichi Ando & N P Ong. *EPL (Europhysics Lett.*, **72**, 3 (2005) 451.

[361] M B Salamon, Jing Shi, Neil Overend & M A Howson. *Phys. Rev. B*, **47**, 9 (1993) 5520–5523.

[362] Biplab Chattopadhyay & Subodh R Shenoy. *Phys. Rev. Lett.*, **72**, 3 (1994) 400–403.

[363] S Kamal, D A Bonn, Nigel Goldenfeld, P J Hirschfeld, Ruixing Liang & W N Hardy. *Phys. Rev. Lett.*, **73**, 13 (1994) 1845–1848.

[364] Mark Friesen. *Phys. Rev. B*, **51**, 1 (1995) 632–635.

[365] L Mathey & A Polkovnikov. *Phys. Rev. A*, **80**, 4 (2009) 41601.

[366] Carsten Honerkamp & Patrick A Lee. *Phys. Rev. Lett.*, **92**, 17 (2004) 177002.

[367] E. Almaas & D. Stroud. *Phys. Rev. B*, **65**, 13 (2002) 134502.

[368] S. Corlevi, W. Guichard, F. W J Hekking & D. B. Haviland. *Phys. Rev. Lett.*, **97**, 9 (2006) 096802.

[369] A.O Caldeira & A.J Leggett. *Ann. Phys. (N. Y).*, **149**, 2 (1983) 374–456.

[370] Rosario Fazio & Gerd Schön. "Quantum phase transitions in Josephson junction arrays". In "AIP Conf. Proc.", volume 427, pages 273–294. American Institute of Physics (1998).

[371] J. Q. You & Franco Nori. *Nature*, **474**, 7353 (2011) 589–597.

[372] R. J. Schoelkopf & S. M. Girvin. *Nature*, **451**, 7179 (2008) 664–669.

[373] I. Chiorescu, P. Bertet, K. Semba, Y. Nakamura, C. J. P. M. Harmans & J. E. Mooij. *Nature*, **431**, 7005 (2004) 159–162.

[374] J. Johansson, S. Saito, T. Meno, H. Nakano, M. Ueda, K. Semba & H. Takayanagi. *Phys. Rev. Lett.*, **96**, 12 (2006) 127006.

[375] Alexandre Blais, Alexander Maassen van den Brink & Alexandre M. Zagoskin. *Phys. Rev. Lett.*, **90**, 12 (2003) 127901.

[376] Alexandre Blais, Ren-Shou Huang, Andreas Wallraff, S. M. Girvin & R. J. Schoelkopf. *Phys. Rev. A*, **69**, 6 (2004) 062320.

[377] A. Wallraff, D. I. Schuster, A. Blais, L. Frunzio, R.-S. Huang, J. Majer, S. Kumar, S. M. Girvin & R. J. Schoelkopf. *Nature*, **431**, 7005 (2004) 162–167.

[378] M.H. Devoret, Steven Girvin & Robert Schoelkopf. *Ann. Phys.*, **16**, 10-11 (2007) 767–779.

[379] H. R. Lewis & W. B. Riesenfeld. *J. Math. Phys.*, **10**, 8 (1969) 1458.

[380] K. F. Riley, M. P. Hobson & S. J. Bence. "Mathematical Methods for Physics and Engineering". Cambridge University Press, 3rd edition (2006).

[381] G. W. Ford, J. T. Lewis & R. F. O'Connell. *Phys. Rev. A*, **37**, 11 (1988) 4419–4428.

[382] Jens M. Dobrindt. "Bio-sensing using toroidal microresonators & Theoretical cavity optomechanics". Phd thesis, École Polytechnique Fédérale de Lausanne (2012).

[383] Miguel Orszag. "Quantum Optics". Springer, Berlin, Heidelberg (2008).

[384] L. D. Landau & E. M. Lifshitz. "Statistical Physics". Butterworth-Heinemann, Oxford, 3 edition (1980).

[385] N.G. Van Kampen. "Stochastic Processes in Physics and Chemistry". Elsevier (2007).

[386] Claude Cohen-Tannoudji, Jacques. Dupont-Roc & Gilbert. Grynberg. "Atom-photon interactions : basic processes and applications". Wiley (1998).

[387] J. J. García-Ripoll, P. Zoller & J. I. Cirac. *Phys. Rev. A*, **71**, 6 (2005) 062309.

[388] Harold J. Metcalf & Peter. Van der Straten. "Laser cooling and trapping". Springer (1999).

[389] Andrew J Daley. *Adv. Phys.*, **63**, 2 (2014) 77–149.

[390] S. Attal & Y. Pautrat. page arXiv 0311002.

[391] A. Aspect, E. Arimondo, R. Kaiser, N. Vansteenkiste & C. Cohen-Tannoudji. *Phys. Rev. Lett.*, **61**, 7 (1988) 826–829.

[392] Mark Kasevich & Steven Chu. *Phys. Rev. Lett.*, **69**, 12 (1992) 1741–1744.

[393] D Marcos, A Tomadin, S Diehl & P Rabl. *New J. Phys.*, **14**, 5 (2012) 055005.

[394] B. Kraus, H. P. Büchler, S. Diehl, A. Kantian, A. Micheli & P. Zoller. *Phys. Rev. A*, **78**, 4 (2008) 042307.

[395] S. Diehl, W. Yi, A. J. Daley & P. Zoller. *Phys. Rev. Lett.*, **105**, 22 (2010) 227001.

[396] A. Metelmann & A. A. Clerk. *Phys. Rev. X*, **5**, 2 (2015) 021025.

[397] Berislav Buca, Joseph Tindall & Dieter Jaksch. page arXiv 1804.06744.

[398] Carlo Beenakker & Christian Schönenberger. *Phys. Today*, **56**, 5 (2003) 37–42.

[399] Henk van Houten & Carlo Beenakker. *Phys. Today*, **49**, 7 (1996) 22–27.

[400] A. I. Yanson, G. Rubio Bollinger, H. E. van den Brom, N. Agraït & J. M. van Ruitenbeek. *Nature*, **395**, 6704 (1998) 783–785.

[401] Y Chu, N P de Leon, B J Shields, B Hausmann, R Evans, E Togan, M J Burek, M Markham, A Stacey, A S Zibrov, A Yacoby, D J Twitchen, M Loncar, H Park, P Maletinsky & M D Lukin. *Nano Lett.*, **14**, 4 (2014) 1982–1986.

[402] Shanying Cui, Andrew S Greenspon, Kenichi Ohno, Bryan A Myers, Ania C Bleszynski Jayich, David D Awschalom & Evelyn L Hu. *Nano Lett.*, **15**, 5 (2015) 2887–2891.

[403] Gopalakrishnan Balasubramanian, Philipp Neumann, Daniel Twitchen, Matthew Markham, Roman Kolesov, Norikazu Mizuochi, Junichi Isoya, Jocelyn Achard, Johannes Beck, Julia Tissler, Vincent Jacques, Philip R. Hemmer, Fedor Jelezko & Jörg Wrachtrup. *Nat. Mater.*, **8**, 5 (2009) 383–387.

[404] M Steger, K Saeedi, M L W Thewalt, J J L Morton, H Riemann, N V Abrosimov, P Becker & H.-J. Pohl. *Science*, **336**, 6086 (2012) 1280–1283.

[405] Lorenza Viola, Emanuel Knill & Seth Lloyd. *Phys. Rev. Lett.*, **82**, 12 (1999) 2417–2421.

[406] Jiangfeng Du, Xing Rong, Nan Zhao, Ya Wang, Jiahui Yang & R B Liu. *Nature*, **461** (2009) 1265.

[407] G de Lange, Z H Wang, D Ristè, V V Dobrovitski & R Hanson. *Science*, **330**, 6000 (2010) 60 LP – 63.

[408] Dieter Suter & Gonzalo A. Álvarez. *Rev. Mod. Phys.*, **88**, 4 (2016) 041001.

[409] Young-Ik Sohn, Srujan Meesala, Benjamin Pingault, Haig A. Atikian, Jeffrey Holzgrafe, Mustafa GündoÄ§an, Camille Stavrakas, Megan J. Stanley, Alp Sipahigil, Joonhee Choi, Mian Zhang, Jose L. Pacheco, John Abraham, Edward Bielejec, Mikhail D. Lukin, Mete Atatüre & Marko Lončar. *Nat. Commun.*, **9**, 1 (2018) 2012.

[410] D. N. Langenberg, D. J. Scalapino, B. N. Taylor & R. E. Eck. *Phys. Rev. Lett.*, **15**, 7 (1965) 294–297.

[411] A.K. Jain, K.K. Likharev, J.E. Lukens & J.E. Sauvageau. *Phys. Rep.*, **109**, 6 (1984) 309–426.

[412] Alexei Koshelev & L N. Bulaevskii. *Phys. Rev. B*, **77**, 014530.

[413] Frank Schlawin, Andrea Cavalleri & Dieter Jaksch. page arXiv 1804.07142.

[414] Jonathan B. Curtis, Zachary M. Raines, Andrew A. Allocca, Mohammad Hafezi & Victor M. Galitski. page arXiv 1805.01482.

[415] Qi Zhang, Minhan Lou, Xinwei Li, John L Reno, Wei Pan, John D Watson, Michael J Manfra & Junichiro Kono. *Nat Phys*, **12** (2016) 1005–1011.

[416] Simone De Liberato. *Phys. Rev. Lett.*, **112**, 016401.

[417] Qi Zhang, Takashi Arikawa, Eiji Kato, John L. Reno, Wei Pan, John D. Watson, Michael J. Manfra, Michael A. Zudov, Mikhail Tokman, Maria Erukhimova, Alexey Belyanin & Junichiro Kono. *Phys. Rev. Lett.*, **113**, 4 (2014) 047601.

[418] M A Sentef, M Ruggenthaler & A Rubio. *Sci. Adv.*, **4**, 11.

[419] Martin Kiffner, Jonathan R Coulthard, Frank Schlawin, Arzhang Ardavan & Dieter Jaksch. *Phys. Rev. B*, **99**, 8 (2019) 85116.

[420] Xinwei Li, Motoaki Bamba, Ning Yuan, Qi Zhang, Yage Zhao, Maolin Xiang, Kai Xu, Zuanming Jin, Wei Ren, Guohong Ma, Shixun Cao, Dmitry Turchinovich & Junichiro Kono. *Science*, **361**, 6404 (2018) 794–797.

[421] Carlos A. Parra-Murillo, Manuel H. Muñoz-Arias, Javier Madroñero & Sandro Wimberger. *Phys. Rev. A*, **95**, 3 (2017) 032125.

[422] Tomaž Prosen & Enej Ilievski. *Phys. Rev. Lett.*, **107**, 6 (2011) 060403.

[423] Matthieu Vanicat, Lenart Zadnik & Tomaž Prosen. *Phys. Rev. Lett.*, **121**, 3 (2018) 030606.

[424] David Oettinger, R. Chitra & Juliana Restrepo. *Eur. Phys. J. B*, **87**, 10 (2014) 224.